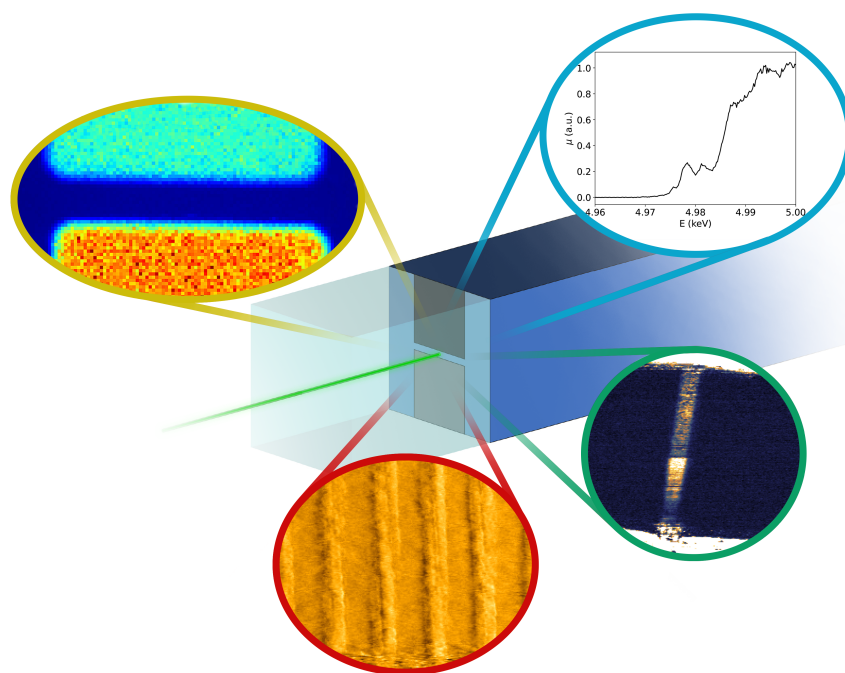**Università degli Studi di Torino**

Doctoral School of the University of Torino

PhD Programme in Chemical and Materials Sciences XXXVI Cycle

High-brilliance X-ray techniques for oxide functionalization and characterization

Andrea Alessio

Supervisor:

Prof. Marco Truccato

Università degli Studi di Torino

Doctoral School of the University of Torino

PhD Programme in Chemical and Materials Sciences XXXVI Cycle

High-brilliance X-ray techniques for oxide functionalization and characterization

Candidate: **Andrea Alessio**

Supervisor: Prof. **Marco Truccato**

Jury members: Prof. **Gloria Subias**
                            Universidad de Zaragoza - CSIC
                            Instituto de Nanociencia y Materiales de Aragón (INMA)

                            Prof. **Roberto Felici**
                            CNR
                            Istituto di Struttura della Materia (ISM)

                            Prof. **Ettore Vittone**
                            Università di Torino
                            Dipartimento di Fisica

Head of the Doctoral School: Prof. Eleonora Bonifacio
PhD Programme Coordinator: Prof. Bartolomeo Civalleri

Torino, 2024

Contents

3

Contents

Introduction

The dramatic increase in X-ray sources brilliance which has taken place in the last decades has opened many new possibilities for the study of materials by means of X-ray based techniques. In particular, the recent development of fourth generation synchrotron sources, led by the European Synchrotron Radiation Facility (ESRF), and the foreseen upgrade of other synchrotron facilities all around the world, together with the development of X-ray Free Electron Lasers (XFELs), has allowed to achieve unprecedented performances.

The increase in brilliance has also corresponded to an increase in X-ray optics performances, with a substantial decrease of the X-ray spot size achievable. Flux densities delivered by synchrotron sources have therefore increased dramatically, making unwanted material modifications much more probable.

Most known X-ray induced damage involves biological systems, in particular in the field of protein crystallography [1–3]. Nevertheless, with the increase of X-ray sources intensity, radiation induced material modifications are not only limited to biological and soft matter, but can affect inorganic materials as well. Indeed, several phenomena have been reported, such as photoreduction, crystallization and phase transitions [4–10].

Looking at these phenomena from a different perspective, localized material modification with nanoscale resolution can also be exploited to tailor the structural and

7

electrical properties of functional materials (such as superconducting and semi-conducting oxides) by means of controlled X-ray irradiation, and to develop a resist-free X-ray nanopatterning (XNP) technique [11, 12]. To precisely control the irradiation parameters needed to achieve the desired outcome, a clear understanding of the microscopic mechanism underlying defects formation in oxides must be determined.

The focus of this thesis is on the investigation of X-ray induced material modifications in semiconducting oxides, in particular TiO_2 and $SrTiO_3$, which has also led to some experimental trials aiming at improving the performances of some electronic devices made up of these materials, like e.g. memristors. The first chapter is intended to give a short introduction about X-ray interactions with matter and related experimental techniques, together with the description of the investigated material and state of the art in X-ray nanopatterning. The second chapter will focus on the functionalization of semiconducting oxides typically used in oxide based memristive devices. In the third chapter the possible thermal origin of material damage will be investigated by means of finite element simulations, atomic force microscopy, photoluminescence and X-ray diffraction. The fourth chapter is devoted to the development of a laboratory scale high brilliance X-ray facility based on a MetalJet source, where these X-ray induced effects could be studied (on a different time and spatial scale) in the near future.

Theoretical background and state of the art

1.1 X-ray interaction with matter

X-rays are high energy electromagnetic radiation, also known in many languages as Röntgen radiation, since Wilhelm Röntgen discovered them in 1895, and was awarded the first Nobel prize in Physics in 1901 for his discovery.

Since their discovery, X-rays have been used in several application, the most widely known being medical diagnosis. Indeed, the first radiograph performed by Röntgen on his wife's hand stands as one of the most famous pictures in science history.

The X-ray region of the electromagnetic spectrum is typically considered to extend between 0.1 and 100 keV as an order of magnitude, between ultraviolet and gamma rays. The wavelength of X-rays are in the order of angstroms (1 Å for a 12.4 keV photon), making them particularly suitable to probe distances in the order of interatomic spacing in condensed matter.

According to their energy, X-rays are commonly divided into two categories: soft X-rays ($E < 5 - 10$ keV) and hard X-rays ($E > 5 - 10$ keV).

X-rays interact with matter in several ways: they can be absorbed, transmitted or scattered (elastically or inelastically). Figure 1.2 shows the cross section of different processes as a function of photon energy.

Figure 1.1: First radiography of Wilhelm Röntgen's wife's hand.
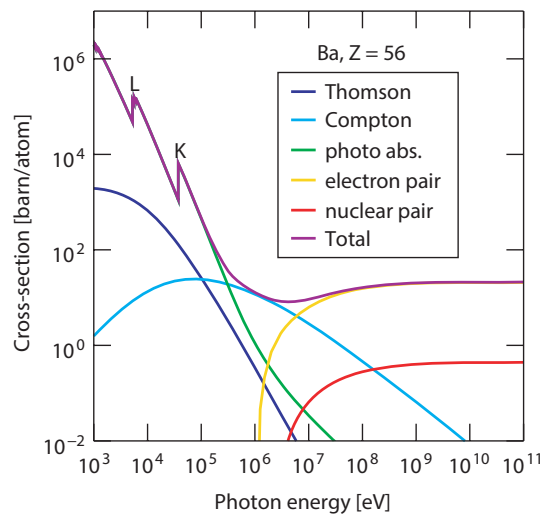
Figure 1.2: Cross section of different interaction processes as a function of the photon energy for Ba [13].

Thompson scattering

Elastic (Thompson) scattering is due to the interaction of the incoming photon with the electrons in the material. The oscillating electric field accelerates the

10

electron, which in turn emits electromagnetic radiation with the same frequency. Elastic scattering is dominant in the low energy range of X-rays with respect to inelastic scattering (see figure 1.2).

Compton scattering

Inelastic (Compton) scattering is the dominant scattering process at high photon energies. The incoming photon loses part of its energy which is transferred to an electron in the material. The wavelength of the outgoing photon can be calculated by applying the conservation of energy and momentum:

$$\lambda' - \lambda = \lambda_C (1 - \cos \theta) \tag{1.1}$$

where λ is the incoming photon wavelength, λ' is the scattered photon wavelength, $\lambda_C = \frac{h}{m_e c}$ is the electron Compton wavelength and θ is the scattering angle.
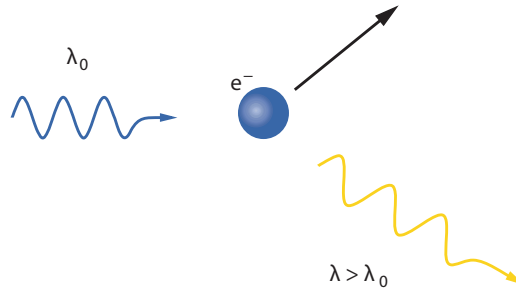
Figure 1.3: Compton scattering process [13].

Photoabsorption

The attenuation of the intensity of the radiation when traveling through a medium can be expressed with the Lambert-Beer law:

$$\frac{I}{I_0} = e^{-\mu z} \tag{1.2}$$

where μ is the absorption coefficient, which is strongly dependent on the atomic number ($\mu \propto Z^4$) and on the photon energy ($\mu \propto E^{-3}$).

11

The absorption coefficient for different elements as a function of photon energy is shown in figure 1.4.
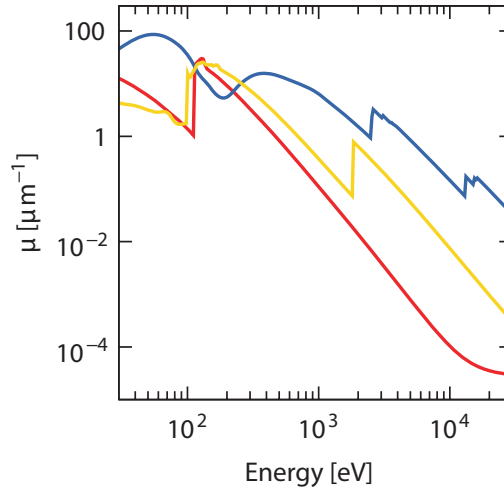
Figure 1.4: Absorption coefficient as a function of the photon energy for Be (red), Si (yellow) and Pb (blue) [13].

Sharp increases in the absorption coefficient (absorption edges) can be seen in figure 1.4 when the incoming photon has enough energy to eject an electron from an atomic orbital to the continuum (photoelectric effect). The free electron generated is usually referred to as photoelectron. Absorption edges are named according to the orbital from which the electron is ejected; for example the K edge is related to the ejection of an electron from the K shell (1s orbital).

After the absorption of the photon and subsequent emission of a photoelectron, two processes can take place: X-ray fluorescence and Auger electron emission.

In X-ray fluorescence (XRF), an electron from an outer atomic shell relaxes to fill the hole left behind by the photoelectron, resulting in the emission of a photon with an energy equal to the separation of the two levels involved. This process occurs on a timescale in the order of tens of femtoseconds. Since the energy levels are well defined, the emission lines are very sharp and are characteristic of the absorbing element.

The nomenclature of the X-ray fluorescence lines is shown in figure 1.5.
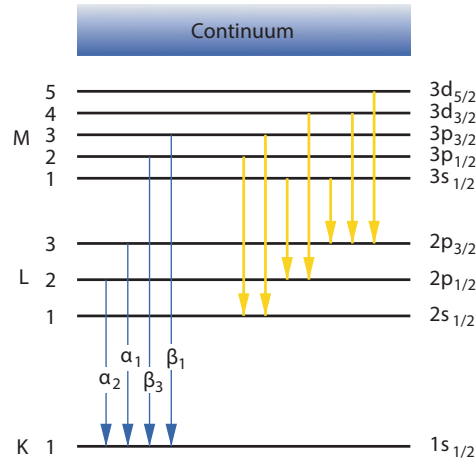
Figure 1.5: Nomenclature of XRF lines [13].

The other possible relaxation phenomenon is the emission of an Auger electron. In this case an electron from an outer shell relaxes to fill in the hole left by the photoelectron, but in this case the excess energy is released with the emission of a second electron from an outer shell, which has a binding energy lower than the excess energy.

The two processes and their yield as a function of the atomic number of the target atom are shown in figure 1.6. It is possible to see that Auger emission is dominant at low Z values, while fluorescence is dominant for heavier elements. Moreover, the yield of fluorescence resulting from a hole in the K shell is higher than fluorescence from a hole in the L shell.

Refraction and reflection

The index of refraction of X-rays can be expressed with the complex quantity:

$$n = 1 - \delta + i\beta \tag{1.3}$$

where β is related to absorption while the real part $n_R = 1 - \delta$ is slightly smaller than unity and is responsible of refraction. Being n_R less than 1, X-rays bend
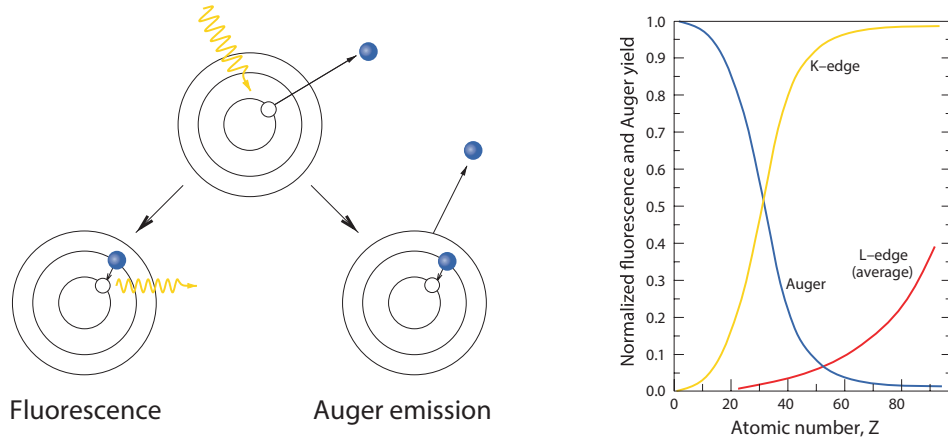
Figure 1.6: Schematic representation of fluorescence and Auger emission processes, and normalized yields as a function of the atomic number of absorbing material [13].

toward a shallower angle with respect to the angle of incidence when passing from a low density material to a denser material, unlike visible light (see figure 1.7). From Snell's law:

$$\frac{\cos \alpha}{\cos \alpha'} = n_R \tag{1.4}$$

a critical angle exists such that $\cos \alpha_c = n_R$. For $\alpha < \alpha_c$, X-rays undergo total external reflection. The critical angle α_c can be approximated to:

$$\alpha_c \approx \sqrt{2\delta} \tag{1.5}$$

Since δ is very small, X-rays can be reflected only for very small incidence angles (few tenths of a degree).

1.2 X-ray sources

1.2.1 X-ray tube

The most widely known and used source for the production of X-rays is the X-ray tube. This device consists of a vacuum tube with two terminals, a cathode and an anode. The cathode is typically a tungsten filament heated by an electric
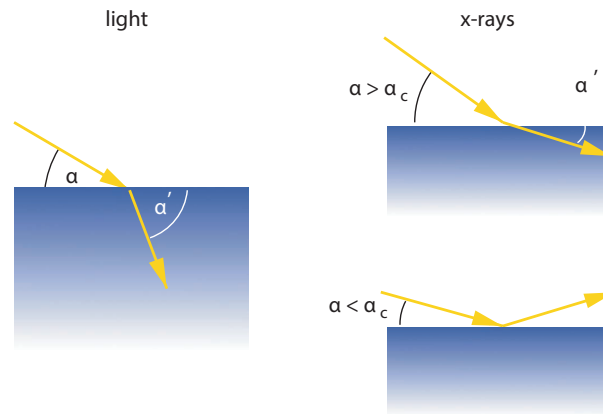
Figure 1.7: Refraction of visible light and X-rays when entering a transparent material [13]. For $\alpha < \alpha_c$, X-rays ungergo total external reflection.

current, which emits electrons by thermionic emission. The electrons emitted by the cathode are accelerated by the high voltage applied between the cathode and the anode (up to 150 kV), and impact on the target anode material, emitting X-ray radiation. The emission spectrum of this kind of source is characterized by a continuous background called Bremsstrahlung or braking radiation, which is caused by the deceleration of the electrons upon entering the target material, and whose kinetic energy is converted into radiation.

On top of the continuous background, the characteristic X-ray fluorescence lines of the target element are emitted.The most common target materials are Cu, Mo and W.

The main limitation of this kind of source is the intense heat generated by the electron beam impacting the anode material, which can reach very high temperature and melt. The typical power of X-ray tubes is therefore limited to a few watts. To overcome this limitation, different designs have been created, such as rotating anode tubes, which use a rotating metal plate as anode material, allowing to distribute the heat generated by the electron beam on a larger area, and MetalJet sources (see section 1.2.4).

1.2.2   Synchrotron radiation

Synchrotron radiation refers to the electromagnetic field radiated by relativistic accelerated particles [14]. Electrons traveling at speed close to the speed of light, with a Lorentz factor

$$\gamma = \frac{E}{mc^2} = 1957E[GeV] \qquad (1.6)$$

emit radiation in a pencil-like beam in the direction they are traveling. The divergence of the beam is $\theta \sim \gamma^{-1}$. Typical electron energies used in synchrotrons range from $3\,GeV$ (e.g. DIAMOND, ALBA, SOLEIL) to $6\,GeV$ (e.g. ESRF-EBS, PETRA-III). The highest energy syncrotron in the world is Spring8 in Japan, with an energy of $8\,GeV$.

This naturally collimated beam is the reason for the very high brilliance of synchrotron radiation source, being the brilliance defined as:

$$B = \frac{photons/s}{(mrad)^2(mm)^2(0.1\% \text{ bandwidth})} \qquad (1.7)$$

A synchrotron is made of different components:

- A source of electrons, which can be generated by thermionic emission by a hot filament, and are accelerated by a linear accelerator (linac);

- a booster ring, where electrons from the linac are accelerated to their final energy and injected into the storage ring;

- a storage ring, where electrons are kept on a closed path by bending magnets (BM). In the straight parts of the ring between bending magnets, insertion devices (ID) are present. Both BMs and IDs produce synchrotron radiation. Energy loss of electrons is compensated by radiofrequency (RF) cavities, which provide the right amount of energy they have lost;

- the beamlines, which are tangential to the storage ring and collect the radiation emitted by BMs and IDs.

BMs produce a flattened cone of radiation with a broad spectral emission, which depends on the electron energy and the strength of the magnetic field (see figure 1.9).
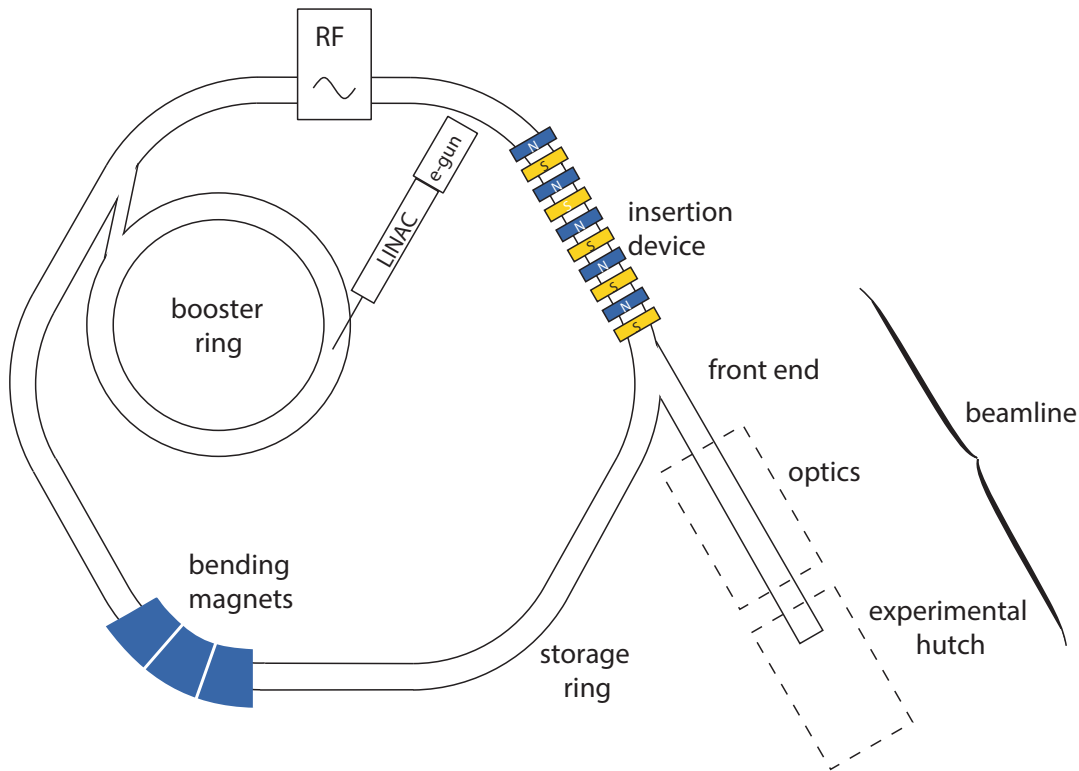
Figure 1.8: Schematic representation of a typical synchrotron radiation facility [13].

IDs consist of sets of magnetic dipoles that produce an alternating magnetic field, which forces the electrons to travel on an oscillatory path on the plane of the storage ring. IDs are devided in two kinds:

- wigglers, which force electrons to oscillate with excursion bigger than the natural γ^{-1} opening angle, which result in non overlapping emission cones for each turn and added intensity. The resulting spectrum is the sum of the individual BM-like spectra produced by each dipole;

- undulators, which are characterized by smaller excursions that cause the emission cones to overlap and interfere with each other. The resulting spectrum is peaked at frequencies that interfere constructively, whose intensity is squared.

Wigglers and undulators can be described by a dimensionless parameter K:

17
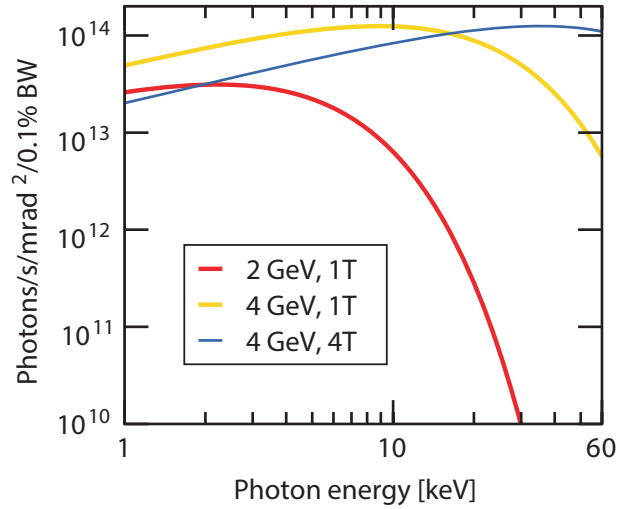
Figure 1.9: Emission spectrum of bending magnets for different electron energies and magnetic field strengths [13].

$$K = \frac{eB\lambda_u}{2\pi\beta mc} \tag{1.8}$$

with B and λ_u being the magnetic field and period of the ID, and $\beta = v/c$ relates to the speed of the electrons. The value of K determines whether an ID is a wiggler ($K >> 1$) or an undulator ($K < 1$), and determines the spectral properties of radiation (see figure 1.10).

The time structure of synchrotron radiation is related to how electrons are bunched in the storage ring. Bunches of electrons travel in the storage ring, so that each time a bunch of electrons is deflected by BMs or IDs, an intense pulse of radiation is produced.

Properties of synchrotron radiation

The main properties of synchrotron radiation which set it apart from traditional laboratory scale sources are coherence, polarization and energy range.

While X-rays from an X-ray tube are completely incoherent, unless filtered and collimated (leading to huge power losses), synchrotron radiation has a large de-
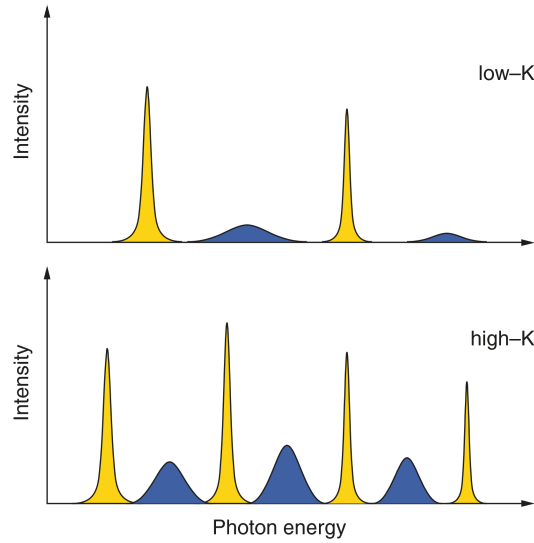
Figure 1.10: Spectra of low-K and high-K undulators. The value of K determines the energy separation and relative intensity of even (blue) and odd (yellow) harmonics [13].

gree of coherence, both spatial and temporal. Because of the non infinitesimal bandwidth of any real-world X-ray source, the different frequencies will eventually get out of phase with one another after travelling a characteristic length called longitudinal (or temporal) coherence length, which can be defined as:

$$l_c^{(l)} = \frac{\lambda^2}{\Delta\lambda} \tag{1.9}$$

Waves with the same wavelength can also interfere with each other because of the slightly different direction of propagation, due to the non-zero source size D and divergence $\Delta\theta$. A transverse (or spatial) coherence length can be therefore defined as:

$$l_c^{(t)} = \frac{\lambda}{2\Delta\theta} = \frac{\lambda R}{2D} \tag{1.10}$$

with R being the distance from the source.

The intrinsic coherence of synchrotron radiation makes it ideal for imaging applications such as phase-contrast imaging.

Since electrons in the insertion devices oscillate on the storage ring plane, the emitted photons are linearly polarized on the same plane for an observer on the same plane. If the observer is above or below the plane, he will observe a left-circular polarized or right-circular polarized light, respectively.

The energy of photons emitted from an ID depends on the K parameter, which in turn depends on strength and pitch of the magnetic dipoles (B and λ_u respectively). Because of this, synchrotron light can be tuned across a wide energy range. IDs can be designed to produce X-rays from soft X-rays to hard X-rays, and energy can be tuned by changing the magnetic field strength. The wide energy range and tunability of synchrotron radiation makes it perfect for spectroscopic applications.

The recent upgrade of the European Synchrotron Radiation Facility (ESRF) to ESRF-EBS (Extremely Brilliant Source), which became the first 4th generation synchrotron in the world, allowed to achieve higher photon fluxes and especially coherence in comparison with previous generation facilities.

1.2.3 X-ray Free Electron Lasers (XFELs)

A relatively novel high brilliance X-ray source are X-ray Free Electron Lasers. The working principle is similar to synchrotron undulators, consisting of a periodic arrangement of magnetic dipoles which accelerate relativistic electron bunches with subsequent emission of electromagnetic radiation. The difference with respect to synchrotrons is the long straight path of the electrons, which are accelerated in a linear accelerator (LINAC) and travel through a single very long undulator.

While in a normal undulator electrons emit without correlation, in an XFEL the magnetic field component of the emitted waves generates a Lorentz force that pushes the electrons into microbunches with a periodicity equal to the wavelength of the emitted wave. Since electrons within a microbunch oscillate in phase, the electric fields of the emitted waves sums up, and the intensity increases with the square of the number of electrons. The emitted power scales exponentially with

the undulator length, up to a saturation length (see figure 1.11e):

$$I = I_0 \exp\left(\frac{x}{L_G}\right) \tag{1.11}$$

where L_G is called gain length and represents the distance required to achieve lasing [15]. The starting wave could be an external X-ray beam (called "seed") or the spontaneous initial emission, with a mechanism called SASE (Self-Amplified Spontaneous Emission) [15, 16].
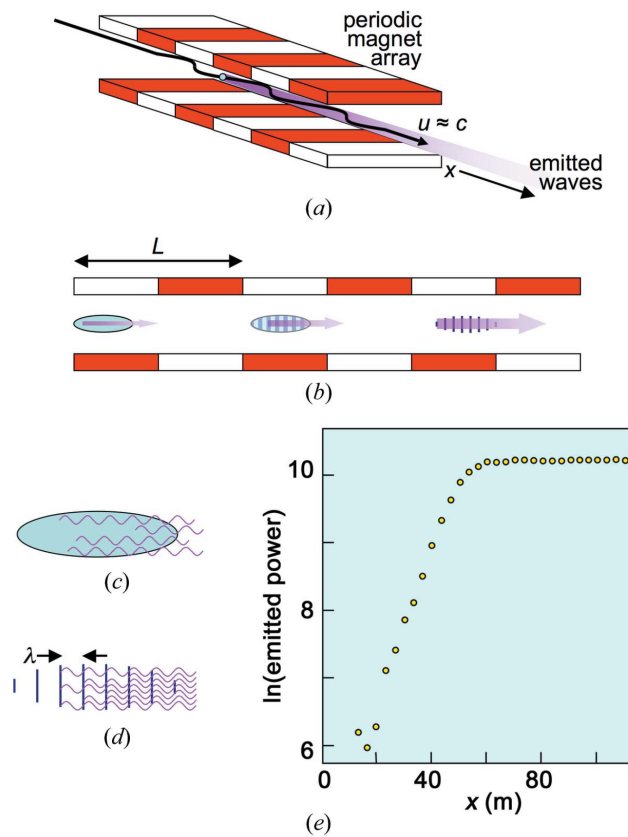
Figure 1.11: a) Schematic representation of a XFEL undulator. b) Evolution of microbunching process. Contrary to non-microbunched electrons (c), the emission of electrons in microbunches (d) separated from each other by one wavelength is correlated. e) Exponential invrease of emitted power as a function of undulator length [15, 17].

Compared to synchrotron radiation, XFELs pulses are much shorter (in the order of femtoseconds) and much more intense (photon fluxes in the order of 10^{13} photons/pulse). For this reason XFELs are suitable to study matter under extreme conditions, or very fast molecular dynamics.

1.2.4   MetalJet source

A novel laboratory scale technology developed to overcome the power limitation of conventional X-ray tubes is the liquid metal jet anode X-ray source [18]. Since the main limitation of conventional sources is the thermal energy deposited by the electron beam on the anode material, power must be limited to avoid melting the anode itself. Liquid metal jet sources use a liquid metal jet with diameter in the order of $170\,\mu m$ flowing at speed around $60\,m/s$ as anode material . Such anode can dissipate the heat generated much easier than conventional solid state anodes.

The selection of the anode material must satisfy different requirements, such as low melting point, high specific heat capacity, large temperature span between melting and boiling and high heat of vaporization. Typical alloys used in metal jet sources contain Pb, In, Sn and Ga. The resulting emission spectrum of the source is characterized by the emission lines of all the elements in the alloy on top of a continuous Bremsstrahlung background.
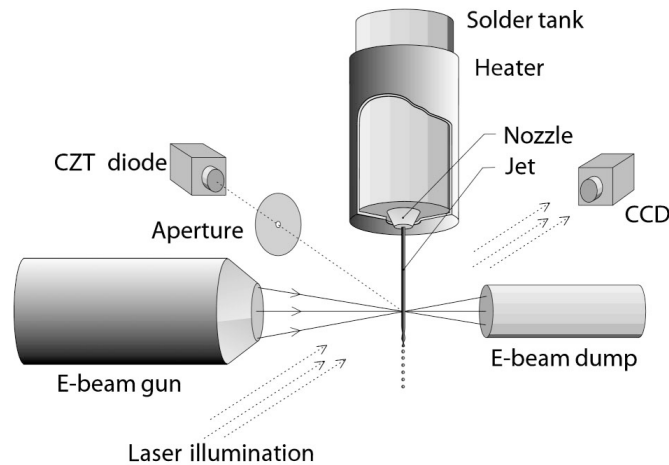
Figure 1.12: Experimental arrangement of the liquid-metal-jet anode x-ray source proof-of-principle experiment [18].

Thanks to this novel technology, liquid anode metal jet sources can achieve brilliance a few orders of magnitudes higher than traditional X-ray tubes (see figure 1.13).
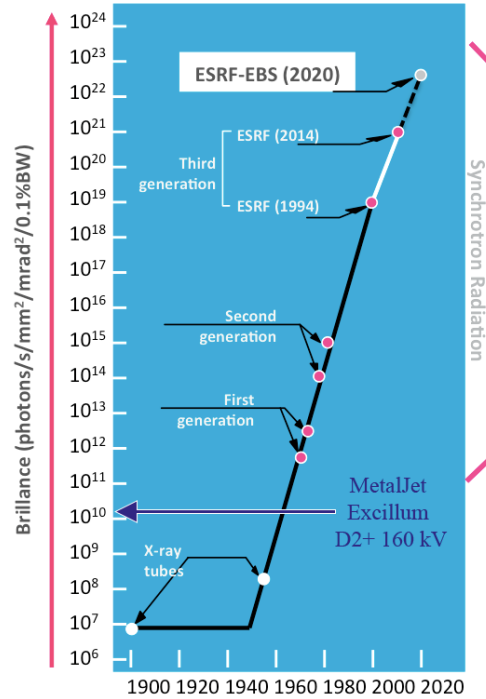
Figure 1.13: Time evolution of X-ray sources brilliance.

1.3 X-ray optics

Kirkpatrick-Baez mirrors

As discussed in the previous sections, since the index of refraction for X-rays $n_R \lesssim 1$, X-rays are totally reflected for very small incidence angles only. To focus the hard X-ray beam from a synchrotron bending magnet or insertion device, ellipsoidal mirrors with two axes of curvature (horizontal and vertical) can be used, with one focal point located at the exit of the X-ray source and the other one at the focal plane of the experiment. Since it is very difficult to fabricate elliptical mirrors with two axes of curvature, a double mirror configuration is commonly used, and is known as Kirkpatrick-Baez (KB) system. Two ortogonal ellipsoidal

mirrors focus the beam on the horizontal and vertical axis respectively, emulating a 3D ellipsoidal surface [19]. A schematic representation of a typical KB mirror is shown in figure 1.14.
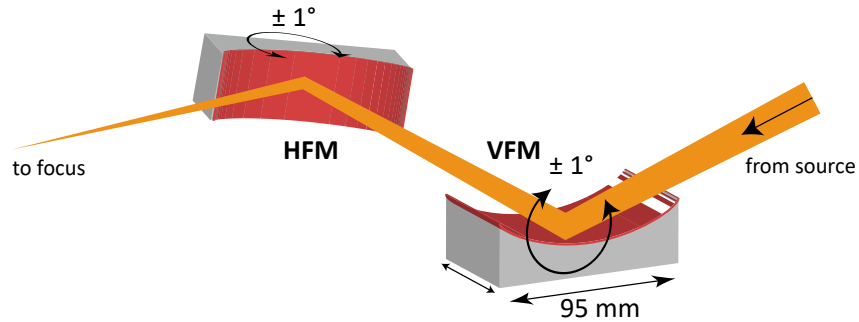
Figure 1.14: Schematic representation of a KB mirrors setup [19].

The design of KB mirrors must take into account a suitable reflectivity (the incidence angle must be smaller than the critical angle), and must have a very precise shape an polished surface to avoid artifacts in imaging applications. Focal spots down to 10 nm can be achieved. To overcome the limited numerical aperture, multilayer coatings can be used [19].

Fresnel zone plates

Fresnel zone plates are diffraction gratings made from concentric rings of alternating high density and low density (air or vacuum) materials. By absorbing light on the opaque rings, constructive interference occurs on a focal spot [19].
Several diffraction orders are obtained by constructive interference, as shown in figure 1.15.

Higher efficiency can be achieved by introducing a π phase shift in the high density regions instead of absorption. This is challenging to achieve because rings must have a thickness in the order of µm, resulting in high aspect ratio structures that can be fabricated with electron beam lithography.
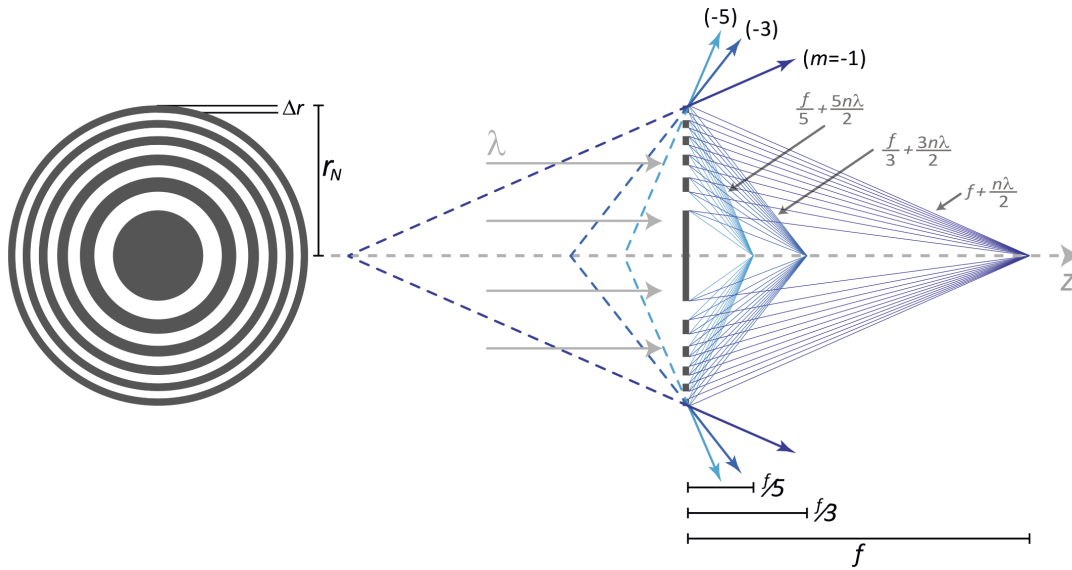
Figure 1.15: Representation of a Fresnel zone plate in the aperture plane (left) and in a plane containing the optical axis (right) [19].

Compound Refractive Lenses

Compound refractive lenses (CRLs) exploit the weak refraction of hard X-rays in condesed matter to focus the beam. They are fabricated by drilling arrays of small holes in a high-transmission material such as Be. According to the orientation of the holes, cylindrical (coplanar holes) or quasi-spherical (alternating holes drilled at 90° to one another) focusing can be achieved [13] (see figure 1.16).

The focal length of CRLs can be expressed as:

$$f = R/2n_h\delta \tag{1.12}$$

with R and n_h being the radius and number of holes and δ being the refractive index decrement.

The main disadvantages of such optics are the photon energy dependence of the focal length and the poor transmission.
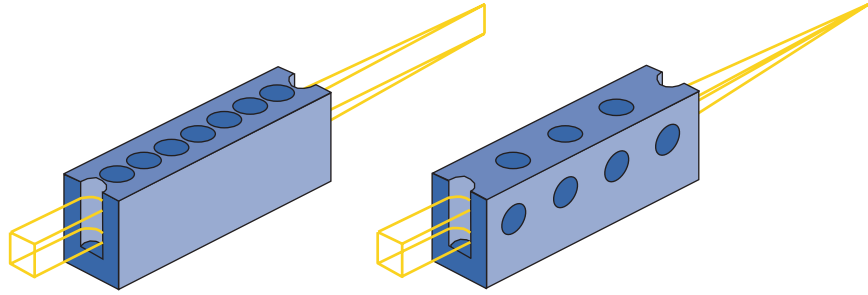
Figure 1.16: Cylindrical (left) and quasi-spherical (right) focusing by CRLs [13].

Polycapillary optics

Polycapillary optics are based on reflection of X-rays inside curved hollow channels, with typical diameter between 2 and 50 µm [20]. The incident angle must remain below the critical angle to achieve multiple reflections in the channel. Thousands of curved guides are glued together forming a monolithic optic which focuses the X-rays to a single point.

Figure 1.17 shows a schematic of the polycapillary optics, where Ω_{in} and Ω_{out} are the divergences on the input and output side respectively, f_1 and f_2 are the input focal distance (IFD) and output focal distance (OFD) and L is the length of the optic.

Polycapillary optics are achromatic, and therefore suitable for broadband applications [20].
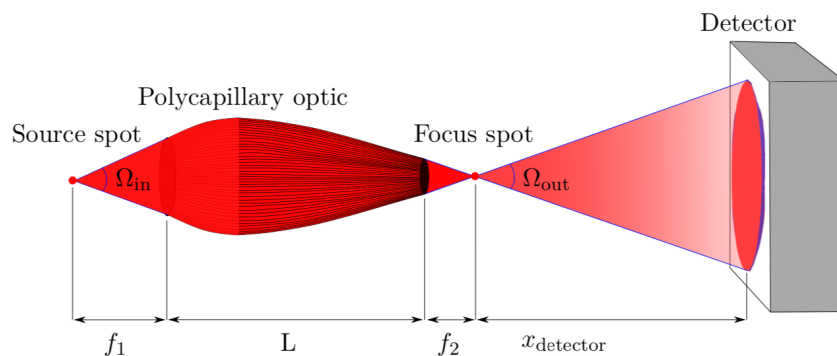
Figure 1.17: Schematic of a polycapillary optic.

Twin paraboloidal mirrors

Twin paraboloidal mirrors are made from a hollow cylinder whose inner surface is shaped with two mirrored paraboloids, one which collimates the X-ray beam and another one that focuses the beam on a single spot. The advantages of such optics are a high output flux, thanks to its high transmission, micrometric spot size and large working distance. Since twin parabolidal mirrors are achromatic, all X-ray energies are concentrated in the same focal point.

Figure 1.18 shows a schematic of twin paraboloidal mirrors from Sigray[1].
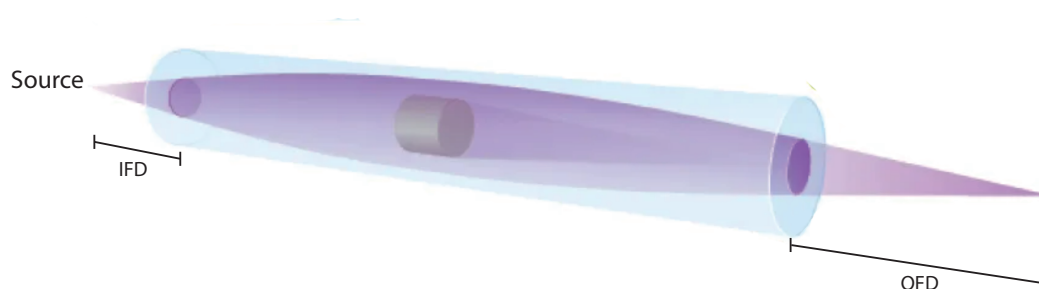
Figure 1.18: Schematic of twin paraboloidal mirrors optic.

1.4 X-ray based characterization techniques

1.4.1 X-ray fluorescence (XRF)

X-ray fluorescence (XRF) is a commonly used technique which allows for the determination of atomic species in the sample under investigation. It is based on the emission of characteristic X-ray photons from an excited atom. These fluorescence photons are generated by electronic transitions from an outer atomic shell to fill a hole left by a photoelectron. Since the energy of these transitions is characteristic of each element, the XRF spectrum shows sharp lines that can be associated with the elements in the sample, giving both qualitative and quantitative information on the elemental composition of the sample.

XRF spectra are typically measured by multichannel analyzers (MCA) of the

---

[1]https://sigray.com/

energy-dispersive signals produced by devices such as PIN diodes or Silicon Drift Detectors (SDD).

If focused X-ray beams are used to excite the sample, spatially resolved information on the sample composition can be obtained. By raster scanning the sample while collecting XRF spectra for each mesh point, hyperspectral images can be measured, from which elemental maps can be extracted by plotting the intensity of the emission lines of each element in each point.

The spatial resolution achievable is only limited by the X-ray beam size. Synchrotron beamlines such as ID16 of European Synchrotron Radiation Facility can therefore reach resolutions down to 50 nm.

1.4.2 X-ray excited optical luminescence (XEOL)

X-ray excited optical luminescence (XEOL) is an energy-transfer event in which the absorption of the X-ray photon produces a large number of energetic electrons (photoelectron and Auger). These electrons in turn cause further ionization and excitation. The energy is transferred to luminescent centers through inelastic processes which ultimately lead to the creation of holes in the valence band and electrons in the conduction band in semiconductors [21].

The recombination of holes and electrons generates photons with an energy corresponding to the energy difference between the states involved in the final step of the de-excitation cascade. XEOL can be therefore used to study the electronic structure and optical properties of materials.

Because of the energy dependence of the attenuation length, energy tunable X-ray sources such as synchrotron radiation can be used to probe different depths inside the material, and, by tuning the energy around the absorption edge of a specific element, site selective information can be obtained by combining XEOL with X-ray absorption spectroscopy (XANES/EXAFS). Excited states can decay optically via more pathways through exciting the core-to-continuum, core-to-quasi-bound and core-to-bound transitions. Different chemical sites of the same element can also be sensitive to a specific channel via selective excitation [22, 23].

Time-resolved XEOL (TR-XEOL) can also be performed thanks to the pulsed time structure of synchrotron radiation, probing the decay time of the luminescence of color centers by using streak cameras to record the time evolution of the luminescence spectrum as a function of time following the initial excitation by an X-ray pulse [22, 24].

1.4.3 X-ray absorption spectroscopy (XAS)

X-ray absorption spectroscopy (XAS) provides information on the electronic, structural and magnetic properties of materials. If a photon has an energy equal or higher than the energy of a core level, the photon can be absorbed, exciting a core electron to an empty state above the Fermi energy [25].

By changing the photon energy, an absorption edge can be measured, which correspond to the core level energy and is therefore element specific.

Two regions can be discerned in an X-ray absorption spectrum:

- the XANES (X-ray Absorption Near Edge Structure) region;

- the EXAFS (Extended X-ray Absorption Fine Structure) region.

The XANES region corresponds to the excitation of a core electron to unfilled bound states, or to continuum. Transitions to empty bound states give rise to pre-edge peaks. The result of photon absorption in the XANES region is a core hole and a low energy photoelectron. At 50 to 1000 eV above the edge, the EXAFS region begins, corresponding to high energy photoelectrons generated after photon absorption.

XANES gives information on the valence, oxidation state, site symmetry, coordination chemistry and orbital hybridization of the target element. Depending on the oxidation state, the position of the main absorption edge, together with the intensity of the pre-edge peaks can change considerably.

The typical oscillations in the EXAFS region on the other hand depend on the autointerference of the photoelectron wavefunction, which modifies the absorption
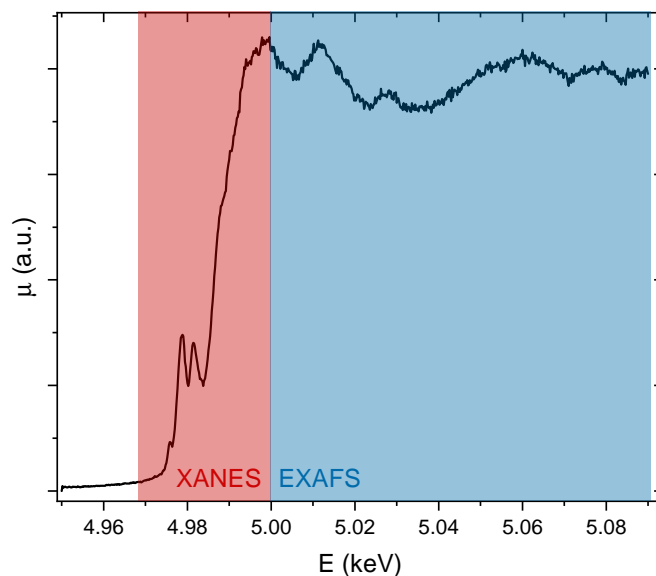
Figure 1.19: Example of Ti K-edge XAS spectrum of a rutile sample.

coefficient. The outgoing photoelectron wavefunction originating from the absorbing atom can interfere with the part of the wavefunction backscattered from neighboring atoms. Interference can be constructive or destructive. Constructive interference increases the absorption probability, giving rise to maxima in the absorption spectrum, while destructive interference decreases the absorption probability, resulting in minima in absorption spectrum. The frequency of the oscillations depends on the distance between target atom and its first neighbors, while their amplitude gives information on the number and type of neighboring atoms.

While EXAFS can be modeled and exact physical interpretation can be obtained, XANES data analysis typically relies on linear combination of known model spectra.

1.4.4 X-ray diffraction (XRD)

X-ray diffraction (XRD) is a widely used experimental technique for the determination of the crystal structure of materials. It is based on the elastic scattering of X-rays by crystalline planes. The direction of diffracted beams can be calculated from Bragg's law:

$$\lambda = 2d_{hkl} \sin \theta \tag{1.13}$$

where λ is the X-ray wavelength, d_{hkl} is the interplanar distance of hkl planes and θ is the incidence angle of the X-ray beam relative to the hkl plane.

The intensity of the scattered beam is proportional to the square modulus of the structure factor:

$$I(\vec{q}) \propto |F(\vec{q})|^2\, \delta(\vec{q} - \vec{\tau}) = \left| \sum_{j=0}^{N} f_j e^{-i(\vec{q}\cdot\vec{r_j})} e^{-W_j} \right|^2 \delta(\vec{q} - \vec{\tau}) \tag{1.14}$$

with $\vec{q} = \vec{k_f} - \vec{k_i}$ being the momentum transfer vector, equal to the difference in wavevector of the incident and scattered photon, f_j and r_j the atomic scattering factor and fractional coordinates of each atom in the unit cell and W_j the Debye-Waller factor, which takes into account the effect of temperature. The Dirac delta $\delta(\vec{q} - \vec{\tau})$ is used to take into account diffraction conditions, which are satisfied for $\vec{q} = \vec{\tau}$, with $\vec{\tau} = h\vec{a^*} + k\vec{b^*} + l\vec{c^*}$ being a reciprocal lattice vector.

In principle, the electron density can be extracted from the complex structure factor:

$$\rho(\vec{r}) = \frac{1}{V} \sum_{\vec{q}} F(\vec{q}) e^{i(\vec{q}\cdot\vec{r})} \tag{1.15}$$

but since $F(\vec{q}) = |F(\vec{q})|\, e^{i\phi}$ and only $|F(\vec{q})|$ can be calculated from diffracted intensity, phase retrieval is one of the main difficulties in X-ray diffraction.

1.5 Materials

This section is devoted to the description of the two main materials investigated in this thesis, namely rutile TiO_2 and $SrTiO_3$.

1.5.1   Titanium dioxide

Titanium dioxide (TiO_2), also known as titania is a well-known and widely used material. Its applications range from pigments and paints (white titania) to photocatalysis.

It comes in three main polymorphs: rutile, anatase and brookite. All three polymorphs exhibit TiO_6 octahedra, with a central titanium cation bonded to six O^{2-} anions. Rutile and anatase have a tetragonal crystal structure, while brookite is orthorombic.

| Rutile | Anatase | Brookite |
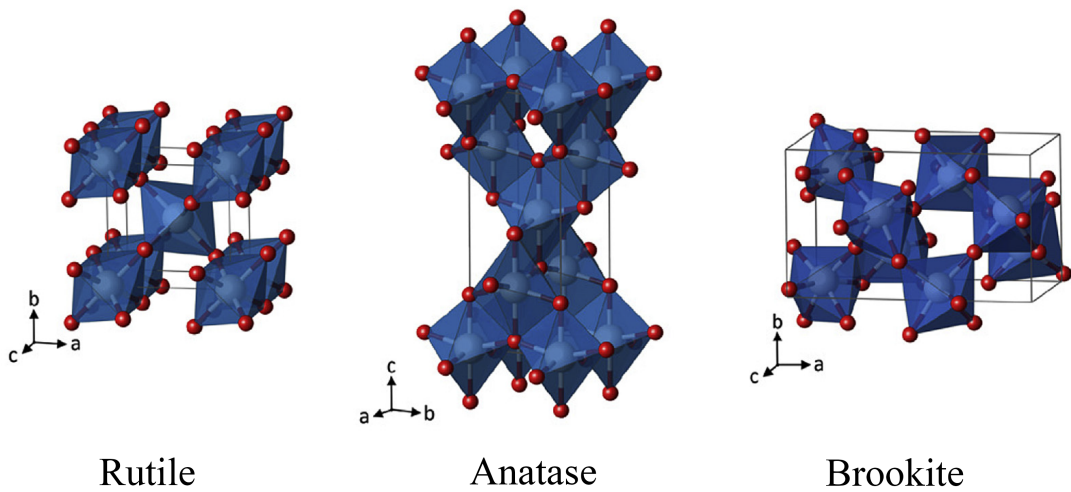
Figure 1.20: Crystal structure of the main polymorphs of TiO_2 [26].

Thermodynamically, the most stable polymorph of titania is rutile, while anatase has been shown to be more stable in the form of nanoparticles (see figure 1.21) [26, 27].

From the electronic point of view, TiO_2 is semiconductor with band gap of $3.05\,\mathrm{eV}$ and $3.18\,\mathrm{eV}$ for rutile and anatase respectively [26]. As shown in panel 1.22b, the valence band states are mainly associated with oxygen p orbitals, while the conduction band states relate to unfilled titanium d orbitals.

Removal of oxygen atoms with consequent formation of oxygen vacancies has the effect of introducing localized states in the band gap, below the conduction band, resulting in n-type doping. Removal of more than a few percent of oxygen results in the formation of suboxides with general formula Ti_nO_{2n-1}, with $3 < n < 10$,
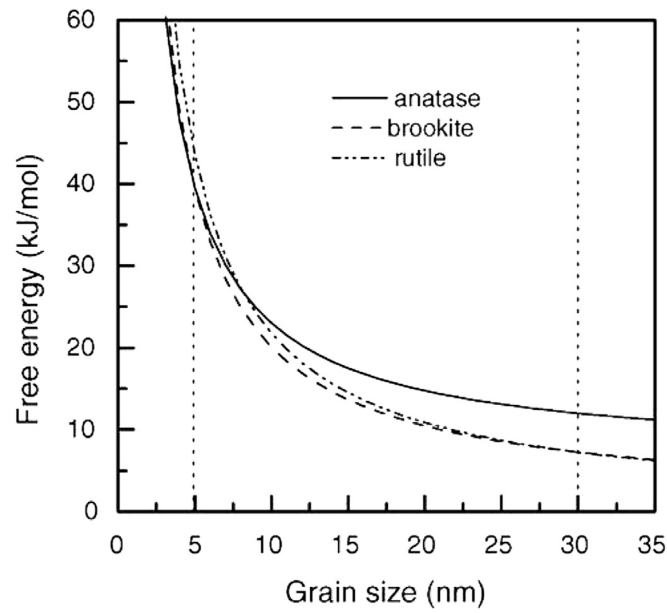
Figure 1.21: Free energy as a function of particle size for rutile, anatase and brookite, showing the higher stability of anatase in nanoparticles [26].
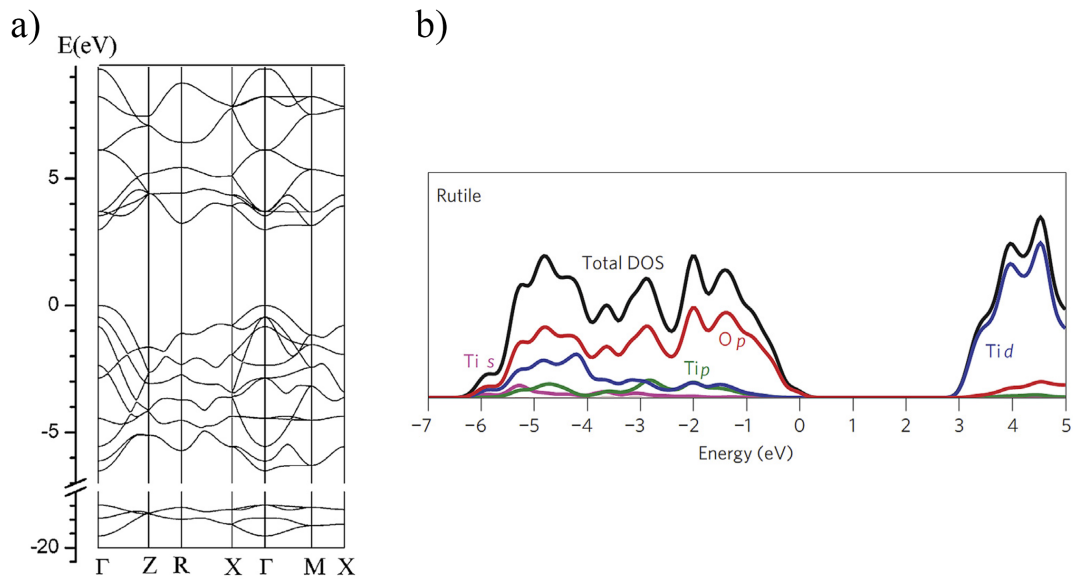
Figure 1.22: Band diagram (a) and total and ion-decomposed electronic density of states (DOS) of rutile (b) [26].

known as Magneli phases, characterized by much higher electrical conductivity with respect to stoichiometric TiO_2.

1.5.2 Strontium titanate

Strontium titanate is a strontium and titanium oxide with formula $SrTiO_3$. It has a perovskite structure with lattice parameter $a = 3.905$Å. The octahedral cornershared TiO_6 units forms a tightly bonded network, which makes up the structural backbone of the lattice. A cubic to tetragonal phase transition occurs when cooling down the material below 105 K. Despite such transition normally leads to ferroelectricity, $SrTiO_3$ does not display such behavior, and belongs to a class of quantum paraelectric materials [28].
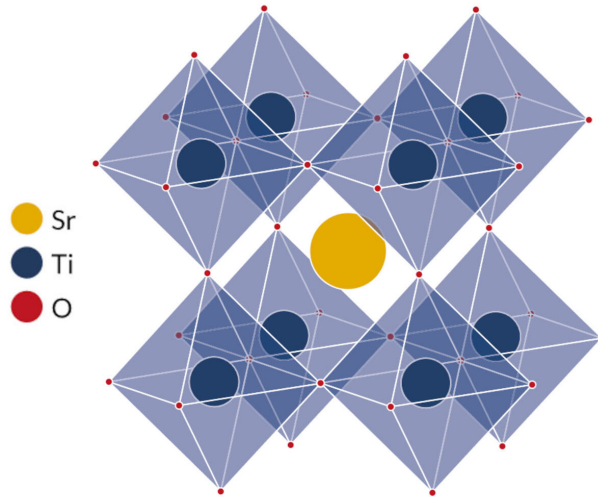
Figure 1.23: Crystal structure of $SrTiO_3$.

It is widely used as a diamond simulant thanks to its refractive index being very similar to the one of diamond.

It is a semiconductor with a 3.25 eV band gap. However, it can exhibit a metallic phase depending on the oxygen concentration.

Point defects can generate free charge carriers or charged ionic species. At room temperature, the charge carriers are predominately electrons introduced by donor impurity doping or heating in a reducing atmosphere. The latter treatment introduces an approximately equivalent density of oxygen vacancies, which are known

to exhibit significantly large lattice mobility. Therefore, $SrTiO_3$ is considered as a mixed electronic-ionic conductor.

Because of its properties, $SrTiO_3$ has several applications, including photocatalysis, hydrogen storage, sensors, fuel cells, Li-ion batteries and memristive devices.

1.6 Metal-semiconductor junction

In a metal or a semiconductor, a work function can be defined as the difference between the vacuum level energy and the Fermi level energy.

A junction between a metal with a work function ϕ_m and a semiconductor with a work function ϕ_s results in the energy band diagram shown in figure 1.24. This band diagram is due to the fact that the Fermi level in the two materials must be equal at thermal equilibrium, and the vacuum level must be continuous.
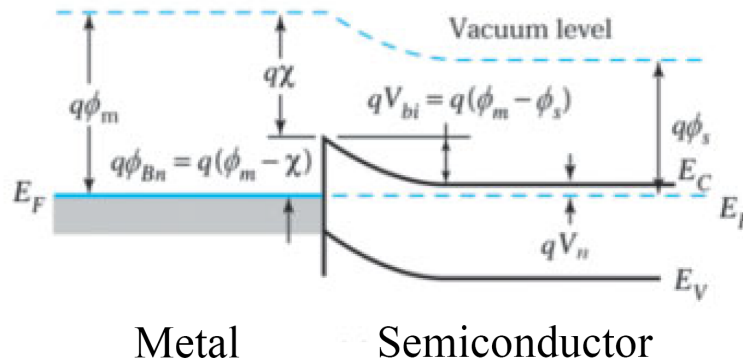
Figure 1.24: Energy band diagram of junction between a metal and a n-type semiconductor [29].

In this way a barrier is formed, with a height:

$$q\phi_{Bn} = q\phi_m - q\chi \tag{1.16}$$

where q is the elementary charge and χ is the semiconductor electron affinity (which is the difference between the conduction band energy and the vacuum level).

35

For large barrier height and low doping concentration (less than the density of states in the conduction or valence band), such metal-semiconductor interface is known as Schottky barrier.

Current transport in a Schottky barrier is mainly due to majority carriers, and the dominant transport mechanism is thermionic emission of majority carriers from the semiconductor over the potential barrier. This results in a rectifying behavior of the junction, with a current-voltage characteristic:

$$J = J_s \big[\exp(qV/kT) - 1\big] \tag{1.17}$$

$$J_s = A^* T^2 \exp(-q\phi_{Bn}/kT) \tag{1.18}$$

where A^* is the effective Richardson constant and T is temperature.

For example, the interface between rutile TiO_2 and Pt, which will be discussed in section 2.3.5, results in the formation of a Schottky barrier with height $\phi_{Bn} \sim 1.2\,\text{eV}$ (which rises from the Pt work function of $5.2\,\text{eV}$ and the TiO_2 electron affinity of $4\,\text{eV}$) [30].

In certain conditions, an ohmic contact can arise at the metal-semiconductor interface, meaning that the contact resistance is negligible with respect to the bulk resistance of the semiconductor. The specific contact resistance of the junction is defined as:

$$R_C = \left(\frac{\partial J}{\partial V}\right)^{-1}_{V=0} \tag{1.19}$$

Depending on the doping concentration, two main conduction mechanisms can be identified:

- Thermionic emission, which is dominant at low defects concentration. The specific contact resistance is independent on the defects concentration and can be expressed as:

$$R_C = \frac{k}{qA^*T} \exp\left(\frac{q\phi_{Bn}}{kT}\right) \tag{1.20}$$

- Tunneling through the Schottky barrier, which becomes dominant at high defects concentration. In this case the specific contact resistance can be approximated as:

$$R_C \sim \exp\left(\frac{4\sqrt{m_n \varepsilon_s}}{N_D}\frac{\phi_{Bn}}{\hbar}\right) \tag{1.21}$$

where m_n is the electron effective mass in the semiconductor, ϵ_s is the dielectric permittivity of the semiconductor and N_D is the donor number density.
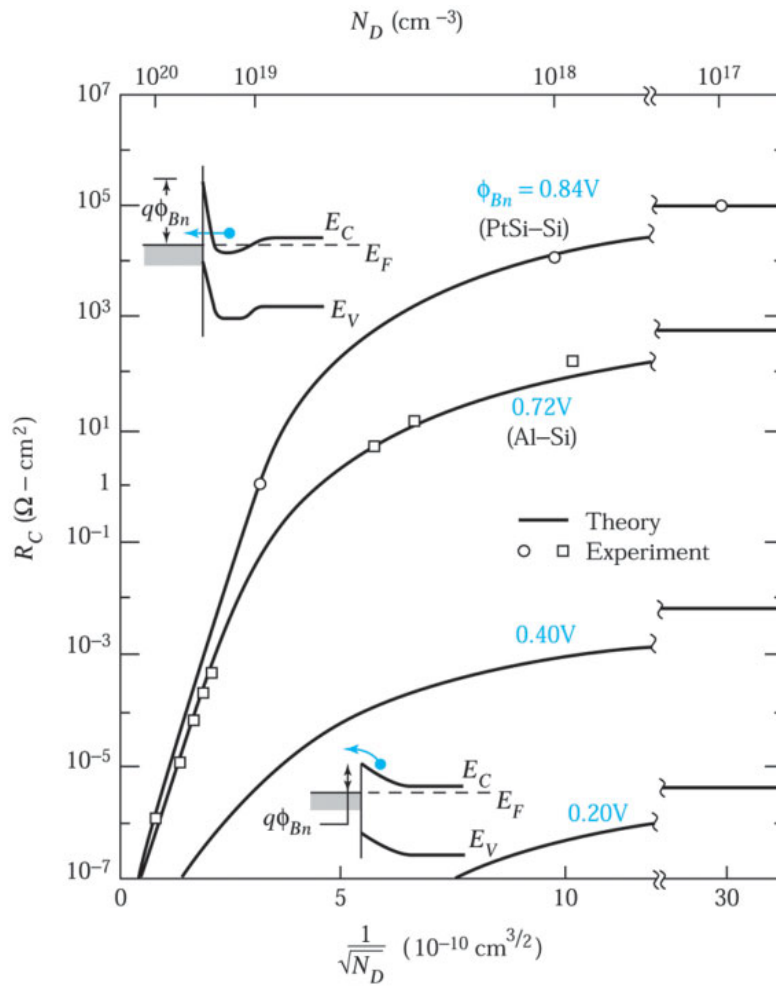
Figure 1.25: Specific contact resistance dependence on the number density of defects for different metal-semiconductor interfaces [29].

1.7 Memristive devices

Memristive devices, or memristors, where first theorized in 1971 by Leon Chua [31]. A memristor is a 2-terminal circuit element characterized by a constitutive relation between two mathematical variables q and φ representing the time integral of the element's current $I(t)$, and voltage $V(t)$ [32]:

$$q(t) = \int_{-\infty}^{t} I(\tau)d\tau \tag{1.22}$$

$$\varphi(t) = \int_{-\infty}^{t} V(\tau)d\tau \tag{1.23}$$

By differentiating:

$$V = \frac{d\varphi}{dt} = \frac{d\varphi}{dq}\frac{dq}{dt} = R(q)I \tag{1.24}$$

where

$$R(q) = \frac{d\varphi}{dq} \tag{1.25}$$

is called memristance and has units of Ohms. Equation 1.24 can be interpreted as Ohm's law, but the resistance $R(q)$ at time t_0 depends on the entire past history of $I(t)$ between $t = -\infty$ and $t = t_0$.

By plotting $(I(t), V(t))$ on the V-I plane for a for a typical memristor fed by a sinusoidal current source, the result is a Lissajous figure with a pinched hysteresis loop, as shown in figure 1.26.
A memristor was firstly realized only in 2008 [33], by sandwiching a double layer of TiO_2 and TiO_{2-x} between two Pt electrodes.
Ideal memristive devices exhibit reversible resistance switch between two different states: a low resistance state (LRS) and a high resistance state, which can be interpreted as logical 1 and 0 respectively [34]. This opens the possibility of applying memristive devices in several fields, such as data storage, data processing, neuromorphic computing, etc...
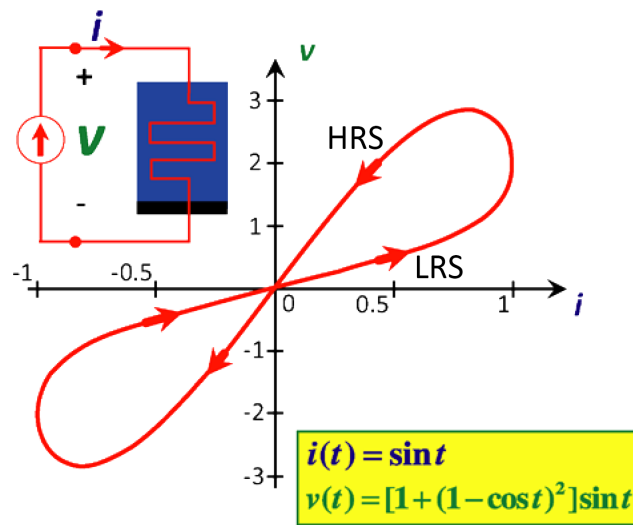
Figure 1.26: Pinched hysteresis loop [32].

Memristive behavior can arise from many physical phenomena. For example valence change mechanism (VCM) takes place in metal oxides with sufficiently high ion mobility. Migration of ions changes the local stoichiometry and leads to a redox-reaction accompanied with a valence change of cations and a change in the electronic conductivity. These changes usually take place within small filaments, but can also be extended over the whole device area. These two cases are schematized in figure 1.27. Redox-based memristors show a so-called bipolar switching process, since two different voltage polarities are needed to switch between the two resistance states.

The most commonly used VCM materials are transition metal oxides such as TiO_2, HfO_2 and Ta_2O_5. Polycrystalline or amorphous oxide films are typically used, sandwiched between two metal electrodes, one providing a non-rectifying ohmic contact (e.g. Ta) and one with a high work function (e.g. Pt), inducing a Schottky barrier.

Prior to operation, redox-based memristors must undergo a so-called electroforming process, which consists in an electrical discharge needed for the formation of a conducting filament connecting the electrodes. By subsequently applying electric field, migration of oxygen vacancies can break and reform the conducting filament reversibly and achieve resistance switch.
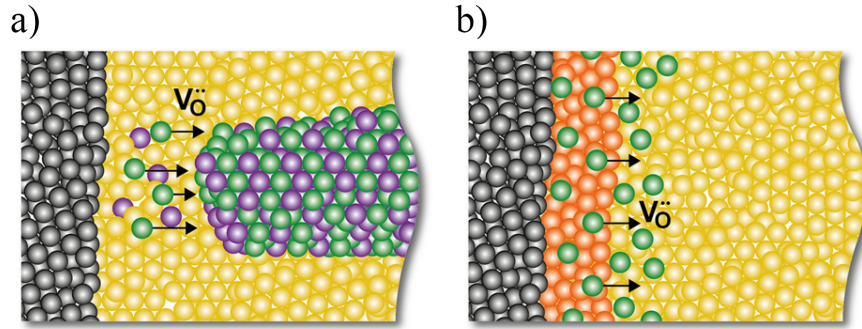
Figure 1.27: a) Sketch of a filamentary VCM cell. Black spheres: high work function electrode; yellow spheres: metal oxide in the fully oxidized state; green spheres: oxygen vacancies; purple spheres: metal oxide in a reduced valence state. b) Sketch of an area-dependent VCM cell. Black spheres: high work function electrode; orange spheres: metal oxide tunnel barrier; green spheres: oxygen vacancies; yellow spheres: metal oxide in the fully oxidized state [34].

The stochastic outcome of this electroforming process is one of the main limitations of VCM, since it leads to variability between devices and cycle-to-cycle variations.

1.8 X-ray nanopatterning of functional oxides

Intense X-ray irradiation with synchrotron nanobeams has been shown to induce damage in many classes of materials. Radiation induced damage is not only limited to soft matter and biological samples, but can also affect hard condensed matter, and is particularly relevant for time resolved experiments, where material alteration can be interpreted as real results instead of radiation related effects [35].

But radiation damage can also be exploited to deliberately modify the properties of materials, and develop a resist-free patterning technique, called X-ray nanopatterning (XNP).
Compared to standard lithographic techniques, XNP does not involve the presence of photoresist and subsequent development and treatment of patterned regions of the sample, but can directly modify the electrical properties of exposed samples.

X-ray lithography typically needs the preparation of masks, which is long and expensive [36], while with XNP it is possible to directly write the desired pattern on the samples by scanning an X-ray nanobeam on the sample.

1.8.1 High temperature superconducting oxides

Several studies have been made on applying XNP to high critical temperature superconducting materials, in particular cuprates such as BSCCO.

These materials belong to a wide class of superconducting materials which has been intensively studied in the last decades, since their discovery in 1986 [37].

Bismuth strontium calcium copper oxide (or BSCCO) is a general class of cuprate high-T_c superconductors that was discovered in 1988. The general formula of these compounds is $Bi_2Sr_2Ca_{n-1}Cu_nO_{2n+4+\delta}$, with n = 1, 2, 3. The three main phases are referred to with the sequence of stoichiometric coefficients of cations in the formula:

- Bi-2201 (n = 1, $T_c \sim 20\,\mathrm{K}$);

- Bi-2212 (n = 2, $T_c \sim 75\text{-}90\,\mathrm{K}$ depending on the oxygen content);

- Bi-2223 (n = 3, $T_c \sim 110\,\mathrm{K}$).

The parameter δ that appears in the general formula takes into account the interstitial oxygen content, which largely influences both structural and electronic properties. The unit cell of BSCCO compounds is orthorombic, with alternating Cu-O, Sr-O, Ca and Bi-O layers. The crystal structure of the different phases is characterized by a different number of Cu-O and Ca layers in the unit cell, which implies different values for the c-axis lattice parameter (i.e about 24.7, 30.5 and 37.1 Å for the Bi-2201, Bi-2212 and Bi-2223 phase, respectively).

Focusing on phase Bi-2212, its crystal structure is made of alternating superconducting planes ($CuO_2-Ca-CuO_2$ layers) and insulating planes ($SrO-BiO-BiO-SrO$ layers) stacked along the c-axis, as shown in figure 1.28a. This alternation of superconducting and insulating blocks makes a stack of intrinsic Josephson junctions stacked along the c-axis direction.

Both the c-axis length and the superconducting transition temperature strongly depend on the interstitial oxygen content [38] (as shown in figure 1.28b), as well as the normal state resistivity [39] (figure 1.28c).

By forcing the supercurrent to flow along the c-axis direction (i.e. across the intrinsic Josephson junctions), and applying a constant voltage V_0, a high frequency alternating current is generated:

$$I = I_c \sin\left(\frac{2\pi}{\Phi_0} V_0 t + \varphi_0\right) = I_c \sin(2\pi\nu_j t + \varphi_0) \qquad (1.26)$$

where I_c is the junction critical current, $\nu_j = V_0/\Phi_0$ is the Josephson frequency, with Φ_0 being the magnetic flux quantum.

This high frequency current can in turn emit electromagnetic radiation, in particular in the THz range. Since the Bi-2212 crystal structure can be considered as a stack of a few-atomic-layer thick, highly packed IJJs, it has been proposed to exploit this material to fabricate high power THz emitters by forcing the supercurrent to flow along the c-axis direction, in such a way to simultaneously excite hundreds of junctions.

Moreover, "mesa" structures can be produced, which act as resonant cavities , enhancing the emission power when the Josephson frequency matches the cavity resonance frequency [40]. By biasing simultaneously several mesa structures, emitted power has been shown to increase with the square of the number of synchronized structures, reaching power up to $600\,\mu\text{W}$ [41].

By creating trenches in a single Bi-2212 microcrystal, it is possible to redirect the supercurrent to flow across the IJJs, and at the same time synchronize many structures within the same crystal. Trenches can be created by etching the material with Focused Ion Beam (FIB), which comes with some drawbacks because of the ion implantation and presence of material/vacuum interfaces, which can reflect part of the emitted radiation and are therefore detrimental to the overall emitted power.

It has been observed that hard X-ray irradiation can change the interstitial oxygen content in Bi-2212, and this change reflects on the normal resistance and critical temperature of the sample.Therefore, in principle, it is possible to exploit XNP on BSCCO to fabricate trenches [11,42,43] and possibly achieve intense THz radiation
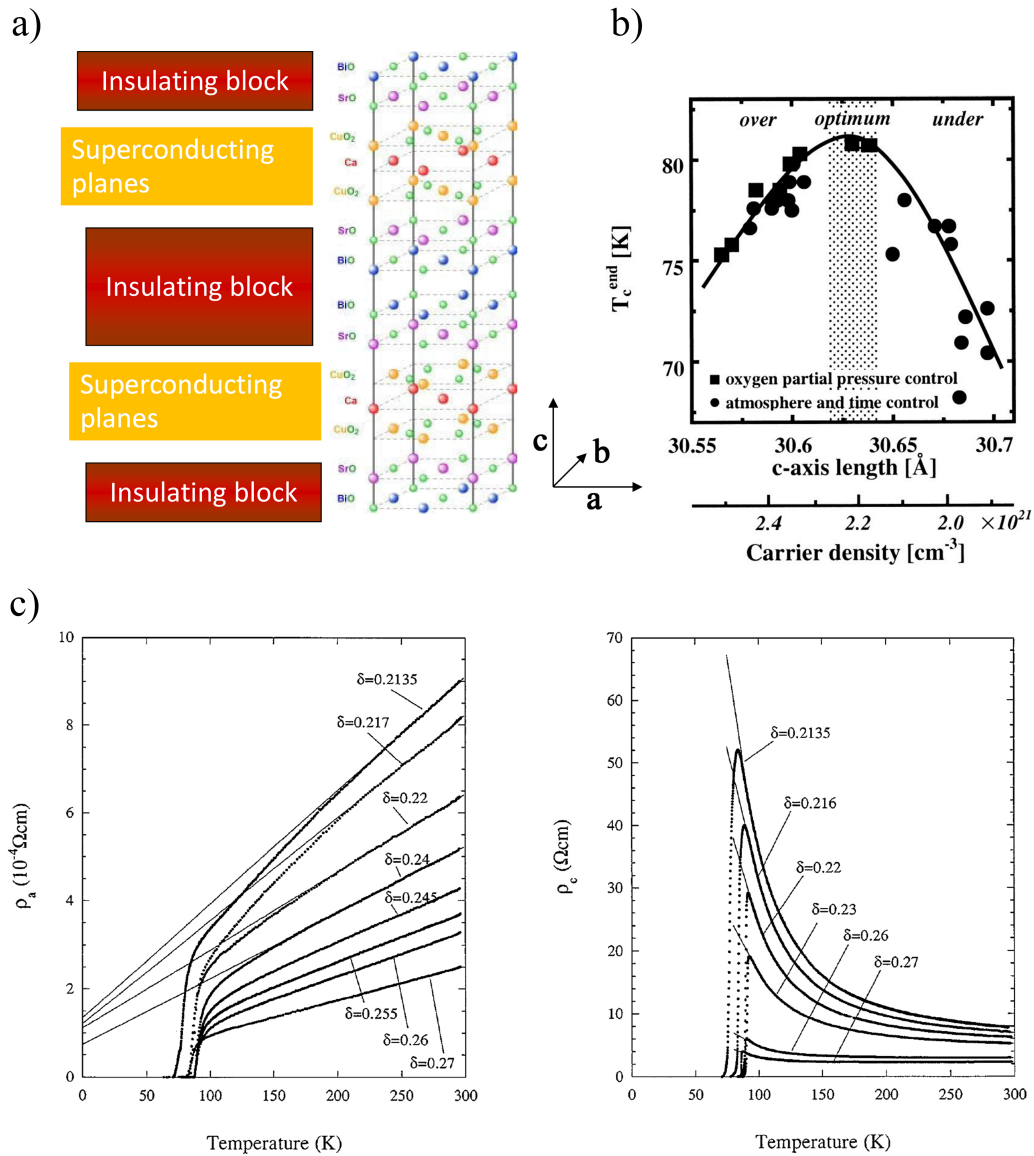
Figure 1.28: a) Crystal structure of Bi-2212, highlighting the alternation of superconducting and insulating blocks. b) Critical temperature dependence on the carrier density [38]. c) Resistance vs. temperature measurements for different oxygen doping concentration, measured on the ab plane (left) and along the c axis (right) [39].

emission.

Indeed, as shown in figure 1.29, after irradiation of the sample, both a decrease in the critical temperature and an increase in the normal state resistance have been observed. Moreover, current-voltage curves shown in panel 1.29d exhibit hysteresis loops ascribable to underdamped Josephson junctions, confirming that current is forced to flow across IJJs.
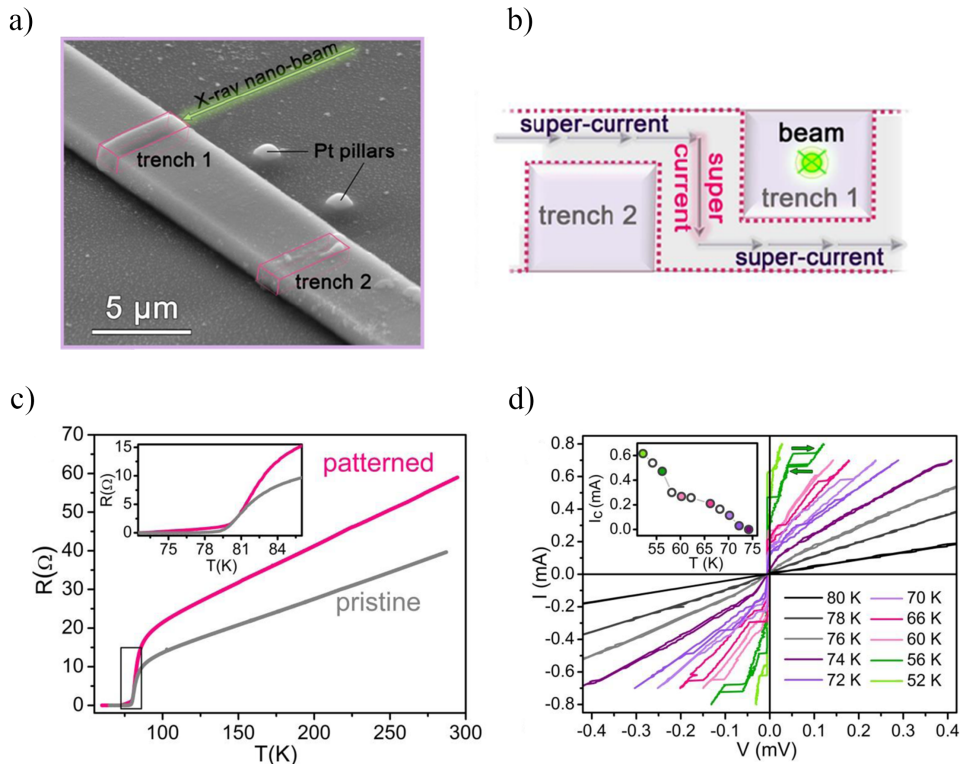
Figure 1.29: a) Sketch of irradiation of Bi-2212 microcrystals. b) Schematic representation of the current flow after trenches irradiation. c) Resistance vs. temperature measurements for pristine and patterned sample, showing the increase in normal state resistance and decrease in critical temperature induced by irradiation. d) Current-voltage curves collected at different temperatures. The inset shows the temperature dependence of the critical current of intrinsic Josephson junctions [11].

The microscopic mechanism underlying interstitial oxygen depletion is still un-

known, but some studies have investigated the possibility of oxygen displacement by energetic secondary electrons [44]. This knock-on interaction has been studied by means of Monte Carlo simulations using MCNP6 code, calculating the fluence of photoelectrons $\phi_e(x, y, z, E)$ generated by the incoming X-ray beam. Momentum and kinetic energy transfer from a photoelectron to an atom initially at rest can lead to displacement of light atoms (in particular interstitial oxygen atoms) in the material. The local number density of displaced oxygen atoms can be evaluated from the photoelectrons fluence.

From experimental results, and in particular from the normal state resistivity, the interstitial oxygen content can be calculated and compared with Monte Carlo simulations. From this comparison, a good agreement has been reported for samples irradiated with low photon fluence, while for heavily irradiated samples knock-on effects do not fully explain the large variations in interstitial oxygen content experimentally determined [44].

Another possible mechanism for material modification is related to heating effects, which have been quantified by means of combined Monte Carlo and finite elements simulations [45]. By taking into account the cascade of de-excitation processes following X-ray photon absorption and the time structure of synchrotron pulses, the temperature increase induced during Bi-2212 irradiation has been estimated, and results allow to exclude ordinary melting of the material. Figure 1.30a shows the maximum temperature reached in a sample irradiated with 16 bunch filling mode as a function of time, and indeed the temperature values are much lower than the melting point of Bi-2212 ($T_m \sim 860\,^{\circ}\mathrm{C}$).

Investigation of the crystalline structure of Bi-2212 by means of XRD measurements upon irradiation has detected a decrease in the degree of crystallinity and an increase in the mosaicity spread of the samples [46, 47]. These changes could be related to thermal fatigue, which is due to the intense temperature gradients and heating rates induced by each synchrotron pulse, which occur with a high repetition rate.

Another possibility could be transient local softening of the chemical bonds taking place during the irradiation pulses and inducing nonthermal melting in the system [48].
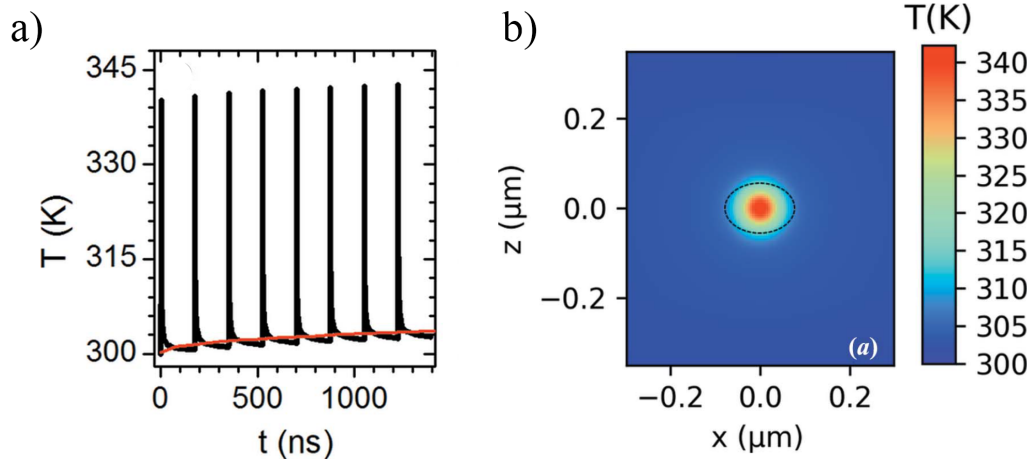
Figure 1.30: a) Maximum temperature as a function of time calculated from finite element simulations and b) temperature map on the sample surface perpendicular to the X-ray beam [45].

1.8.2   Semiconducting oxides

On top of the possibility of functionalizing materials with loosely bound oxygen atoms such as high temperature superconductors by means of X-ray nanopatterning, it has been shown that also oxides with tightly bound oxygen atoms are affected by radiation damage.

For example, it has been demonstrated that TiO_2 can be affected by synchrotron microbeams, leading to both volatile and non-volatile resistance change during and after non-localized irradiation [49]. The volatile resistance change can be associated to a photovoltaic-like effect, due to photoexcited electrons injected in the conduction band during irradiation, which can decrease the sample resistance by some orders of magnitude. However, resistance goes back to high values as soon as irradiation is stopped. This volatile resistance change is directly proportional to the incoming photon flux.

On top of volatile resistance change, non-volatile increase in sample conductivity has been detected upon Conducting Atomic Force Microscopy (C-AFM), which from TEM analysis has been explained with the formation of Ti_4O_7 Magneli phase, testifying oxygen depletion of the material upon X-ray irradiation.
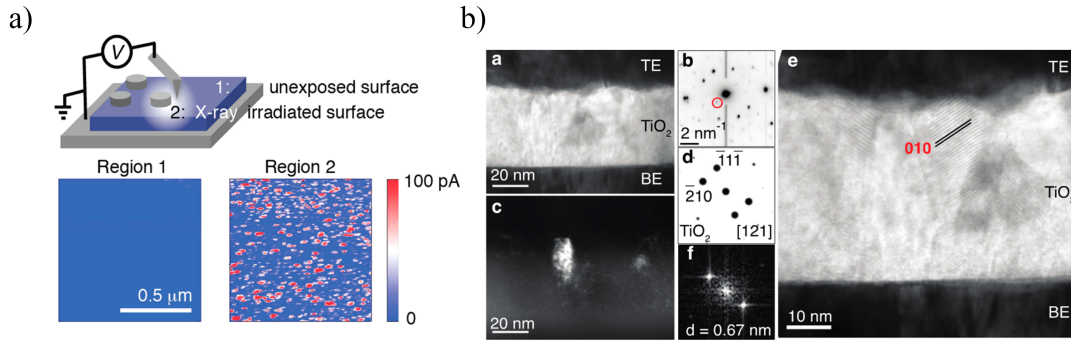
Figure 1.31: a) C-AFM of irradiated and unexposed TiO_2. b) Cross-section TEM analysis of conducting filaments, highlighting the formation of Ti_4O_7 Magnel phase [49].

Starting from this evidence, experiments have been performed to apply XNP to TiO_2 single crystals [12]. A gap separating two Au electrodes deposited on the top surface of a rutile bulk sample has been irradiated by scanning with an X-ray nanobeam a line connecting the two electrodes. Just like in the case of non-localized irradiation, both volatile and non-volatile resistance changes have been detected, as shown in figure 1.32.
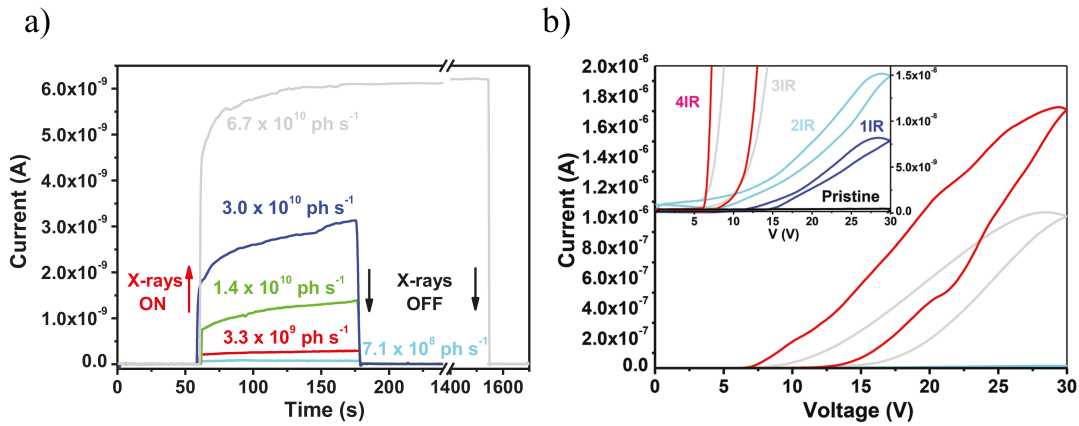
Figure 1.32: a) Time-dependent current change for X-ray irradiation of a single point between two Au electrodes for different photon fluxes ($V = 1$ V). b)IV curves acquired after subsequent irradiation steps [12].

Non-volatile resistance changes can be ascribed to the introduction of oxygen va-
cancies, which can migrate under the effect of an externally applied electric field,
leading to the formation of a conducting channel. Surface vacancies can recom-
bine with atmospheric oxygen, reducing the surface conductivity of the sample
with time.

XNP can be therefore used to locally tune the electrical conductivity of in principle
any semiconducting material, at nanometric scale. To achieve full control of the
process, the effect of irradiation parameters (in particular temperature, filling mode
and irradiation time) on the final device properties has to be understood, and this
has been the main focus of this thesis.

Functionalization of oxide based memristive-like devices

2.1 Pristine samples

For functionalization experiments of functional oxides, memristive-like devices have been fabricated in order to test the possibility of guiding the electroforming process[1]. Due to the nature of the experiments to be performed, a lateral geometry has been chosen instead of the typical sandwiched structure normally used in memristive devices.

Rutile TiO_2 samples have been prepared from commercial single crystals purchased from Shinkosha. These crystals are $5 \times 5 \times 0.5\,mm^3$ plates with (110)-oriented surface.

Strontium titanate samples have been prepared from (001)-oriented $Fe:SrTiO_3$ single crystals from Crystec ($5 \times 5 \times 0.5\,mm^3$). Iron dopings of 0.022 wt.% and 0.06 wt.% have been used.

Electrode pairs have been deposited on the crystals top surface. The electrodes are

---

[1]Samples prepared by Regina Dittmann and collaborators at Peter Gruenberg Institute, Forschungszentrum Juelich GmbH

made of 60 nm of Pt on one side and 30 nm of Pt on top of 30 nm of Ta on the other side. The electrodes in each pair are separated by a gap (0.7 to 3.3 µm in size).

A SEM picture of a representative sample together with a schematic representation of the electrodes layout is shown in figure 2.1.

a)

b)
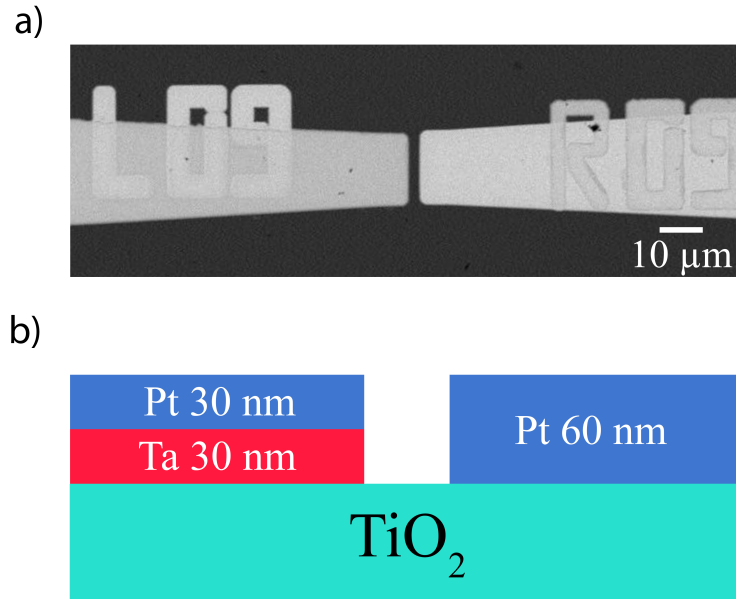
Figure 2.1: a) Scanning electron microscopy (SEM) image of a typical sample (top view) and b) schematic cross section [50].

Sample have also been annealed in a reducing atmosphere to introduce a suitable number density of oxygen vacancies and therefore increase their electrical conductivity. Annealing has been performed in Ar/H_2 (4%) atmosphere for 2 hours. Annealing temperatures have been 300 °C for TiO_2 and 900 °C for $Fe:SrTiO_3$. $SrTiO_3$ requires a much higher annealing temperature, which also leads to recrystallization of Pt electrode, resulting in a more textured appearance of the metal surface.

The upper limit of oxygen vacancies concentration in TiO_{2-x} as a result of annealing can be estimated in x=10^{-5} [50]. Moreover, more oxygen vacancies are formed at the Ta/TiO_2 interface due to the formation of a Ta_2O_{5-x} interface layer [51].

The asymmetry of the electrodes results in a rectifying diode-like behavior of the devices, because of the presence of an ohmic contact between TiO_2 or $Fe:SrTiO_3$ and the Ta electrode, while the Pt electrode forms a Schottky barrier with the oxide [30].

This asymmetry is required to achieve bipolar resistance switching, since an active electrodes and an inactive ohmic contact are needed in MIM (metal-insulator-metal) resistive switching devices [52].

2.2 Experimental setups and procedures

2.2.1 ID16B

Irradiation of samples has been performed at beamline ID16B of the European Synchrotron Radiation Facility (ESRF). This nano-analysis beamline is dedicated to 2D or 3D analysis of nano-scaled materials, thanks to its nanosized beam whose dimension can range between $1.0{\times}0.1\,\mu m^2$ and $50{\times}50\,nm^2$.

In terms of energies available, ID16B provides hard X-rays in the 6.0-65.0 keV range.

After the upgrade to the new fourth generation of synchrotron sources named extremely brilliant source (EBS), ID16B provides a maximum time-averaged flux $\Phi_0 = 4 \times 10^{12}$ ph/s (pink beam mode, E=17.5 keV and beam size $50{\times}50\,nm^2$).

Several characterization techniques can be exploited and combined, including:

- micro X-ray fluorescence (MicroXRF),

- X-ray excited optical luminescence (XEOL),

- X-ray diffraction (XRD),

- micro X-ray absorption near-edge structure (MicroXANES),

- tomography,

- phase constrast imaging.

The typical experimental setup used during the irradiation experiments is shown in figure 2.2.

a)

b)
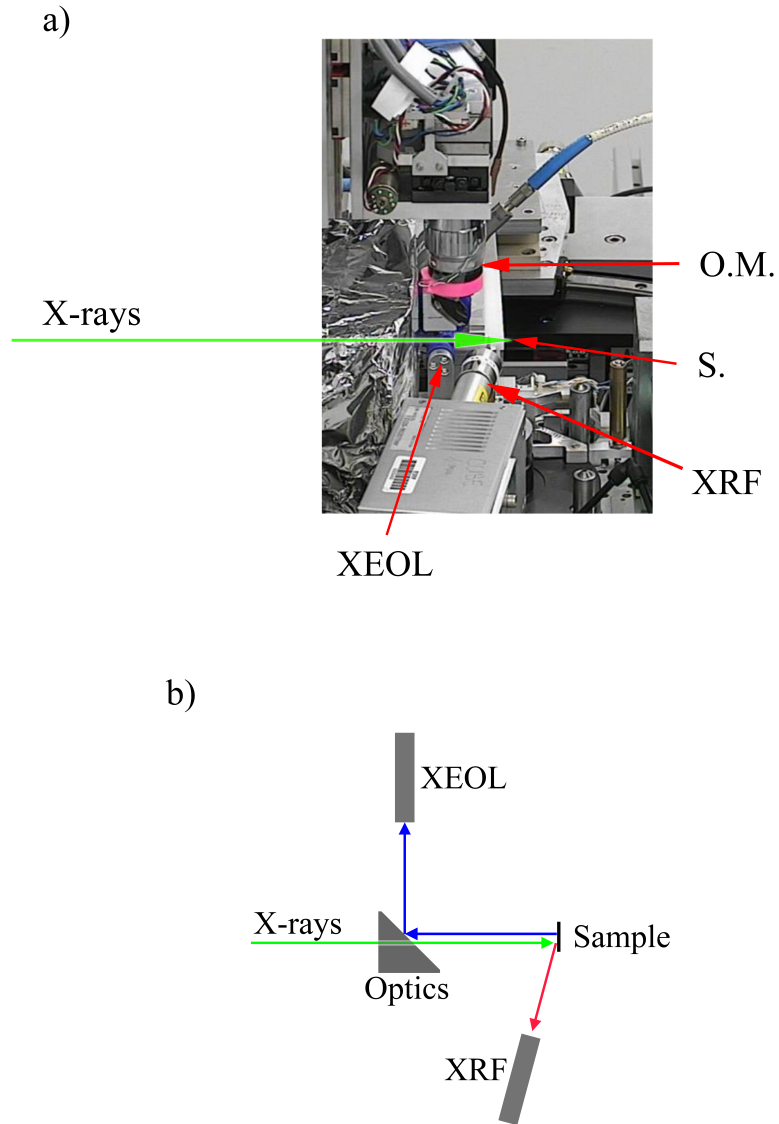
Figure 2.2: a) Picture of experimental setup at ID16B (O. M.: optical microscope, S: sample position) and b) schematic top view [50].

This setup allows the simultaneous acquisition of XRF and XEOL maps. XRF

spectra can be acquired through a two custom-made spectrometers, one by Hitachi and one by Mirion. Optical luminescence is measured through a Maya 2000 pro spectrometer by Ocean Optics. Luminescence is measured on the X-ray nanobeam axis, through a high numerical aperture collection optics.

The sample is mounted on a custom sample holder (see figure 2.3) which allows electrical connection of the sample to the electrometer for online electrical characterization. The sample holder is mounted on a motorized stage which allows fine movement of the sample both along the beam axis (z direction) and on the plane normal to the incident beam (xy plane).
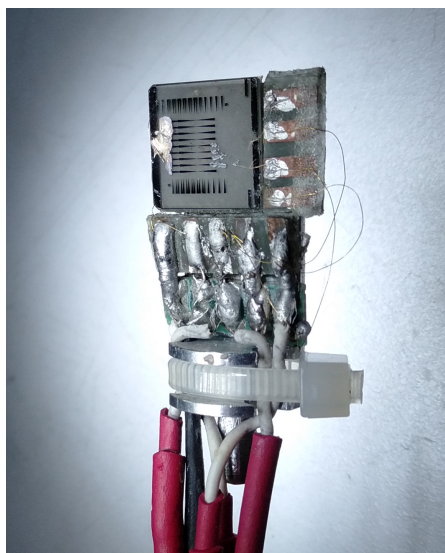
Figure 2.3: Customized sample holder for online electrical characterization

An optical microscope equipped with a 45° angle mirror can be used for optical localization of the sample. A hole in the mirror allows the X-ray beam to reach the sample unobstructed while the optical microscope is in place.

XRF and XEOL mapping

Prior to irradiation, the sample has been focused thanks to the optical microscope, whose focus coincides with the X-ray beam focus, and roughly localized on the xy plane.

53

To precisely localize the gap under investigation, a X-ray fluorescence map has been acquired. To avoid unwanted modifications induced by the intense nanobeam, filters have been inserted to lower the photon flux impinging on the sample.

The sample has been then moved to raster scan the area under investigation with the nanobeam, and for each point a XRF spectrum has been acquired. The minimum spatial resolution achievable is limited by the beam size, which in our experiments is typically in the order of $50 \times 50\,\mathrm{nm}$.

The spectra have been fitted with PyMca software [53], by taking into account all the elements present in the samples, the geometrical parameters of the measurement and pile-up peaks due to photons with different energies reaching the detector at the same time, which result in counts with energy equal to the sum of the two photons. Moreover, Ar and Kr from the air must be considered, together with impurities that can be present in the substrates.

Once the spectrum corresponding to each point of the fluorescence map is fitted, the integral intensity of each element can be plotted, obtaining the spatial distribution of all the elements.

At this point, in order to normalize the intensities with respect to the incoming photon flux, each spectrum has been divided by the intensity of the Ar signal (which is supposed to be proportional to the photon flux only), and the fitting procedure has been repeated again.

Simultaneously to the acquisition of XRF spectra, a XEOL spectrum has been acquired for each point of the map. This allows the investigation of the luminescence signal that results from the final de-excitation process in the cascade following the absorption of X-ray photons.

Irradiation

Once the gap under investigation has been localized by optical imaging and XRF mapping, the irradiation of the sample can be performed. A line extending between the metal contacts has been irradiated by moving the sample motor by a given step and exposing each point of the line for a given exposure time. During

this irradiation step filters have been removed, so that the whole available flux has impinged on the sample. Alternatively, an area can be irradiated by raster scanning the sample and exposing each mesh point for a defined exposure time.

The amount of energy delivered to the sample can be quantified in two ways:

- the fluence, which is defined as the energy delivered per unit surface:

$$F = \frac{\phi_0 \Delta t E_0}{A} \tag{2.1}$$

  where ϕ_0 is the time-averaged photon flux, Δt is the total exposure time, E_0 is the photon energy and A is the total irradiated area;

- the absorbed dose, which is defined as the energy absorbed per unit mass:

$$D = \frac{\phi_0 \Delta t E_0 (1 - e^{-l/\lambda_a})}{V \rho} \tag{2.2}$$

  where l is the thickness of the sample, λ_a is the attenuation length of photons with energy E_0 in the material, $V = Al$ is the irradiated volume and ρ is the material mass density.

It is important to note that no fast shutter is implemented on ID16B beamline, and therefore the sample is exposed to radiation even during the time it takes for the motor to move between different points. This must be taken into account when calculating the fluence and dose absorbed by the samples.

After each irradiation, online electrical characterization has been performed, and the irradiation can be repeated on the same area. In this way we can investigate the changes in material properties as a function of the cumulative fluence (CF) and cumulative dose(CD).

Electrical characterization

Thanks to the customized sample holder shown in figure 2.3, online electrical characterization can be performed during and in between irradiations.
Electrical measurements have been performed by using a Keithley 6487 electrometer. The instrument is controlled by a LabView program which allows to acquire

current-voltage (IV) curves. The maximum and minimum voltage and the number of points in the IV curves can be defined in the software, and it is also possible to keep a fixed voltage applied to the sample and monitor the current as a function of time.

When bias is applied during irradiation, the most intense effect that can be seen is the photocurrent due to photoelectrons produced. This volatile conductivity change is correlated to the incoming beam, and the sample resistance goes back to the original value when the shutter is closed. For example, figure 2.4 shows the current flowing across the gap when a constant voltage of $1\,V$ is applied between the electrodes and a single point inside the gap is irradiated with different photon fluxes.
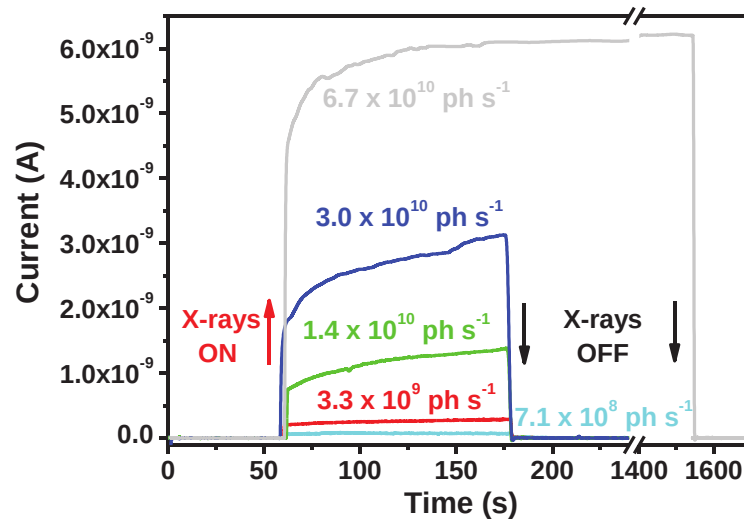
Figure 2.4: Current vs. time curve of a TiO_2 sample showing the photocurrent induced by incoming X-rays with different photon fluxes [12].

2.2.2   AFM characterization

Conducting atomic force microscopy (C-AFM) has been performed on-site during the experiment, thanks to the Partnership for Soft Condensed Matter (PSCM) of

ESRF. AFM images have been collected on a Cypher S system by Asylum research. Measurements were performed in contact mode, while applying a constant 10 V voltage to the tip and grounding the Ta electrode.

Simultaneous topographic and electrical information can be obtained by measuring the current.

2.2.3   ID21

XANES spectroscopy on irradiated and electroformed TiO_2 and $Fe:SrTiO_3$ has been performed at beamline ID21 of the ESRF [54, 55].

This beamline is specialized in in-vacuum scanning X-ray microscope (SXM), in the energy range 2.1-10.0 keV and beam sizes between $0.7{\times}0.3\,\mu m^2$ (H×V) and $2.0{\times}2.0\,mm^2$.

The main experimental techniques available are micro X-ray absorption near-edge structure (MicroXANES) and micro X-ray fluorescence (MicroXRF), with applications ranging from cultural heritage and environmental studies to materials and medicine. The tender X-rays energy range allows XAS investigation of most elements' K, L and M absorption edges.

A scheme of the experimental setup is shown in figure 2.5.

Figure 2.5: Schematics of experimental setup of ID21 [54].

The experimental setup allows acquisition of fluorescence and absorption data while raster scanning the sample, obtaining hyperspectral images. For bulk sam-

ples, absorption information can be obtained in fluorescence mode only.

2.2.4   Raman spectroscopy

Raman spectroscopy[2] has been performed at room temperature in the region of interest employing an HORIBA Soleil micro-spectrometer equipped with an excitation light of 532 nm and a UV/Vis/NIR Syncerity CCD detector Peltier-cooled at -60°C.
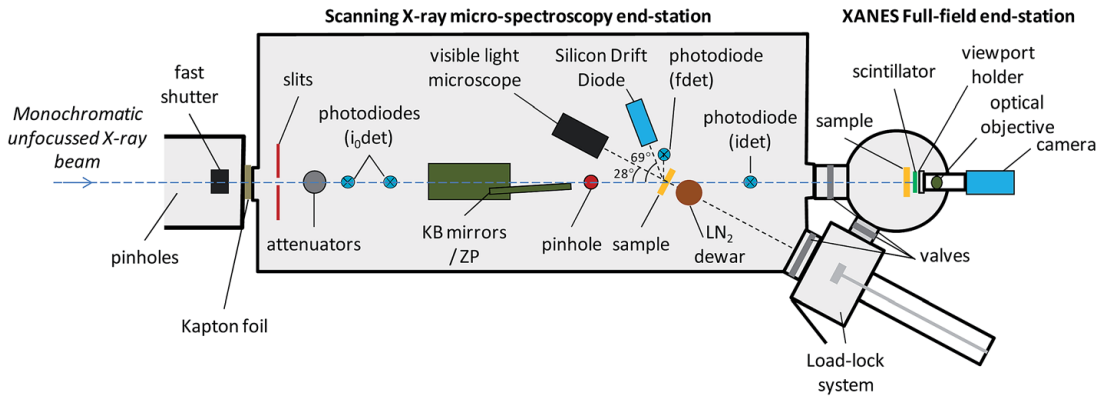
Maps have been acquired using a 100x HORIBA Plain Fluo objective with a working distance of 1 mm, a numerical aperture of 0.90, acquisition times of 1 second per point, and a laser power of 0.57 mW. A grating of 2400 lines/mm centered at 400 nm and a hole diameter of 200 µm at the spectrometer entrance have been employed to achieve an optimal signal-to-noise ratio with minimum imaging time at the largest spectral resolution. Autofocus on spectral signal has been employed for each point of the map. The beam size for this imaging technique is limited by diffraction, allowing for a spatial resolution of about 720 nm. The data treatment included the corresponding background subtraction, a smoothing procedure to reduce the noise, and a normalization of the peak intensities.

This analysis is intended to get information about the vibrational modes of the sample on the surface layer, to be compared to the results of XANES mapping, which instead gives information on the local environment of Ti atoms in the bulk of the sample.

2.3   Rutile TiO$_2$

2.3.1   Pristine samples

Electrical characterization of pristine devices has been performed and a clear diode-like exponential behavior can be seen. Current-voltage (IV) curves have been acquired grounding the Ta electrode and sweeping the voltage applied to the Pt electrode between positive and negative voltages (with typical values ranging from a few volts to tens of volts). A typical IV curve of a TiO$_2$ pristine sample is

---

[2]Performed by Jorge Serrano and collaborators at University of Valladolid

reported in figure 2.6. In this case the current is reported as a function of the electric field ($E = V/d$, where d is the gap size).
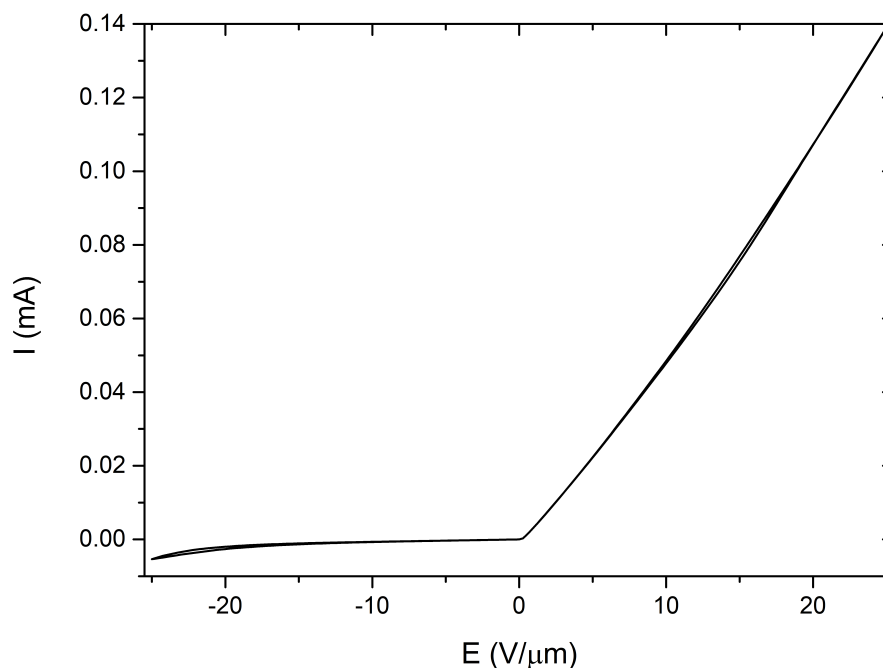
Figure 2.6: I vs. E curve of a TiO$_2$ sample (1.9 µm gap) before irradiation. [50]

During alignment, XRF maps for pristine samples have been acquired for precise localization of the gap to be irradiated. A representative XRF spectrum for TiO$_2$ is shown in figure 2.7.

The elements inserted in the configuration file for the fit are Ti, Pt, Ta, Ar and Kr, together with Si, Sr, Fe, and Y, which are the main impurities that can be present in the substrates. The final results for a typical pristine sample are the elemental maps shown in figure 2.8. From the Pt and Ta maps it is possible to see clearly the electrodes and precisely localize the gap separating them. The Ti map shows a lower intensity in correspondence of the electrodes due to absorption of Ti fluorescence by the electrodes themselves.

Together with XRF, a XEOL spectrum is collected for each point of the map. A typical XEOL spectrum for TiO$_2$ is shown in figure 2.9.

The broad photoluminescence band in the near infrared region (NIR) observed in rutile has already been reported and has been attributed to the radiative recombination of electrons trapped in a midgap state with free holes in the valence
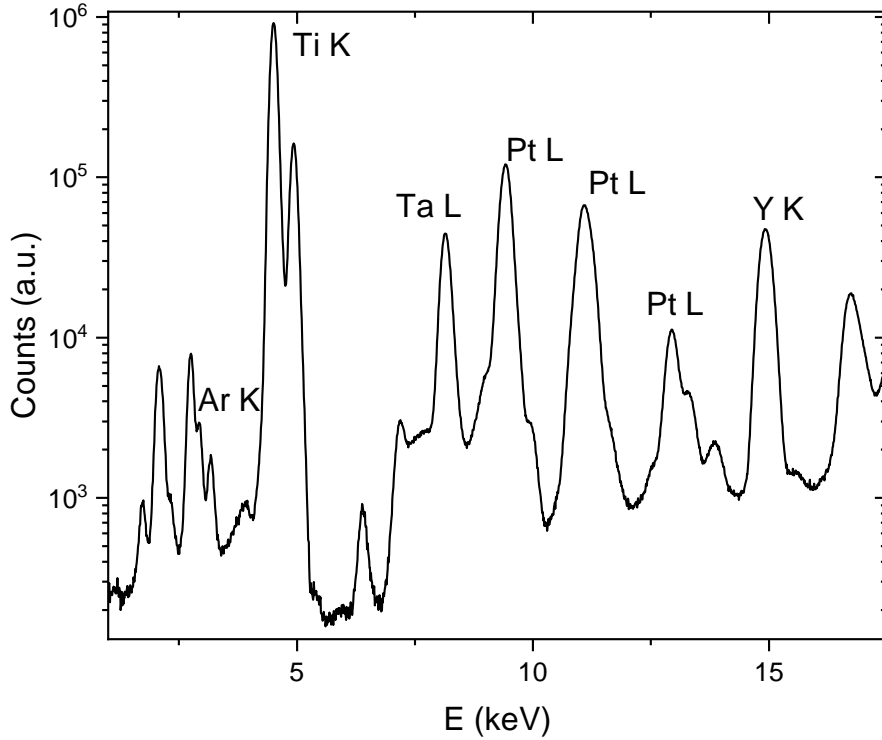
Figure 2.7: Typical XRF spectrum of a TiO_2 sample.

band [56], as shown in figure 2.10. The origin of these midgap states, located at around $1.5\,eV$ below the conduction band edge, can be explained with the presence of oxygen vacancies in the material, which are present also in pristine sample as a consequence of the annealing [56].

The spectra recorded at each point have been fitted through PyMca [53] with a linear combination of gaussian curves:

$$I(\lambda) = \sum_{i=0}^{n} \frac{A_i}{\sigma_i \sqrt{2\pi}} e^{-\frac{1}{2}\left(\frac{\lambda - \lambda_{0i}}{\sigma_i}\right)^2} \tag{2.3}$$

In this way, maps can be obtained for each parameter defining each gaussian (namely A_i, σ_i and λ_{0i}). Figure 2.11 shows an example of a map showing the intensity A_1 for the most intense gaussian component (red line in figure 2.9) in a pristine TiO_2 sample.
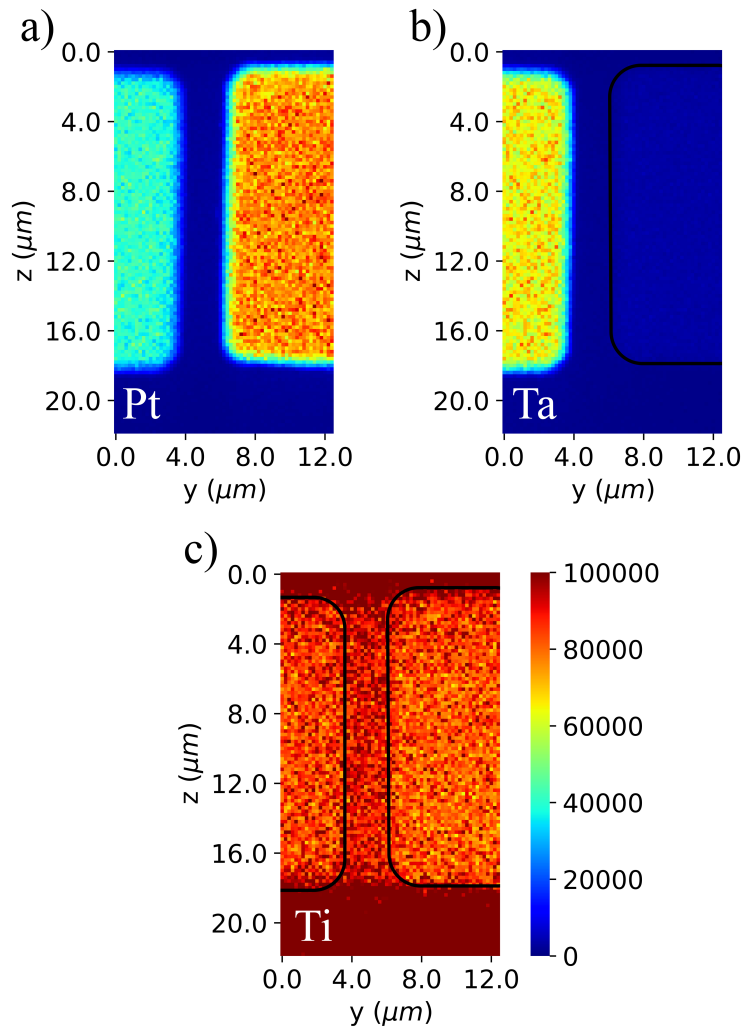
Figure 2.8: XRF maps collected at ID16B corresponding to Pt L lines (a), Ta L lines (b) and Ti K lines (c) [50].

This map shows a lower intensity on the metal electrodes, due to a screening effect by the metal electrodes analogous to what observed for the Ti XRF signal.
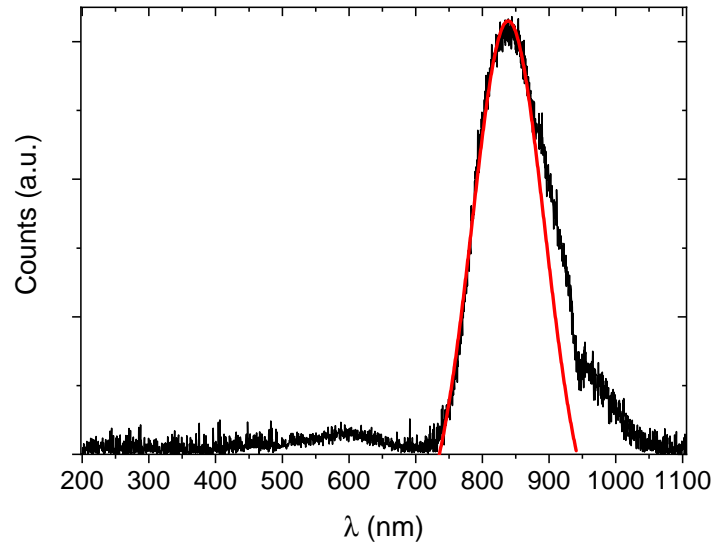
Figure 2.9: Typical XEOL spectrum of a TiO_2 sample. The red line shows the main gaussian contribution.
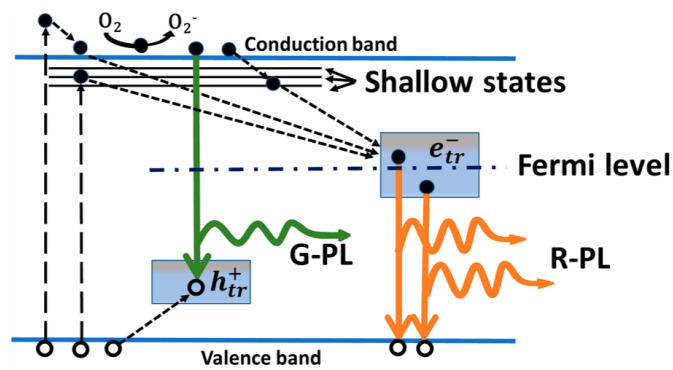
Figure 2.10: Schematic band diagram for TiO_2 showing the origin of luminescence in the NIR (orange lines) [56].
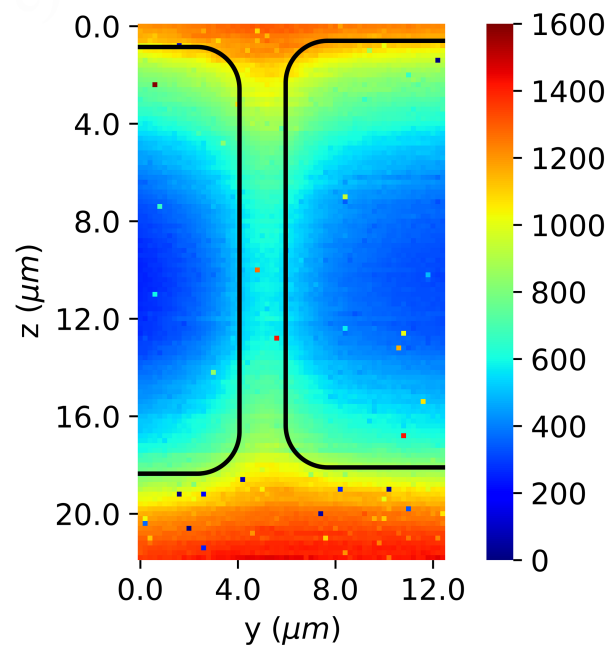
Figure 2.11: 2D map corresponding to the height A_1 of the main gaussian component of TiO$_2$ XEOL spectrum [50].

2.3.2 Irradiated samples

After irradiations, samples have been investigated by means of C-AFM, as shown in figure 2.12.

This figure refers to a TiO_2 sample which has been irradiated by drawing a single line with 200 nm step and 25 s/point exposure time, with a resulting fluence $F = 9.9 \times 10^{11}$ J/m^2. No electric field has been applied to the sample prior to AFM characterization, in order to determine the modifications induced by the X-ray beam only. The topography shows a small change in the surface morphology, but most importantly a clear trace in the conducting AFM image can be seen connecting the two electrodes. Moreover, both electrodes show a high current signal, highlighting the presence of a superficial conducting filament connecting the electrodes. This surface conductivity can be ascribed to oxygen vacancies introduced in the material during irradiation [57].
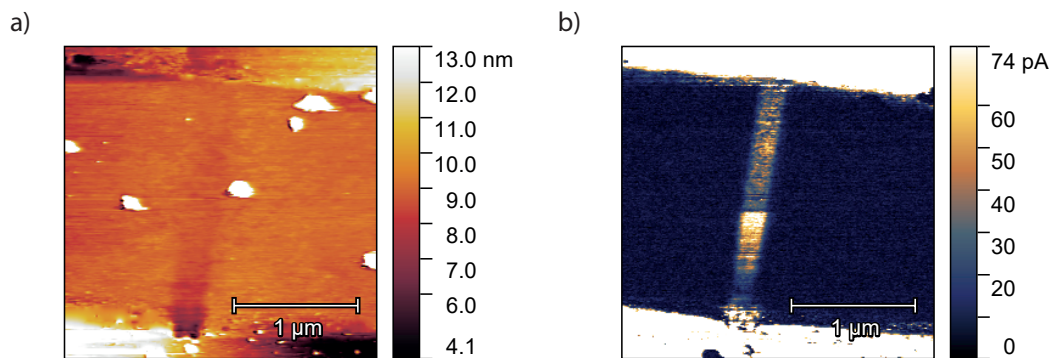
Figure 2.12: Topographic AFM (a) and conducting AFM (b) maps of TiO_2 after X-ray irradiation without previously applying any bias [57].

Figure 2.13 shows instead the non-volatile change in the sample electrical properties after several irradiation steps with progressively increasing photon fluxes. A clear increase in the sample conductivity can be observed, together with the appearance of hysteresis loops. This hysteresis can be considered as related to trapping of carriers at trap levels, which creates a spatial charge distribution and induces an electric counter field, leading to a decrease in the device conductivity with time [50, 58]. Indeed, a decrease of the current with time when a constant voltage is applied can be seen in figure 2.14, where a constant voltage of 40 V is

applied to an irradiated samples for about 5 minutes.
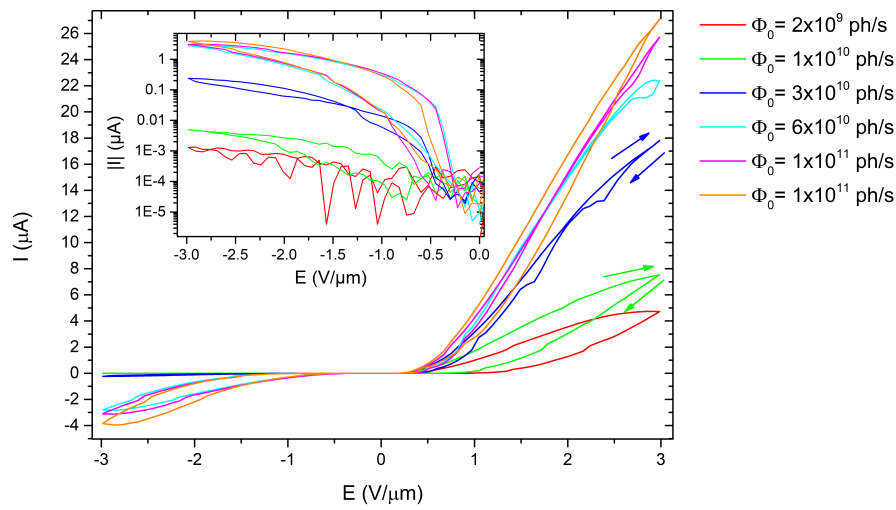
Figure 2.13: I vs. E curves collected between subsequent irradiations with progressively increasing photon fluxes [50].
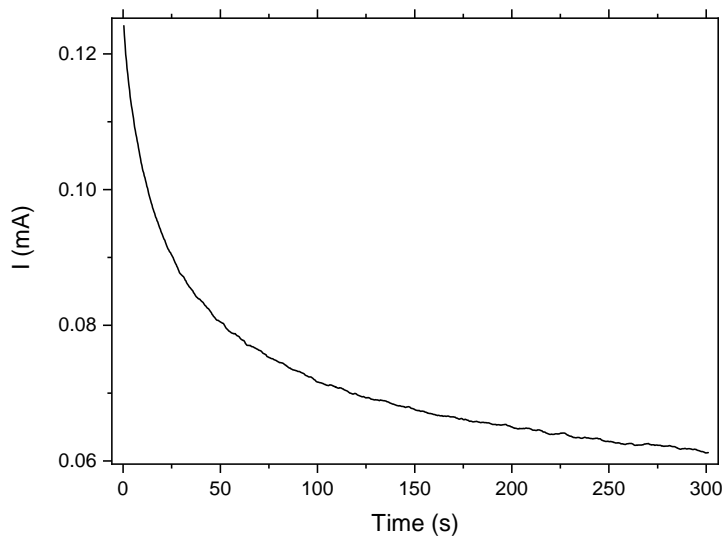
Figure 2.14: I vs. time curve for TiO$_2$ sample ($F = 9.9 \times 10^{11}$ J/m^2), showing the decay of the current when a constant voltage (40 V) is applied.

Moreover, as better shown in the inset of figure 2.13, also the reverse current in-

65

creases with irradiation by at least three orders of magnitude, and this can be ascribed to a change in the properties of the Pt/TiO_2 interface, which leads to the formation of a ohmic contact in parallel to the original rectifying interface (see section 2.3.5).

AFM characterization of samples irradiated with 16 bunch filling mode also shows the appearance of a topographic wave-like pattern, made by lines extending in the direction perpendicular to the fast scanning direction. The height of these features is quite small, but they are clearly visible from the deflection signal (figure 2.15). This pattern is only visible in the irradiated part of the gap, and the length of the lines corresponds to the height of the irradiation mesh. Moreover, the pitch of the lines is equal to the 200 nm step used during irradiation.
The origin of this pattern is not yet clear, but could be related to thermal effect which will be discussed in the next chapter.
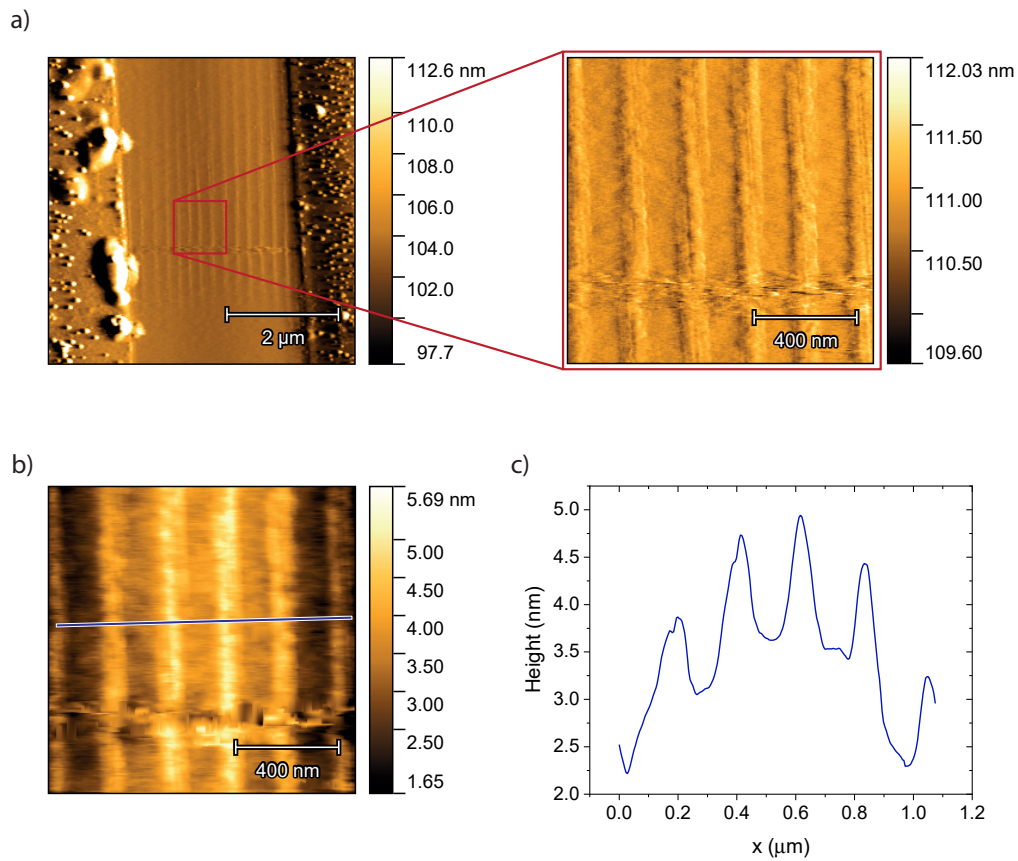
Figure 2.15: a) Deflection signal showing the wave pattern on irradiated sample (5 s/point, 200 nm step). b) Height signal collected in the same region and c) height profile extracted on the line in panel b).

2.3.3 Irreversible electroforming

After irradiation, some samples underwent electrical characterization with progressively increasing maximum voltage, as shown in figure 2.16. This particular sample was irradiated repeatedly, with exposure times up to 25 s per point on a 5 lines mesh with 200 nm spacing in both directions. This resulted in a cumulative dose $CD = 2.4 \times 10^{13}$ Gy and a cumulative fluence $CF = 5.3 \times 10^{13}$ J/m^2.

At a certain point, a sudden increase in the current flowing in the device has been measured, rapidly reaching the current compliance value set on the electrometer (in this case the compliance was set to a value of 2.5 mA).

This jump in the electrical conductivity of the device corresponds to the electroforming process, and subsequent IV curves collected on a smaller voltage range show a resistance value significantly lower with respect to pre-electroforming curves. Moreover, the rectifying effect of the Schottky barrier disappears completely. Despite many attempts of applying reverse biases to the device, the system was irreversibly set to this low resistance state, making it impossible to repeat the resistance switch and revert the device to the previous high resistance state.

The reason for the irreversibility of the electroforming process can be ascribed to the high value of current compliance set during the acquisition of the IV curves, which lead to a high current density in the conducting channel created by X-ray irradiation and subsequent intense Joule heating. The excessive heating may have caused melting and recrystallization of the material, creating a highly defective and highly conducting region connecting irreversibly the electrodes. Another possibility that could explain this behavior could be electromigration of metals under the intense electric field, but this option can be excluded thanks to post-electroforming XRF maps that have been taken immediately after the electrical characterization. These maps are shown in figure 2.17, and show the absence of metals inside the gap.

Moreover, from the Pt fluorescence map a huge damage of the electrode can be seen, highlighting the fact that the discharge actually happened in the same region that was irradiated, demonstrating that X-ray irradiation can indeed guide the electroforming process in the desired location of the gap.
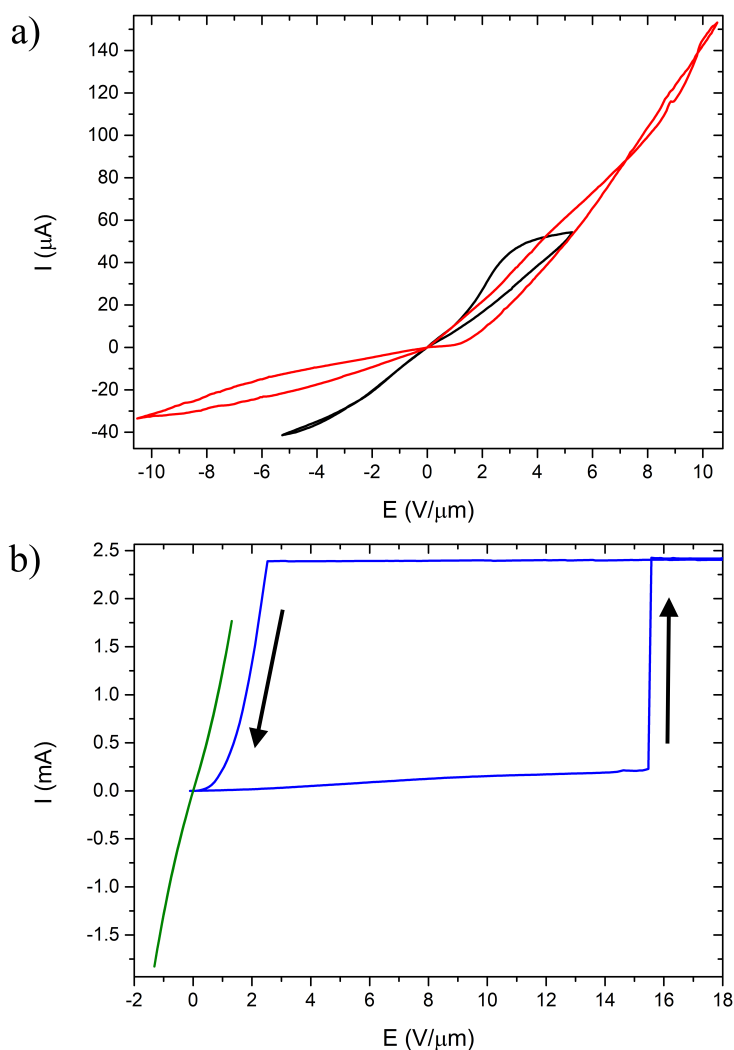
Figure 2.16: a) I vs. E curves collected with increasing voltage ranges (first measurement in black, second measurement in red) and b) I vs. E curves showing the electroforming step (in blue) and post-electroforming curve (in green) [50].

This sample has also been characterized by conducting AFM after the electrical characterization. The results are shown in figure 2.18.
As expected from the results of post-electroforming XRF maps, topographic AFM shows a damage on the Pt electrode (on the right). Inside the gap a huge bump created during the discharge process is detected, with a height around 150 nm extending across the whole width of the gap. This bump can be considered a
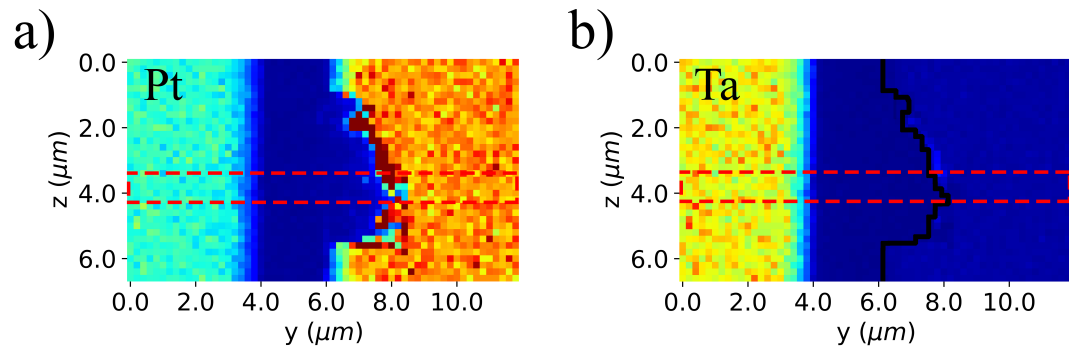
Figure 2.17: Pt and Ta XRF maps of electroformed TiO$_2$ sample. The red lines highlight the irradiated portion of the gap [50].

consequence of the high current flowing across the device during electroforming, and the resulting intense Joule heating with possible local melting. The red lines in figure 2.18a highlight the portion of the sample that was irradiated, confirming once again that X-ray irradiation guides the electroforming in the desired location. Panel b shows the C-AFM image acquired in the same region. Signal coming from both electrodes testifies the presence of a low resistance path, as already shown in the IV curves, and more importantly a high surface conductivity can be detected on one side of the gap (red circle).
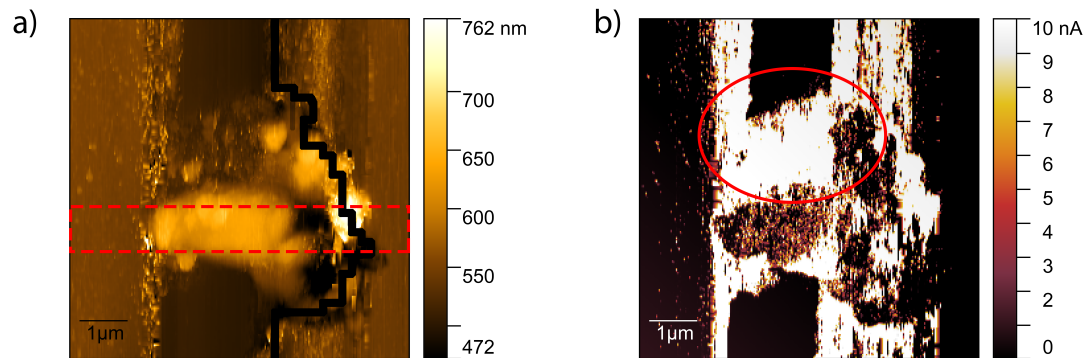
Figure 2.18: Topographic AFM (a) and conducting AFM (b) maps of TiO$_2$ after electroforming [50].

By comparing this C-AFM image with the XEOL map acquired simultaneously

with XRF maps (figure 2.19), this high conductivity region can be associated with the dip in XEOL intensity measured in the same region.
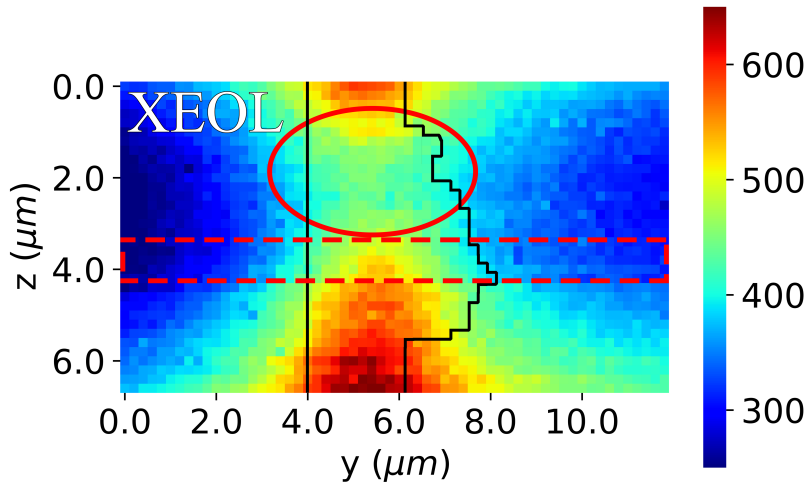
Figure 2.19: XEOL intensity map after electroforming measured at ID16B [50].

A possible explanation for these two observations could be represented by the presence of a high density of oxygen vacancies in this region of the device, which induces a variety of electronic states located within 0.7 eV from the bottom of the conduction band [59, 60]. These electronic states may, on one hand, increase the local surface conductivity of the material, and on the other hand open some non-radiative recombination path for photoelectrons, leading to the observed decrease in the luminescence intensity [56].

A TiO$_2$ sample that underwent a similar irradiation and irreversible electroforming process has been investigated by means of XANES spectroscopy.
The SEM image in figure 2.20 shows indeed a morphological bump compatible with a localized electrical discharge guided by X-ray irradiation previously performed at ID16B.

XANES mapping has been performed at ID21 by taking several fluorescence maps by scanning the area of interest with a 800×400 nm^2 beam. A map has been measured for each incoming photon energy between 4950.0 and 5039.6 eV, with an

71
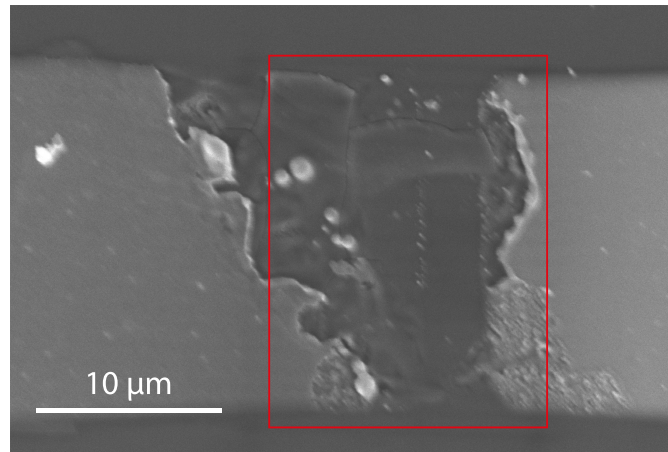
Figure 2.20: SEM image of the electroformed sample that has been investigated with XANES mapping. The red box indicates the extension of the XANES map.

energy step $\Delta E = 0.2$ eV, around Ti K edge (4966 eV).

The red box in figure 2.20 indicates the extension of the $15 \times 20\,\mu m^2$ XANES map that has been measured with a $1\,\mu m$ step in both directions. For each energy a fluorescence map has been measured; as an example a fluorescence map showing the sum of Pt and Ta M lines signals is shown in figure 2.21.
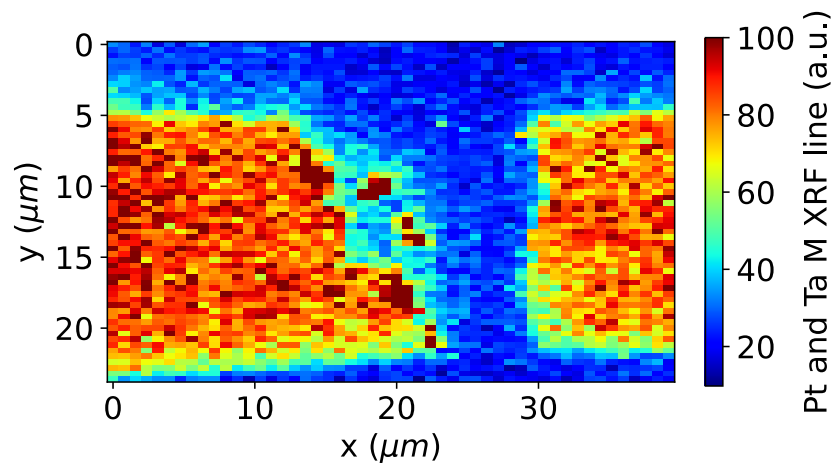
Figure 2.21: XRF map collected at ID21 prior to XANES map. The sum of intensities of Pt and Ta M lines is shown.

From the intensity of the fluorescence signal for each energy, a XANES spectrum can be obtained for each point of the map. A representative spectrum is shown in figure 2.22
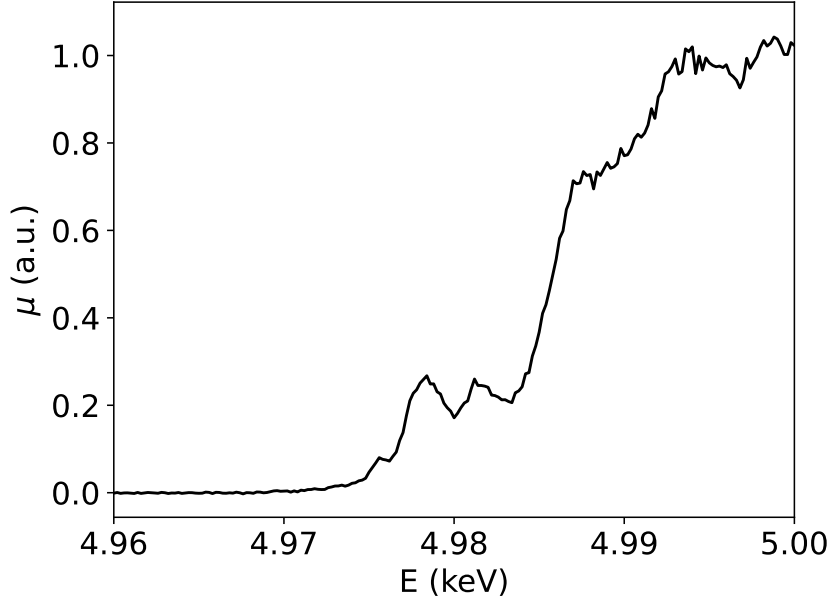
Figure 2.22: Representative TiO$_2$ XANES spectrum

The analysis of XANES data has been performed through a Python code developed for this purpose.

The first step for the analysis of XANES spectra is the normalization of the absorption. Linear fits are performed in the pre-edge and post-edge regions, obtaining two baselines $\mu_0^{pre}(E)$ and $\mu_0^{post}(E)$. The absorption is then normalized in the following way:

$$\mu(E) = \frac{I(E) - \mu_0^{pre}(E)}{\mu_0^{post}(E) - \mu_0^{pre}(E)} \tag{2.4}$$

where $I(E)$ is the measured intensity and $\mu(E)$ is the normalized intensity.

After each spectrum in the map has been normalized, different energy ranges have been fitted with different models.

The spatial distribution of each parameter of the model under investigation can be obtained, allowing to detect spatial correlation of such parameters with the position of the electroformed channel.

The most expected change in the XANES spectra collected on the electroformed channel would be a shift of the absorption edge, which would indicate a local reduction of Ti from Ti^{4+} to Ti^{3+}, as a consequence of an increase in the number density of oxygen vacancies.

For this reason, the edge region has been fitted with a sum of step functions, but no clear shift of the edge has been detected.
Therefore, we have focused the analysis on the three pre-edge peaks around $4.98\,keV$. These peaks are associated to electronic transitions from inner electronic shells to unoccupied excited levels.
This part of the spectrum has been fitted with a linear combination of three gaussians:

$$\mu(E) = \sum_{i=1}^{3} \frac{A_i}{\sqrt{2\pi}\sigma_i} e^{-\frac{1}{2}\left(\frac{E-E_{0i}}{\sigma_i}\right)^2} \tag{2.5}$$

where A_i is the amplitude, σ_i is the standard deviation and E_{0i} is the center energy of each peak.
The spectrum relative to each point of the map has been fitted with this model in the energy range marked in grey in figure 2.23, where a fit is shown.
In this way, maps corresponding to each parameter of the model can be obtained. Despite no clear difference can be visually appreciated in XANES spectra collected on the electroformed channel with respect to unaffected portions of the sample, by looking at the map corresponding to the center position of the most intense pre-edge peak (namely E_{02}), a tiny shift towards lower energies can be detected in the channel region. Such map is shown in figure 2.24a.
As already reported in literature, a shift of the pre-edge peaks corresponds to a decrease in the Ti-apical O distance in TiO_6 octahedra [61]. This shift can be therefore interpreted as the consequence of the creation of a high density of oxygen vacancies which induce such distortion.
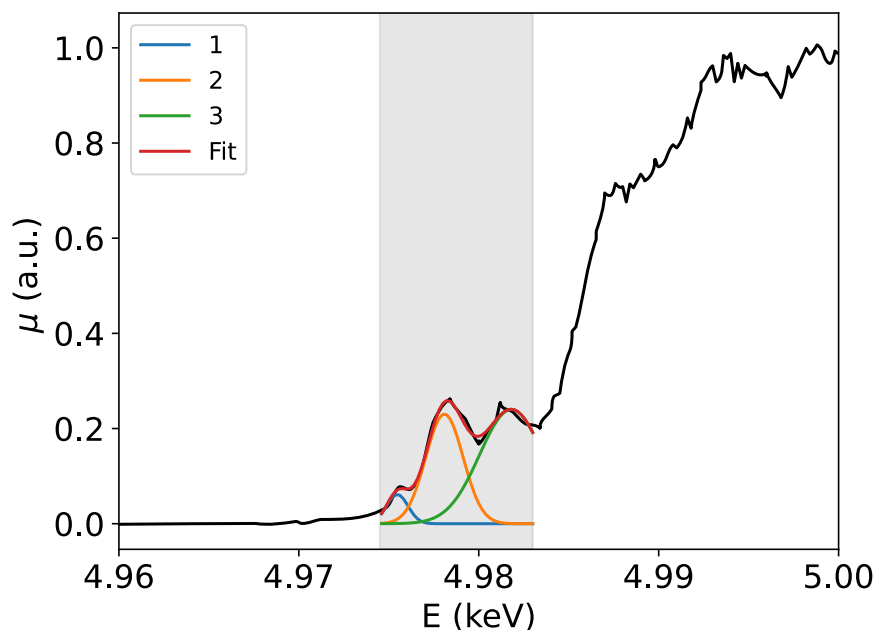
Figure 2.23: Example of fit of TiO$_2$ pre-edge peaks

Moreover, since reference spectra for stoichiometric rutile and anatase have also been collected prior to XANES mapping of the electroformed sample (figure 2.25), it is possible to compare these spectra and notice that anatase has a higher ratio of the amplitudes A_1/A_2. For this reason the corresponding map in figure 2.24b has been calculated, and it shows a higher ratio value in correspondence of the channel.

This higher value could be an indication of the presence of anatase in the channel, which could have formed during the recrystallization that followed local melting of the material induced by the discharge process.

These changes detected with XANES spectroscopy are very small, and this can be ascribed to the relatively long penetration depth of X-rays in the energy range of the fits (over 5 µm). Since AFM images (figure 2.18) show a typical height of the channel in the order of 200 nm, this means that most of the XANES signal comes from a sub-superficial volume of the sample which is unaffected by the electroforming, which makes it really difficult to detect any change.
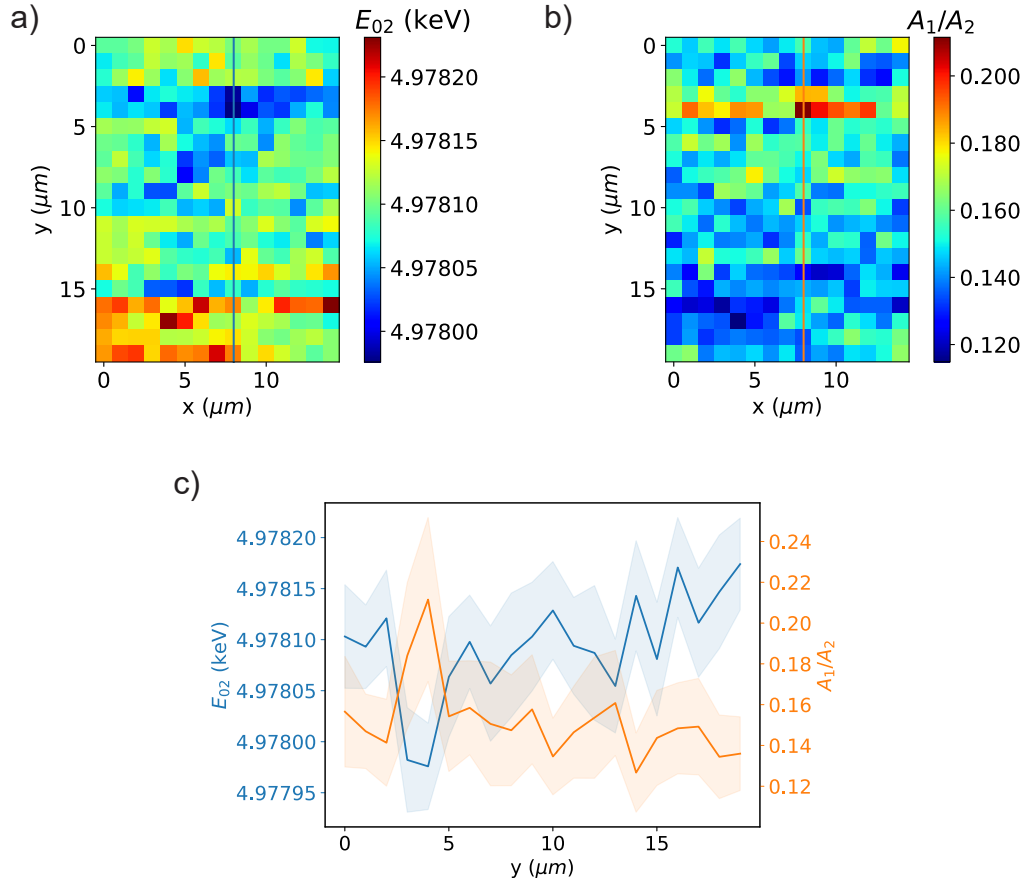
Figure 2.24: Space distribution of the peak 2 center E_{02} (a), and of the A_1/A_2 amplitude ratio (b). Panel c) shows the profiles extracted from maps a) and b) along the shown vertical lines (x=8 µm). Shaded regions represent the error bars.

To confirm this hypothesis, Raman maps have been acquired with a step size of $1{\times}1\,\mathrm{\mu m}^2$ on the same region investigated by XANES spectroscopy. Figure 2.26 shows the results of Raman mapping.

Two representative spectra corresponding to points 1 and 2 on the SEM image (panel a) are shown in panel c). The spectrum corresponding to point 1, which is not affected by the discharge, shows two main peaks around 450 and $610\,\mathrm{cm}^{-1}$ which are related to E_g and A_{1g} vibrational modes of rutile, and a broad band centered at $250\,\mathrm{cm}^{-1}$, which is ascribable to multi-phonon processes [62].

On point 2, the spectrum shows the same rutile-related peaks, but a new peak
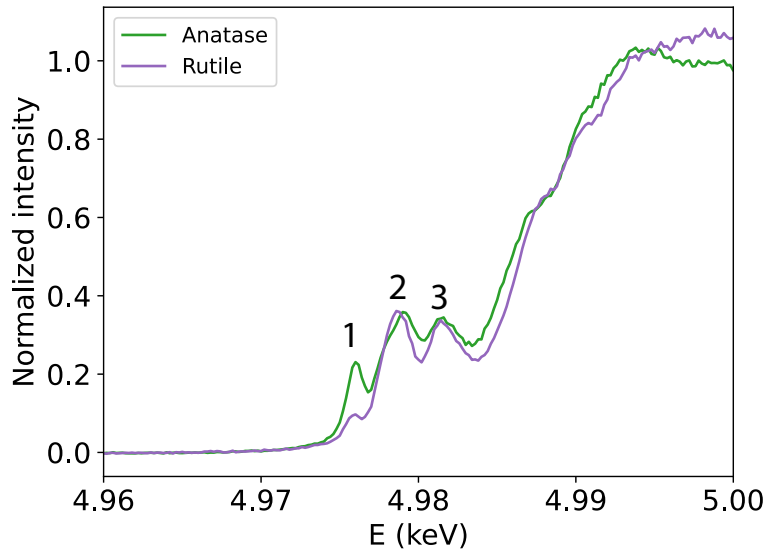
Figure 2.25: XANES spectra of anatase (green) and rutile (violet) standards.

around $140 \, \text{cm}^{-1}$ con be seen. This new peak can be ascribed to the E$_\text{g}$ mode of anatase TiO$_2$ [63].

Figure 2.26b) shows the ratio between the areas of the intensity map corresponding to the anatase and rutile peaks, and it allows to localize the presence of anatase on the electroformed channel, confirming the results obtained from XANES mapping.

Since anatase is thermodynamically more stable than rutile only in case of nanometric particle sizes [27, 64], we can assume that anatase is formed during recrystallization in the form of nanocrystals embedded in a highly defective rutile matrix. Indeed, the formation of anatase phase in memristive devices in the surroundings of electroformed channels was already reported in literature [65–67], but in devices made from amorphous TiO$_2$. Our results demonstrate that anatase can form (along with strongly reduced TiO$_2$) also starting from rutile single crystals, implying that temperatures in excess of the rutile melting point ($1850 \, °\text{C}$) are locally achieved during the electroforming.
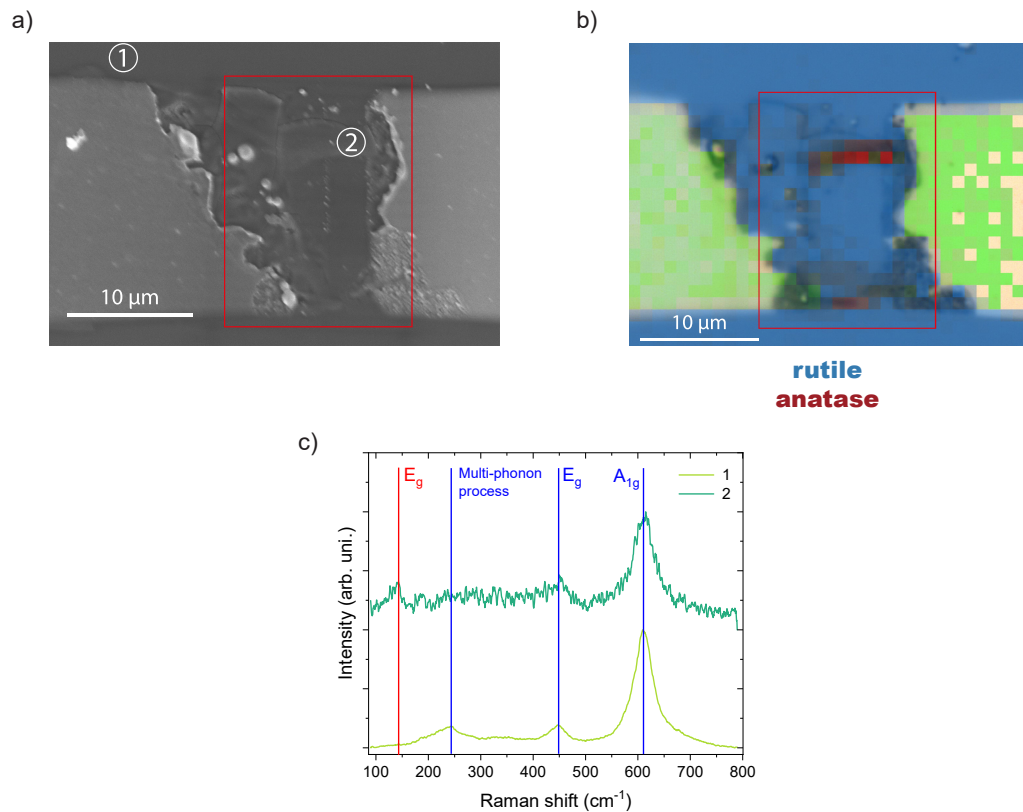
Figure 2.26: a) SEM image showing the extension of the XANES map (red box); b) intensity map showing the intensity of rutile peaks (blue) and anatase peaks (red); c) Raman spectra collected in points 1 and 2 in panel a). Peaks highlighted in red correspond to rutile TiO_2, whereas the peak highlighted in blue corresponds to anatase TiO_2.

2.3.4   Reversible electroforming

Because of these results, electrical characterization on another irradiated sample has been performed with a lower current compliance of $250\,\mu A$. On this sample a single line has been irradiated between the electrodes, with a 100 nm step and an exposure time of 20 s/point.

Indeed, by limiting the Joule heating of the device, it was possible to switch back to the high resistance state after the initial electroforming (steps 1 and 2 in figure 2.27a). It was also possible to make another OFF→ON transition (curve 3),

but then the current compliance had to be increased up to $2.5\,\text{mA}$ to induce the ON→OFF transition (curve 4). Then the system became unstable showing something similar to an OFF→ON transition in the negative branch (curve 5). This is a further indication that current compliance during operation is a crucial parameter to be kept under control for successful reversible switch, meaning that XNP does have potential for guiding reversible electroforming in TiO$_2$ memristors, but still requires further optimization.
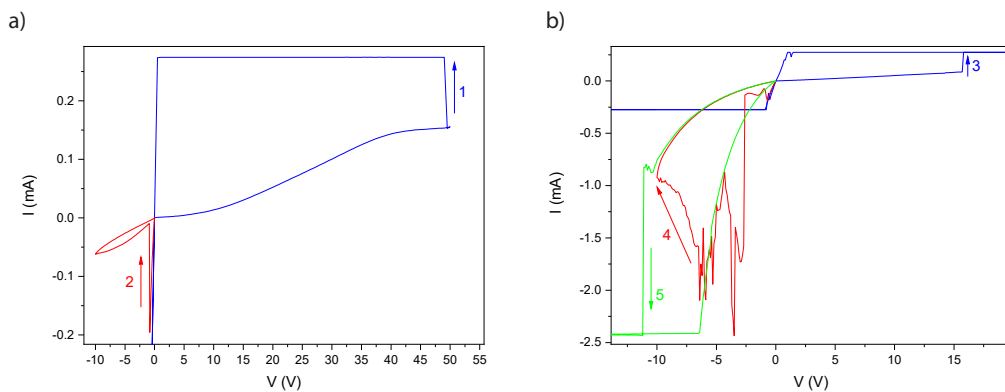
Figure 2.27: IV curves showing the reversible resistance switch achieved on an irradiated sample.

2.3.5 Schottky barrier modification

As shown in figure 2.13, irradiation induces changes in both branches of the IV curves. Since the device has a rectifying behavior due to the presence of the Schottky barrier between Pt and TiO$_2$, we can model the system as a Schottky diode in series with a big resistance corresponding to the gap separating the electrodes. By using such model, the change in the negative branch of the IV curve qualitatively corresponds to the insertion of a resistance in parallel with the diode. Such resistance is due to the irradiated portion of the Pt electrode, where defects at the interface are created and the height of the Schottky barrier is modified. This leads to the formation of an ohmic contact and also explains the symmetry of IV curves

collected after electroforming.

Figure 2.28 shows a schematic representation of the equivalent circuit. The Pt/TiO_2 interface is represented by the Schottky diode, while the TiO_2 resistance in series with the Ta/TiO_2 interface is represented by the series resistance R_s. Resistance R_0 represents the parallel parasitic resistance of the diode, which is already present in pristine samples and is supposed to remain constant, as long as the irradiated area is negligible with respect to the much larger contact area.
On the other hand, resistance R_1 is the parallel resistance introduced by irradiation, and its value decreases at increasing defects concentration (i.e. at increasing irradiation time).
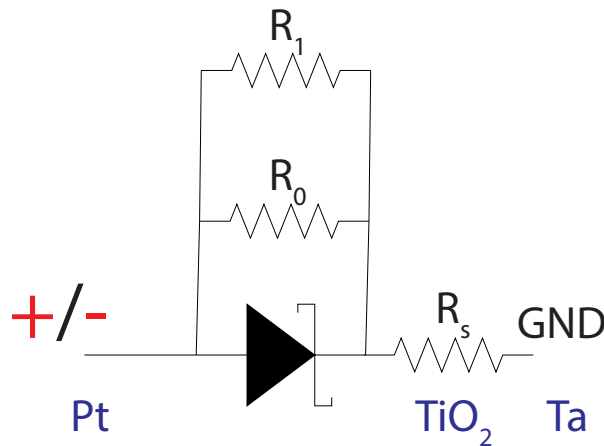
Figure 2.28: Circuit diagram representing the device under investigation.

When a positive voltage is applied to the Pt electrode (positive branch of the IV curve), current mostly flows through the forward biased Schottky diode, with negligible contribution from the parallel resistances. When bias is reversed, current mainly flows through the parallel resistances, and the progressive increase in the absolute value of the current observed during irradiation is compatible with a decreasing R_1 value.

According to this model, the effect observed during irradiation of the whole gap

width (figure 2.13) can be ascribed to a decrease in both R_s and R_1 values. The current increase in the positive branch is related to the decrease of TiO$_2$ conductivity in the irradiated channel, while the increase of current in the negative branch is due to the decrease of R_1.

To test this hypothesis we have irradiated a small portion of the Pt electrode only, shown in figure 2.29, expecting this time a change in the negative branch of the IV curve only, since the series resistance of the gap is unchanged.
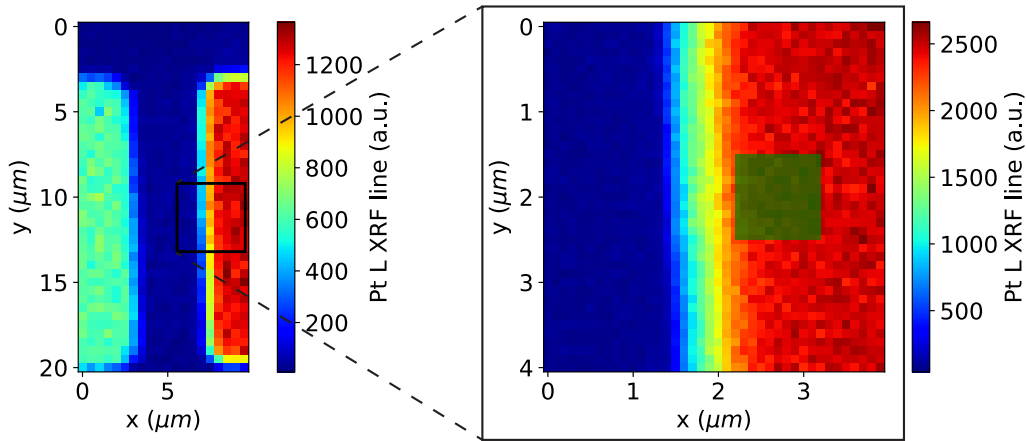
Figure 2.29: XRF maps showing the irradiated portion of the Pt electrode (in green).

The green region shown in figure 2.29 has been irradiated at ID16B by raster scanning the 1×1 µm^2 area with a 74×60 nm^2 beam (E=17.5 keV). The scan has been performed with a 200 nm step in both direction, starting with an exposure time of 1 s/point, and repeating the same procedure with 4 s/point and 20 s/point on the same area, resulting in cumulative irradiation times of 1, 5 and 25 s/point. After each irradiation an IV curve has been acquired, as shown in figure 2.30. Indeed the main difference between the different curves is the negative branch due to a decreasing R_1 value, while the positive branch, which is mainly related to the series resistance R_s is substantially unchanged.
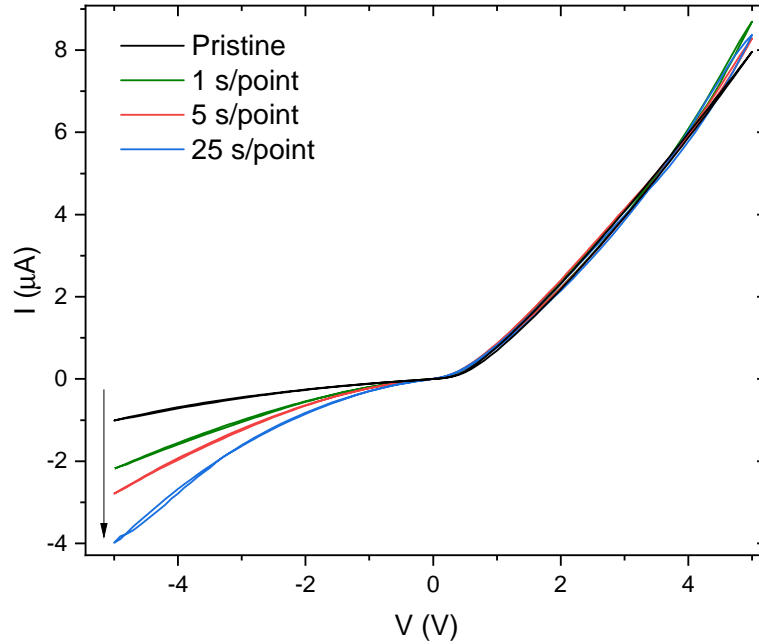
Figure 2.30: IV curves collected after subsequent irradiations.

To quantify the values of the resistances, we can consider the general diode law with a series and a parallel resistance:

$$I(V) = I_0 \exp\left(\frac{e(V - R_s I)}{n k_B T} - 1\right) + \frac{V - R_s I}{R_p} \tag{2.6}$$

where $R_p = \left(\frac{1}{R_0} + \frac{1}{R_1}\right)^{-1}$ is the equivalent parallel resistance.

For large positive voltage, we can suppose that the junction behaves as a short circuit, and perform a linear fit of the IV curve, whose slope corresponds to R_s. The parallel resistance can be instead determined by the slope of the linear fit in the large negative voltage region. This slope corresponds to $R_s + R_p$. The parallel resistance corresponds to R_0 alone in the pristine IV curve. Since R_0 is supposed to be constant, the value of R_1 can be calculated for each irradiation step as:

$$R_1 = \left(\frac{1}{R_p} - \frac{1}{R_0}\right)^{-1} \tag{2.7}$$

The results of these fittings are reported in figure 2.31.
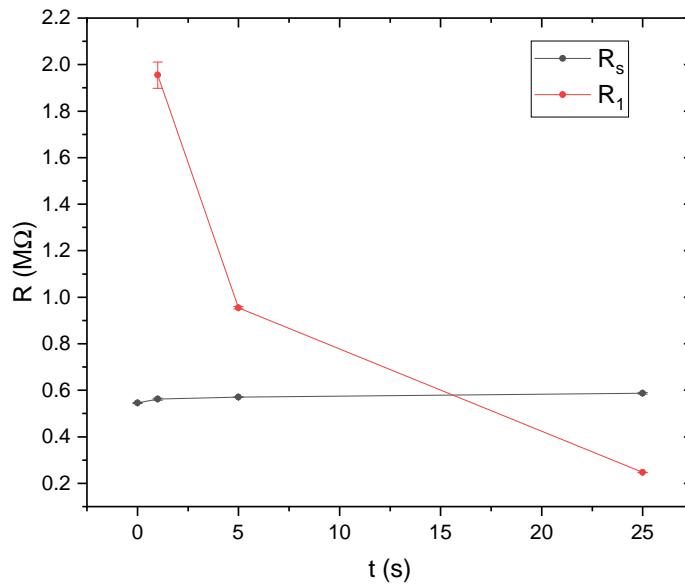
Figure 2.31: Values of series (R_s) and parallel (R_1) resistance values as a function of cumulative irradiation time.

By making the assumption that the number density of defects is proportional to the irradiation time, it would be possible to correlate the change in contact resistance to the change in material doping and identify the dominant conduction mechanism across the Pt/TiO$_2$ interface (see section 1.6). Unfortunately, the data currently available are not sufficient to make a systematic study, and more data are needed spanning a larger range of exposure times.

2.4 Iron doped strontium titanate (Fe:SrTiO$_3$)

2.4.1 Pristine samples

Unlike TiO$_2$ samples, pristine Fe:SrTiO$_3$ samples don't show a rectifying diode-like behavior, and in general the conductivity is much higher than rutile (see figure 2.32).
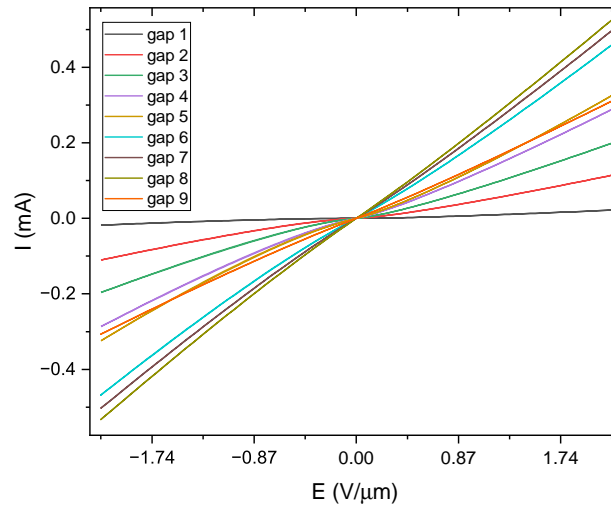
Figure 2.32: I vs. E curves for pristine Fe:SrTiO$_3$ samples (Fe doping 0.06 wt.%).

Prior to irradiation, XRF and XEOL maps have been acquired. XRF maps are reported in figure 2.33. The electrodes are clearly visible and moreover the recrystallization of the Pt electrode as a consequence of annealing can be seen from the irregular distribution of Pt on the right electrode.

XEOL spectrum of Fe:SrTiO$_3$ shows a broad photoluminescence in the visible region, centered around 550 nm, as shown in figure 2.34.
Similar photoluminescence spectra have already been reported [68]. The origin of the emission band in the visible region can be ascribed to the presence of Fe^{3+}, Fe^{4+} and oxygen vacancies in the material.
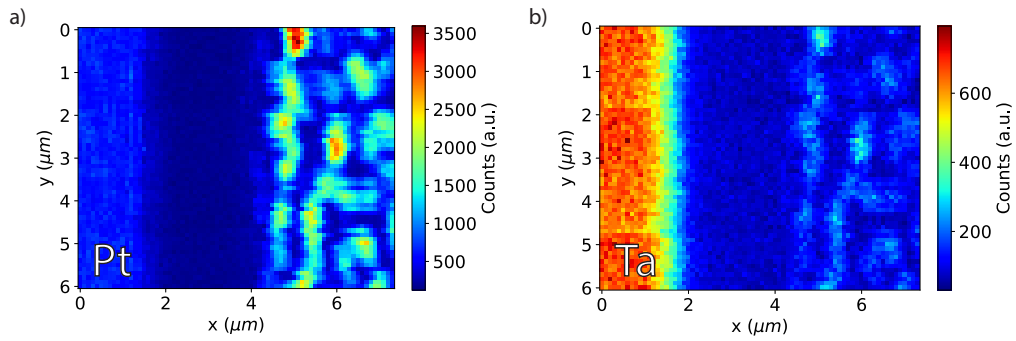
Figure 2.33: XRF maps collected at ID16B showing Pt (a) and Ta (b) distribution in the sample.
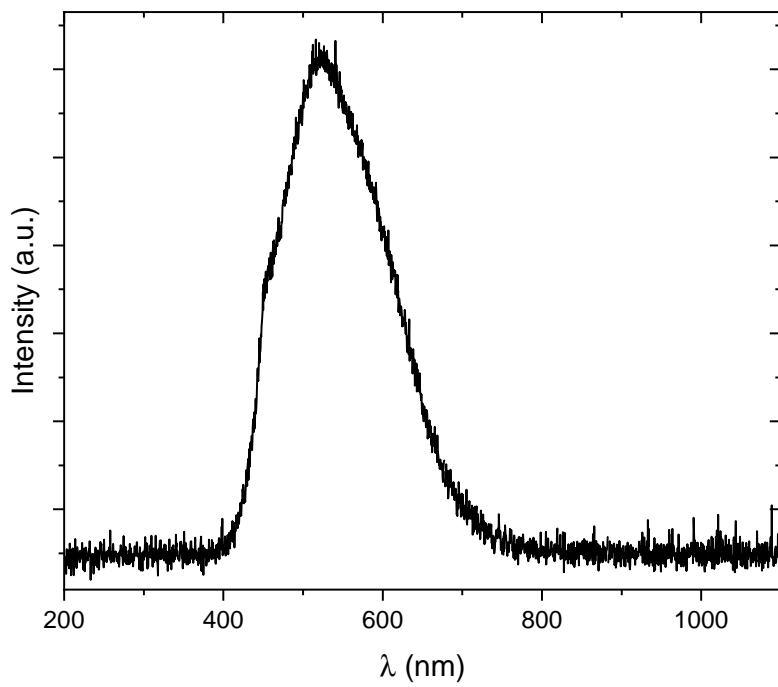
Figure 2.34: Typical XEOL spectra of a Fe:SrTiO$_3$ sample.

2.4.2 Irradiated samples

The IV curve of an irradiated Fe:SrTiO$_3$ sample is reported in figure 2.35. This sample has been irradiated by drawing a single line between the electrodes with a 50 nm step and an exposure time of 20 s/point.
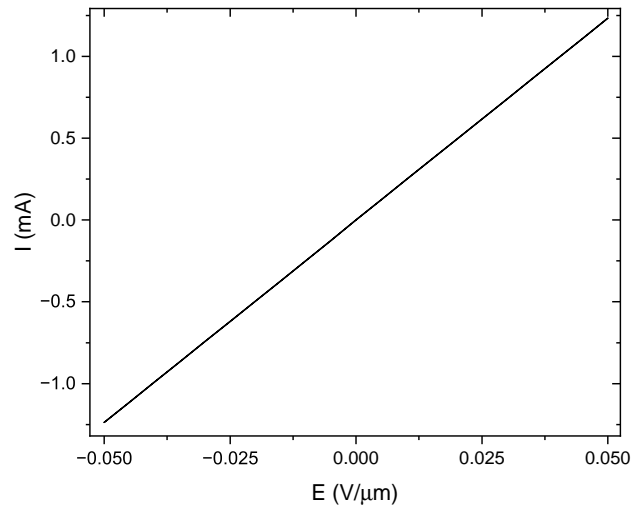
Figure 2.35: I vs. E curve for an irradiated Fe:SrTiO$_3$ sample (Fe doping 0.022 wt.%, single line irradiated with 160 nm×1 µm beam, 20 s/point, 50 nm step).

This IV curve has been collected on a much smaller voltage range (± 0.1 V) with respect to pristine IV curves, since the higher current flowing in the device would otherwise saturate to the electrometer compliance value.

Moreover, despite the lower Fe doping concentration (0.022 wt.% compared to 0.06 wt.% of previously reported pristine samples in figure 2.32), this sample shows a lower resistance, confirming once again the effect of XNP in tuning the sample conductivity.

CHAPTER 3

Investigation of thermal effects

Several mechanisms have been proposed to explain the modifications induced by X-ray irradiation in oxides, like for instance knock-on of interstitial oxygen atoms by secondary electrons in Bi-2212 [44]. This mechanism has been proved to be able to explain changes in normal resistivity of the material as a consequence of moderate irradiation, but is not able to reproduce the effect of heavy irradiation. For this reason, it is necessary to investigate other possible mechanisms underlying defects formation in irradiated oxides. One option could involve the temperature gradients induced in the samples by the X-ray nanobeam. Thermal simulations have been already performed in Bi-2212, allowing to exclude the possibility of local melting of the material [45].

Despite ordinary melting can be excluded, extreme temperature gradients can be created in the material, and the repeated pulsed irradiation of synchrotron light can induce thermal fatigue related to the high repetition rate of the dilation and contraction cycles.

In this chapter we explore such thermal effects in semiconducting oxides, using the same model previously used to investigate superconducting oxides.

87

3.1   Monte Carlo simulations

The energy deposited by the X-ray nanobeam has been evaluated by Monte Carlo simulations, using the MCNP6 code[1]. These simulations take into account many of the phenomena that take place during the interaction of photons with the material, such as photoelectric effect, Compton scattering, coherent and incoherent scattering, electron-energy loss, electron angular deflection, Bremsstrahlung emission, Auger electrons and knock-on of electrons [45]. The crystal structure of the material is not taken into account, and a low-energy threshold of $1\,\mathrm{keV}$ is applied during the tracking of secondary particles.

The incoming photon beam is defined considering the energy E_0 of the photons and the 2D Gaussian profile of the beam. The number of events considered is typically 10^8 photons, and the average energy deposited per photon can be obtained as a function of the three spatial coordinates.

A section of the simulation volume is reported in figure 3.1, showing the deposited energy density (in $\mathrm{MeV/cm^3}$) on the yz plane ar $x = 0$, with the X-ray nanobeam impinging at coordinates $(x, y, z) = (0, 0, 0)$. This figure refers to $\mathrm{SrTiO_3}$ irradiated with a $17.5\,\mathrm{keV}$ X-ray beam with size in the order of $50{\times}50\,\mathrm{nm^2}$. It is possible to see the attenuation of X-rays in the material, with an attenuation length λ which for $\mathrm{SrTiO_3}$ at $17.5\,\mathrm{keV}$ is around $39.5\,\mathrm{\mu m}$.

To explicitly get an analytical form for the deposited energy density, different energy density profiles where extracted from the (0, y, z) and (x, y, 0) planes, and fitted with a double Gaussian model (see figure 3.1b). The sharpest gaussian can be interpreted as the energy deposited by the nanobeam, while the broad contribution represents the energy deposition spread due to photoelectrons. The amplitude of each Gaussian as a function of depth was also fitted with an exponential function. The deposited energy density can be therefore expressed as:

$$
\begin{aligned}
E(x, y, z) =& A_1 \exp\left(-\frac{y}{\lambda_1}\right) \exp\left(-\frac{(x - x_c)^2}{\sigma_{1x}^2} - \frac{(z - z_c)^2}{\sigma_{1z}^2}\right) + \\
&+ A_2 \exp\left(-\frac{y}{\lambda_2}\right) \exp\left(-\frac{(x - x_c)^2}{\sigma_{2x}^2} - \frac{(z - z_c)^2}{\sigma_{2z}^2}\right)
\end{aligned}
\tag{3.1}
$$

---

[1]Simulations performed by Daniele Torsello (Department of Applied Science and Technology, Politecnico di Torino)
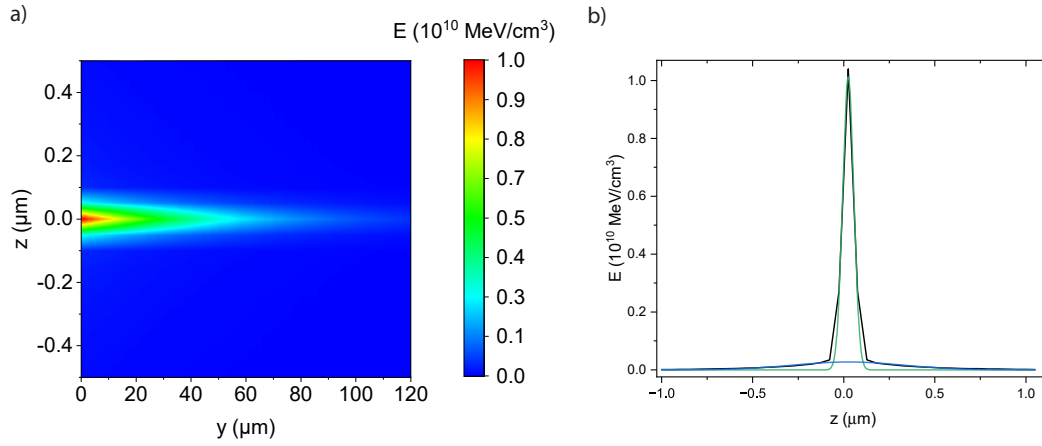
Figure 3.1: Results of Monte Carlo simulation (Fe:SrTiO$_3$, 17.5 keV X-ray beam, with size of 50×50 nm^2, impinging on SrTiO$_3$ at the axes origin). a) 2D map at $x = 0$; b) energy profile at $(0, 0, z)$. The green and blue lines in panel b) represent the two gaussian contribution used for fitting.

This fitting procedure is schematized in figure 3.2.
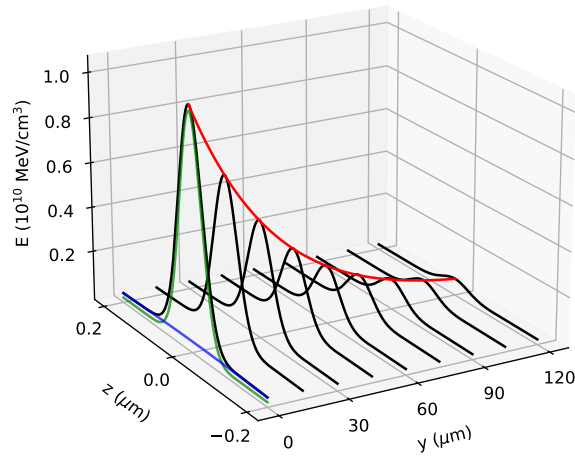
Figure 3.2: Schematic of the fitting procedure for Monte Carlo simulations. The profiles extracted at different depths are fitted with a sum of two gaussians (green and blue lines) with an exponential decay along the y direction (red line).

3.2 FEM simulations

Finite elements method (FEM) simulations have been used to simulate the temperature increase in the material during X-ray irradiation. Simulations have been carried out with COMSOL Multiphysics (version 5.5) [69].

Figure 3.3 shows the typical geometry which has been defined in FEM simulations. Irradiation experiment described in chapter 2 has been simulated, concerning both TiO_2 and $Fe:SrTiO_3$.
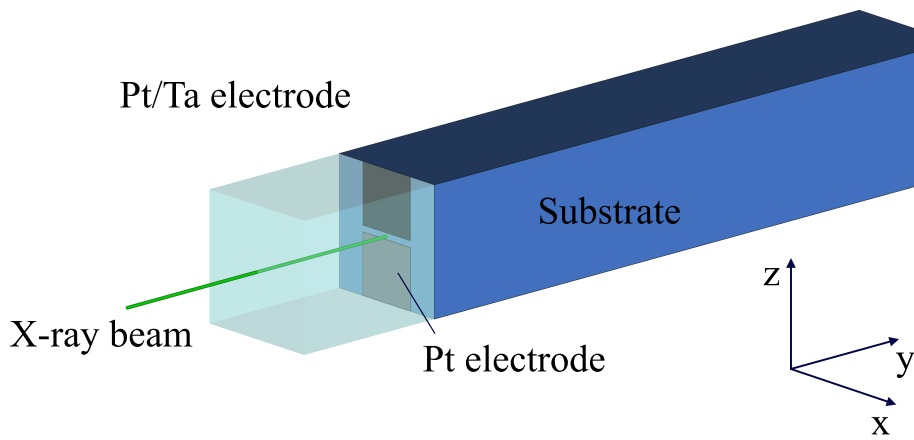
Figure 3.3: Geometry of the model used for FEM simulations.

A portion of the samples described in the previous chapter is modeled, including a portion of the electrodes when the irradiation takes place in the gap, and a layer of air on the top surface of the crystal. The portion of material considered is typically a $40 \times 40 \times 300\,\mu m^3$ block.

The whole simulation volume is filled with tetrahedral mesh elements, down to a minimum size of $10\,nm$ in correspondence of the intersection point between the beam and the material.
The classical Fourier heat diffusion equation is solved numerically:

$$\rho(T)c_p(T)\frac{\partial T}{\partial t} + \nabla \cdot \left(-k(T)\nabla T\right) = Q(x, y, z, t) \tag{3.2}$$

where $\rho(T)$ is the temperature-dependent material density, $c_p(T)$ is the temperature-

dependent specific heat capacity and $k(T)$ is the temperature-dependent thermal conductivity. The input power density $Q(x, y, z, t)$ is considered to be the product of the energy density per photon calculated from Monte Carlo simulation, multiplied by the time dependent ($\phi(t)$) or time averaged ($\overline{\phi}$) photon flux.

$$Q(x, y, z, t) = E(x, y, z)\phi(t) \tag{3.3}$$

Regarding boundary conditions, a constant temperature T_0 has been imposed on the external surfaces of the model. Simulations have been performed with two different base temperatures: 295 and 8 K. For simulations at $T_0 = 8$ K, no air layer was inserted in the model and thermal insulation condition was imposed on the top sample surface ($-\mathbf{n} \cdot \mathbf{q} = 0$), in order to better simulate the real experimental conditions (see section 3.3).

3.2.1 Time averaged flux

At first, simulations have been carried out considering a constant photon flux $\phi(t) = \overline{\phi} = const$. The value of $\overline{\phi}$ has been experimentally measured at ID16B thanks to a photodiode located around 0.5 m behind the sample position. By taking into account the transmission of 0.5 m of air (94.5% at 17.5 keV), it is possible to calculate the time averaged photon flux $\overline{\phi}$ reaching the sample.
In this case the heat source is therefore time independent:

$$Q(x, y, z) = E(x, y, z)\overline{\phi} \tag{3.4}$$

3.2.2 Pulsed time structure

On top of the simplified case of time-averaged flux, the intrinsic time structure of synchrotron radiation must be taken into account. The time dependence of the photon flux is dependent on the filling mode of the storage ring. Packets of electrons with different sizes and spacings are constantly circling the storage ring, and each time an electron bunch travels through an insertion device or a bending magnet, a photon pulse is generated. Photon pulses have therefore the same time structure of the electron beam, and the intensity of the pulse depends on the current carried by each electron bunch.

The most common filling modes of the storage ring are:

- 7/8+1, where 7/8 of the ring are filled with 868 uniformly spaced 0.23 A bunches, and the remaining 1/8 of the ring is filled in the center with a single 8 mA bunch. The RMS length of each bunch is 20 ps;

- 16 bunch, made by 16 evenly spaced bunches for a total current of 90 mA. The RMS length of each bunch is 48 ps.
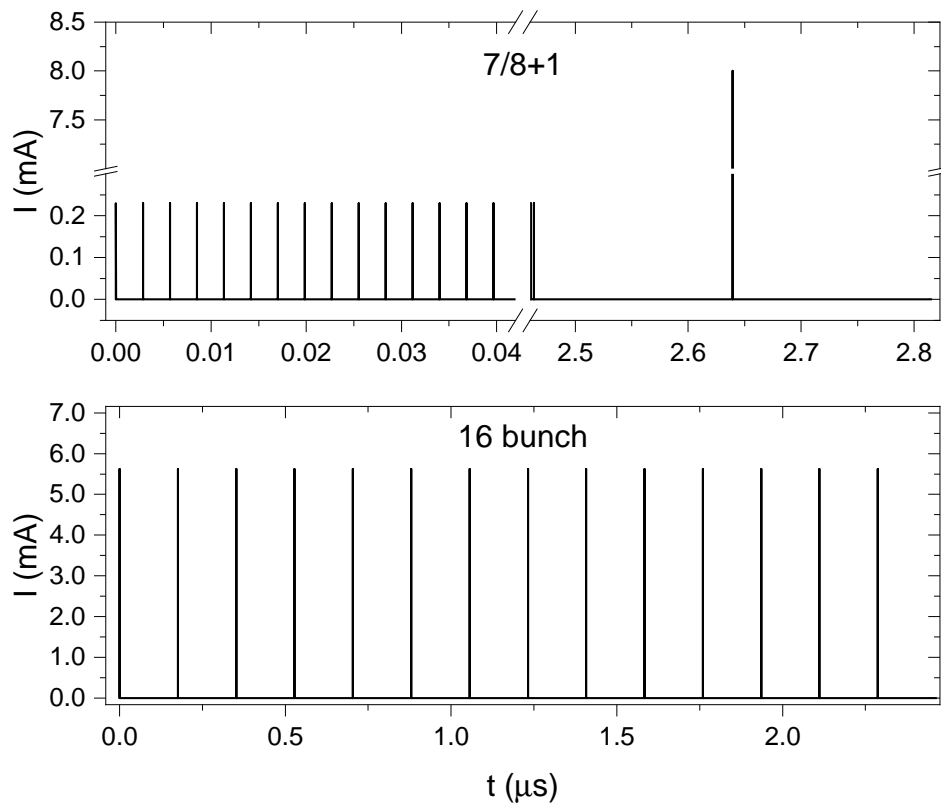
Figure 3.4: Storage ring current as a function of time for 7/8+1 and 16 bunch filling modes.

To analytically define the time dependent photon flux, each pulse can be represented as a Gaussian peak with the RMS width previously reported. To calculate

the height of each pulse, we can start from the definition of $\overline{\phi}$. For 7/8+1 filling mode the time-averaged flux is:

$$
\begin{aligned}
\overline{\phi} &= \frac{1}{T_{rev}} \int_0^{T_{rev}} \phi(t)dt = \\
&= \frac{1}{T_{rev}} \int_0^{T_{rev}} (8\phi_x + 868 \cdot 0.23\phi_x)e^{-\frac{2(t-t_0)^2}{w_t^2}} dt = \\
&= \frac{\phi_x(8 + 868 \cdot 0.23)}{T_{rev}} \int_{-\infty}^{+\infty} e^{-\frac{2(t-t_0)^2}{w_t^2}} dt = \\
&= \frac{207.64\phi_x}{T_{rev}} \sqrt{\frac{\pi}{2}} w_t
\end{aligned}
\tag{3.5}
$$

where $T_{rev} = 2.82\,\mu s$ is the revolution period of the electrons in the storage ring, $w_t \simeq 1.996$ RMS is the pulse duration and ϕ_x is the photon flux corresponding to a 1 mA bunch.

From this relation, ϕ_x can be calculated from the measured time averaged flux:

$$
\phi_x = \frac{\overline{\phi}T_{rev}}{207.64 w_t \sqrt{\frac{\pi}{2}}}
\tag{3.6}
$$

The time dependent photon flux in 7/8+1 filling mode can be therefore expressed as:

$$
\phi(t) = \sum_{n=0}^{867} 0.23\phi_x e^{-\frac{2(t-n\Delta t_1)^2}{w_t^2}} + 8\phi_x e^{-\frac{2(t-867\Delta t_1 - \Delta t_2)^2}{w_t^2}}
\tag{3.7}
$$

where $\Delta t_1 = 2.8$ ns is the spacing between the 0.23 mA bunches and $\Delta t_2 = 176$ ns is the spacing between the 8 mA bunch and the 0.23 mA bunches.

A similar calculation can be used to estimate the height of each pulse in the case of 16 bunch filling mode:

$$\bar{\phi} = \frac{1}{T_{rev}} \int_0^{T_{rev}} \phi(t)dt =$$
$$= \frac{1}{T_{rev}} \int_0^{T_{rev}} 16\phi_x e^{-\frac{2(t-t_0)^2}{w_t^2}} dt =$$
$$= \frac{16\phi_x}{T_{rev}} \int_{-\infty}^{+\infty} e^{-\frac{2(t-t_0)^2}{w_t^2}} dt =$$
$$= \frac{16\phi_x}{T_{rev}} \sqrt{\frac{\pi}{2}} w_t$$

(3.8)

In this case the quantity ϕ_x represents the height of each pulse:

$$\phi_x = \frac{\bar{\phi} T_{rev}}{16 w_t \sqrt{\frac{\pi}{2}}}$$

(3.9)

The time dependent photon flux is therefore defined as:

$$\phi(t) = \sum_{n=0}^{15} \phi_x e^{-\frac{2(t-n\Delta t)^2}{w_t^2}}$$

(3.10)

where $\Delta t = 176$ ns is the spacing between pulses.

3.2.3 Results

FEM simulations have been performed for both TiO_2 and $SrTiO_3$ irradiated with 7/8+1 and 16 bunch filling modes, with starting temperature of 295 K and 8 K. Both time dependent and time averaged photon fluxes have been simulated.
Simulations carried out with the time independent heat source show a smooth increase in temperature. Simulations with the time dependent photon flux have been carried out considering only the first four pulses. To simulate the most intense peak in 7/8+1 filling mode, the time-averaged photon flux on the first 7/8 of the revolution period has been considered, and the result has been used as a starting state for the simulation of the intense peak.

In general, the solutions of pulsed heat source simulations show intense temperature spikes in correspondence of the X-ray pulses, which are not present in the simulations with the time-averaged photon flux. In the following, for the sake of

clarity and for direct comparison with experimental results reported in the next section, only results related to 16 bunch filling mode are shown.

Figure 3.5 shows the results obtained for TiO_2 and $SrTiO_3$ irradiated at $T_0 =$295 K and $T_0 =$8 K. The difference ΔT between the maximum temperature in the model and the starting temperature is reported as a function of time, and the main difference between the two materials is the height of the temperature spikes corresponding to the X-ray pulses: about 50 K for TiO_2, and about 130 K for $SrTiO_3$, respectively. This is due to the different attenuation lengths inTiO_2 and $SrTiO_3$ (168 µm and 39.5 µm at 17.5 keV, respectively [70]), which leads to a more concentrated energy deposition in $SrTiO_3$.

Temperature spikes are also more intense at low temperature compared to room temperature. This can be explained by taking into account the lower heat capacity c_p of materials at lower temperature, and also the presence of air during irradiation at room temperature, which can slightly dissipate part of the heat generated.

By differentiating the maximum temperature as a function of time, a maximum heating rate of 1×10^{12} K/s can be estimated for $SrTiO_3$ irradiated at 8 K (figure 3.7c).

Temperature gradient has been estimated from the derivative of a temperature profile extracted on the plane perpendicular to the X-ray beam (figure 3.6). In the case of $SrTiO_3$ at 8 K, temperature gradient in the order of 1×10^9 K/m has been estimated (figure 3.7d).

From these results, it seems that low temperature irradiation should give rise to higher temperature gradients and heating rates compared with room temperature irradiation. If thermal fatigue plays a role in material damage, we should therefore expect more evident radiation damage at lower temperatures. This is unexpected since lowering the temperature is common practice to reduce sample damage during measurements, especially for soft and biological matter.
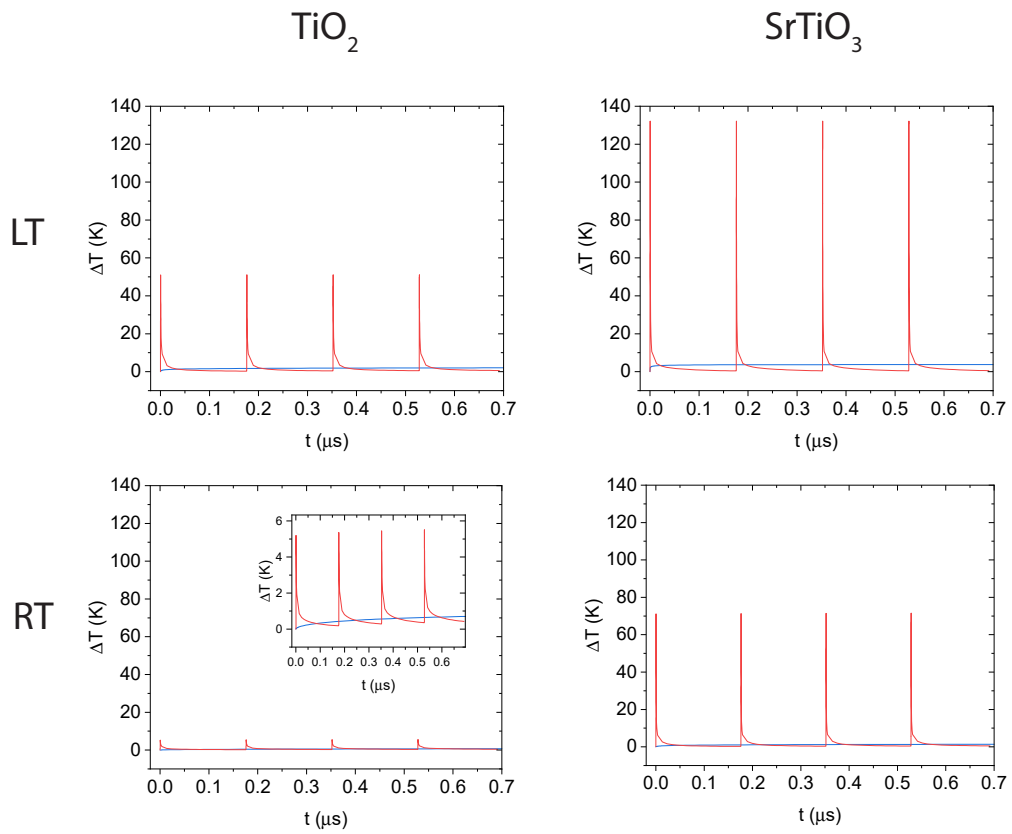
Figure 3.5: $\Delta T = T_{max} - T_0$ as a function of time. Red lines correspond to the case of the instantaneous photon flux, blue lines correspond to the case of time-average photon flux.
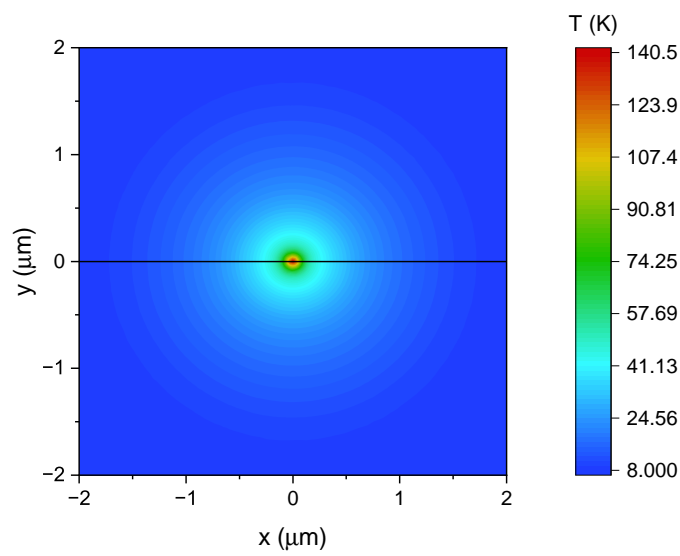
Figure 3.6: xz map corresponding to the instant when the maximum temperature is reached. The black line indicates the line from which the temperature profile in figure 3.7 has been extracted.
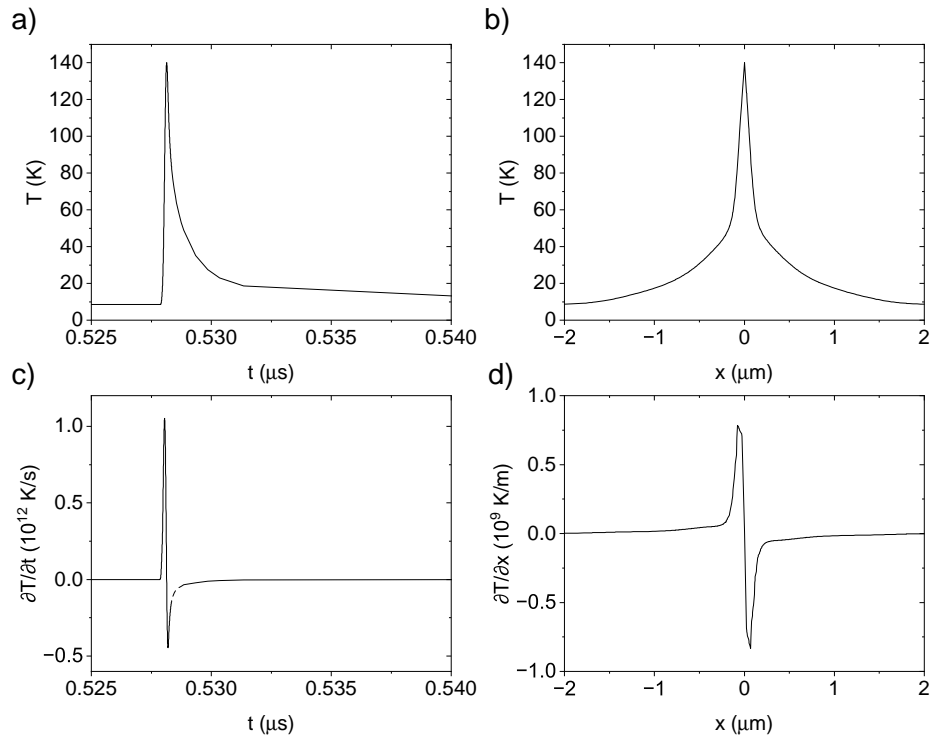
Figure 3.7: a) Maximum temperature as a function of time for $SrTiO_3$ irradiated at $8\,K$ and corresponding heating rate (c). b) Temperature profile extracted along the line shown in figure 3.6 and corresponding temperature gradient (d).

3.3 Irradiation at different temperatures

To test the hypothesis of thermal effects being more pronounced at low temperatures, we have irradiated TiO_2 and $SrTiO_3$ samples in different conditions. Irradiation has been performed at ID16B, with 16 bunch filling mode both at room temperature and at 8K.

Room temperature irradiation has been performed in a similar way as described in the previous chapter. Samples have been irradiated with a $80{\times}77\,nm^2$ beam with an energy of $17.1\,keV$ and a time averaged flux of 1.51×10^{12} photons/s.

Low temperature irradiation has been performed by using a liquid helium flow cryostat. The cryostat is kept under static vacuum, with the sample positioned inside. The cryostat can be mounted on the sample positioning motors, and the X-ray beam can reach the sample through a (400 ± 50) µm thick diamond window, with a 94% transmittance at $17.5\,keV$.
Samples have been irradiated with a $74{\times}60\,nm^2$ beam with an energy of $17.5\,keV$ and a time averaged flux of 9.9×10^{11} photons/s.

To have a good comparison between irradiation at room temperature and low temperature, similar size areas have been irradiated in the two conditions, both on TiO_2 and $SrTiO_3$ samples. Areas far away from the metal electrodes were selected in order to avoid heat dissipation through the electrodes themselves.

For each material at each temperature, different areas have been irradiated with different exposure times, ranging from 1 s/point to 625 s/point. A summary of all irradiations is reported in table 3.1.

3.3.1 AFM characterization

After irradiation, AFM characterization has been performed to compare the surface morphology changes at different irradiation temperatures. This characterization has been performed with a Cypher S system by Asylum research at Forschungszentrum Jülich.

Table 3.1: Summary of irradiations performed at room temperature and cryogenic temperature on TiO_2 and $Fe:SrTiO_3$.

Material	Irradiation temperature (K)	Exposure time (s/point)	Area (μm^2) (H×V)	Step (nm) (H×V)
TiO_2	295	1	6×9	286×375
		5	6×6.38	286×290
	8	1	6×9	200×410
		5	6×9	200×300
		25	6×9	300×450
		125	6×4	400×667
		625	2×2	500×500
$SrTiO_3$	295	1	6×9	286×290
		5	6×9	286×290
	8	1	6×9	200×410
		5	6×9	200×300
		25	6×9	300×450
		125	6×4	400×667

As expected from the different penetration depths of X-rays in TiO_2 and $SrTiO_3$, damage on $SrTiO_3$ is more pronounced in comparison to TiO_2, since energy deposition is concentrated on a smaller volume. This was evident from thermal simulations and is confirmed by AFM imaging, as shown in figure 3.8. The height of the morphological features created by X-ray irradiation is indeed much higher on $SrTiO_3$ surface than in TiO_2.

On the other hand, by comparing $SrTiO_3$ samples irradiated at room temperature and at cryogenic temperatures, it is possible to see a more intense damage (i.e. a larger portion of the irradiated surface that shows X-ray generated bumps) after room temperature irradiation, in contrast to what was expected from the results of FEM simulations.
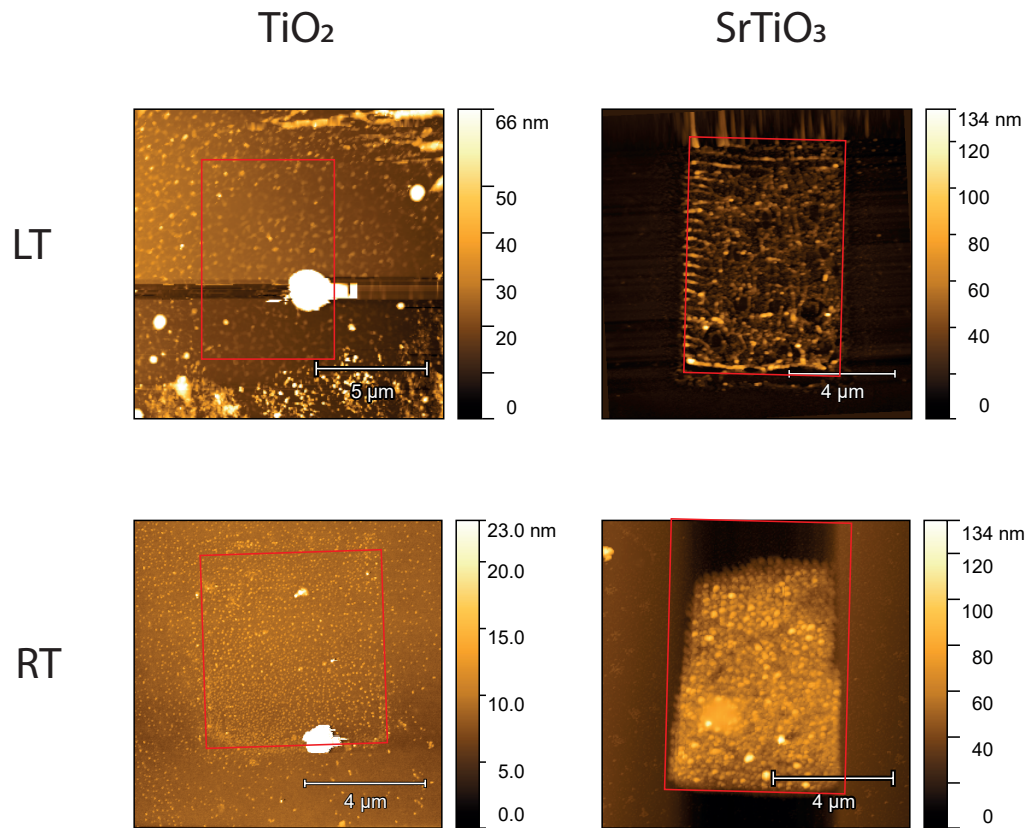
Figure 3.8: AFM images of samples irradiated with an exposure time of 5 s/point. Red boxes surround the irradiated areas

Moreover, the extension of the damaged region at low temperature matches the extension of the irradiation mesh, while the region irradiated at room temperature shows morphological changes on a smaller area with a trapezoidal shape. This could indicate a possible diffusion of X-ray induced defects at room temperature, resulting in an accumulation towards the lower part of the irradiation mesh.

The AFM image corresponding to $SrTiO_3$ irradiated at low temperature also shows in the leftmost part of the irradiated region a characteristic line pattern.
A height profile along the vertical direction is shown in figure 3.9, together with a 2D FFT. The profile shows a uniform spacing of the height peaks compatible

with the 300 nm vertical step used during the raster scan irradiation. The 2D FFT shows two bright spots symmetrical with respect to the origin at a distance around $3\,\mu m^{-1}$, again compatible with the irradiation step.
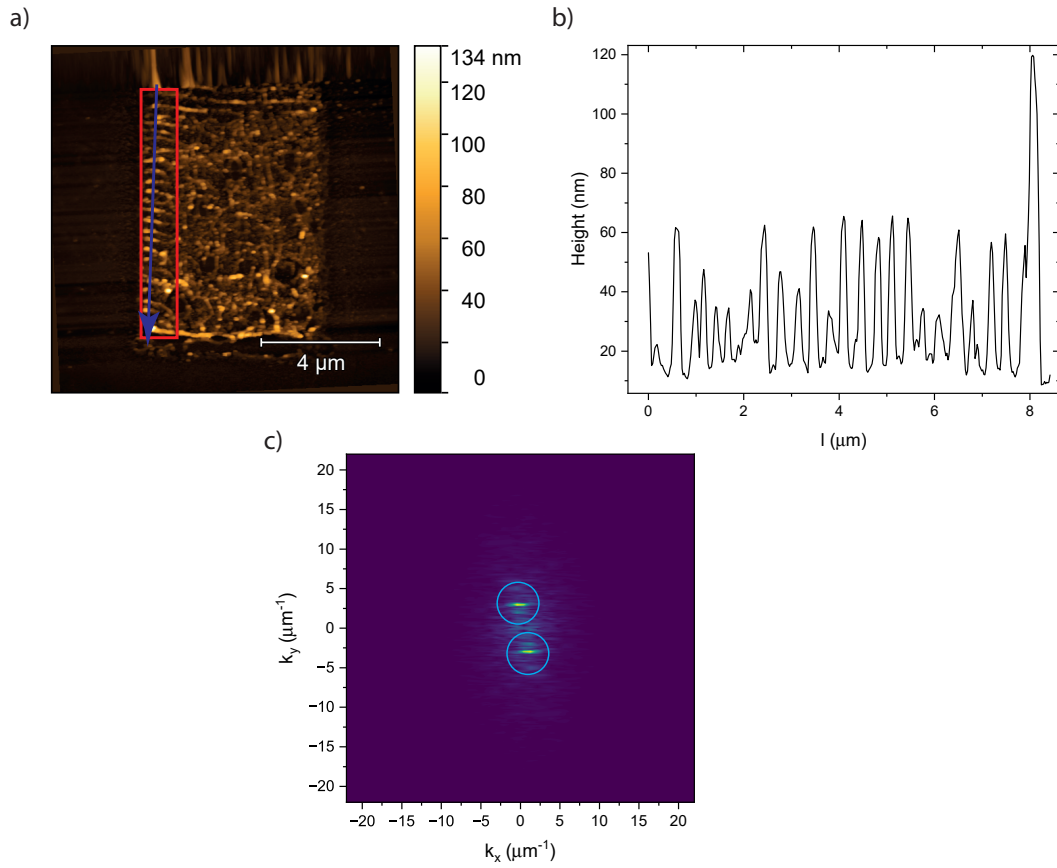
Figure 3.9: a) AFM image of Fe:SrTiO$_3$ sample irradiated at 8 K with an exposure time of 5 s/point. b) Height profile along the blue line in panel a). c) 2D FFT of the red box in panel a).

3.3.2 Photoluminescence measurements

Irradiated Fe:SrTiO$_3$ samples have been investigated by means of photoluminescence (PL) measurements[2]. PL measurements have been performed with a 325 nm excitation laser with a 15 mW power.

A reference PL spectrum of a pristine portion of the sample is shown in figure 3.10. The spectrum shows a series of sharp peaks located around 670 nm which could correspond to Fe d-d transitions. Two broad bands are visible at 420 nm (blue band) and 510 nm (green band).
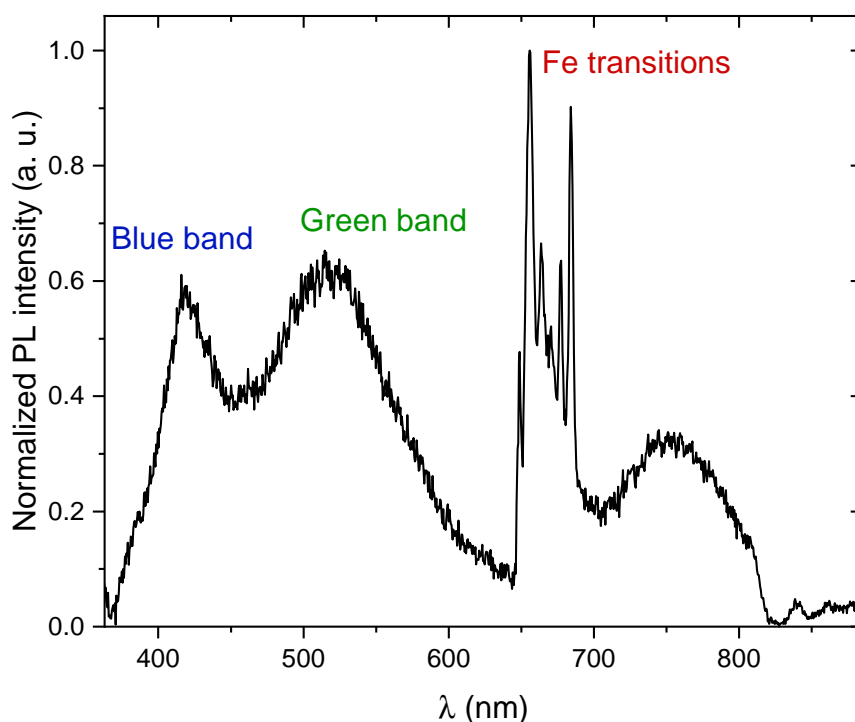
Figure 3.10: Reference PL spectrum of pristine Fe:SrTiO$_3$ sample.

Since the experimentally determined band gap of SrTiO$_3$ is 3.25 eV [71], these two bands correspond to electronic transitions from gap states located at 0.82 eV and

---

[2]Performed by Jorge Serrano and collaborators at University of Valladolid

0.3 eV below the conduction band, suggesting the presence of two different defect species in the material. Specifically, the green band is related to recombination of localized electrons (small polarons), while the blue band corresponds to the recombination of delocalized electrons [72]. The origin of the broad IR band between 700 and 800 nm is still under investigation.

Results from the regions irradiated with an exposure time of 1 s/point are shown in figure 3.11.

The most evident difference between room temperature and low temperature irradiation is the relative intensity of the green, blue and infrared bands, suggesting that a higher amount of defects responsible for the blue emission was created during room temperature irradiation.
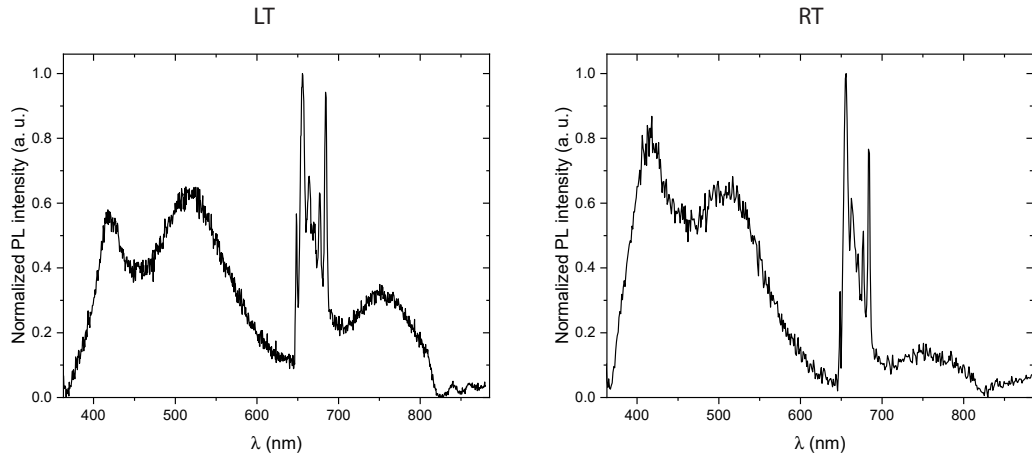
Figure 3.11: PL spectra of Fe:SrTiO$_3$ samples irradiated at low temperature and room temperature (1 s/point).

PL measurements on the regions irradiated at low temperature and room temperature with an exposure time of 5 s/point are reported in figure 3.12. The main differences between the two cases is the intensity of Fe transitions lines with respect to the other bands. Since Fe related lines are expected to have a constant intensity, it seems that irradiation at low temperature with 5 s/point exposure time create a much higher defect density than all other irradiation conditions. Another evident difference is the absence of the IR band after room temperature irradiation. The reason for this is still unclear since the origin of this band is still to be determined.

Another interesting difference is the different relative intensity of the blue and green bands, which seems to indicate that low temperature irradiation favors the formation of defects responsible for the blue band.
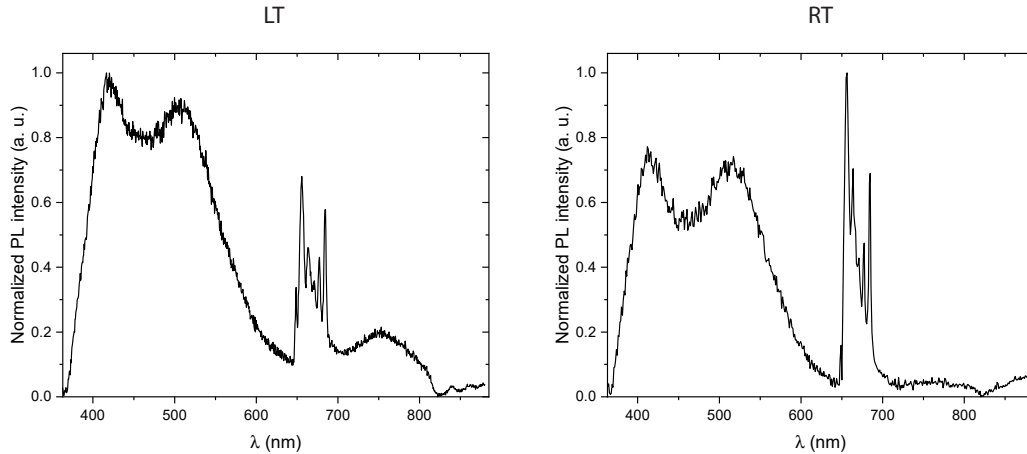
Figure 3.12: PL spectra of Fe:SrTiO$_3$ samples irradiated at low temperature and room temperature (5 s/point).

These preliminary results are still to be completely understood, but they suggest a dependence of the amount and kind of defects on both irradiation temperature and exposure time.

3.4 Determination of thermal expansion by XRD

To try to experimentally confirm the results of thermal simulations, XRD experiments have been performed at ID01 of ESRF. The basic idea is to exploit the pulsed time structure of the beam to simultaneously heat the material and collect XRD data.

Some studies have already been published trying to quantify the X-ray induced temperature increase with fourth generation synchrotrons [73], but the time structure of the beam has not been taken into account.

105

3.4.1 Experimental setup ID01

ID01 is an X-ray diffraction beamline for the study of materials, from nanostructures to bulk. Several diffraction techniques are available:

- CDI (coherent diffraction imaging);

- XRD (X-ray diffraction);

- GISAXS (grazing incidence small-angle scattering);

- ptychography;

- FFXM (Full Field X-ray Microscopy).

The beamline provides a hard X-ray beam in the energy range 6.0-24.0 keV, with beam size ranging from $35.0 \times 35.0 \, \text{nm}^2$ to $6.0 \times 1.0 \, \text{mm}^2$.

For XRD measurements, the sample is mounted on piezo motors on top of a hexapod, allowing for precise alignment of the sample. Sample motors are mounted on a goniometer allowing the angular movement of the sample on the θ angle.

A 2D Maxipix pixel detector (516×516 pixels) with 55 μm pitch in both directions is mounted on a motorized arm which can rotate on the 2θ angle. The experimental setup is shown in figures 3.13 and 3.14.
The sample is mounted on the piezo motors, and the detector is moved to intercept a single diffraction peak. When the peak is centered on the detector, a small θ-2θ scan is performed, by simultaneously moving the sample and arm motors and for each position of the detector an image is acquired.

Measurements have been repeated with different photon fluxes, obtained by inserting a variable amount of Al filters (each one with 100 μm thickness) before the sample position. The hypothesis is that higher photon fluxes should heat up the sample more and cause a shift in the diffraction peak position as a consequence of lattice expansion.
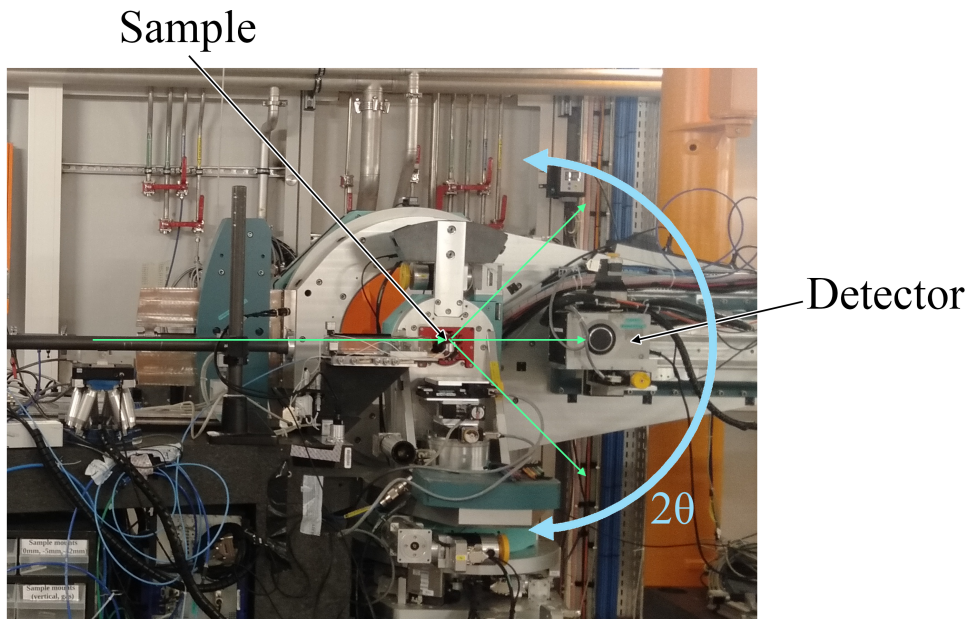
Figure 3.13: Experimental setup at ID01.
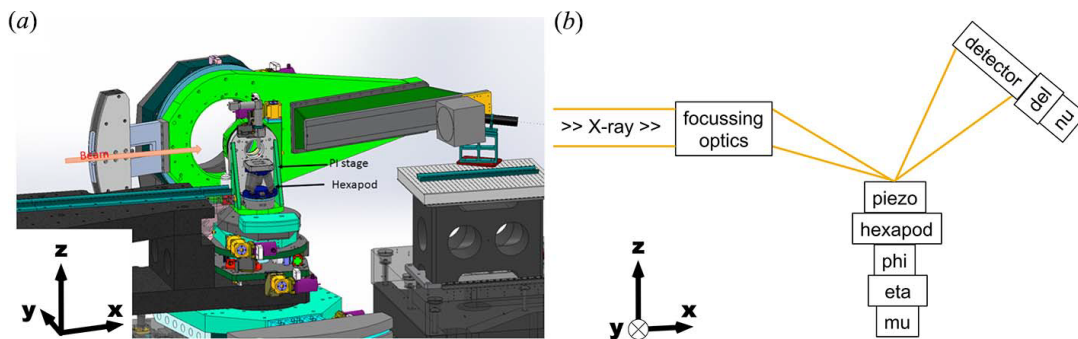
Figure 3.14: Schematics of the experimental setup of ID01 [74].

3.4.2 Data analysis

The data analysis has been performed with a Python script developed for this purpose. A rectangular region of interest (ROI) has been defined on the detector, and for each angular position the integral of the counts inside the ROI has been

extracted. In this way, the peak profile can be obtained by plotting the counts as a function of the angular position θ or 2θ.

Resulting peaks can be fitted with peak functions such as Gaussians or PseudoVoigt profiles, and the evolution of peak position, width or intensity as a function of the photon flux on the sample can be obtained.

3.4.3   Results

Scans have been performed on a barium fluoride (BaF_2) single crystal at room temperature. This material has been selected for its high thermal expansion coefficient ($18.4 \times 10^{-6}\,K^{-1}$ [75]) and its relatively short attenuation length ($8.65\,\mu m$ at $8.5\,keV$ [70]). This should result in a concentrated energy deposition inducing high temperature gradients and consequently easily detectable thermal expansion.

Figure 3.15 shows the maximum projection (the maximum value measured by each pixel during the scan) of (444) peak measured with 6 Al filters.
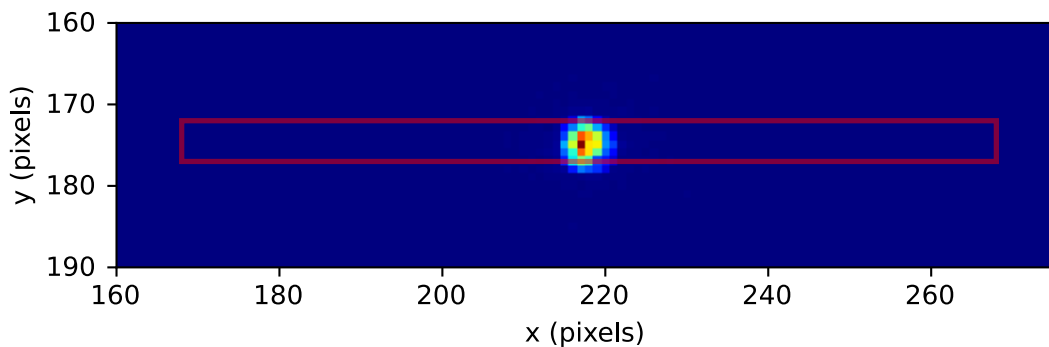
Figure 3.15: Maximum projection of (444) peak of BaF_2.The red rectangle indicates the extension of the ROI we are considering.

Figure 3.16a shows peaks obtained alternating between 6 filters and no filter (full available photon flux reaching the sample), and a clear broadening of the peak towards lower θ values is visible, which indicates an increase in the interplanar distance. A few cycles have been performed inserting and removing the filters to test the reversibility of heating effects, and indeed this effect seems to be completely

reversible in this experimental conditions (see figure 3.17). This effect can be therefore ascribed to thermal dilation only.
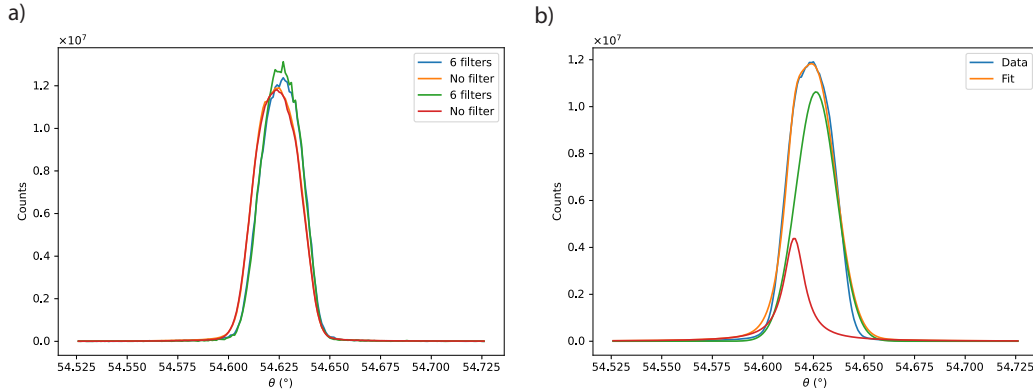
Figure 3.16: a) Comparison of diffraction peaks measured with 6 Al filters and without any filter. b) Fitting of the red curve in panel a) with a two gaussian model.
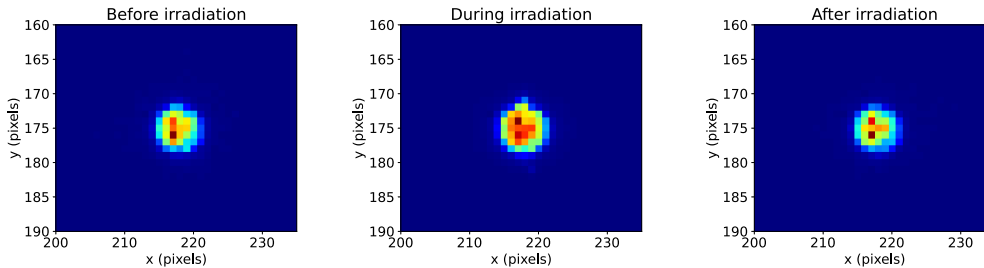
Figure 3.17: Maximum projections before, during and after irradiation (obtained with 6, 0 and 6 filters respectively).

The peak obtained with 6 filters has been fitted with a PseudoVoigt function, obtaining the position and width of the peak which can be considered unaffected by heating. The peak obtained by irradiation without filters has been fitted with a linear combination of two PseudoVoigt peaks, one corresponding to the unheated portion of the sample having the same center and sigma of the 6 filters one, and one corresponding to the heated portion of the material. This is a simplification since we are actually probing a material with a non uniform temperature distribution, but it is useful to get an estimation of the temperature increase in the sample.

The result of the fit with the double PseudoVoigt function is shown in figure 3.16b. From the peaks angular positions, the interplanar distances and corresponding uncertainties can be calculated:

$$d = \frac{\lambda}{2\sin\theta} \tag{3.11}$$

$$\sigma_d = d\cot\theta\sigma_\theta \tag{3.12}$$

From the d and d' values obtained from the two peaks, being d the starting interplanar distance and d' the interplanar distance on the heated part of the sample, the temperature increase corresponding to the observed thermal dilation can be calculated:

$$\Delta T = \frac{d' - d}{\alpha d} \tag{3.13}$$

where α is the thermal expansion coefficient of the material. The corresponding uncertainty can be calculated by error propagation:

$$\sigma_{\Delta T} = \sqrt{\left(\frac{\partial \Delta T}{\partial d'}\sigma_{d'}\right)^2 + \left(\frac{\partial \Delta T}{\partial d}\sigma_d\right)^2} = \tag{3.14}$$

$$= \sqrt{\left(\frac{1}{\alpha d}\sigma_{d'}\right)^2 + \left(-\frac{d'}{\alpha d^2}\sigma_d\right)^2} \tag{3.15}$$

The temperature increase corresponding to the observed thermal dilation has been estimated to be $\Delta T = (7.2 \pm 0.2)\text{K}$.

From the thermal diffusivity of the material ($D = k/\rho c_p$), it is possible to calculate the time heat takes to diffuse out of a radius Δr. If this time is longer than the duration of an X-ray pulse, the adiabatic approximation can be used to estimate the maximum temperature increase in the material [45]. This characteristic time, considering $\Delta r = FWHM_{beam}/2$ is:

$$\Delta t = \frac{\Delta r^2}{D} \simeq 6.8 \text{ ns} \tag{3.16}$$

which is much longer than the 48 ps RMS pulse duration. Therefore, supposing that the temperature increase is uniform on a cylindrical volume with radius Δr

and height $\Delta l = \lambda/10$, with $\lambda =$ 8.65 μm being the attenuation length of 8.5 keV photons in BaF$_2$, ΔT can be estimated as:

$$\Delta T = \frac{E_{bunch}[1 - \exp(-0.1)]}{mc_p} \tag{3.17}$$

where $m = \rho\pi\Delta r^2\Delta l$ is the mass of the cylindrical volume. The maximum temperature estimated in this way is $\Delta T \simeq$ 16.6 K.

The estimation from adiabatic approximation has the same order of magnitude as the experimental result, which gives a lower value because the XRD signal comes from a bigger volume of material with a non-uniform temperature distribution and because the adiabatic approximation supposes a zero heat propagation velocity.

FEM simulations have also been performed for this experiment, and the average temperature calculated on the same volume used for adiabatic approximation is shown in figure 3.18. The volume considered is placed on the surface of the sample around the impact point of the X-ray beam. The maximum temperature increase in this case is around 4.6 K.

The adiabatic approximation and the FEM simulations of the heat equation represent extreme cases, since heat propagation velocity is considered equal to zero in adiabatic conditions, and infinite in the Fourier equation. Since in reality the speed of sound is a non-zero but finite value (4.38 km/s in BaF$_2$ [76]), and the experimentally determined value lies in between these two calculated extremes, we can assume that XRD is indeed measuring the instantaneous temperature increase related to individual pulses, and not the time averaged heating, which is further from the experimentally determined value. This has also been confirmed by simulating the stationary heat equation with the time averaged power density, where the maximum temperature increase has been estimated to be around 1 K.

From this result it is evident that synchrotron filling mode is very important from the point of view of radiation damage of material and it can also influence XRD measurements.
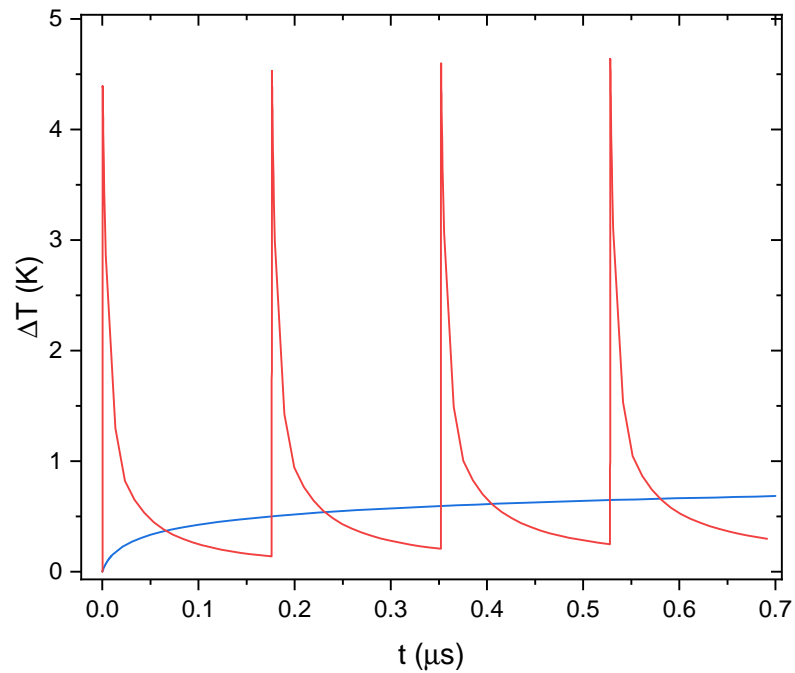
Figure 3.18: Average temperature variation as a function of time over a cylindrical volume with radius $r = FWHM_{beam}/2$ and height $\lambda/10$ calculated from FEM simulations.
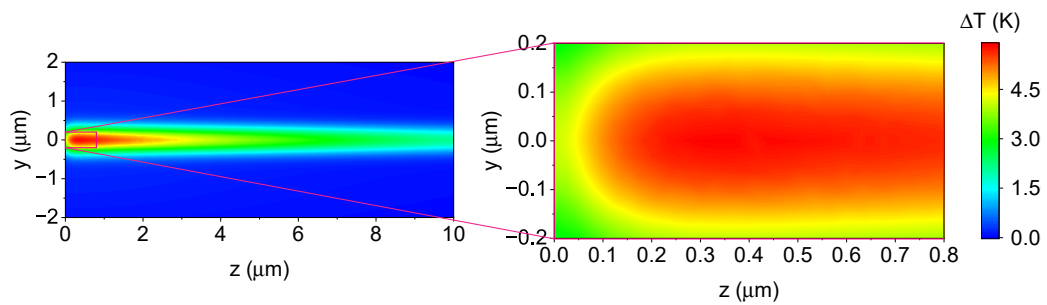
Figure 3.19: yz temperature map at the instant corresponding to the maximum temperature. Right panel shows the region from which the average temperature has been extracted.

Effect of temperature on reversibility

Room temperature measurements in the previous section show the effect of heating, which is completely reversible. When inserting back Al filters to attenuate the beam after measurement without any filter, the peak shape and position is the same as for pristine sample, as already shown in figure 3.16a.
This is not the case during low temperature measurements, which have been performed placing the sample in a He flow cryostat at a fixed temperature around 8 K.

As shown in the maximum projections in figure 3.17, after irradiation with no attenuation the peak remains symmetric and in the same position at room temperature, while at low temperature the peak becomes asymmetric (figure 3.20).
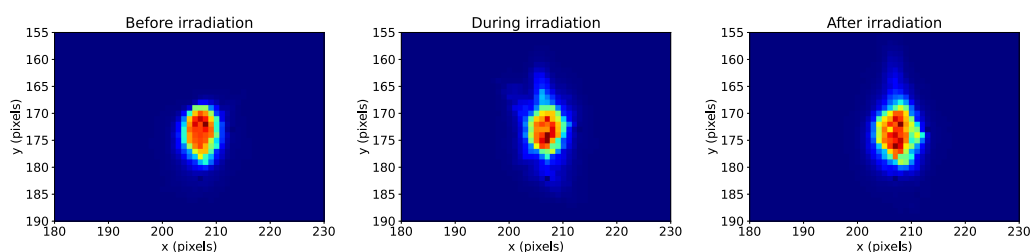
Figure 3.20: Maximum projections before, during and after irradiation (obtained with 6, 0 and 6 filters respectively) at low temperature.

This can be better visualized by projecting the intensity on the vertical axis of the detector (figure 3.21). Whereas the pre- and post-irradiation curves coincide at room temperature, post-irradiation measurements at low temperature show an asymmetric peak, with a tail corresponding to a portion of the sample diffracting at lower 2θ angles, and correspondingly with bigger cell parameters. This evidence demonstrates that at low temperature two effects are induced by high flux irradiation: a reversible heating effect and an irreversible material damage. For this reason the temperature increase induced in the sample at low temperature is not easy to determine, since the two effects cannot be disentangled.
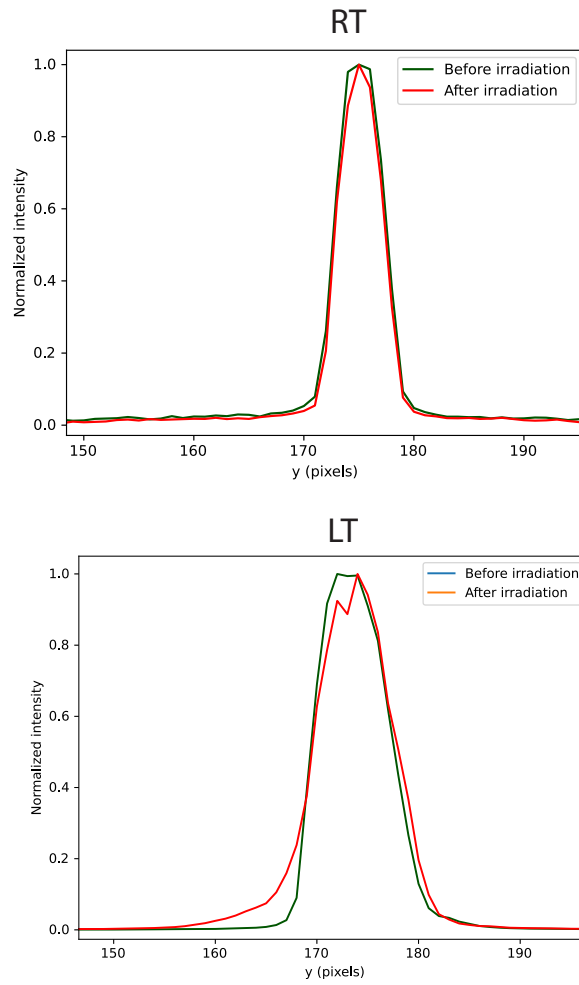
Figure 3.21: Projections of the maximum projections on the vertical detector axis.

CHAPTER 4

HibriXLab

This chapter is focused on the description of the HibriXLab (HIgh-BRIliance X-ray LABoratory) at University of Torino, together with some experimental procedures developed for beam characterization and preliminary results obtained so far.
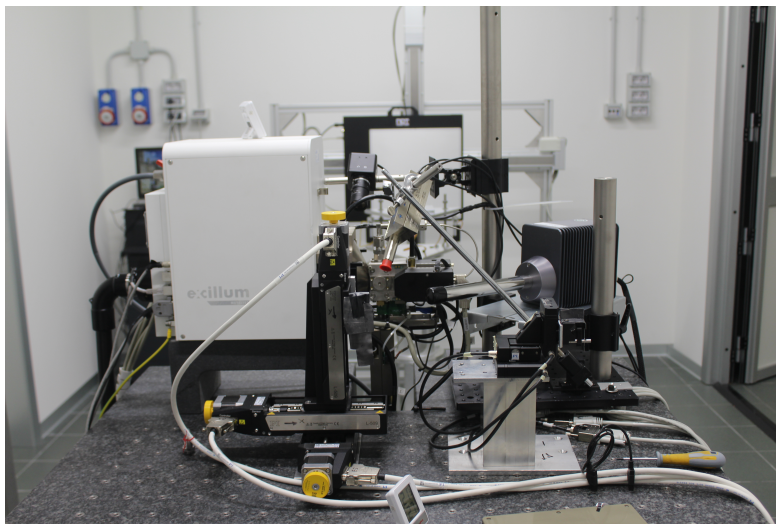
Figure 4.1: Microbeam setup at HibriXLab.

4.1 Microbeam setup

MetalJet source

The experimental setup is based on a MetalJet D2+ 160 kV source by Excillum[1].

This source uses a jet of low melting point In-Ga-Sn alloy (EXALLOY-I1) with a 170-180 µm diameter as anode material. The minimum focal spot size achievable is around 5 µm, with electron acceleration voltage that can vary in the 40-160 kV range, and a maximum power of the electron beam of 250 W. The maximum nominal peak brightness achievable is 1.7×10^{10} photons/(s mm^2 mrad^2) for the Ga K$_\alpha$ peak (9.2 keV).
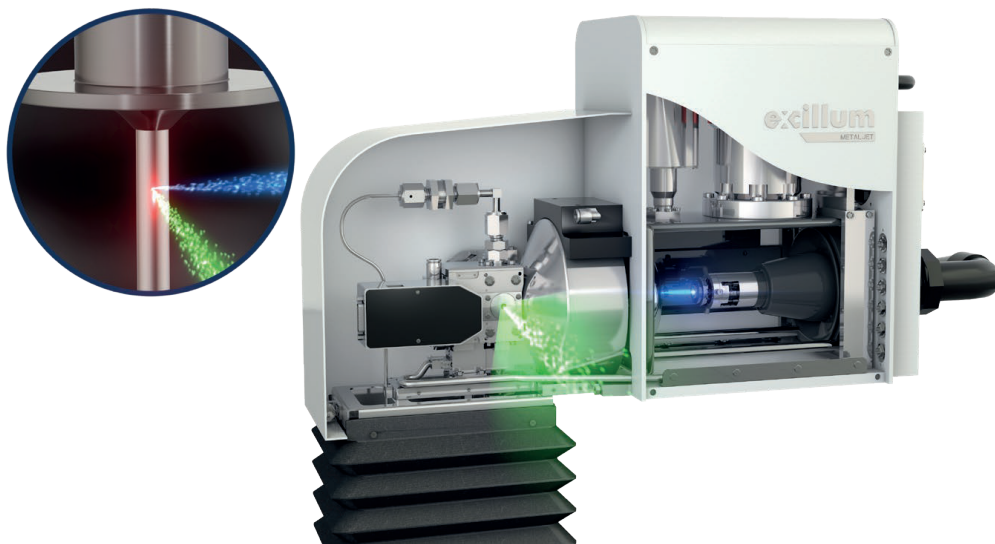
Figure 4.2: Schematics of Excillum MetalJet source. The blue dots represent the electron beam, and the green dots the emitted X-ray photons.

Two beryllium windows allow X-rays to be emitted from both sides of the machine. Two different aperture angle windows are mounted: a 30° window is used on one side for imaging, while a 13° window is used on the other side, where the X-ray

---

[1]https://www.excillum.com/

beam is focused into a microbeam.

The spectrum of X-rays emitted by the Metal Jet source is shown in figure 4.3. It shows the emission lines of the metals in the anode alloy (In, Ga, Sn), on top of a Bremsstrahlung background. Pile up peaks corresponding to two photons reaching the detector at the same time and being registered as a single event are also present.
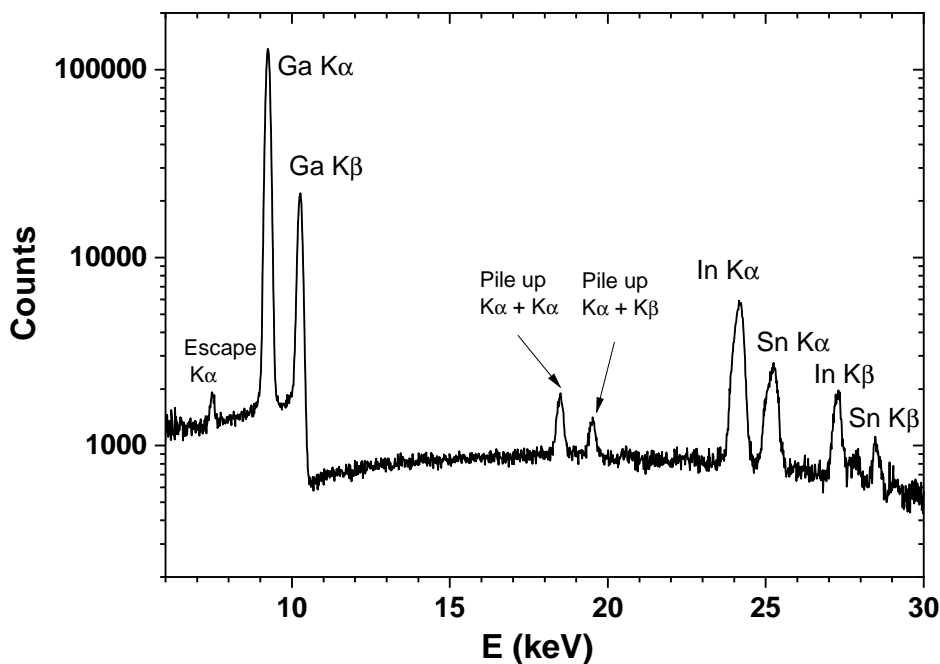
Figure 4.3: Spectrum of the MetalJet source.

Optics

To focus the X-rays emitted by the source, optics are positioned in front of the microbeam side window. In particular, two different optics have been tested and characterized, namely a polycapillary optics and a twin paraboloidal mirrors optics. The polycapillary optics has been produced by Frascati laboratories of the Italian Institute for Nuclear Physics (INFN), while the twin paraboloidal mirrors lens has

117

been purchased from Sigray. The two optics are shown in figure 4.4.

a)   b)
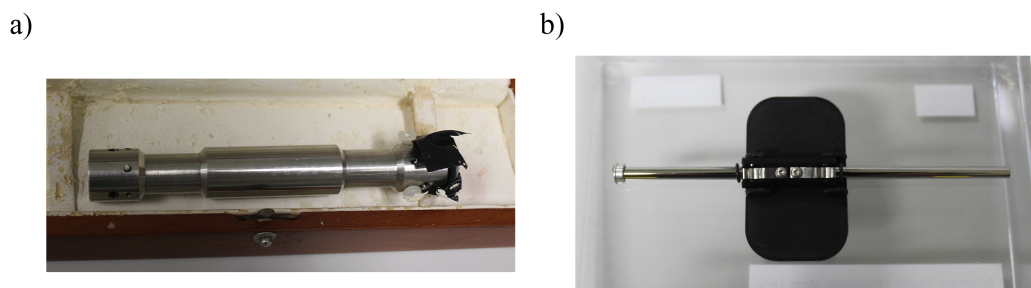
Figure 4.4: a) Polycapillary optics and b) twin paraboloidal mirrors optics.

The lens is mounted on three PI M110 motors, allowing movement of the optics along the x, y and z directions (figure 4.5). This allows for fine movements with a maximum range of 15 mm, needed to precisely align the optics with the beam axis and place it at the correct distance from the metal jet, providing optimal focus on the source side.
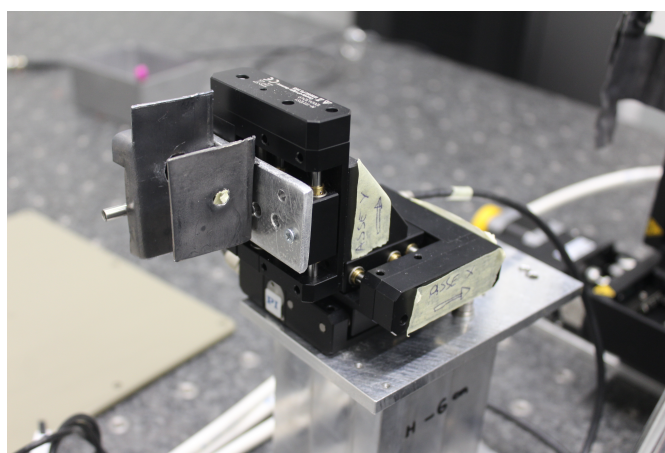
Figure 4.5: Optics motors (PI M110).

Sample holder and movement

The sample can be mounted on a set of three PI L-509 motors which provide a range of movement of 10.5 cm with micrometric precision in the three directions.

118

The software for the control of PI motors also allows to perform automatic scans in one or two directions, acquiring the value of an analog input as a function of motor position. This feature is useful for the acquisition of XRF maps (section 4.4).
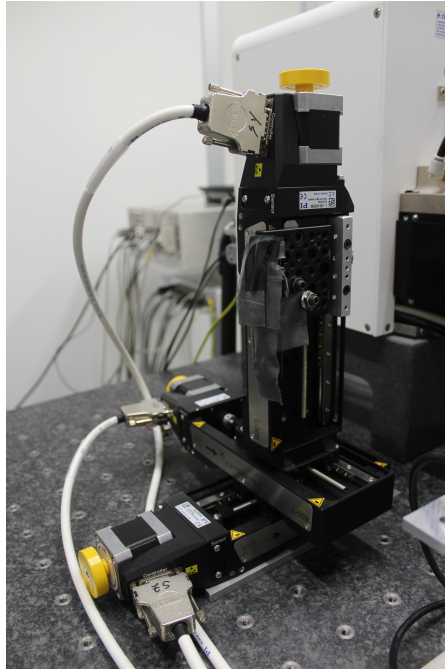
Figure 4.6: PI L-509 motors for sample movement.

Detectors

The experimental setup is currently equipped with two XRF detectors:

- XR-123 Fast SDD by Amptek;

- Vortex-EM model EM-5524-2mm by Hitachi.

A Rad-icon flat panel by Teledyne Dalsa with a $11 \times 15 \, cm^2$ area and $50 \, \mu m$ resolution is also used to collect images from the lenses during the alignment procedure. For the determination of photon flux (see section 4.3), a partially depleted pips detector (PD 300-14-500 AM by Canberra) is used. This Si photodiode has an active area of $300 \, mm^2$ and $500 \, \mu m$ thickness and is interfaced with a Keythley electrometer which provides the $120 \, V$ bias needed and the current reading.

119

a)   b)
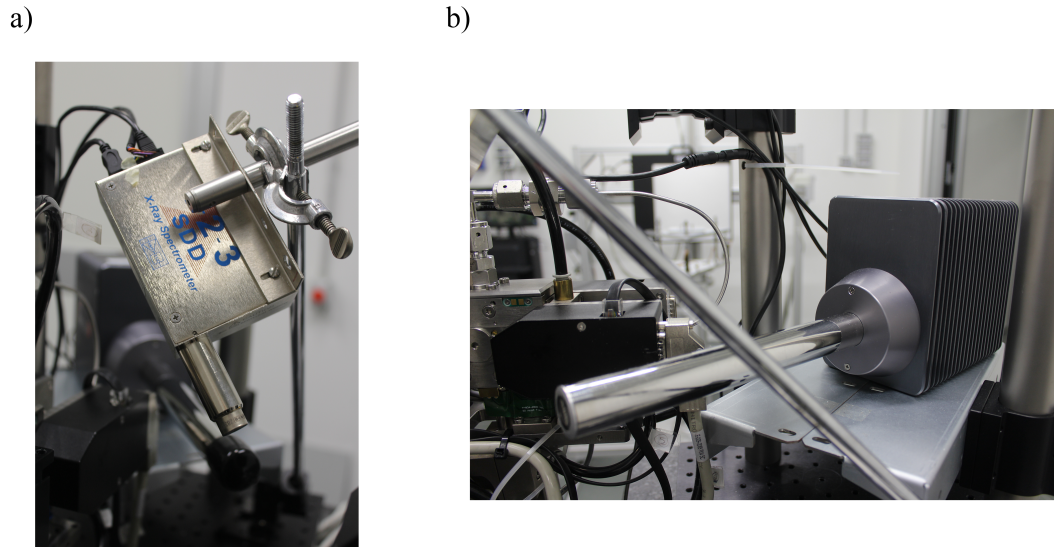
Figure 4.7: a) Amptek XR-123 Fast SDD and b) Hitachi Vortex-EM model EM-5524-2mm.

4.2   Optics alignment

4.2.1   Input focal distance

The alignment procedure for the polycapillary lens and for the twin parabolidal mirrors are very similar. In the following we will refer from time to time to the data from either of them, according to the most convenient option.

In order to properly align the optics, the lens has been mounted on the optics motors, and radiographies have been collected while moving the optics in the plane perpendicular to the X-ray beam (xy plane). This procedure has been repeated until a symmetric and uniform focal spot is visible on the flat panel (see figure 4.8). Once the optics has been aligned in plane, the photodiode is used to find the distance from the source (i.e.the z position) showing the highest photocurrent value. The lens is then re-aligned in the xy plane to find the optimal alignment in the new z position. This procedure is repeated iteratively.

In this way the lens is positioned at the optimal input focal distance (IFD).
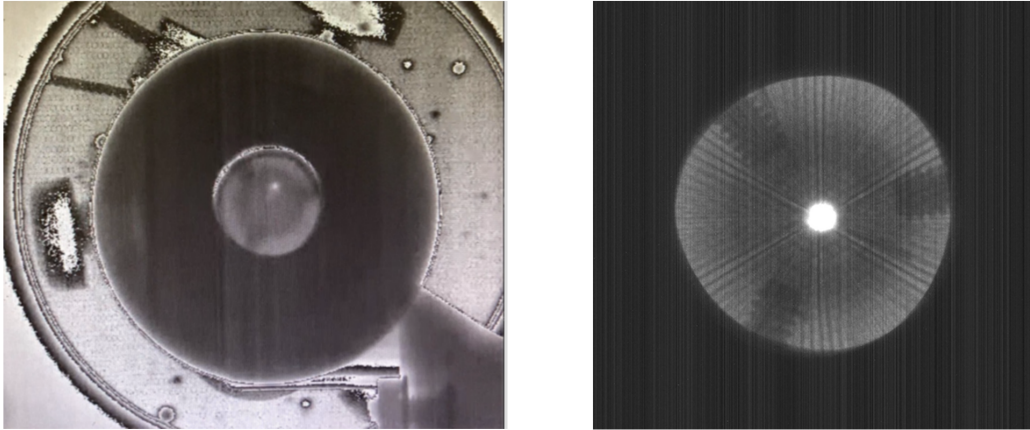
Figure 4.8: Radiographies of the polycapillary lens collected during alignment. A bad (left) and a good (right) alignment is shown.

4.2.2 Output focal distance

To determine the output focal distance (OFD), the knife edge method has been used. It consists in measuring the XRF intensity while scanning across a sharp metal edge. The fluorescence intensity as a function of the scanning direction shows a sigmoidal trend. The beam profile can be obtained by the derivative of the fluorescence profile, which can be fitted with a Gaussian profile, and consequently the full width at half maximum (FWHM) of the beam can be determined (see figure 4.9). By repeating the scan at different distances, the OFD can be determined as the minimum of the FWHM as a function of distance.

The knife edge used for the determination of the OFD is a TiO_2 substrate with a thin layer of gold deposited on its top surface in a square pattern. The Ti fluorescence has been measured, and the fluorescence intensity decreases while crossing the Au pad edges. The derivative of the fluorescence profile at each distance has been fitted with a Gaussian profile. Figure 4.9 shows the bidimensional map obtained by measuring the Ti fluorescence intensity while scanning across the gold pad edge at different z values. This figure has been acquired by focusing with twin paraboloidal mirrors, with a power of 250 W at 70 kV and an electron beam focal spot of $20{\times}80\,\mu m^2$, which should correspond to an apparent size of the X-ray

source of $20 \times 20 \, \mu m^2$ (the X-ray emission takes place at an angle of approximately $90°$ with respect to the direction of the electron beam).

The beam size is taken as the minimum value measured, in this case around $20 \, \mu m$, comparable to the dimension of the apparent size of the X-ray emission spot.
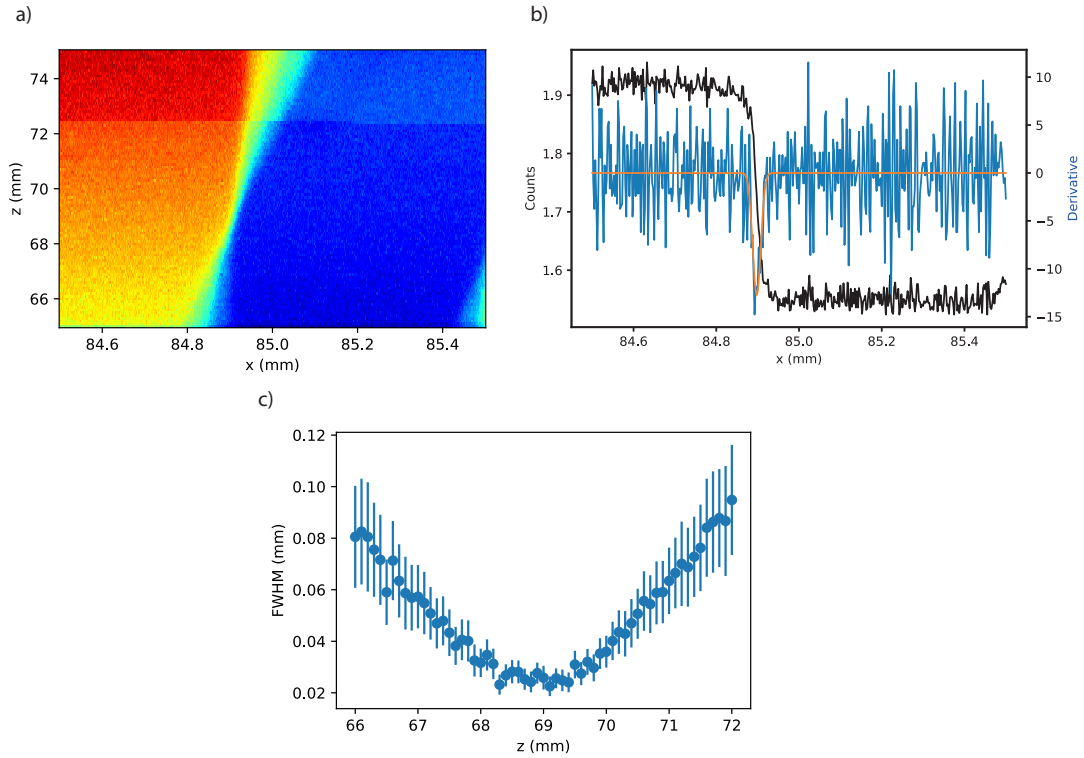
Figure 4.9: a) Ti K$_\alpha$ XRF map showing different knife edge profiles at different distance z from the lens. b) Example fit at $z = 68.3$ showing the extracted profile (black curve), its derivative (blue curve) and the Gaussian fit (orange curve). c) FWHM of the beam as a function of z.

4.3 Flux determination

As a first step for the determination of the photon flux at the focus, the spectrum at the focal point has been measured with the Amptek spectrometer and corrected for the detector efficiency. Then, the photocurrent produced by the incoming X-ray beam in the photodiode has been measured; to convert the measured photocurrent

into the corresponding photon flux value, the following procedure has been followed [77].

Considering that a photon with energy E generates in the photodiode a charge

$$Q(E) = \frac{eE(1 - e^{-A\rho t})}{\varepsilon} \tag{4.1}$$

(where A is the photoelectronic cross section for Si, ρ is the Si density, t is the detector thickness and $\varepsilon = 3.66 \pm 0.03$ eV is the average energy needed for the creation of an electron-hole pair in Si), the current generated by a monochromatic beam is:

$$I = Q\phi = \frac{eE(1 - e^{-A\rho t})}{\varepsilon}\phi \tag{4.2}$$

The photon flux is therefore proportional to the measured photocurrent ($\phi = CI$). The current generated by a photon beam with energy between E and $E + dE$ is:

$$I(E)dE = Q(E)\phi(E)dE = \frac{eE(1 - e^{-A\rho t})}{\varepsilon}\phi(E)dE \tag{4.3}$$

where $\phi(E)$ is the photon flux density as a function of energy (i.e. its measurement unit is photons $\cdot$ s^{-1}eV^{-1}).

The total current is therefore:

$$I = \int_0^{+\infty} I(E)dE = \int_0^{+\infty} \frac{eE(1 - e^{-A\rho t})}{\varepsilon}\phi(E)dE \tag{4.4}$$

Since

$$\phi = \int_0^{+\infty} \phi(E)dE \tag{4.5}$$

the proportionality constant between flux and current is:

$$C = \frac{\phi}{I} = \frac{\int_0^{+\infty} \phi(E)dE}{\int_0^{+\infty} \frac{eE(1 - e^{-A\rho t})}{\varepsilon}\phi(E)dE} \tag{4.6}$$

Supposing that $\phi(E)$ is proportional to the measured spectrum $S(E)$ and limiting the energy integration only to the energy range where the measured (and corrected for air absorption) spectrum is reliable, i.e. between 6 keV and 30 keV, we obtain:

$$C = \frac{\phi}{I} = \frac{\int_6^{30} S(E)dE}{\int_6^{30} \frac{eE(1-e^{-A\rho t})}{\varepsilon} S(E)dE} = 2.563 \times 10^{15} \ \mathrm{phA^{-1}s^{-1}} \qquad (4.7)$$

The photon flux as a function of the source power can now be measured and is shown in figure 4.10. The maximum flux achievable, corresponding to a power of $250\,\mathrm{W}$, is $1.27 \times 10^8 \ \mathrm{ph/s}$.
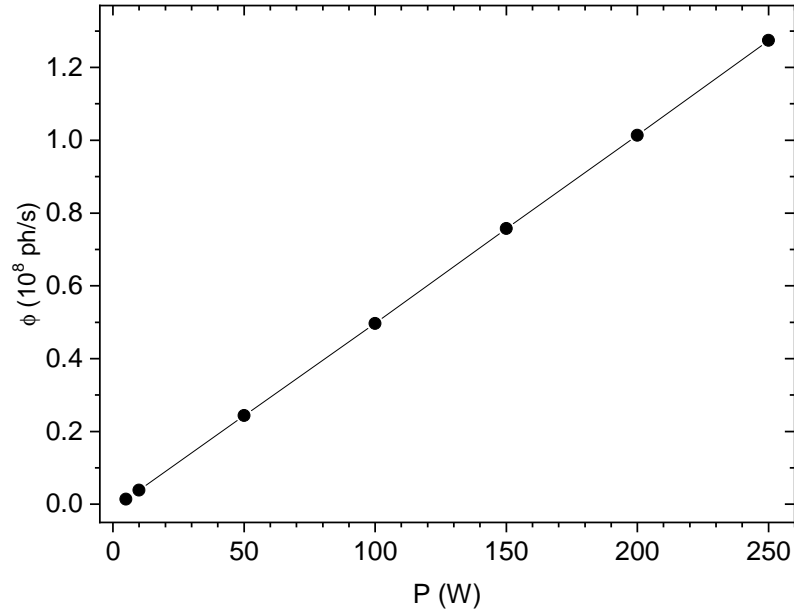
Figure 4.10: Photon flux as a function of source power.

A summary of measured beam sizes and photon flux densities in different working conditions is reported in table 4.1.

4.4 XRF mapping

Once the optics are correctly aligned and the OFD is determined, XRF mapping can be performed. To do so, the capability of the PI sample motors to perform an automatic 2D scan while taking as an input an analog signal is exploited. A custom interface based on an Arduino Due board has been designed and implemented in

Table 4.1: Summary of measured beam sizes and fluxes in different working conditions.

	Voltage (kV)	e⁻ beam size (µm²)	X-ray beam size (µm²)	Photon flux density (photons · s⁻¹µm²)
Polycapillary lens	70	20×20	70×70	3×10^4
Paraboloidal mirror	70	20×20	30×30	9×10^4
	150	20×20	30×30	1×10^5
		10×10	10×10	1×10^6

order to convert the counts measured by the Amptek spectrometer in a given energy range into a suitable analog input for the PI motors.

An example of a Cu XRF map collected on a Shapal board is shown in figure 4.11. The Cu pads and traces are clearly visible.
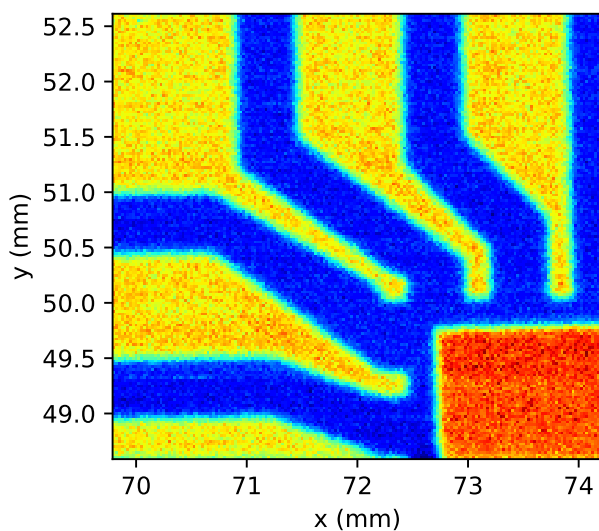
Figure 4.11: Example XRF map for the Cu K$_\alpha$ signal coming from a circuit printed onto a Shapal square substrate (approximately one quarter only of the sample is shown).

4.5 Preliminary irradiation test on BSCCO

To test the possibility of modifying the electrical properties of materials by irradiation at laboratory scale, some preliminary tests have been performed on superconducting BSCCO samples.

Samples have been fabricated by gluing a BSCCO whisker on a glass substrate, and subsequently depositing Ag contacts by thermal evaporation through a metallic mask. An SEM picture of the sample is shown in figure 4.12.
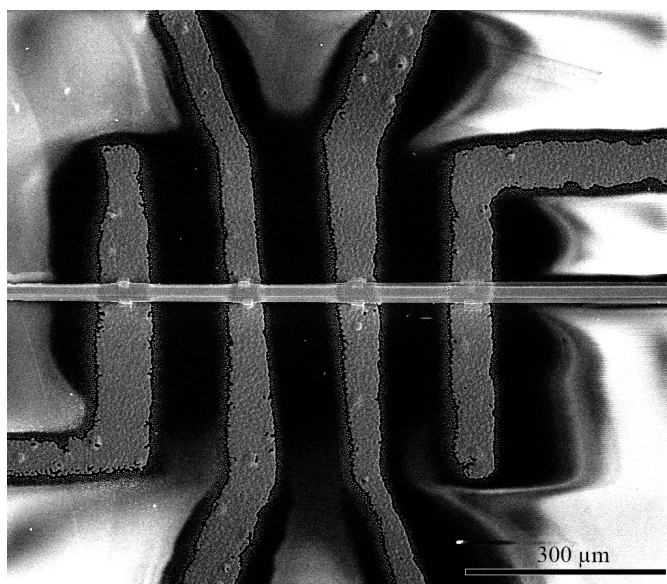
Figure 4.12: SEM of the BSCCO sample under investigation. The BSCCO crystal lays along the horizontal direction, whereas the vertical stripes correspond to Ag electrical contacts

The sample has been localized by collecting a Cu K_α XRF map over a large area (figure 4.13a). In this map the Cu signal from the BSCCO whisker can be seen, with lower fluorescence intensity in correspondence of the electrodes due to absorption by the Ag layer.

The sample has then been irradiated by collecting an XRF map with very long exposure time lasting several hours (figure 4.13b). This map has been collected with a step of 10 µm in both direction, with a source power of 50 W, an electron spot size of 20 µm and 420 s/point exposure time. The X-ray beam has been focused by means of the twin paraboloidal mirrors optics, with the sample placed

in the focal point.
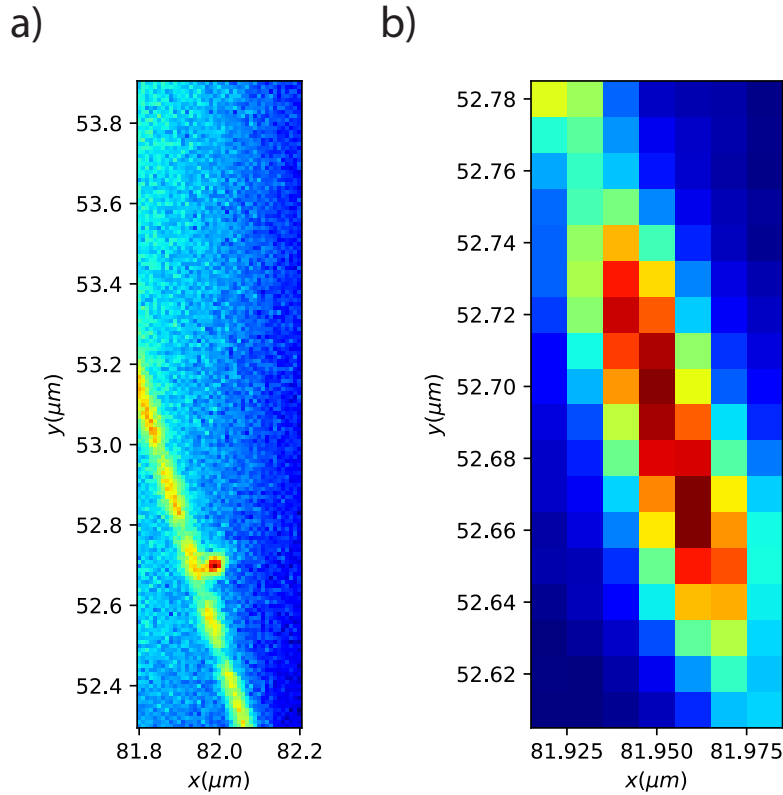
Figure 4.13: a) Localization Cu K_α XRF map. The BSCCO whisker and the decrease in intensity corresponding to the Ag electrodes are clearly visible. b) Irradiation map on a section of the whisker.

Electrical characterization of the sample is reported in figure 4.14. Resistance vs. temperature measurements have been performed in four probe configuration for the pristine sample, on the same sample after 4 months aging and immediately after irradiation.

The pristine curve shows a critical temperature around $100\,\mathrm{K}$, which is compatible with the phase Bi-2223. After aging, the critical temperature drops to about $93\,\mathrm{K}$, testifying the well known aging of this material as a consequence of exposure to air and subsequent reaction with moisture and atmospheric oxygen [78, 79]. A secondary small transition around $70\,\mathrm{K}$ is also visible, and is related to the presence of heavily oxygen depleted material. Moreover the normal state resistance of the

sample increases for the same reason.

After irradiation, the main superconducting transition temperature drops further
more to around 90 K, and the normal state resistance increases even more. The
height of the lower transition also increases, probably because the amount of oxy-
gen depleted material has increased. Since the last measurement has been per-
formed immediately after irradiation, aging effects between irradiation and elec-
trical characterization are supposed to be negligible, and the detected changes are
purely due to irradiation.

From this preliminary test, irradiation of superconducting oxides with the Metal-
Jet source seems to induce changes in the electrical properties comparable with
several months of exposure to the environment. Further tests are needed to fully
understand the capabilities of this system for tailored material modifications, but
these results are encouraging.
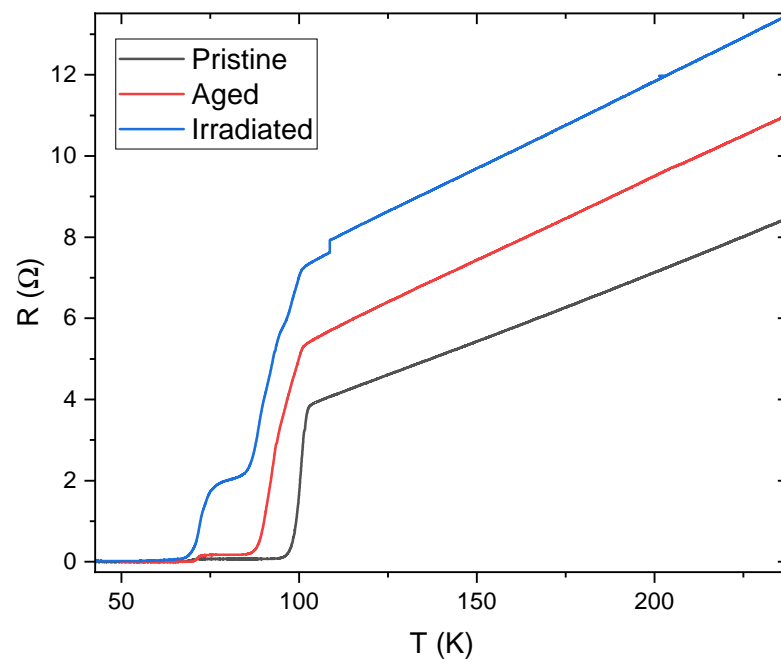
Figure 4.14: Resistance as a function of temperature measured for pristine, aged
and irradiated sample.

4.6 Preliminary XRD measurements

By using a BSCCO whisker and the flat panel detector, some tests have been performed to detect diffraction spots. The BSCCO whisker has been glued to a glass substrate to avoid peaks coming from the substrate, and placed at grazing incidence angle with the focused beam. Lead shields have been placed in front of the flat panel to screen it from the direct beam.

Figure 4.15 shows a comparison of the images collected on the whisker and outside the whisker. The red circle highlights the spot which is visible only with the beam located on the whisker, which is ascribed to a (00l) diffraction spot, due to the sample orientation..

Since the flat panel is not meant for diffraction measurements, a good XRD signal is difficult to detect. Nevertheless these results suggest that it is possible to implement a diffraction setup, by installing rotation stages and suitable detectors, and monochromatizing the radiation by placing a zinc foil (K-edge at $9.66\,\mathrm{keV}$) to filter out the Ga K_β line and higher energy X-rays.
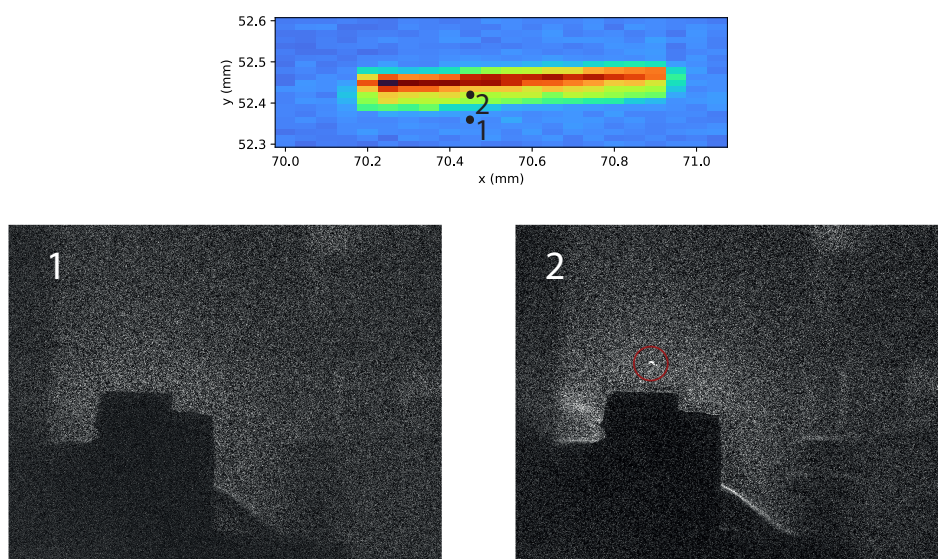
Figure 4.15: Cu K_α XRF map of BSCCO whisker and corresponding flat panel images collected on points 1 and 2. The red circle highlights the diffraction spot.

4.7 Future development of the setup

The microbeam setup at HibriXLab (HIgh-BRIlliance X-ray LABoratory) is currently still under development in the framework of the INFN experiment RE-SOLVE, funded by the National Commision of Group 5.

In particular, the implementation of the Vortex spectrometer is still to be completed, and acquisition of hyperspectral XRF maps is not yet possible. Indeed, only the integrated counts over a given channel range can be obtained, meaning that only single element maps are possible right now, and multi-elemental XRF maps cannot be measured.

Moreover, an optical microscope setup is being produced, which would allow an easier localization of the samples under investigation.The microscope will be equipped with a 45° mirror with a hole in the middle to allow X-rays to reach the sample. Once the microscope setup will be in place, it will be possible to make its focal plane coincide with the X-ray optics focal spot, allowing an easy and fast positioning of the sample, which right now only relies on XRF signals.

Motors for sample rotation and suitable XRD detectors will also be implemented. The future plan for the experimental setup is shown in figure 4.16.
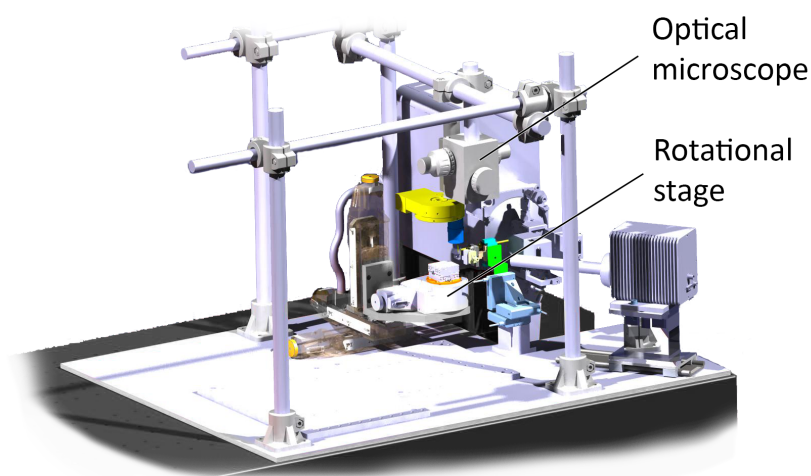
Figure 4.16: Schematics of the future development of the microbeam experimental setup.

Conclusions

Materials modifications induced by synchrotron X-rays irradiation on functional oxides have been investigated.

Irradiation of memristive-like devices fabricated from rutile single crystals has led to a localized increase in the material conductivity, which has also been detected by C-AFM following irradiation with no prior bias applied, testifying that irradiation alone can introduce localized oxygen vacancies. The formation of a conducting path allows to localize the electroforming electrical discharge in the desired position of the device. Such devices can display reversible bipolar resistance switch upon biasing with suitable voltages and current compliance. The changes induced by the discharge process itself have been analyzed by XEOL, XANES and Raman mapping, allowing to identify the presence of anatase nanocrystals alongside the defective rutile matrix. This also implies that very high temperatures, in excess of the rutile melting temperature (i.e. about $1800\,°C$), are locally induced by the Joule effect during the electroforming discharge.

The possible thermal origin of material X-ray damage, related to the pulsed time structure of synchrotron radiationthat induces high repetition rate thermal expansion and contraction cycles, has been investigated by means of FEM simulations, which show extreme temperature gradients in the material, especially at low tem-

perature. This supposed enhancement of material damage at low temperature has been experimentally investigated by irradiating $SrTiO_3$ single crystals at room temperature and at cryogenic temperature and by comparing the morphological and optical changes by means of AFM and photoluminescence. The results are still preliminary, but they seem to indicate that material damage is more localized at low temperature, while room temperature irradiation could also induce defects migration and damage accumulation when raster scanning the sample. A direct measurement of the temperature increase induced by high flux density X-ray beam over the timescale of about $50\,ps$ has been performed on a BaF_2 single crystal, monitoring the shape and position of a single diffraction peak at various incoming photon fluxes. The results are in good agreement with FEM simulations and probably represent one of the highest time resolutions ever achieved in determining the temperature increase of a bulk material.

The current state and capabilities of the HibriXLab at University of Torino have also been discussed, together with the foreseen future development of the facility. Preliminary results from irradiation of superconducting BSCCO microcrystals reveal the possibility of inducing material modifications on a laboratory scale too.

Acknowledgments

At the end of this journey I have many people to thank, without whom this work would not have been possible.

First of all thanks to all the professors, researchers and fellow PhD students in the Solid State Physics group, who have always been willing to help and give guidance and support.

Thanks to all the people I have had the pleasure to work with, in particular to Federico Picollo, Lorenzo Mino, Angelo Agostino, Santanu Kumar Padhi and Sachin Singh. Thanks to Valentina Bonino, Gema Martinez-Criado and Tobias Schulli from ESRF for their help during synchrotron experiments, which really taught me a lot.

Thanks to our collaborators at Forschungszentrum Jülich, in particular to Regina Dittmann, Kalle Goß and Thomas Heisig, and to Jorge Serrano and Vanessa Hinojosa from University of Valladolid.

A special thank to Carmelo Prestipino for his help and kind hospitality during my research period in Caen.

And my deepest gratitude goes to Marco Truccato, for guiding me in my research activity, for his motivation and for everything I learned from him during these years.

Bibliography

[1] J. M. Holton, "A beginner's guide to radiation damage," *Journal of Synchrotron Radiation*, vol. 16, pp. 133–142, Mar. 2009.

[2] C. Nave and E. F. Garman, "Towards an understanding of radiation damage in cryocooled macromolecular crystals," *Journal of Synchrotron Radiation*, vol. 12, pp. 257–260, May 2005.

[3] A. Cheng and M. Caffrey, "Free radical mediated x-ray damage of model membranes," *Biophysical Journal*, vol. 70, pp. 2212–2222, May 1996.

[4] H. B. Stanley, D. Banerjee, L. Van Breemen, J. Ciston, C. H. Liebscher, V. Martis, D. H. Merino, A. Longo, P. Pattison, G. W. M. Peters, G. Portale, S. Sen, and W. Bras, "X-ray irradiation induced reduction and nanoclustering of lead in borosilicate glass," *CrystEngComm*, vol. 16, no. 39, pp. 9331–9339, 2014.

[5] P. Gonçalves Ferreira, D. De Ligny, O. Lazzari, A. Jean, O. Cintora Gonzalez, and D. Neuville, "Photoreduction of iron by a synchrotron X-ray beam in low iron content soda-lime silicate glasses," *Chemical Geology*, vol. 346, pp. 106–112, May 2013.

[6] D. Tatchev, A. Hoell, M. Eichelbaum, and K. Rademann, "X-Ray-Assisted Formation of Gold Nanoparticles in Soda Lime Silicate Glass: Suppressed Ostwald Ripening," *Physical Review Letters*, vol. 106, p. 085702, Feb. 2011.

[7] V. Duffort, V. Caignaert, V. Pralong, B. Raveau, M. Suchomel, and J. Mitchell, "Photo-induced low temperature structural transition in the "114" YBaFe4O7 oxide," *Solid State Communications*, vol. 182, pp. 22–25, Mar. 2014.

[8] V. Kiryukhin, D. Casa, J. P. Hill, B. Keimer, A. Vigliante, Y. Tomioka, and Y. Tokura, "An X-ray-induced insulator–metal transition in a magnetoresistive manganite," *Nature*, vol. 386, pp. 813–815, Apr. 1997.

[9] F. Tu, A. Späth, M. Drost, F. Vollnhals, S. Krick Calderon, R. H. Fink, and H. Marbach, "Exploring the fabrication of Co and Mn nanostructures with focused soft x-ray beam induced deposition," *Journal of Vacuum Science & Technology B, Nanotechnology and Microelectronics: Materials, Processing, Measurement, and Phenomena*, vol. 35, p. 031601, May 2017.

[10] P.-C. Hsu, Y.-S. Chen, Y. Hwu, J. H. Je, G. Margaritondo, and E. S. Tok, "X-ray-induced Cu deposition and patterning on insulators at room temperature," *Journal of Synchrotron Radiation*, vol. 22, pp. 1524–1527, Nov. 2015.

[11] M. Truccato, A. Agostino, E. Borfecchia, L. Mino, E. Cara, A. Pagliero, N. Adhlakha, L. Pascale, L. Operti, E. Enrico, N. De Leo, M. Fretto, G. Martinez-Criado, and C. Lamberti, "Direct-Write X-ray Nanopatterning: A Proof of Concept Josephson Device on Bi $_2$ Sr $_2$ CaCu $_2$ O $_{8+\delta}$ Superconducting Oxide," *Nano Letters*, vol. 16, pp. 1669–1674, Mar. 2016.

[12] L. Mino, V. Bonino, F. Picollo, M. Fretto, A. Agostino, and M. Truccato, "Tailoring the Local Conductivity of TiO_2 by X-Ray Nanobeam Irradiation," *Advanced Electronic Materials*, vol. 5, p. 1900129, June 2019.

[13] P. R. Willmott, *An Introduction to Synchrotron Radiation: Techniques and Applications.* Hoboken: John Wiley & sons, 2nd ed ed., 2019.

[14] J. Baruchel, J. L. Hodeau, M. S. Lehmann, J.-R. Regnard, and C. Schlenker, *Neutron and Synchrotron Radiation for Condensed Matter Studies.* Berlin Heidelberg New-York [etc.] Les Ulis: les Éd. de Physique, 1994.

[15] G. Margaritondo and P. Rebernik Ribic, "A simplified description of X-ray free-electron lasers," *Journal of Synchrotron Radiation*, vol. 18, pp. 101–108, Mar. 2011.

[16] R. Bonifacio, C. Pellegrini, and L. Narducci, "Collective instabilities and high-gain regime in a free electron laser," *Optics Communications*, vol. 50, pp. 373–378, July 1984.

[17] P. Emma, R. Akre, J. Arthur, R. Bionta, C. Bostedt, J. Bozek, A. Brachmann, P. Bucksbaum, R. Coffee, F.-J. Decker, Y. Ding, D. Dowell, S. Edstrom, A. Fisher, J. Frisch, S. Gilevich, J. Hastings, G. Hays, Ph. Hering, Z. Huang, R. Iverson, H. Loos, M. Messerschmidt, A. Miahnahri, S. Moeller, H.-D. Nuhn, G. Pile, D. Ratner, J. Rzepiela, D. Schultz, T. Smith, P. Stefan, H. Tompkins, J. Turner, J. Welch, W. White, J. Wu, G. Yocky, and J. Galayda, "First lasing and operation of an ångstrom-wavelength free-electron laser," *Nature Photonics*, vol. 4, pp. 641–647, Sept. 2010.

[18] O. Hemberg, M. Otendal, and H. M. Hertz, "Liquid-metal-jet anode electron-impact x-ray source," *Applied Physics Letters*, vol. 83, pp. 1483–1485, Aug. 2003.

[19] T. Salditt, A. Egner, and D. R. Luke, eds., *Nanoscale Photonic Imaging*, vol. 134 of *Topics in Applied Physics.* Cham: Springer International Publishing, 2020.

[20] C. A. MacDonald, "Focusing Polycapillary Optics and Their Applications," *X-Ray Optics and Instrumentation*, vol. 2010, pp. 1–17, Mar. 2010.

[21] T. Sham, R. Sammynaiken, Y. Zhu, P. Zhang, I. Coulthard, and S. Naftel, "X-ray excited optical luminescence (XEOL): A potential tool for OELD studies," *Thin Solid Films*, vol. 363, pp. 318–321, Mar. 2000.

[22] B.-H. Lin, Y.-H. Wu, X.-Y. Li, H.-C. Hsu, Y.-C. Chiu, C.-Y. Lee, B.-Y. Chen, G.-C. Yin, S.-C. Tseng, S.-H. Chang, M.-T. Tang, and W.-F. Hsieh, "Capabilities of time-resolved X-ray excited optical luminescence of the Taiwan Photon Source 23A X-ray nanoprobe beamline," *Journal of Synchrotron Radiation*, vol. 27, pp. 217–221, Jan. 2020.

[23] T.-K. Sham and R. A. Rosenberg, "Time-Resolved Synchrotron Radiation Excited Optical Luminescence: Light-Emission Properties of Silicon-Based Nanostructures," *ChemPhysChem*, vol. 8, pp. 2557–2567, Dec. 2007.

[24] C. T. Plass, V. Bonino, M. Ritzer, L. R. Jäger, V. Rey-Bakaikoa, M. Hafermann, J. Segura-Ruiz, G. Martínez-Criado, and C. Ronning, "Spatially Resolved Dynamics of Cobalt Color Centers in ZnO Nanowires," *Advanced Science*, vol. 10, p. 2205304, Jan. 2023.

[25] F. Hippert, E. Geissler, J. L. Hodeau, E. Leliévre-Berna, and J.-R. Regnard, *Neutron and X-ray Spectroscopy*. Dordrecht: Springer, 2006.

[26] N. Rahimi, R. A. Pax, and E. M. Gray, "Review of functional titanium oxides. I: TiO2 and its modifications," *Progress in Solid State Chemistry*, vol. 44, pp. 86–105, Sept. 2016.

[27] H. Zhang and J. F. Banfield, "Understanding Polymorphic Phase Transformation Behavior during Growth of Nanocrystalline Aggregates: Insights from TiO$_2$," *The Journal of Physical Chemistry B*, vol. 104, pp. 3481–3487, Apr. 2000.

[28] B. L. Phoon, C. W. Lai, J. C. Juan, P.-L. Show, and W.-H. Chen, "A review of synthesis and morphology of SrTiO$_3$ for energy and other applications," *International Journal of Energy Research*, vol. 43, pp. 5151–5174, Aug. 2019.

[29] S. M. Sze and M. K. Lee, *Semiconductor Devices, Physics and Technology*. Hoboken, N.J: Wiley, 3rd ed ed., 2012.

[30] G. A. Hope and A. J. Bard, "Platinum/titanium dioxide (rutile) interface. Formation of ohmic and rectifying junctions," *The Journal of Physical Chemistry*, vol. 87, pp. 1979–1984, May 1983.

[31] L. Chua, "Memristor-The missing circuit element," *IEEE Transactions on Circuit Theory*, vol. 18, no. 5, pp. 507–519, 1971.

[32] L. Chua, "Resistance switching memories are memristors," *Applied Physics A*, vol. 102, pp. 765–783, Mar. 2011.

[33] D. B. Strukov, G. S. Snider, D. R. Stewart, and R. S. Williams, "The missing memristor found," *Nature*, vol. 453, pp. 80–83, May 2008.

[34] R. Dittmann and J. P. Strachan, "Redox-based memristive devices for new computing paradigm," *APL Materials*, vol. 7, p. 110903, Nov. 2019.

[35] W. Bras, D. A. A. Myles, and R. Felici, "When x-rays alter the course of your experiments*," *Journal of Physics: Condensed Matter*, vol. 33, p. 423002, Oct. 2021.

[36] A. Bharti, A. Turchet, and B. Marmiroli, "X-Ray Lithography for Nanofabrication: Is There a Future?," *Frontiers in Nanotechnology*, vol. 4, p. 835701, Feb. 2022.

[37] J. G. Bednorz, "Possible High Tc Superconductivity in the Ba - La- Cu- 0 System,"

[38] K. Inomata, T. Kawae, K. Nakajima, S.-J. Kim, and T. Yamashita, "Junction parameter control of Bi2Sr2CaCu2O8+δ stacked junctions by annealing," *Applied Physics Letters*, vol. 82, pp. 769–771, Feb. 2003.

[39] T. Watanabe, T. Fujii, and A. Matsuda, "Anisotropic Resistivities of Precisely Oxygen Controlled Single-Crystal Bi2Sr2CaCu2O81d: Systematic Study on "Spin Gap" Effect," *PHYSICAL REVIEW LETTERS*, vol. 79, no. 11, 1997.

[40] L. Ozyuzer, A. E. Koshelev, C. Kurter, N. Gopalsami, Q. Li, M. Tachiki, K. Kadowaki, T. Yamamoto, H. Minami, H. Yamaguchi, T. Tachiki, K. E. Gray, W.-K. Kwok, and U. Welp, "Emission of Coherent THz Radiation from Superconductors," *Science (New York, N.Y.)*, vol. 318, pp. 1291–1293, Nov. 2007.

[41] T. M. Benseman, K. E. Gray, A. E. Koshelev, W.-K. Kwok, U. Welp, H. Minami, K. Kadowaki, and T. Yamamoto, "Powerful terahertz emission from Bi $_2$ Sr $_2$ CaCu $_2$ O $_{8+\delta}$ mesa arrays," *Applied Physics Letters*, vol. 103, p. 022602, July 2013.

[42] L. Mino, V. Bonino, A. Agostino, C. Prestipino, E. Borfecchia, C. Lamberti, L. Operti, M. Fretto, N. De Leo, and M. Truccato, "Maskless X-Ray Writing of Electrical Devices on a Superconducting Oxide with Nanometer Resolution and Online Process Monitoring," *Scientific Reports*, vol. 7, p. 9066, Aug. 2017.

[43] L. Mino, E. Borfecchia, A. Agostino, C. Lamberti, and M. Truccato, "Oxygen doping tuning in superconducting oxides by thermal annealing and hard X-ray irradiation," *Journal of Electron Spectroscopy and Related Phenomena*, vol. 220, pp. 69–75, Oct. 2017.

[44] D. Torsello, L. Mino, V. Bonino, A. Agostino, L. Operti, E. Borfecchia, E. Vittone, C. Lamberti, and M. Truccato, "Monte Carlo analysis of the oxygen knock-on effects induced by synchrotron x-Ray radiation in the Bi2Sr2CaCu2O8+δ superconductor," *Physical Review Materials*, vol. 2, p. 014801, Jan. 2018.

[45] V. Bonino, D. Torsello, C. Prestipino, L. Mino, and M. Truccato, "Time and space resolved modelling of the heating induced by synchrotron X-ray nanobeams," *Journal of Synchrotron Radiation*, vol. 27, pp. 1662–1673, Nov. 2020.

[46] V. Bonino, A. Agostino, C. Prestipino, O. Hernandez, M. Fretto, L. Mino, and M. Truccato, "Structural and functional modifications induced by X-ray nanopatterning in Bi-2212 single crystals," *CrystEngComm*, vol. 20, no. 42, pp. 6667–6676, 2018.

[47] M. W. Rabbani, V. Bonino, L. Spessa, A. Agostino, N. De Leo, C. Prestipino, and M. Truccato, "Mapping of Structural Changes Induced by X-ray Nanopatterning via Nano-X-ray Diffraction and Corresponding Electrical Effects," *Crystal Growth & Design*, vol. 21, pp. 3299–3309, June 2021.

[48] N. Medvedev and I. Milov, "Nonthermal phase transitions in metals," *Scientific Reports*, vol. 10, p. 12775, July 2020.

[49] S. H. Chang, J. Kim, C. Phatak, K. D'Aquila, S. K. Kim, J. Kim, S. J. Song, C. S. Hwang, J. A. Eastman, J. W. Freeland, and S. Hong, "X-ray Irradiation Induced Reversible Resistance Change in Pt/TiO $_2$ /Pt Cells," *ACS Nano*, vol. 8, pp. 1584–1589, Feb. 2014.

[50] A. Alessio, V. Bonino, T. Heisig, F. Picollo, D. Torsello, L. Mino, G. Martinez-Criado, R. Dittmann, and M. Truccato, "Functional Modifications Induced via X-ray Nanopatterning in TiO_2 Rutile Single Crystals," *physica status solidi (RRL) – Rapid Research Letters*, vol. 15, p. 2100409, Oct. 2021.

[51] D.-Y. Cho, M. Luebben, S. Wiefels, K.-S. Lee, and I. Valov, "Interfacial Metal–Oxide Interactions in Resistive Switching Memories," *ACS Applied Materials & Interfaces*, vol. 9, pp. 19287–19295, June 2017.

[52] R. Waser, R. Dittmann, G. Staikov, and K. Szot, "Redox-Based Resistive Switching Memories – Nanoionic Mechanisms, Prospects, and Challenges," *Advanced Materials*, vol. 21, pp. 2632–2663, July 2009.

[53] V. Solé, E. Papillon, M. Cotte, Ph. Walter, and J. Susini, "A multiplatform code for the analysis of energy-dispersive X-ray fluorescence spectra," *Spectrochimica Acta Part B: Atomic Spectroscopy*, vol. 62, pp. 63–68, Jan. 2007.

[54] M. Cotte, E. Pouyet, M. Salomé, C. Rivard, W. De Nolf, H. Castillo-Michel, T. Fabris, L. Monico, K. Janssens, T. Wang, P. Sciau, L. Verger, L. Cormier, O. Dargaud, E. Brun, D. Bugnazet, B. Fayard, B. Hesse, A. E. Pradas Del Real, G. Veronesi, J. Langlois, N. Balcar, Y. Vandenberghe, V. A. Solé, J. Kieffer, R. Barrett, C. Cohen, C. Cornu, R. Baker, E. Gagliardini, E. Papillon, and J. Susini, "The ID21 X-ray and infrared microscopy beamline at the ESRF: Status and recent applications to artistic materials," *Journal of Analytical Atomic Spectrometry*, vol. 32, no. 3, pp. 477–493, 2017.

[55] M. Salomé, M. Cotte, R. Baker, R. Barrett, N. Benseny-Cases, G. Berruyer, H. Castillo-Michel, C. Cornu, B. Fayard, E. Gagliardini, R. Hino, E. Papillon, E. Pouyet, C. Rivard, V. A. Solé, J. Susini, and G. Veronesi, "The ID21 Scanning X-ray Microscope at ESRF," *Journal of Physics*, 2012.

[56] D. K. Pallotti, L. Passoni, P. Maddalena, F. Di Fonzo, and S. Lettieri, "Photoluminescence Mechanisms in Anatase and Rutile TiO$_2$," *The Journal of Physical Chemistry C*, vol. 121, pp. 9011–9021, Apr. 2017.

[57] L. Mino, V. Bonino, A. Alessio, F. Picollo, A. Kuncser, I. Mercioniu, A.-M. Vlaicu, P. Badica, R. Brescia, M. Fretto, K. Goss, R. Dittmann, and M. Truccato, "Improving the control of the electroforming process in oxide-based memristive devices by X-ray nanopatterning," *Journal of Materials Chemistry C*, p. 10.1039.D4TC01815J, 2024.

[58] M. R. Hummon, A. J. Stollenwerk, V. Narayanamurti, P. O. Anikeeva, M. J. Panzer, V. Wood, and V. Bulović, "Measuring charge trap occupation and energy level in CdSe/ZnS quantum dots using a scanning tunneling microscope," *Physical Review B*, vol. 81, p. 115439, Mar. 2010.

[59] J. Bonkerud, C. Zimmermann, F. Herklotz, P. M. Weiser, C. Seiffert, E. F. Verhoeven, L. Vines, and E. V. Monakhov, "Electrically-active defects in reduced and hydrogenated rutile TiO2," *Semiconductor Science and Technology*, vol. 36, p. 014006, Jan. 2021.

[60] Á. Morales-García, O. Lamiel-García, R. Valero, and F. Illas, "Properties of Single Oxygen Vacancies on a Realistic (TiO$_2$)$_{84}$ Nanoparticle: A Challenge for Density Functionals," *The Journal of Physical Chemistry C*, vol. 122, pp. 2413–2421, Feb. 2018.

[61] N. Jiang, D. Su, and J. C. H. Spence, "Determination of Ti coordination from pre-edge peaks in Ti K -Edge XANES," *Physical Review B*, vol. 76, p. 214117, Dec. 2007.

[62] V. Swamy, B. C. Muddle, and Q. Dai, "Size-dependent modifications of the Raman spectrum of rutile TiO2," *Applied Physics Letters*, vol. 89, p. 163118, Oct. 2006.

[63] J. Dhanalakshmi, S. Iyyapushpam, S. T. Nishanthi, M. Malligavathy, and D. Pathinettam Padiyan, "Investigation of oxygen vacancies in Ce coupled TiO$_2$ nanocomposites by Raman and PL spectra," *Advances in Natural Sciences: Nanoscience and Nanotechnology*, vol. 8, p. 015015, Mar. 2017.

[64] C. Perego, R. Revel, O. Durupthy, S. Cassaignon, and J.-P. Jolivet, "Thermal stability of TiO2-anatase: Impact of nanoparticles morphology on kinetic phase transformation," *Solid State Sciences*, vol. 12, pp. 989–995, June 2010.

[65] J. P. Strachan, J. Joshua Yang, R. Münstermann, A. Scholl, G. Medeiros-Ribeiro, D. R. Stewart, and R. Stanley Williams, "Structural and chemical characterization of TiO $_2$ memristive devices by spatially-resolved NEXAFS," *Nanotechnology*, vol. 20, p. 485701, Dec. 2009.

[66] J. P. Strachan, M. D. Pickett, J. J. Yang, S. Aloni, A. L. David Kilcoyne, G. Medeiros-Ribeiro, and R. Stanley Williams, "Direct Identification of the Conducting Channels in a Functioning Memristive Device," *Advanced Materials*, vol. 22, pp. 3573–3577, Aug. 2010.

[67] J. P. Strachan, D. B. Strukov, J. Borghetti, J. Joshua Yang, G. Medeiros-Ribeiro, and R. Stanley Williams, "The switching location of a bipolar memristor: Chemical, thermal and structural mapping," *Nanotechnology*, vol. 22, p. 254015, June 2011.

[68] K. Sedeek, Sh.A. Said, T. Amer, N. Makram, and H. Hantour, "Band gap tuning in nanocrystalline SrTi0.9Fe0.1O2.968 perovskite type for photocatalytic and photovoltaic applications," *Ceramics International*, vol. 45, pp. 1202–1207, Jan. 2019.

[69] "COMSOL Multiphysics v. 5.5." COMSOL AB, Stockholm, Sweden.

[70] B. Henke, E. Gullikson, and J. Davis, "X-ray interactions: Photoabsorption, scattering, transmission, and reflection at E=50-30000 eV, Z=1-92," *Atomic Data and Nuclear Data Tables*, vol. 54, pp. 181–342, July 1993.

[71] K. Van Benthem, C. Elsässer, and R. H. French, "Bulk electronic structure of SrTiO3: Experiment and theory," *Journal of Applied Physics*, vol. 90, pp. 6156–6164, Dec. 2001.

[72] S. Dadgostar, J. L. Pura Ruiz, J. Serrano Gutierrez, B. Lepine, P. Schieffer, and J. Jimenez, "Luminescence in undoped and Nb-doped SrTiO3 crystals: Bulk and surface emission," *Materials Science and Engineering: B*, vol. 283, p. 115830, Sept. 2022.

[73] E. Lawrence Bright, C. Giacobbe, and J. P. Wright, "Beam heating from a fourth-generation synchrotron source," *Journal of Synchrotron Radiation*, vol. 28, pp. 1377–1385, Sept. 2021.

[74] S. J. Leake, G. A. Chahine, H. Djazouli, T. Zhou, C. Richter, J. Hilhorst, L. Petit, M.-I. Richard, C. Morawe, R. Barrett, L. Zhang, R. A. Homs-Regojo, V. Favre-Nicolin, P. Boesecke, and T. U. Schülli, "The Nanodiffraction beamline ID01/ESRF: A microscope for imaging strain and structure," *Journal of Synchrotron Radiation*, vol. 26, pp. 571–584, Mar. 2019.

[75] R. B. Roberts and G. K. White, "Thermal expansion of fluorites at high temperatures," *Journal of Physics C: Solid State Physics*, vol. 19, pp. 7167–7172, Dec. 1986.

[76] G. Lin, S. Diallo, K. Saleh, R. Martinenghi, J.-C. Beugnot, T. Sylvestre, and Y. K. Chembo, "Cascaded Brillouin lasing in monolithic barium fluoride whispering gallery mode resonators," *Applied Physics Letters*, vol. 105, p. 231103, Dec. 2014.

[77] R. L. Owen, J. M. Holton, C. Schulze-Briese, and E. F. Garman, "Determination of X-ray flux using silicon pin diodes," *Journal of Synchrotron Radiation*, vol. 16, pp. 143–151, Mar. 2009.

[78] M. Truccato, S. Cagliero, A. Agostino, M. Panetta, and G. Rinaudo, "Electrical study of an unusual phase transformation in a $Bi_2 Sr_2 Ca_2 Cu_3 O_{10+x}$ whisker at room temperature," *Superconductor Science and Technology*, vol. 19, pp. 1003–1009, Oct. 2006.

[79] S. Cagliero, A. Piovano, C. Lamberti, M. M. Rahman Khan, A. Agostino, G. Agostini, D. Gianolio, L. Mino, J. A. Sans, C. Manfredotti, and M. Truccato, "Synchrotron study of oxygen depletion in a Bi-2212 whisker annealed at 363 K," *Journal of Synchrotron Radiation*, vol. 16, pp. 813–817, Nov. 2009.

Appendices

Courses and Schools

- OPTOFEM 2020, ICMAB-CSIC, 22-23/10/2020

- Raman Day, PhD Doctorate in Earth Sciences, Università di Torino, 28-29/01/2021

- Radiate Spring School, 28-30/04/2021

- Crystallography School 2021, CrisDi – Interdepartmental Centre for Crystallography, Università di Torino, 21/06/2021-09/07/2021

- Introduction to Scientific Programming (in Python), PhD Programme in Chemical and Materials Sciences, Università di Torino

- CHARISMA Raman School 2022, Torino, 18-19/10/2022

- HERCULES European School 2023, Grenoble, France / Hamburg, Germany, 27/02/2023 – 31/03/2023

- Ion Beam Based Techniques for Materials Science, PhD Programme in Chemical and Materials Sciences, Università di Torino

Presentations at congresses

- A. Alessio, V. Bonino, F. Picollo, M. W. Rabbani, L. Mino, T. Heisig, R. Dittmann, G. Martinez-Criado, M. Truccato, Memristive switching in TiO_2 rutile single crystals induced by an X-ray nanobeam, SILS Meeting 2021, 21-23/06/2021, oral presentation

- A. Alessio, V. Bonino, F. Picollo, M. W. Rabbani, L. Mino, T. Heisig, R. Dittmann, G. Martinez-Criado, M. Truccato, X-ray nanopatterning of TiO_2 single crystals and its possible application to memristive devices, 107° Congresso Nazionale Società Italiana di Fisica, 13-17/09/2021, oral presentation

- A. Alessio, V. Bonino, T. Heisig, F. Picollo, D. Torsello, L. Mino, G. Martinez-Criado, R. Dittman, M. Truccato, X-ray nanobeam effects on TiO_2 and $SrTiO_3$ at 17.5 keV, E-MRS Spring 2022, 30/05/2022-03/06/2022, oral presentation

- A. Alessio, K. Goß, V. Bonino, V. Hinojosa, S. K. Padhi, F. Picollo, L. Mino, J. Serrano, G. Martinez-Criado, R. Dittmann, M. Truccato, Local modifications of TiO_2 and $SrTiO_3$ properties intentionally induced by hard X-ray nanobeams, Optics Damage and Materials Processing by EUV/X-ray Radiation (XDam8), 2023, DOI: 10.1117/12.2665689, oral presentation

Publications

- A. Alessio, V. Bonino, T. Heisig, F. Picollo, D. Torsello, L. Mino, G. Martinez-Criado, R. Dittmann, and M. Truccato, "Functional Modifications Induced via X-ray Nanopatterning in TiO_2 Rutile Single Crystals," *physica status solidi (RRL) – Rapid Research Letters*, vol. 15, p. 2100409, Oct. 2021

- S. K. Padhi, X. Liu, M. C. Valsania, L. Andreo, A. Agostino, A. Alessio, L. Pastero, A. Giordana, Z. Wu, G. Cravotto, and M. Truccato, "Structure and physicochemical properties of MgB_2 nanosheets obtained via sonochemical liquid phase exfoliation," *Nano-Structures & Nano-Objects*, vol. 35, p. 101016, July 2023

- A. Alessio, E. Bernardi, E. Moreva, I. P. Degiovanni, M. Genovese, and M. Truccato, "Limitations of Bulk Diamond Sensors for Single-Cell Thermometry," *Sensors*, vol. 24, p. 200, Dec. 2023

- L. Mino, V. Bonino, A. Alessio, F. Picollo, A. Kuncser, I. Mercioniu, A.-M. Vlaicu, P. Badica, R. Brescia, M. Fretto, K. Goss, R. Dittmann, and M. Truccato, "Improving the control of the electroforming process in oxide-based memristive devices by X-ray nanopatterning", *Journal of Materials Chemistry C*, p. 10.1039.D4TC01815J, 2024

- A. Alessio, V. Bonino, F. Picollo, L. Mino, S. K. Padhi, M. Fretto, J. Serrano, V. Hinojosa-Chasiquiza, K. Goß, R. Dittmann, G. Martinez-Criado, and M.

Truccato, "Formation of anatase phase during electroforming of TiO_2 rutile memristor-like devices," *In preparation*

Functional Modifications Induced via X-ray Nanopatterning in TiO₂ Rutile Single Crystals

Andrea Alessio, Valentina Bonino, Thomas Heisig, Federico Picollo, Daniele Torsello, Lorenzo Mino, Gema Martinez-Criado, Regina Dittmann, and Marco Truccato*

The possibility to directly write electrically conducting channels in a desired position in rutile TiO₂ devices equipped with asymmetric electrodes—like in memristive devices—by means of the X-ray nanopatterning (XNP) technique (i.e., intense, localized irradiation exploiting an X-ray nanobeam) is investigated. Device characterization is carried out by means of a multitechnique approach involving X-ray fluorescence (XRF), X-ray excited optical luminescence (XEOL), electrical transport, and atomic force microscopy (AFM) techniques. It is shown that the device conductivity increases and the rectifying effect of the Pt/TiO₂ Schottky barrier decreases after irradiation with doses of the order of 10^{11} Gy and fluences of the order of 10^{12} J m^{-2}. Irradiated regions also show the ability to pin and guide the electroforming process between the electrodes. Indications are that XNP should be able to promote the local formation of oxygen vacancies. This effect could lead to a more deterministic implementation of electroforming, being of interest for production of memristive devices.

1. Introduction

Silicon-based electronics has recorded an exponential decrease for decades about the sizes of its basic components to achieve larger and larger integration scales and keep the pace of the so-called Moore's law. Nowadays, approaching the 7 nm technological node, the unavoidable process fluctuations create new challenges and require more and more sophisticated and expensive engineering solutions.[1] In this scenario, alternative approaches and novel device concepts are clearly desirable both to sustain further increase in the integration scale and to improve device functionality and performances. Oxide electronics has recently emerged as one of such promising approaches, having already been able to provide monolithic full-oxide integrated circuits, for instance.[2] But the advent of this new oxide-based technology has also opened the way to the fabrication of conceptually new devices like memristors,[3] i.e., resistive devices with inherent memory properties that previously existed just as theoretical models. Since then, memristor-based electronics has seen a rapid progress and showed great potential for many applications spanning from neuromorphic computing to on-chip memory and storage.[4–6] These devices are typically based on the reversible change of the electrical properties of transition metal oxides upon the application of an electric field that causes the introduction and migration of oxygen vacancies, which act as mobile donors in these systems. The typical two-terminal device structure of memristors consists of a dielectric layer of a material like TiO₂, SrTiO₃, or HfO₂ placed between two metallic electrodes. Prior to the reversible operation of the devices, a voltage

A. Alessio, F. Picollo, M. Truccato
Department of Physics, Interdepartmental Centre NIS
University of Torino
via P. Giuria 1, I-10125 Torino, Italy
E-mail: marco.truccato@unito.it

V. Bonino
European Synchrotron Radiation Facility – Experiments Division
71 Avenue des Martyrs, F-38000 Grenoble, France

T. Heisig, R. Dittmann
Forschungszentrum Juelich GmbH
Peter Gruenberg Institute 7, D-52425 Juelich, Germany

The ORCID identification number(s) for the author(s) of this article can be found under https://doi.org/10.1002/pssr.202100409.

T. Heisig, R. Dittmann
JARA-FIT
RWTH Aachen University
D-52056 Aachen, Germany

D. Torsello
Department of Applied Science and Technology
Politecnico di Torino
10129 Turin, Italy

D. Torsello
Istituto Nazionale di Fisica Nucleare
Sezione di Torino, 10125 Turin, Italy

L. Mino
Department of Chemistry, Interdepartmental Centre NIS and INSTM Centro di Riferimento
University of Torino
via P. Giuria 7, I-10125 Torino, Italy

G. Martinez-Criado
Instituto de Ciencia de Materiales de Madrid
Consejo Superior de Investigaciones Científicas
28049 Cantoblanco, Spain

exceeding the usual switching voltage has to be applied in order to turn the highly insulating dielectric layers into a switchable state. This so-called electroforming process comprises complex electronic and ionic processes,[7] often mediated by Joule heating and thermal runaways, and results in a release of oxygen from the lattice and the formation of oxygen vacancies along one[8,9] or several nanosized filaments.[10] During subsequent switching, the device resistance changes when proper voltage pulses are applied and move the oxygen vacancies, establishing or interrupting conducting filaments between the electrodes, which can be associated to two different logical states.[11] One of the major problems hindering large-scale diffusion of these devices is represented by the highly stochastic nature of the filament formation, which leads to a large variability of the performances from device to device and even from cycle to cycle for the same device. The size of the filament can be influenced by the electroforming conditions such as forming voltage and current compliance.[12,13] However, the size, shape, and position of the filaments might change upon cycling and thereby cause cycle-to-cycle variations.[14] Therefore, different approaches have been used to pinpoint the filament position by means of modifications of the material stack that locally enhance the electric field, such as embedding nanoparticles into the electrode[15] or the dielectric film,[16,17] or using pyramidal-shaped electrodes.[18] Moreover, methods to confine the ionic motion by providing holes in an oxygen-blocking graphene interlayer[19] and by fabricating nanocavities along misfit dislocations[20] have been used to guide the ionic filament formation process.

In addition to the stochasticity of the filament formation, the need of an electroforming process in filamentary memristors has additional drawbacks with respect to circuit design and power consumption. In particular, the need to form all devices with a higher voltage prior to the circuit operation is a time- and energy-consuming step that strongly limits the circuit design flexibility and increases the power consumption. In this sense, the ability to replace the electroforming step and to develop methods to control the formation and ordering of oxygen vacancies in memristive oxides by other means would represent a great step toward large-scale production and application of memristors.

Some steps in the direction of inducing a localized, controlled amount of oxygen vacancies have already been moved in the field of superconducting oxides. Indeed, some of us have already shown that, using synchrotron radiation nanoprobes with sizes of the order of $50 \times 50 \, nm^2$ and modifying the corresponding photon flux and dose, it is possible to switch from ordinary material characterization to material modification.[21–27] In the case that a superconducting oxide is irradiated in an approximately uniform way, this treatment corresponds to a variation of its oxygen doping level,[28–30] but if only some carefully designed portions are irradiated, a current path can be drawn in the material in such a way to fabricate a Josephson device.[31]

Thus, the whole technique can be considered an alternative X-ray nanopatterning (XNP) method to locally introduce defects in oxides and fabricate devices as desired without etching the crystals. Actually, the microscopic mechanism responsible for these material modifications is not clear yet. Careful space- and time-resolved numerical simulations of the interaction between the superconducting oxides and the X-ray nanobeam have shown that ordinary melting must be excluded,[32] leaving

room for thermal fatigue or marginal non-thermal melting as two possible candidates (see also Supporting Information).[33–36] Nevertheless, the first indications that this mechanism could be relevant also for a transition metal oxide like TiO_2 were reported in the past for $Pt/TiO_2/Pt$ cells, where it was shown that prolonged, nonspatially controlled synchrotron irradiation acting in synergy with an applied DC electric field was able to induce structural changes corresponding to oxygen depletion and transition to the Ti_4O_7 Magneli phase.[37] Following these indications, we have applied the XNP method to nonannealed TiO_2 rutile single crystals with two Au electrodes and shown that controlled irradiation can open a subsurface conduction channel in the insulating region between two electrodes.[38] This experiment proved that XNP can be applied also to materials where the binding energy for oxygen is much greater than the one corresponding to the interstitial atoms present in the superconducting oxides. However, we were neither able to prove the ability of XNP to locate and pin the formation of conducting channels nor to observe which kind of changes could be associated in our case to the device-resistance transition. This is the problem this article is intended to face.

2. Experimental Section

The devices were fabricated by depositing two metal electrodes on a (110)-oriented TiO_2 rutile single crystal. The corresponding geometry is shown in **Figure 1**b. One electrode was made of Pt (60 nm in thickness), whereas the other one was made by depositing 30 nm of Pt on top of 30 nm of Ta (Figure 1c). Two sizes of the gap between the electrodes were used during the experiments, about 1.9 and 6.7 µm in width, respectively. The samples with a 1.9 µm gap were annealed at 300 °C in H_2/Ar (4%) atmosphere for 2 h. This annealing procedure was strongly reducing and was expected to cause the formation of oxygen vacancies in rutile and thereby to increase the sample electronic conductivity. A temperature as low as 300 °C was selected to minimize the change of the surfaces and interfaces of the electrodes. However, as the oxygen exchange reaction was strongly kinetically limited at this temperature and due to the lack of reference studies in this temperature range, it was impossible to accurately predict the oxygen vacancy concentration caused by this annealing step. Based on extrapolations from
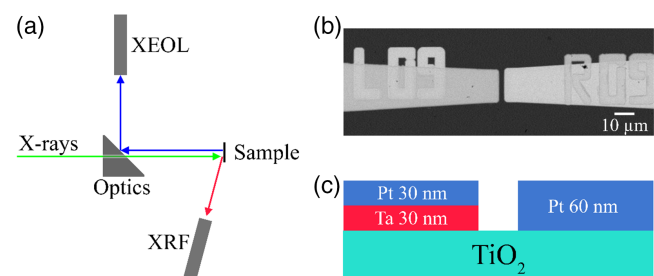

Figure 1. a) Sketch of the experimental setup used at beamline ID16B (XRF represents the X-ray fluorescence detector, XEOL indicates the X-ray excited optical luminescence detector). b) Scanning electron microscopy (SEM) image of a typical sample (top view) and c) schematic cross section.

ADVANCED
SCIENCE NEWS
www.advancedsciencenews.com

pss
physica status solidi rrl
www.pss-rapid.com

1000 to 300 °C,[39] one can regard $x = 10^{-5}$ as the upper limit for the oxygen deficiency in TiO_{2-x}. In addition to this, additional oxygen vacancies were caused at the Ta/TiO_2 interface due to the formation of a Ta_2O_{5-x} interface layer.[40] The Pt electrode was expected to form a Schottky barrier with rutile, resulting in a rectifying effect for the devices, whereas the Ta one formed an ohmic contact. This provided the asymmetry generally needed to observe bipolar resistive switching.[41]

X-ray characterization and irradiation sessions were carried out during two subsequent experimental campaigns at the nanoprobe beamline ID16B of the European Synchrotron Radiation Facility (ESRF) in Grenoble, France.[42] The first campaign took place before the ESRF upgrade to the new fourth generation of synchrotron light sources, which has been named as extremely brilliant source (EBS), whereas the second campaign was scheduled after the upgrade. In both cases, the X-ray beam was focused by means of Kirkpatrick–Baez mirrors into a spot size of the order of $50 \times 50 \, nm^2$ and the experimental setup consisted of an optical microscope for preliminary sample alignment, a X-ray fluorescence (XRF) detector and a X-ray excited optical luminescence (XEOL) system equipped with a high numerical aperture collection optics, whose axis coincides with the X-ray nanobeam. Devices were mounted on a customized sample holder with electrical connections, which also allowed to carry out 2-probe electrical characterizations between subsequent irradiation sessions without removing the sample from the beamline.

As a typical procedure for characterization before irradiation of all the devices, a preliminary localization of the gap was obtained through an optical microscope, and the subsequent acquisition of XRF maps allowed a precise localization of the metal electrodes. Simultaneous XRF and XEOL characterization maps were acquired by raster scanning the sample area of interest in the X-ray nanobeam, after inserting Si filters to reduce the photon flux to avoid unwanted material modifications. Elemental maps were obtained by fitting the collected XRF spectra with the PyMCA code[43] using the X-ray emission lines of the elements present in the samples (Ti, Pt, and Ta), together with Ar and Kr from the atmosphere and some expected impurities in rutile crystals (Sr, Y, Si, and Fe).

After electrical characterization of their pristine state, devices were irradiated by scanning the samples across the X-ray nanobeam along lines connecting the two metal electrodes. The details of the irradiation procedure were different for the two experimental campaigns. The nonannealed samples with a 6.7 μm gap were irradiated during the first campaign with a $55 \times 52 \, nm^2$ nanobeam, with an energy of 17.8 keV in pink beam mode ($\Delta E/E \approx 10^{-2}$) and the 16-bunch filling mode of the storage ring, corresponding to a maximum current of 90 mA. This filling mode consisted of a train of 16 equally spaced, equally highly populated electron bunches rotating in the storage ring, each of them generating a current equal to 90 mA/16 bunch = 5.6 mA/bunch. These bunches originated X-ray pulses with a Gaussian time profile with a rms duration $RMS_t \approx 48 \, ps$ and separated by $t_{sep} = 1.76 \times 10^{-7} \, s$ from each other. A single line connecting the two electrodes was irradiated multiple times with a 50 nm step at increasing exposure times and photon fluxes by progressively removing Si filters from the beam, up to a maximum time-averaged photon flux $\Phi_0 = 1 \times 10^{11} \, ph \, s^{-1}$. In this 16-bunch filling mode, such a maximum value of Φ_0 corresponds to about 1.76×10^4 photons per pulse and to a fluence of

$1.76 \times 10^4 \, J \, m^{-2}$ per pulse (see Supporting Information). At the pulse repetition rate of $1/t_{sep} = 5.68 \times 10^6 \, s^{-1}$, the exposure times used during the whole experiment corresponded to a total cumulative dose $CD = 7.51 \times 10^{11} \, Gy$ and to a total cumulative fluence of $CF = 1.70 \times 10^{12} \, J \, m^{-2}$. After each irradiation step, a current–voltage characteristic (i.e., a so-called IV curve) was also recorded. The annealed samples with a 1.9 μm gap were irradiated during the second campaign with a $57 \times 59 \, nm^2$ beam with an energy of 17.5 keV in pink beam mode and $7/8 + 1$ filling mode of the storage ring. This mode consisted in filling 7/8 of the storage ring length with 868 equally spaced bunches of about 0.23 mA/bunch, having at their extremes two bunches of 1 mA. The remaining 1/8 of the storage ring was filled in its center by a single bunch of 2 mA. This resulted in a typical rms duration of the pulses $RMS_t \approx 20 \, ps$, with a separation time between the 0.23 mA bunches equal to $2.84 \times 10^{-9} \, s$ and another separation time of $1.76 \times 10^{-7} \, s$ between the 1 and the 2 mA bunches. In this campaign, as a first step, an area of $6.8 \times 1 \, μm^2$ was irradiated, with a 200 nm step size for the mesh in both directions, in such a way so as to connect the two metal electrodes. This irradiation pattern was repeated multiple times at increasing photon fluxes and exposure times, up to a maximum time-averaged flux $\Phi_0 = 4 \times 10^{12} \, ph \, s^{-1}$ and a maximum exposure time of 5 s per point. In the $7/8 + 1$ filling mode, this maximum value of Φ_0 corresponded to about 1.12×10^5 photons forming the largest X-ray pulse, i.e., the one generated by the 2 mA bunch, which produced a fluence of $9.38 \times 10^4 \, J \, m^{-2}$ per each of these pulses (see Supporting Information). As a second step, a single line was irradiated in the same region, with maximum photon flux and 25 s per point. This corresponded to a total cumulative dose, $CD = 2.4 \times 10^{13} \, Gy$ and to a total cumulative fluence, $CF = 5.3 \times 10^{13} \, J \, m^{-2}$. IV curves were also acquired between irradiations.

Then, after both irradiation and electrical characterization, XRF and XEOL maps were simultaneously acquired once more. At the end of each campaign, samples were also analyzed by means of conducting atomic force microscopy (C-AFM) with a Cypher S system by Asylum Research available at the Partnership for Soft Condensed Matter (PSCM) of ESRF.

3. Results and Discussion

Figure 2a–c shows representative XRF elemental maps corresponding to Pt–L, Ta–L, and Ti–K lines, respectively, for a pristine sample. Samples from both experimental campaigns invariably show the same features: a sample from the second experimental campaign is shown in Figure 2 for the ease of comparison with the following.

It is possible to observe a smaller Pt signal on the left electrode, which corresponds to the Pt/Ta electrode, due to the lower amount of Pt compared with the right electrode. This is confirmed by the Ta map, where only the left electrode is visible, as expected. In contrast, the Ti–K signal shows a lower intensity in correspondence with the two electrodes. Keeping in mind that at 17.5 keV the attenuation length in TiO_2 is over 160 μm, this result can be ascribed to a shadow effect of the metal electrodes partially absorbing the XRF signal coming from the bulk of the substrate underneath.
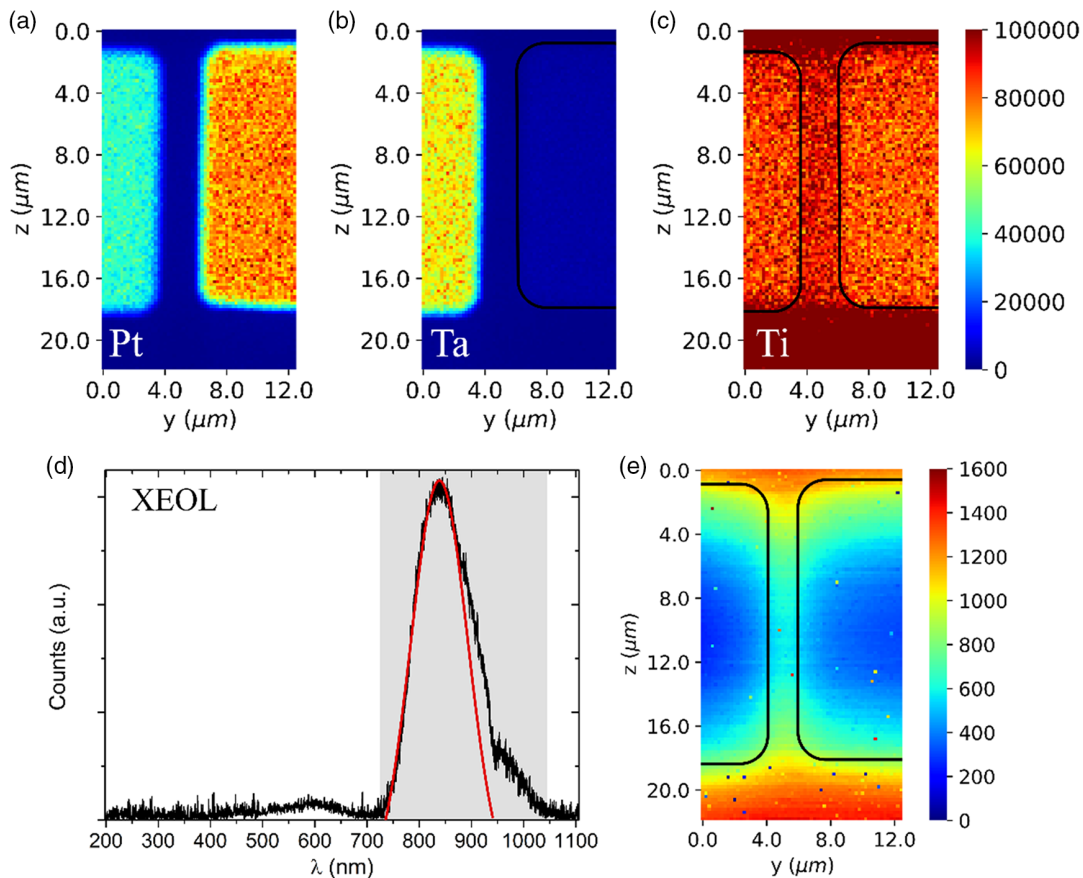
Figure 2. a–c) XRF maps corresponding to Pt–L lines (a), Ta–L lines (b), and Ti–K lines (c) collected from a typical pristine sample. d) XEOL spectrum integrated over the whole scanning area. The red curve highlights the main Gaussian contribution to the spectrum in the NIR region (shaded area). e) XEOL map corresponding to the intensity of the main Gaussian contribution of (d). The black solid lines in (b), (c), and (e) represent the metal electrode contours.

The corresponding XEOL spectrum integrated over the whole scanning sample area is shown in Figure 2d. It shows a broad emission component in the near infrared region with a maximum located around $\lambda = 830$ nm, corresponding to a photon energy $E = hc/\lambda = 1.49$ eV. Similar photoluminescence spectra have already been reported for rutile single crystals[44–46] and have been attributed to the radiative recombination of electrons trapped in a midgap state with free holes in the valence band.[45] This midgap state, located about 1.5 eV below the conduction band edge, in principle could be related both to the presence of interstitial Ti atoms[45] and to the presence of oxygen vacancies inducing the reduction of Ti^{4+} to Ti^{3+}.[47] However, the study of the temperature dependence of photoluminescence spectra in rutile has pointed out the importance of oxygen vacancies in trapping the carriers at low temperature ($T = 20$ K) and in producing a discrete set of lines, which are smoothed over and transformed into a continuous spectrum at higher temperatures ($T \geq 100$ K) due to the increasing mobility of the carriers.[44] Therefore, experimental indications are in favor of oxygen vacancies as the origin of the midgap state in rutile.

The XEOL spectrum was fitted with multiple Gaussian contributions, obtaining the spatial distributions of the three parameters defining each Gaussian curve (height, full width at half maximum,

and wavelength of the maximum). In Figure 2e, the map corresponding to the height of the main Gaussian contribution located around 830 nm is reported as the most informative one. A significant decrease in the intensity can be observed in the location of the metal electrodes, due to a screening effect by the metal electrodes analogous to what observed for the XRF signal.

3.1. First Experimental Campaign

Figure 3 shows the current I versus electric field E curves obtained during the first experimental campaign after each irradiation for a nonannealed sample (6.7 μm gap). A clear increase in the sample conductivity is observed with increasing the irradiation dose, along with the appearance of a hysteresis. This hysteresis can be considered as related to trapping of carriers at trap levels,[48,49] which creates a spatial charge distribution and induces an electric counter field, leading to a decrease in the device conductivity with time. The typical timescale observed for the current decrease at constant E value is of the order of 10–100 s (see Supporting Information). Therefore, upon increasing and subsequently decreasing E during acquisition of the IV curves, current values corresponding to the same E values progressively decrease, inducing the appearance
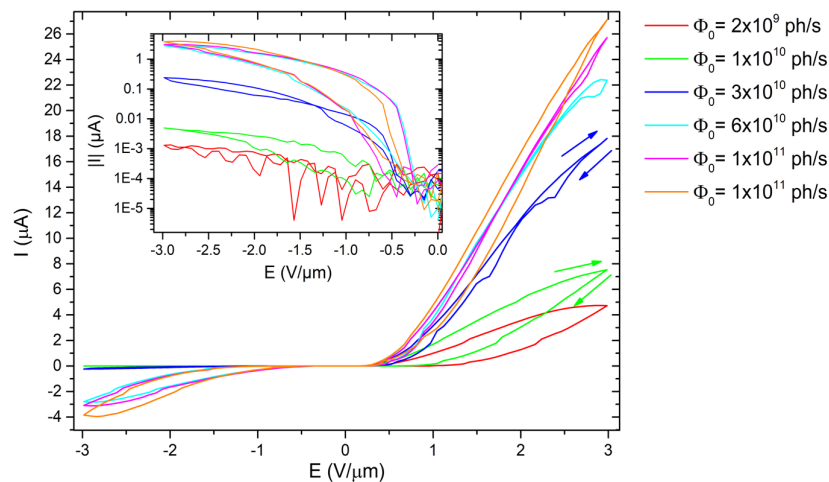
Figure 3. *I* versus *E* curves after multiple irradiations at increasing time-averaged photon fluxes, measured for a first-campaign sample (nonannealed, 6.7 μm gap). The exposure time was 1 s per point for each irradiation, except for the last one corresponding to the orange curve, whose exposure time was increased to 10 s per point. Cumulative doses correspond to $CD = 1.96 \times 10^9$ (red), 1.19×10^{10} (green), 4.25×10^{10} (blue), 1.03×10^{11} (cyan), 2.03×10^{11} (magenta), and 7.51×10^{11} (orange) Gy, and cumulative fluences to $CF = 4.43 \times 10^9$ (red), 2.70×10^{10} (green), 9.60×10^{10} (blue), 2.33×10^{11} (cyan), 4.59×10^{11} (magenta), and 1.70×10^{12} (orange) J m^{-2}. The inset shows the absolute value of the current of the negative branch in a logarithmic scale.

of a hysteresis (see arrows in Figure 3). Moreover, the rectifying effect due to the Schottky barrier between rutile and Pt becomes less pronounced with increasing irradiation, with a remarkable increase in the reverse current by at least three orders of magnitude (see inset of Figure 3).

Analogous hysteretic behaviors were recently reported for instance in ZrO$_x$ memristors, with a practically identical timescale for the current decay.[50] These features were explained by means of a microscopic model where donor-type traps are located close to the interface between the oxide and the Pt electrode. The energy of these trap levels lies in the energy gap below the Fermi level and shows a continuous distribution about 1 eV wide. During the acquisition of the *IV* curves, these trap levels get charged, slightly changing their energy position in the gap and generating a space charge which also affects the height and width of the Schottky barrier. Such a model can also explain the behavior of the irradiated samples shown in Figure 3,

provided that we identify the donor-type trap levels with nonmobile oxygen vacancies located under the Pt electrode.

After irradiation and electrical characterization, topographic and C-AFM images were collected as well. In **Figure 4**a, the topographic signal from AFM is reported, showing a morphological trace in correspondence with the irradiation line with a maximum height of about 14 nm. This feature could be explained in terms of a chemical expansion of the rutile unit cell because of the local increase in the density of oxygen vacancies.[51] Moreover, the C-AFM image reported in Figure 4b clearly shows at the same position an electrically conducting path induced by the X-ray irradiation, which extends up to the surface of the sample and testifies that TiO$_2$ has been locally turned into a conducting material. This behavior further supports the hypothesis of a local increase in the density of oxygen vacancies and significantly differs with respect to previous XNP experiments carried out on rutile single crystals with two Au electrodes, where no evident change
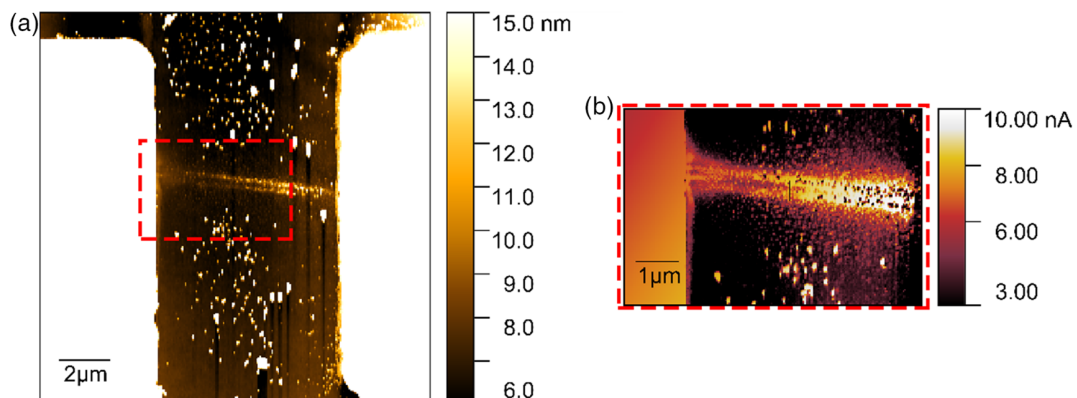

Figure 4. a) Topographic and b) C-AFM images of a gap after irradiation of a first-campaign sample (nonannealed, 6.7 μm gap).
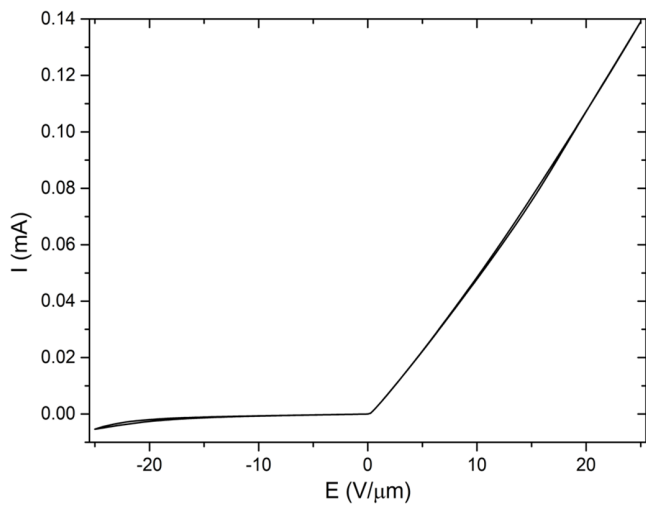
**ADVANCED
SCIENCE NEWS**

www.advancedsciencenews.com

pssrrl

physica status solidi

www.pss-rapid.com

Figure 5. *I* versus *E* curve of a second-campaign sample (annealed, 1.9 μm gap) before irradiation.

in surface conductivity was highlighted after irradiation.[38] This was attributed to the formation of subsuperficial conductive channels. By comparing these two experiments, we can observe that in the present case, the use of an ohmic electrode (i.e., Ta) has resulted in a direct-polarization current in the *IV* curves that is one order of magnitude larger than the previous one. Most likely, such a more intense current has induced a more significant heating of the conduction channel, with a corresponding higher mobility and higher concentration of the oxygen vacancies on the surface, which has allowed them to be detected by C-AFM. However, these data are not enough to discriminate whether a similar concentration of oxygen vacancies was already present on the surface after the XNP irradiation, excluding any significant influence of the bias applied to measure the *IV* curves.

3.2. Second Experimental Campaign

To try to obtain the resistive switching, we changed many experimental parameters and moved to annealed samples in which a higher concentration of oxygen vacancies was induced by the treatment in H_2 atmosphere (see Experimental Section). We also used a shorter gap (1.9 μm) to achieve higher electric field values. In **Figure 5**, a typical *I* versus *E* curve of a pristine device of the second campaign is reported. It is possible to see that before irradiation these samples show a clear rectifying behavior and no hysteresis, even for *E* values considerably higher than the ones shown in Figure 3.

After irradiation with $CD = 2.4 \times 10^{13}$ Gy and $CF = 5.3 \times 10^{13}$ J m^{-2}, *I* versus *E* curves were acquired by progressively increasing the maximum *E* value (see **Figure 6**a). Once again, a hysteresis can be observed, especially in the positive branch, corresponding to a less rectifying behavior with respect to the one of pristine samples. By further increasing the maximum *E* value, an electroforming process takes place (see Figure 6b), as testified by the sudden increase in the current up to the compliance value of the voltage source (≈2.5 mA).

Subsequently, some *I* versus *E* curves were acquired with a lower maximum value for *E*, and all of them corresponded to a low-resistance state (the so-called "on" state, see the green curve in Figure 6b), confirming a nonvolatile change in the device resistance. Despite many attempts to reverse the device behavior back to its pristine high-resistance state were made, no more transition was observed.

XRF and XEOL maps were then acquired for these samples around the irradiated region after device electroforming, with a typical step size of 200 nm in both directions. They are shown in **Figure 7**. From the Pt–L and Ta–L line maps (Figure 7a,b), it is clear that the Pt electrode was partially damaged as a consequence of the sudden discharge during the onset process, whereas the Ta/Pt electrode remained unchanged. We can also

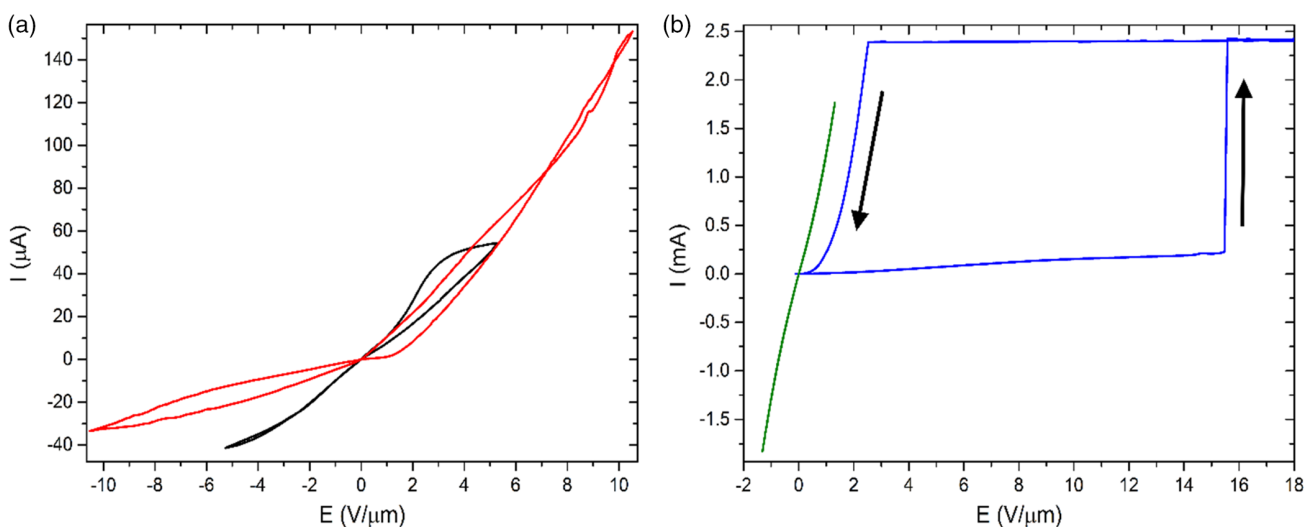**Figure 6.** a) *I* versus *E* curves measured for a second-campaign sample (annealed, 1.9 μm gap) after irradiation with $CD = 2.4 \times 10^{13}$ Gy and $CF = 5.3 \times 10^{13}$ J m^{-2}, at increasing maximum voltages. b) *I* versus *E* curve showing the electroforming process (blue) and subsequent *I* versus *E* curve in the so-called "on" state (green).
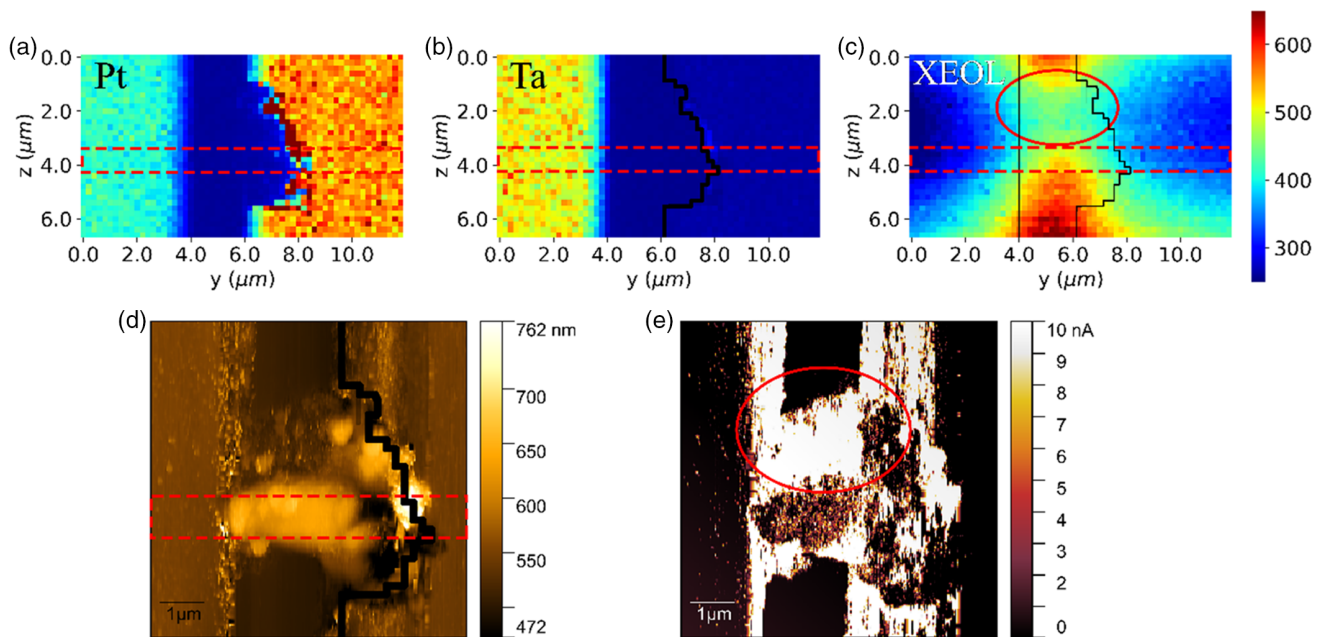
Figure 7. a,b) Typical XRF maps collected for a second-campaign sample (annealed, 1.9 μm gap) after irradiation and electroforming, corresponding to Pt–L (a) and Ta–L (b) lines. c–e) Corresponding XEOL (c), topographic (d), and C-AFM (e) images after irradiation and electroforming are also displayed. The dashed red boxes highlight the irradiated region, and the solid red circles indicate the minimum in the XEOL (c) and the maximum in the C-AFM (e) signals.

observe the absence of metal traces inside the gap, which excludes the possibility of electromigration of metal electrode ions such as Pt or Ta as an explanation for the onset of the low-resistance state of the device.

An AFM image was also acquired after electroforming and is shown in Figure 7d. It is possible to see a morphological bump about 150 nm in height that is centered on the irradiated line and that is also in correspondence with the damaged portion of the electrode. The device polarization (positive Pt vs negative Ta/Pt) and the asymmetrical shape of the bump are in agreement with the scenario of the thermally enhanced oxygen vacancy assembly for the electroforming process, where irregularities of the cathode can result in high values of the local current density, and therefore, induce a remarkable increase in the local temperature due to the Joule effect. This local heating facilitates the drift of oxygen ions under the action of the strong electric field, leading to the accumulation of oxygen vacancies near the cathode and to the growth of the oxygen vacancy filament from the cathode toward the anode.[52–54] It can also be observed that the bump shows a rounded shape and droplet-like structures around it, which could be considered as an indication of possible local melting to have occurred during the electroforming, further confirming the involvement of significant local Joule heating in the process. Moreover, this oxygen vacancy assembly scenario also implies the migration of oxygen ions and their release at the Pt anode, which explains the local delamination of this electrode.

On the whole, position and structure of the electroformed bump represent an evidence that XNP can provide the sample irregularities necessary to start and guide the electroforming process in the desired position, probably because of the large local density of oxygen vacancies induced in the nanobeam track. Apparently, this process made the switch to the "on" state for

the conducting channel irreversible, but at the same time indicates that a possible strategy to obtain a reversible resistance transition could be represented by the use of lower current compliances in order to accurately modulate the local heating intensity and, consequently, the migration of oxygen vacancies and the filament size.

Figure 7c shows the XEOL signal collected over the same area as the XRF maps. Again, a lower intensity can be observed in correspondence with the two electrodes, as expected. Also, the luminescence intensity in the gap region was expected to be consistent with the XEOL maps acquired before electroforming, i.e., practically constant over the 6 μm vertical scale of Figure 7c. On the contrary, it is possible to observe a ≈30% modulation of the XEOL signal, with a lower intensity in the region highlighted by the solid red circle, which is close to but does not correspond exactly to the irradiated portion of the sample (dashed red lines). Moreover, it is also possible to observe that the C-AFM image reported in Figure 7e shows a higher conductivity region on the border of the bump, which corresponds to the same position as the low intensity area of the XEOL signal.

A possible explanation for these two observations could be represented by the presence of a high density of oxygen vacancies in this region of the device, which induces a variety of electronic states located within 0.7 eV from the bottom of the conduction band.[47,55] Indeed, on one hand, this situation would offer non-radiative recombination paths to photoexcited electrons, which results in a local decrease in the luminescence signal.[45] On the other hand, it could increase the surface conductivity because of thermally excited electrons coming from these defective states, which could be considered as shallow donor levels for the conduction band and that can also affect the overall band structure at the rutile/metal Schottky barrier in such a way to favor the

injection of mobile carriers, similarly to what has already been proved in $SrTiO_3$ and in ZrO_x.[50,56]

4. Conclusion

We have pursued a global picture of the phenomena occurring during XNP of memristive devices by carrying out a multitechnique investigation (XRF, XEOL, *IV* curves, AFM). We have shown that it is possible to open conducting microchannels in insulating TiO_2 rutile single crystals by means of local X-ray irradiation with typical doses of the order of 10^{11} Gy and fluences of the order of 10^{12} J m^{-2}. This phenomenon consists both in an increase in the electrical conductivity and in a decrease in the rectifying effect of the Schottky barrier between rutile and the Pt contact, in agreement with an increase in the oxygen vacancy donor concentration in the space charge region. Moreover, these microchannels have shown the ability to locate and guide the electroforming process between the electrodes, most likely involving intense local Joule heating but no atomic migration of the metal electrodes. Indications are that the formation of oxygen vacancies should probably be promoted by XNP on a local basis, and that the electroforming process could subsequently rearrange their position into continuous highly conductive regions that also act as nonradiative recombination centers for electrons, although experimental evidences to support this picture are not conclusive yet.

These results could be interesting from the point of view of the production technology of memristive devices, as they could pave the way toward a more reliable and deterministic performances of electroforming. However, the nature of the structural defects induced by irradiation and the corresponding microscopic mechanisms responsible for their formation are presently unclear and call for further investigations to fully exploit the potential of this method. Of course, this would also imply an optimization of the process parameters to avoid excessive local heating and to achieve a reversible resistance switching.

Supporting Information

Supporting Information is available from the Wiley Online Library or from the author.

Acknowledgements

Conflict of Interest

The authors declare no conflict of interest.

Data Availability Statement

The data that support the findings of this study are available from the corresponding author upon reasonable request.

Keywords

[1] M. Anees, K. Rahul, S. A. Swarnkar, S. Yachareni, in *IEEE 14th Dallas Circuits and Systems Conf. (DCAS)*, IEEE, Piscataway, NJ **2020**, https://doi.org/10.1109/DCAS51144.2020.9330648.

[2] R. Jany, C. Richter, C. Woltmann, G. Pfanzelt, B. Forg, M. Rommel, T. Reindl, U. Waizmann, J. Weis, J. A. Mundy, D. A. Muller, H. Boschker, J. Mannhart, *Adv. Mater. Interfaces* **2014**, 1, 1300031.

[3] D. B. Strukov, G. S. Snider, D. R. Stewart, R. S. Williams, *Nature* **2008**, 453, 80.

[4] R. Dittmann, J. P. Strachan, *Appl. Mater.* **2019**, 7, 110903.

[5] D. Ielmini, *Semicond. Sci. Technol.* **2016**, 31, 063002.

[6] M. A. Zidan, J. P. Strachan, W. D. Lu, *Nat. Electron.* **2018**, 1, 22.

[7] A. A. Sharma, I. V. Karpov, R. Kotlyar, J. Kwon, M. Skowronski, J. A. Bain, *J. Appl. Phys.* **2015**, 118, 114903.

[8] J. J. Yang, M. D. Pickett, X. M. Li, D. A. A. Ohlberg, D. R. Stewart, R. S. Williams, *Nat. Nanotechnol.* **2008**, 3, 429.

[9] D. H. Kwon, K. M. Kim, J. H. Jang, J. M. Jeon, M. H. Lee, G. H. Kim, X. S. Li, G. S. Park, B. Lee, S. Han, M. Kim, C. S. Hwang, *Nat. Nanotechnol.* **2010**, 5, 148.

[10] H. C. Du, C. L. Jia, A. Koehl, J. Barthel, R. Dittmann, R. Waser, J. Mayer, *Chem. Mater.* **2017**, 29, 3164.

[11] S. Kim, S. Choi, W. Lu, *ACS Nano* **2014**, 8, 2369.

[12] Z. Wei, T. Takagi, Y. Kanzawa, Y. Katoh, T. Ninomiya, K. Kawai, S. Muraoka, S. Mitani, K. Katayama, S. Fujii, R. Miyanaga, Y. Kawashima, T. Mikawa, K. Shimakawa, K. Aono, in *2011 Int. Electron Devices Meeting*, IEEE Piscataway, NJ, USA **2011**, https://doi.org/10.1109/IEDM.2011.6131650.

[13] T. Heisig, J. Kler, H. C. Du, C. Baeumer, F. Hensling, M. Glss, M. Moors, A. Locatelli, T. O. Mentes, F. Genuzio, J. Mayer, R. A. De Souza, R. Dittmann, *Adv. Funct. Mater.* **2020**, 30, 2004118.

[14] C. Baeumer, R. Valenta, C. Schmitz, A. Locatelli, T. O. Mentes, S. P. Rogers, A. Sala, N. Raab, S. Nemsak, M. Shim, C. M. Schneider, S. Menzel, R. Waser, R. Dittmann, *ACS Nano* **2017**, 11, 6921.

[15] Q. Liu, S. B. Long, H. B. Lv, W. Wang, J. B. Niu, Z. L. Huo, J. N. Chen, M. Liu, *ACS Nano* **2010**, 4, 6162.

[16] C. Lee, I. Kim, H. Shin, S. Kim, J. Cho, *Nanotechnology* **2010**, 21, 7.

[17] N. Raab, D. O. Schmidt, H. C. Du, M. Kruth, U. Simon, R. Dittmann, *Nanomaterials* **2018**, 8, 869.

[18] K. Y. Shin, Y. Kim, F. V. Antolinez, J. S. Ha, S. S. Lee, J. H. Park, *Adv. Electron. Mater.* **2016**, 2, 1600233.

[19] J. Lee, C. Du, K. Sun, E. Kioupakis, W. D. Lu, *Acs Nano* **2016**, 10, 3571.

[20] S. Choi, S. H. Tan, Z. F. Li, Y. Kim, C. Choi, P. Y. Chen, H. Yeon, S. M. Yu, J. Kim, *Nat. Mater.* **2018**, 17, 335.

[21] P. Badica, A. Agostino, M. M. R. Khan, S. Cagliero, C. Plapcianu, L. Pastero, M. Truccato, Y. Hayasaka, G. Jakob, *Supercond. Sci. Technol.* **2012**, *25*, 105003.

[22] S. Cagliero, E. Borfecchia, L. Mino, L. Calore, F. Bertolotti, G. Martinez-Criado, L. Operti, A. Agostino, M. Truccato, P. Badica, C. Lamberti, *Supercond. Sci. Technol.* **2012**, *25*, 125002.

[23] L. Gozzelino, R. Gerbaldo, G. Ghigo, F. Laviano, M. Truccato, *J. Supercond. Novel Mag.* **2017**, *30*, 749.

[24] L. Mino, V. Bonino, A. Agostino, C. Prestipino, E. Borfecchia, C. Lamberti, L. Operti, M. Fretto, N. De Leo, M. Truccato, *Sci. Rep.* **2017**, *7*, 9066.

[25] L. Mino, E. Borfecchia, A. Agostino, C. Lamberti, M. Truccato, *J. Electron Spectrosc. Rel. Phen.* **2017**, *220*, 69.

[26] A. Pagliero, L. Mino, E. Borfecchia, M. Truccato, A. Agostino, L. Pascale, E. Enrico, N. De Leo, C. Lamberti, G. Martinez-Criado, *Nano Lett.* **2014**, *14*, 1583.

[27] C. Plapcianu, A. Agostino, P. Badica, G. V. Aldica, E. Bonometti, G. Ieluzzi, S. Popa, M. Truccato, S. Cagliero, Y. Sakka, O. Vasylkiv, R. Vidu, *Ind. Eng. Chem. Res.* **2012**, *51*, 11005.

[28] V. Bonino, A., Agostino, C. Prestipino, O. Hernandez, M. Fretto, L. Mino, M. Truccato, *Crystengcomm* **2018**, *20*, 6667.

[29] M. W. Rabbani, V. Bonino, L. Spessa, A. Agostino, N. De Leo, C. Prestipino, M. Truccato, *Cryst. Growth Des.* **2021**, *21*, 3299.

[30] D. Torsello, L. Mino, V. Bonino, A. Agostino, L. Operti, E. Borfecchia, E. Vittone, C. Lamberti, M. Truccato, *Phys. Rev. Mater.* **2018**, *2*, 014801.

[31] M. Truccato, A. Agostino, E. Borfecchia, L. Mino, E. Cara, A. Pagliero, N. Adhlakha, L. Pascale, L. Operti, E. Enrico, N. De Leo, M. Fretto, G. Martinez-Criado, C. Lamberti, *Nano Lett.* **2016**, *16*, 1669.

[32] V. Bonino, D. Torsello, C. Prestipino, L. Mino, M. Truccato, *J. Synchr. Radiat.* **2020**, *27*, 1662.

[33] N. Medvedev, *J. Phys. Condens. Matter* **2020**, *32*, 435401.

[34] N. Medvedev, Z. J. Fang, C. Y. Xia, Z. Li, *Phys. Rev. B* **2019**, *99*, 144101.

[35] N. Medvedev, I. Milov, *Sci. Rep.* **2020**, *10*, 12775.

[36] R. A. Voronkov, N. Medvedev, A. E. Volkov, *Phys. Status Solidi RRL* **2020**, *14*, 1900641.

[37] S. H. Chang, J. Kim, C. Phatak, K. D'Aquila, S. K. Kim, J. Kim, S. J. Song, C. S. Hwang, J. A. Eastman, J. W. Freeland, S. Hong, *ACS Nano* **2014**, *8*, 1584.

[38] L. Mino, V. Bonino, F. Picollo, M. Fretto, A. Agostino, M. Truccato, *Adv. Electron. Mater.* **2019**, *5*, 1900129.

[39] P. Kofstad, *Nonstoichiometry, Diffusion, and Electrical Conductivity in Binary Metal Oxides*, Wiley-Interscience, New York **1972**.

[40] D. Y. Cho, M. Luebben, S. Wiefels, K. S. Lee, I. Valov, *ACS Appl. Mater. Interfaces* **2017**, *9*, 19287.

[41] R. Waser, R. Dittmann, G. Staikov, K. Szot, *Adv. Mater.* **2009**, *21*, 2632.

[42] G. Martinez-Criado, J. Villanova, R. Tucoulou, D. Salomon, J. P. Suuronen, S. Laboure, C. Guilloud, V. Valls, R. Barrett, E. Gagliardini, Y. Dabin, R. Baker, S. Bohic, C. Cohen, J. Morse, *J. Synchrotron Rad.* **2016**, *23*, 344.

[43] V. A. Sole, E. Papillon, M. Cotte, P. Walter, J. Susini, *Spectrochim. Acta, Part B* **2007**, *62*, 63.

[44] M. Gallart, T. Cottineau, B. Honerlage, V. Keller, N. Keller, P. Gilliot, *J. Appl. Phys.* **2018**, *124*, 133104.

[45] D. K. Pallotti, L. Passoni, P. Maddalena, F. Di Fonzo, S. Lettieri, *J. Phys. Chem. C* **2017**, *121*, 9011.

[46] X. L. Wang, Z. C. Feng, J. Y. Shi, G. Q. Jia, S. A. Shen, J. Zhou, C. Li, *Phys. Chem. Chem. Phys.* **2010**, *12*, 7083.

[47] A. Morales-Garcia, O. Lamiel-Garcia, R. Valero, F. Illas, *J. Phys. Chem. C* **2018**, *122*, 2413.

[48] A. Fissell, M. Czernohorsky, R. Dargis, H. J. Osten, *Mater. Sci. Forum* **2007**, *556–557*, 655.

[49] M. R. Hummon, A. J. Stollenwerk, V. Narayanamurti, P. O. Anikeeva, M. J. Panzer, V. Wood, V. Bulovic, *Phys. Rev. B* **2010**, *81*, 115439.

[50] C. La Torre, A. Kindsmuller, D. J. Wouters, C. E. Graves, G. A. Gibson, J. P. Strachan, R. S. Williams, R. Waser, S. Menzel, *Nanoscale* **2017**, *9*, 14414.

[51] Y. Dang, A. R. West, *J. Am. Ceram. Soc.* **2019**, *102*, 251.

[52] K. M. Kim, B. J. Choi, Y. C. Shin, S. Choi, C. S. Hwang, *Appl. Phys. Lett.* **2007**, *91*, 012907.

[53] K. M. Kim, D. S. Jeong, C. S. Hwang, *Nanotechnology* **2011**, *22*, 254002.

[54] K. C. Tang, A. C. Meng, F. Hui, Y. Shi, T. Petach, C. Hitzman, A. L. Koh, D. Goldhaber-Gordon, M. Lanza, P. C. McIntyre, *Nano Lett.* **2017**, *17*, 4390.

[55] J. Bonkerud, C. Zimmermann, F. Herklotz, P. M. Weiser, C. Seiffert, E. F. Verhoeven, L. Vines, E. V. Monakhov, *Semicond. Sci. Technol.* **2021**, *36*, 014006.

[56] C. Baeumer, C. Funck, A. Locatelli, T. O. Mentes, F. Genuzio, T. Heisig, F. Hensling, N. Raab, C. M. Schneider, S. Menzel, R. Waser, R. Dittmann, *Nano Lett.* **2019**, *19*, 54.
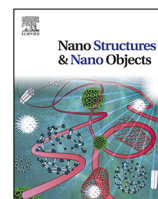
Structure and physicochemical properties of MgB$_2$ nanosheets obtained via sonochemical liquid phase exfoliation

Santanu Kumar Padhi [a], Xiaolin Liu [b], Maria Carmen Valsania [c], Luca Andreo [c], Angelo Agostino [c], Andrea Alessio [a], Linda Pastero [d], Alessia Giordana [c], Zhilin Wu [b], Giancarlo Cravotto [b], Marco Truccato [a,*]

[a] NIS Interdepartmental Centre and Physics Dept., University of Torino, Via P. Giuria 1, 10125 Torino, Italy
[b] Drugs Dept., University of Torino, Via P. Giuria 9, 10125 Torino, Italy
[c] NIS Interdepartmental Centre and Chemistry Dept., University of Torino, Via P. Giuria 7, 10125 Torino, Italy
[d] NIS Interdepartmental Centre and Earth Science Dept., University of Torino, Via Valperga Caluso 35, 10125 Torino, Italy

ARTICLE INFO

ABSTRACT

We have performed ultrasonic liquid phase exfoliation (LPE) of MgB$_2$ in ethanol and investigated the resulting nano-assemblies as a function of the ultrasound processing time. TEM morphological and structural analysis, along with STM topographic characterization, showed that for short sonication times the exfoliated grains preserve the MgB$_2$ crystal structure, have a 2D character and produce Moiré patterns corresponding to stacked layers with rotational misalignment. On the other hand, the longest process times result in spheroidal nanoparticles with diameters of the order of 10 nm, which can also coalesce into larger agglomerates. Optical absorbance spectra confirmed that the exfoliated material preserves a metallic nature with a predominant 2D character corresponding to the *ab*-plane, whereas Raman spectra showed the presence of extra-modes induced by 3D symmetry breaking in the exfoliated products, along with indications of some B-H stretching modes. The detection of a positive zeta potential confirms that an active surface hydrogenation process has taken place during sonication. The mechanochemistry of the exfoliation mechanism has been attributed to particle–particle collisions and particle-shockwave interactions originating from the implosive bubble-collapse. The present study provides important information useful for implementing the LPE process in different contexts for MgB$_2$, like few-layer superconductivity, antibacterial coating and nano-drug preparation.

1. Introduction

Liquid phase exfoliation (LPE) is a simple and versatile processing method to produce atomically thin, scalable quantities of two-dimensional (2D) sheets by direct exfoliation [1–7]. Its primary microscopic mechanism is represented by cavitation bubble collapse, which generates a combination of high energy microjets, interparticle collisions and direct shockwave-solid interactions to yield exfoliated 2D-nanosheets [8–13]. Typically, bulk solids of layered materials are the candidates of choice to undergo the LPE process, but recently also non-layered materials with non-isotropic 3D bonding arrangements (like, for instance, strong in-plane ionic or covalent bonds versus weaker out-of-plane van der Waals or metallic bonding forces) have been successfully treated [14–16].

Generally speaking, 2D-nanostructures have already been obtained from several metal-boride materials and their possible

applicability to various fields, like e.g. sensing, electronics, catalysis, energy harvesting, ion transport, hydrogen generation and storage, has been recently discussed [17]. In the specific case of MgB$_2$, its crystal structure is analogous to that of intercalated graphite, having alternate graphene-like boron basal honeycomb layers (borophene) sandwiched by a close-packed Mg-triangular layer [18,19]. This implies that non-isotropic atomic bonds exist, with strong covalent bonding within each layer and weaker metallic bonding between different layers [20]. For this reason, MgB$_2$ is expected to preferably cleave at the site of the Mg-B bonds between adjacent layers [21]. In principle, this material could be of interest as a starting point for the production of borophene single layers and indeed several methods have already been used in this direction to obtain MgB$_2$ nanosheets, including chemical exfoliation by means of chelating agents [22,23], sonication in water [21] or high energy ball milling in an inert atmosphere [24]. However, these methods have shown a deep influence on the MgB$_2$ structure and properties, resulting in amorphization or high distortion of its crystal structure [21,23], in the heavy reconstruction of the B surfaces [24] and in the

presence of hydroxyl- and oxy-functional groups on the surfaces of these nanosheets [21,22].

On the other hand, the possibility of having nearly-ideal, few-layer MgB_2 nanosheets would be important to discriminate between theoretical models which predict a semiconducting behaviour [25] or a superconducting one (sometimes with a remarkable superconductivity enhancement), providing a good prototype system to understand the real role of surface states in determining superconductivity [26–29]. In this respect, the use of LPE with a solvent to induce minimal perturbation to MgB_2, unlike water, could represent a viable method to achieve this goal. Of course, the efficiency of LPE also depends on other process details and requires a suitable choice of matched surface tension components [30,31], but anhydrous ethanol is a good candidate to minimize chemical interactions and has already been shown to disperse MgB_2 2D-nanosheets in a very effective way [15].

Actually, it should be considered that MgB_2 2D-nanosheets are also being tested in several fields beyond superconductivity, and their use in biomedical applications is at its initial stages of investigation and evaluation. Preliminary indications show that they could be effective and economical for bone tissue engineering [32] and the treatment of some cancers, hypomagnesemia and bacteria-infected wounds [33–36]. Specifically to this biomedical field, the LPE method has great potential as the starting point for further chemical functionalization of the generated MgB_2 2D-nanosheets, also by making use of non-inert solvents. Thereby, it could enable a controlled modification of the properties of nanosheets during LPE to increase biocompatibility, targeted drug delivery or antimicrobial activities [37–40].

However, in the present paper we focus on the LPE method used for MgB_2 in ethanol. The goal consists of understanding the mechanochemistry of the process as a function of its duration and in investigating the features of the MgB_2 nanoparticles and their surface physicochemical attributes in comparison with bulk MgB_2. This represents an important step towards the production of nearly ideal MgB_2 nanosheets, with possible developments both for basic superconductivity studies and for subsequent surface functionalization with a variety of bioadaptive chemical groups to be grafted in a controlled way for desired applications.

2. Materials and methods

MgB_2 powder has been produced by means of the Mg-Reactive Liquid Infiltration (Mg-RLI) method using an amorphous B powder (Sigma Aldrich, Taufkirchen, Germany, nominal purity > 95%, particle size ≤ 1 μm) and Mg granules (Alfa Aesar, Kandel, Germany, nominal purity 99.8%, 1.70 mm) as precursors, with a stoichiometric ratio Mg:B = 1.4:2 [37].

These precursors were placed inside a degassed stainless steel container one after the other, in an alternate configuration. Then, the ends of the precursor-filled container were sealed by hydraulic pressing. Before filling with precursors, the steel reaction chamber was degassed at 200 °C for 7 h in a 0.2 L/min Ar flux and then stored in a glove box. Both the precursor and steel container handling were carried out inside the glove box to minimize contamination by oxygen.

The thermal cycle for the material synthesis consisted of heating the sealed container in a quartz furnace up to 800 °C for 6 h. The heating ramp was performed at a rate of 5 °C/min and an intermediate plateau at 150 °C (1 h dwell) was maintained before reaching the final temperature. During the synthesis, a constant Ar flux of 0.2 L/min was maintained.

The sample extraction from the steel container was performed by cutting it to obtain lumpy grains of the product. They underwent XRD measurements and the corresponding Rietveld analysis
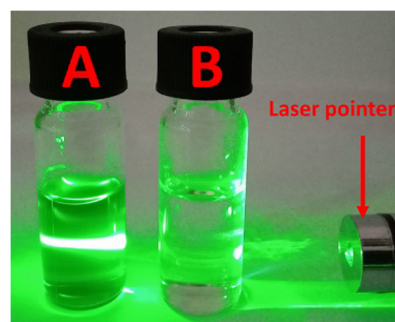

Fig. 1. Observation of light scattering for a green laser beam by (A) the 1 h sonicated product and (B) pure ethanol solvent. The Tyndall scattering is visible for the sonicated dispersion only.

showed the sample consisted of 98 wt% MgB_2 and 2 wt% MgO (sample code: MBNB06, see Fig.S1 in the Supplementary Information). This grainy mass was manually ground with a mortar and pestle for almost 10 min to obtain a MgB_2 fine powder ready for sonochemical exfoliation activity.

The LPE was carried out by means of a cup horn cavitating tube (Danacamerini srl, Turin, Italy) working at 19.5 kHz and 75 W (input power). The cavitating tube was cooled with refrigerated fluid.

Three different batches of 200 mg MgB_2 powder were mixed in 20 mL ethanol (anhydrous, assay $\geq$99%, Sigma Aldrich) and sonicated for 1, 2 and 3 h duration, respectively. Ice water circulation around the titanium alloy transducers plus a 10 min off-cycle every 30 min of continuous sonication were employed to dissipate solvent heat generated by the ultrasonic treatment. The exfoliated mass was separated by centrifugation (Allegra 64 R centrifuge, Beckman Coulter) at 15000 rpm for 1 min.

Confirmation of the presence of nanoparticles in the supernatant liquid dispersion after only 1 h of sonication can be observed in Fig. 1; the Tyndall effect can be clearly observed along the path of the laser light in the sonicated dispersion only, implying successful exfoliation.

In order to study the nanoparticle features, the exfoliated ethanol dispersions were deposited by drop casting over lacey-carbon films on copper TEM grids. Their microstructural and aggregation features were investigated with a JEOL 3010 UHR TEM microscope (JEOL Ltd., Tokyo, Japan), operated at an acceleration voltage of 200 kV. The subsequent image analysis was performed with TEM digital micrograph software. On the other hand, the general structure of grains of the MgB_2 precursor powder was studied by means of a table-top compact Scanning Electron Microscope COXEM EM-30 for secondary electron images.

Nanoparticle STM data were acquired with a Danish Micro-Engineering (Herlev, Denmark) SPM Microscope (DME Igloo) equipped with a DS95-50E scanner (scan volume 50 × 50 × 5 μm) and Pt-Ir tips. Exfoliated supernatant samples were prepared by drop-casting 0.1 mL of the MgB_2 suspension in ethanol onto sapphire substrates coated with 20 nm Au and drying them under an incandescent lamp. Topographic imaging was performed at a constant tunnelling current of 2 nA with 0.1 V bias and under Ar flux to remove humidity. Scanning areas were selected at the rim of the dried droplets to increase statistics.

Optical absorption data were acquired with a Perkin Elmer Lambda 900 spectrophotometer. Samples were collected in quartz cuvettes of 0.1 cm optical path. Raman spectroscopic investigations of the exfoliated products were performed using a Bruker Vertex 70 spectrometer, equipped with the RAMII accessory and a Ge detector, by exciting the samples with a Nd:YAG laser source
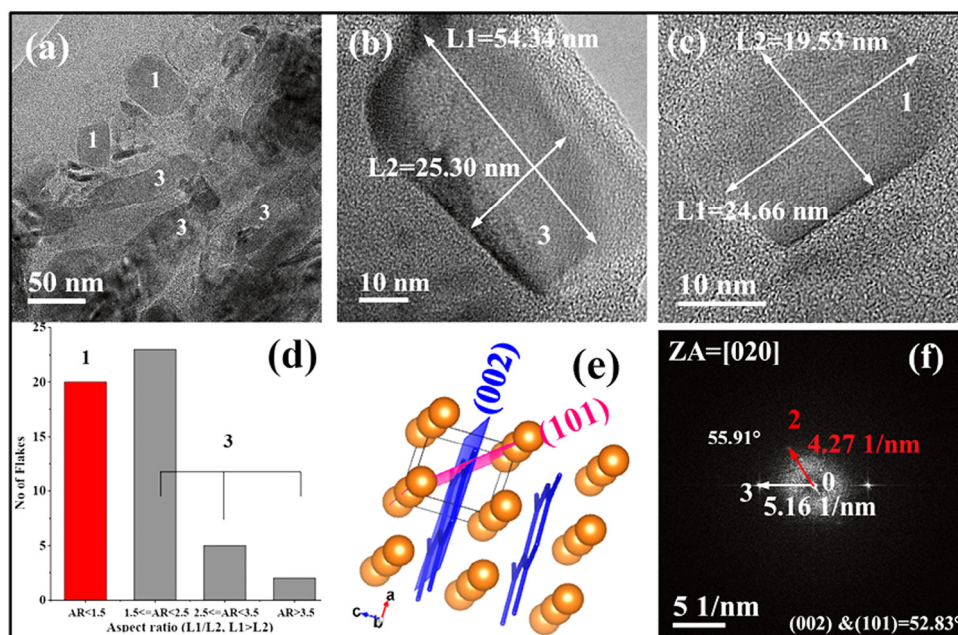
Fig. 2. TEM observations of the MgB$_2$ exfoliated layers obtained after 1 h sonication. (a) Bright Field (BF) general view of the exfoliated layers on the TEM grid: the labels "1" indicate particles with similar sizes along both directions, the labels "3" indicate particles more elongated in one direction. (b) Zoom-in of an individual particle of type "3". (c) Zoom-in of an individual particle of type "1". (d) Histogram of the statistical distribution of the particle aspect ratio (AR) calculated over more than 50 particles: the red bar refers to type "1" particles, whereas the grey bars are associated with type "3" particles. (e) Sketch of the MgB$_2$ crystal structure, with B atoms represented by the blue network and Mg atoms by the orange spheres: the (002) and (101) crystal planes are also highlighted. (f) Fast Fourier Transform (FFT) of panel (c): the main components of the reciprocal lattice have been identified as the vector $\overrightarrow{02}$ (red arrow, modulus equal to 4.27 nm^{-1}) and the vector $\overrightarrow{03}$ (white arrow, modulus equal to 5.16 nm^{-1}). The angle measured between these two vectors is equal to about 55.9°. (For interpretation of the references to colour in this figure legend, the reader is referred to the web version of this article.)

(1064 nm) and with a minimum resolution of 4 cm^{-1}. Zeta potential investigations were carried out employing a Zetasizer Nano Z instrument (Malvern Panalytical). The exfoliated dispersion was taken in a disposable folded capillary cell for measurement, whereas its pH value was recorded with an 827 pH meter by Metrohm, Italy.

3. Results and discussion

The TEM observations concerning the 1 h sonicated MgB$_2$ supernatant dispersion are summarized in Fig. 2.

The general view displayed in Fig. 2(a) shows that particles with different morphologies are present. Indeed, two types of almost isotropic particles can be detected, i.e. with a different aspect ratio (AR) of the particle sizes along the different directions (L1 and L2): AR = L1/L2 ≤ 1.5 (which have been labelled as type "1" particles) and more elongated particles with AR > 1.5 (which have been labelled as type "3" particles). Their typical sizes range between approximately 20 and 100 nm (see Fig. 2(a)) and the statistical distribution of their aspect ratio shows that about 40% of the particles falls in the isotropic type "1" category, whereas the remaining 60% belongs to the elongated type "3". Closer inspections of typical type "3" and typical type "1" particles can be carried out in Fig. 2(b) and (c), respectively.

The Fast Fourier Transform of Fig. 2(c) is reported in Fig. 2(f) for further analysis. It can be noticed that, on top of the amorphous halo around the origin, two main crystalline contributions can be detected. The most apparent one is represented by the vector $\overrightarrow{03}$ (white arrow in Fig. 2(f)), whose modulus is equal to 5.16 nm^{-1}, corresponding to a d-spacing value for the crystal planes d = 1.94 Å. According to the MgB$_2$ standard diffraction card ICDD PDF-2#65-3383, the expected d-spacing for the (002) planes is d$_{(002)}$ = 1.767 Å. The difference between the measured and expected values is about 9.7%, which falls within the typical

uncertainty for d-spacing measurements via TEM. Moreover, another weaker crystalline contribution can be observed in Fig. 2(f) as the red vector $\overrightarrow{02}$, whose modulus is equal to 4.27 nm^{-1}. This implies a corresponding d-spacing for the crystal planes d = 2.34 Å. According to the same standard diffraction card for MgB$_2$, the expected d-spacing for the (101) planes is d$_{(101)}$ = 2.128 Å. Again, the difference between the expected and the measured values is about 10%, which is acceptable. Finally, the angle measured via TEM between these two vectors is about 55.9°, which compares favourably with the theoretically expected value of about 53° for the angle between the (002) and the (101) planes. Fig. 2(e) displays a scheme of the crystal structure of MgB$_2$, highlighting the orientation of the (002) and (101) crystalline planes, which allows visualization of the angle between them and making a direct comparison with the orientation of the vectors $\overrightarrow{03}$ and $\overrightarrow{02}$ of Fig. 2(f), respectively.

Therefore, the match between the d-spacing values and the angle allows the conclusion that the nanoparticle observed in Fig. 2(c) is really a nanoparticle consisting of MgB$_2$. Moreover, the detection of the (002) and (101) planes implies that, in principle, both of planes can represent termination surfaces of these nanoparticles. However, this gives no special information about the chemical nature of the B- or Mg-termination surfaces of the nanoparticles, leaving both of them equally probable. More insight about the structure of the MgB$_2$ nanoparticles resulting from 1h-sonication can be obtained from the High-Resolution TEM images shown in Fig. 3.

It is possible to observe that the particle reported in Fig. 3(a) is about 80 nm in size and actually consists of a stack of 6 different layers, which are labelled as L1 to L6. The FFT of the area corresponding to the red box is displayed in Fig. 3(b), where, on top of the amorphous halo, 3 main crystalline components can be detected: the vector $\overrightarrow{01}$ (red arrow, modulus equal to 3.96 nm^{-1}), the vector $\overrightarrow{02}$ (white arrow, modulus equal to 4.45 nm^{-1}) and the
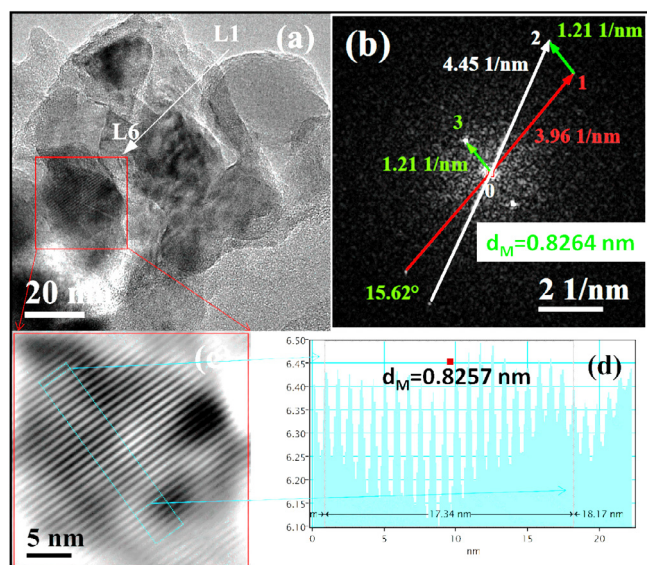
Fig. 3. HRTEM imaging of the MgB_2 exfoliated layers obtained after 1 h sonication. (a) overview of a 2D-nanosheet consisting of 6 stacked layers (L1 to L6); (b) FFT of the portion of panel (a) corresponding to the L6 layer and surrounded by the red box: the main components of the reciprocal lattice have been identified as the vector $\overrightarrow{01}$ (red arrow, modulus equal to 3.96 nm^{-1}), the vector $\overrightarrow{02}$ (white arrow, modulus equal to 4.45 nm^{-1}) and the vector $\overrightarrow{03}$ (green arrow, modulus equal to 1.21 nm^{-1}). The angle measured between $\overrightarrow{01}$ and $\overrightarrow{02}$ is equal to about 15.6°; (c) Inverse FFT of panel (b) after masking the vectors $\overrightarrow{01}$ and $\overrightarrow{02}$; (d) line profile of the fringes visible in panel (c): their period is equal to 0.8257 nm. (For interpretation of the references to colour in this figure legend, the reader is referred to the web version of this article.)

Table 1
Reciprocal vectors and corresponding angles shown in Fig. 3(b).

Reciprocal vector	Modulus (1/nm)	d-spacing (Å)	Angle (°) with respect to vector $\overrightarrow{01}$
$\overrightarrow{01}$	3.967	2.521	0
$\overrightarrow{02}$	4.450	2.247	15.62
$\overrightarrow{03}$	1.211	8.258	76.16

concluded that the MgB_2 nanoparticle of Fig. 3(a) actually consists of a few stacked nanosheets slightly misaligned to each other.

This situation can be visualized in a more clear way by taking the inverse FFT of Fig. 3(b), while masking the vectors $\overrightarrow{01}$ and $\overrightarrow{02}$, which is shown in Fig. 3(c). In this picture the fringes of the Moiré pattern corresponding to the vector $\overrightarrow{03}$ are very apparent and their period reported in Fig. 3(d) is practically the same as the d-spacing of the vector $\overrightarrow{03}$, as expected.

To obtain a clear confirmation about the layered nature of the exfoliated nanoparticles, we have compared TEM and STM acquisitions for the 1 h sonicated supernatant dispersion. The corresponding results are shown in Fig. 4. Even if the nanoparticles considered are obviously not exactly the same in both measurements, it is possible to see that on a typical length scale of about 200 nm, what in the TEM image seems to be a nanosheet really corresponds to a layer about 14 nm in thickness in the STM image, with an average surface roughness $S_{rms} = 1.5$ nm, that has to be compared with the value $S_{rms} = 0.58$ nm of the substrate (see Fig. S2 in Supplementary Information). Therefore, the 2D nature of the nanosheets observed in the TEM image is confirmed, with a typical length-to-height ratio greater than 10.

Fig. 5(a) and (d) display a TEM overview of the exfoliated MgB_2 nanosheets obtained after 2 h of sonication. The extension of some individual nanosheets, identified as domains with coherent lattice fringes, is indicated by the violet arrows: It is possible to notice that practically all of the sheets look like isotropic flakes with characteristic sizes below 10 nm. This seems to indicate that longer sonication times induce higher fragmentation of the MgB_2 nanosheets.

The FFTs of the regions surrounded by red boxes and labelled as "2" in Fig. 5(a) and (d) are displayed in Fig. 5(b) and (e), respectively. Even over such small regions, it is possible to identify many crystalline contributions corresponding to many reciprocal vectors. However, practically all of them lay on two circles, meaning that two moduli are dominant, even if the reciprocal vector orientations can be very different. This situation is typical of a polycrystalline sample. In Fig. 5(b) and (e) two representative vectors have been highlighted. The vector $\overrightarrow{01}$ has a modulus of 3.67 and 3.80 nm^{-1} in Fig. 5(b) and (e), respectively, corresponding to d-spacing values of 2.72 and 2.63 Å, respectively. Again, these vectors can be identified with the reciprocal vector (100) of the ICDD card, which predicts a theoretical value $d_{(100)} = 2.671$ Å that is just 2% different from the measured one. The vector $\overrightarrow{03}$ has a modulus of 4.26 nm^{-1} in both Figs. 5(b) and 5(e), corresponding to a d-spacing value d = 2.35 Å. This vector can be identified with the reciprocal vector (101), whose d-spacing is $d_{(101)} = 2.128$ Å, in reasonable agreement (about 10% difference) with the measured value. Interestingly, the (101) and (100) Bragg reflections are the two most intense ones expected from a polycrystalline MgB_2 sample, which makes the present spot indexing fully self-consistent. The additional features emerging from Fig. 5(b) and (e) are represented by the vectors $\overrightarrow{02}$. Again, they can be interpreted as Moiré patterns originating from superimposed, misaligned MgB_2 nanosheets. Indeed, according to Eq. (1), the periods of the Moiré patterns generated by the vectors

vector $\overrightarrow{03}$ (green arrow, modulus equal to 1.21 nm^{-1}), with an angle between $\overrightarrow{01}$ and $\overrightarrow{02}$ equal to about 15.6°. The corresponding d-spacing for the crystalline planes are 2.53, 2.25 and 8.26 Å, respectively. By comparing these values with the ones reported in the above mentioned ICDD card, it is easy to identify the vector $\overrightarrow{01}$ as the reciprocal vector (100) ($d_{(100)} = 2.671$ Å) and the vector $\overrightarrow{02}$ as the reciprocal vector (101) ($d_{(101)} = 2.128$ Å), since in both cases the expected and measured moduli agree to within a very reasonable uncertainty of about 5%.

However, the interpretation of vector $\overrightarrow{03}$ requires some more discussion. Indeed, in the crystal structure of MgB_2 the longest interplanar distance is $d_{(001)} = 3.522$ Å, which is less than 50% of the measured value. This observation unequivocally implies that this contribution cannot originate from the MgB_2 crystal structure itself. On the other hand, the observation of the presence of up to 6 different layers opens the way to a correct interpretation. Indeed, it is well-known that two lattices superimposed with some misalignment angle can originate interference patterns with a new periodicity, i.e. the so-called Moiré patterns. The general mathematical formula for the period d_M of the Moiré pattern generated by two lattices with periods d_{01} and d_{02}, featuring a misalignment angle α_{102}, is reported in Eq. (1):

$$d_M = \frac{d_{01} d_{02}}{\sqrt{d_{01}^2 + d_{02}^2 - 2 d_{01} d_{02} \cos \alpha_{102}}}. \quad (1)$$

Table 1 lists the features of the reciprocal vectors identified in Fig. 2(b) with more precise measurements. Based on these data, Eq. (1) predicts a value for the period d_M of the Moiré pattern generated by the vectors $\overrightarrow{01}$ and $\overrightarrow{02}$ $d_M = 8.066$ Å. This value agrees very well (i.e. within about 2%) with the experimental d-spacing of the vector $\overrightarrow{03}$ reported in Table 1. Therefore, it can be

Fig. 4. Comparison between TEM and STM measurements of the 1 h sonicated supernatant dispersion. (a) TEM BF morphology and (b) STM topographic map of similar nanosheets with the same typical length scale of about 200 nm. (c) STM profile of a nanosheet, taken along the blue line shown in panel (b). (For interpretation of the references to colour in this figure legend, the reader is referred to the web version of this article.)

Fig. 5. HRTEM imaging of the MgB$_2$ exfoliated layers obtained after 2 h sonication, (a) and (d) overview of the nanoparticles at different magnifications: violet lines indicate the approximate extension of some individual sheets; (b) and (e) FFT of the regions surrounded by red boxes and labelled as "2" in panels (a) and (d), respectively. In both panels, vectors $\vec{01}$ and $\vec{03}$ represent the contribution from the planes of the MgB$_2$ crystal structure, whereas vector $\vec{02}$ represents the Moiré pattern emerging from stacked misaligned MgB$_2$ nanosheets; (c) and (f) intensity profiles measured along a line normal to the Moiré fringes observed in the regions "2" of panels (a) and (d), respectively. (For interpretation of the references to colour in this figure legend, the reader is referred to the web version of this article.)

$\vec{01}$ and $\vec{03}$ are equal to d$_M$ = 9.620 Å and d$_M$ = 5.568 Å for Fig. 5(b) and (e), respectively. On the other hand, the periods measured in Fig. 5(c) and (f) for the fringes visible in the regions labelled as "2" in Fig. 5(a) and (d) are d$_M$ = 9.66 Å and d$_M$ = 5.81 Å, in good agreement with the expected values.

In order to compare the TEM observations with the STM ones for the 2 h sonicated supernatant dispersion, we focussed on the length scale of 100 nm. Fig. 6 shows the corresponding observations for two different nanosheets with approximately the same shape and size. The STM topographic map indicates that this nanosheet is about 7 nm in height, with a width-to-height ratio of at least 15 (depending on the profile orientation) and an average surface roughness S$_{rms}$ = 0.8 nm. These measurements confirm the 2D nature of the 2 h exfoliated nanosheets, too.

One of the liquid dispersions was sonicated for 3 h and then treated in two different ways. Part of the product was dried from ethanol by keeping it at 80 °C for 48 h in air: the corresponding TEM images are shown in Fig. 7(a) and (b). Another part of the

dispersion was tested as usual by taking 5 mL of the supernatant liquid obtained via centrifugation and casting it on the TEM grid: the corresponding images are shown in Fig. 7(c) and (d).

Fig. 7(a) shows that the desiccated dispersion results in a set of aggregated particles with sizes between 5 and 10 nm, which stick on the edge of a non-transparent bulky particle. Considering the size of this bulky particle and the fact that the pristine MgB$_2$ powder consists of grains with an average size of about 1.4 μm (see Fig. S3 in Supplementary Information), it is natural to identify this bulky particle as a grain of the pristine powder that underwent no or minimal fragmentation process during the 3 h sonication.

Focussing on the edge region of this aggregate (see Fig. 7(b)), it is possible to clearly distinguish the single crystallites and their fringes, with a measurement of the d-spacing equal to d = 2.706 Å. This spacing matches well with the one of the (100) planes d$_{(100)}$ = 2.671 Å, confirming that this is the dominant orientation for these MgB$_2$ planes and that the aggregate on the
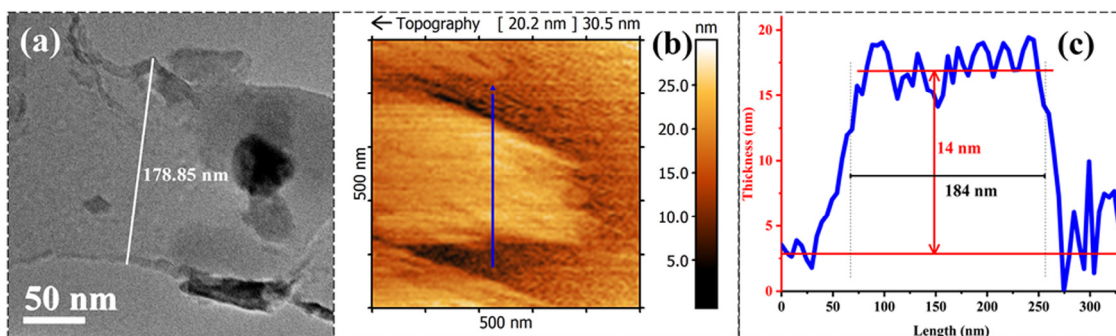
Fig. 6. Comparison between TEM and STM measurements of the 2 h sonicated supernatant dispersion. (a) TEM BF morphology and (b) STM topographic map of similar nanosheets with the same typical length scale of about 100 nm. (c) STM profile of a nanosheet, taken along the blue line shown in panel (b). (For interpretation of the references to colour in this figure legend, the reader is referred to the web version of this article.)
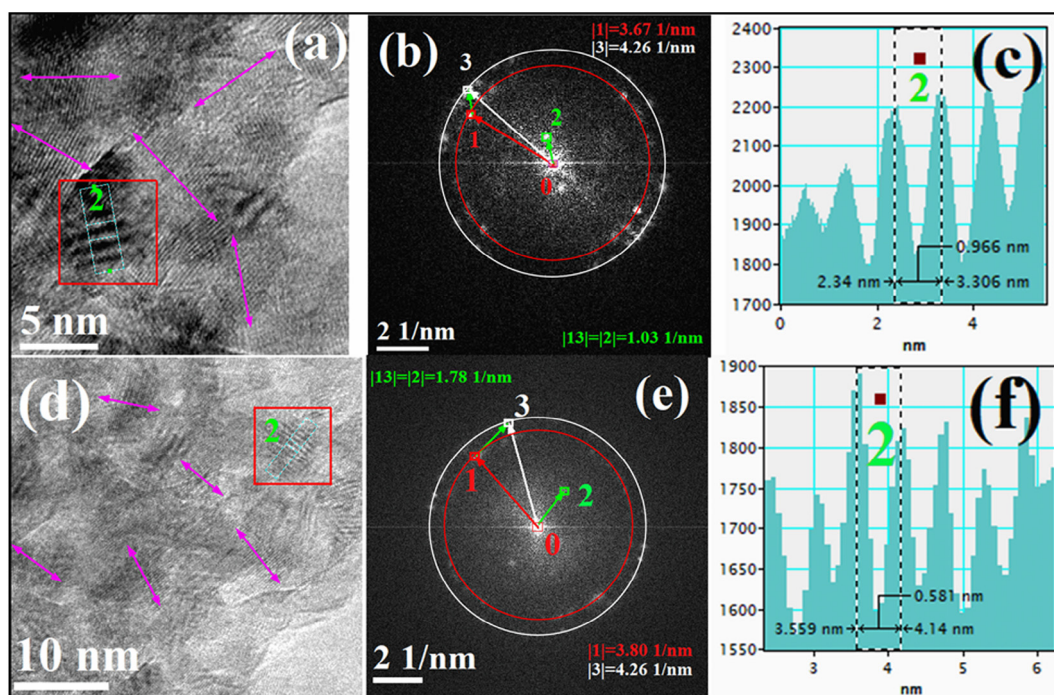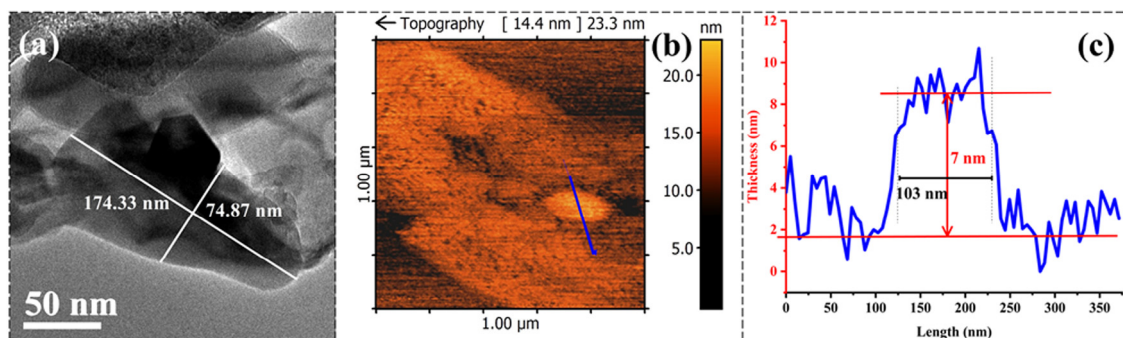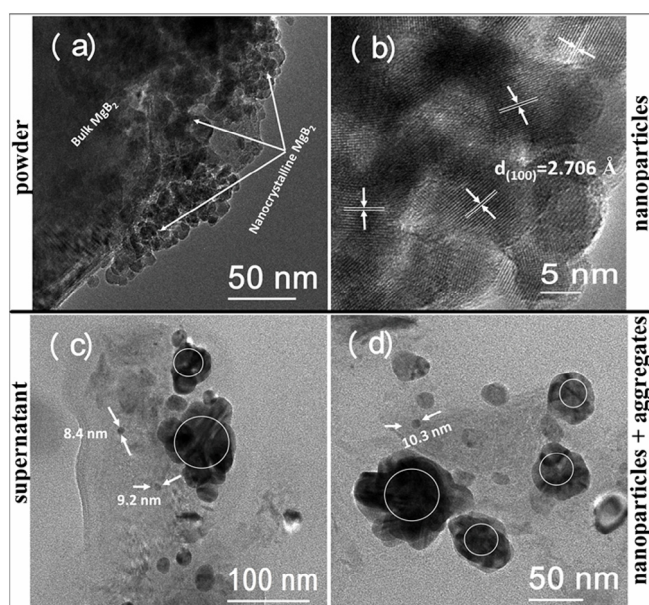

Fig. 7. TEM imaging of the MgB_2 exfoliated particles obtained after 3 h sonication. (a) low-magnification BF image representing both the bulk and the edge regions of the MgB_2 nanoparticle aggregate obtained via oven-drying; (b) HR image of the edge region of panel (a): lattice fringes with d = 2.706 Å are indicated; (c) and (d) low-magnification BF images of MgB_2 nanoparticles obtained from a centrifuge-derived supernatant drop. Some approximately circular particles with diameters of about 10 nm are indicated by white arrows. Bigger particles, about one order of magnitude larger in size and formed by many aggregated particles, are highlighted by white circles.

edge of the bulky particle consists of densely packed MgB_2 single nanocrystals.

Fig. 7(c) and (d) show that these nanoparticles, about 5–10 nm in size, can also be observed in an isolated form in the case of the supernatant solution. As we will discuss in the following, these isolated particles can be indicated as primary particles and their aggregation can lead to the formation of more complex bodies about one order of magnitude larger, as indicated by the white circles in Fig. 7(c) and (d).

To gain further insight about the nature of the isolated nanoparticles observed in the case of the supernatant solution, we carried out a comparison between TEM and STM observations, which is summarized in Fig. 8. In the TEM image, these particles show a rounded shape with a diameter ranging between 10 and 40 nm, approximately (Fig. 8(a)). Nanoparticles with analogous shape and size have also been detected in the STM image and a typical profile is shown in Fig. 8(c). It is clear that in this

case it is no longer possible to define a "flat" top surface of the nanoparticle and that the prolonged sonication process has resulted in objects resembling spheroidal or ellipsoidal shapes.

All of these observations lead to the following picture for the present sonication process, which is graphically summarized in Fig. 9 and discussed in the following.

As it is well-known, the LPE technique is based on the cavitation bubble-collapse mechanism. Generally speaking, the microscopic processes that can take place during this kind of treatment are represented by: (i) interparticle collisions, (ii) surface damage (e.g. from micro-jets or particle collisions or direct shockwave damage) and iii) particle fragmentation (mostly from direct shockwave-particle interactions) [13–16,18]. In principle, all of these mechanisms can coexist, but the dominant process largely depends on the suspension particle density and secondly on the length of the sonication. Indeed, for instance, the surface damage by micro-jets rapidly decreases when the mean size of the solid surface becomes less than the resonant bubble dimensions just before collapsing [16].

As a matter of fact, many of previous research efforts employing sonication on MgB_2 have resulted in chemically modified 2D-layered products with different structures, stoichiometries and functionalities [21,23,41]. For instance, the use of a high load of MgB_2 spherical particles (about 45 μm in diameter) in decalin has induced interparticle coalescence by fusion just within 1 h of sonication treatment [42].

On the other hand, very few reports exist about direct bulk-MgB_2 exfoliation [15,43]. Our study, being intended to investigate the ability of sonication to deliver nanostructured MgB_2 products with unmodified stoichiometry and minimal surface contamination, has used a low particle concentration for the suspension (i.e. 1 g/100 mL) and a prolonged sonication time to facilitate particle fragmentation.

During the sonication process, vapour bubbles have nucleated and grown in the low-density regions generated by the ultrasound pressure waves until they have reached the resonant size of about 150-200 μm in diameter (see Fig. 9(a)). At this point, the bubbles have collapsed into a core of a few nm in size, where the local pressure conditions are equivalent to a temperature of the order of $T = 5000$ K (Fig. 9(b)). In these very high-energy-density conditions, many radical species can be produced by fragmentation of the ethanol molecules, but the most abundant one is represented by the H^+ species [44] (see Fig. 9(c)). Of course, these radicals diffuse from the collapsed core into the bulk of the liquid and can also recombine into neutral molecules, nevertheless they are continuously created by subsequent collapses in a dynamical way, resulting in a higher amount of H^+ ions available during sonication.

Concerning the exfoliation mechanism, it should be considered that the average size of the grains of the precursor powder is
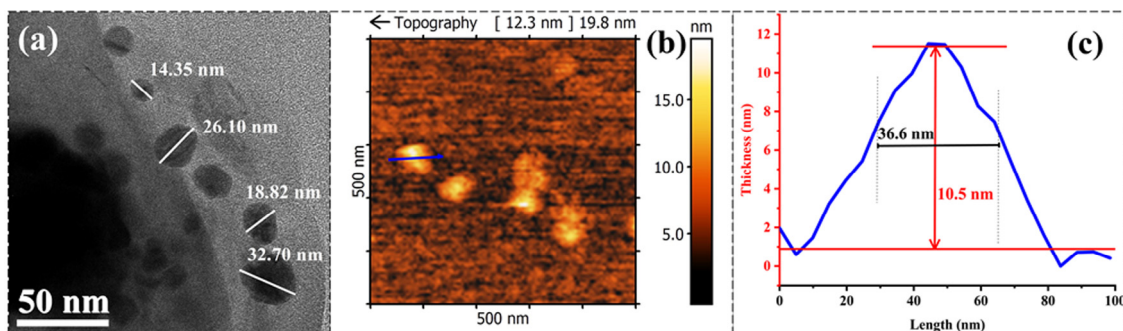
Fig. 8. Comparison between TEM and STM measurements of the 3 h sonicated supernatant dispersion. (a) TEM BF morphology and (b) STM topographic map of similar nanoparticles with the same typical length scale of about 30 nm. (c) STM profile of a nanoparticle, taken along the blue line shown in panel (b). (For interpretation of the references to colour in this figure legend, the reader is referred to the web version of this article.)

just 1.4 μm, to be compared with the size of about 150-200 μm for the resonant bubbles in ethanol just before collapsing. This implies that direct surface damage of the grains by the microjets is expected to be highly inefficient and therefore negligible. On the other hand, MgB_2 grains located close to a collapsed core should be highly affected by the pressure fronts of the generated shockwaves: the discontinuities in the fluid pressure and temperature are expected to result in grain fragmentation and exfoliation, depending on the reciprocal orientation between the grain surface and the wave front (Fig. 9(d)). Another process taking place during sonication is represented by particle–particle collisions. Indeed, even if the microjets originating from bubble collapse are ineffective in directly hitting the MgB_2 grain surfaces, they produce local microstreams that during the collapse can accelerate the grains located close to the bubble walls over the distance of the bubble diameter (i.e. about 150-200 μm) up to a striking speed of approximately 1200 m/s. This can lead to a particle–particle collision between the accelerated particle and another stationary grain located close to the opposite wall of the collapsed bubble. However, since pristine MgB_2 grains are typically 2D-hexagonal in shape, the probability of head-on collisions is expected to be negligible. Other reciprocal orientations corresponding to large glancing-angle collisions should lead to surface damage (and thereby to fragmentation) for one of the particles and to possible exfoliation for the other one (Fig. 9(e)).

Indeed, a comparison between Fig. 2(a) and Fig. 7(a)–(d) indicates a morphological degradation of MgB_2 due to nanosheet fragmentation, likely due to these large glancing-angle particle–particle collisions or to direct shockwave-particle interaction. This observation seems also to exclude a grain growth process derived from individual particle head-on collisions, confirming that this process has really a negligible probability.

Fig. 7(c) and (d) show that this fragmentation process continues up to the point when the cavitation-generated nanoparticles reach a minimum size of approximately 10 nm, which can be indicated as the size of the primary particles. At that point (which in our experiment occurred after about 2 h of sonication) particle coalescence becomes the dominant process: aggregation takes place between primary particles, each of them retaining its crystalline nanostructure (see e.g. Fig. 7(b)), via particle–particle collision, up to the formation of agglomerates with a typical size of 50–100 nm.

Finally, it should also be considered that at any stage of these processes, the H^+ ions resulting from ethanol fragmentation can be adsorbed on the MgB_2 nanoparticle surfaces at convenient atomic sites, producing positively charged nanoparticles (see Fig. 9(f)). Experimental evidences of this fact will be discussed in the following.

In order to gain more knowledge about the physical properties of these MgB_2 nanoparticles, we have investigated their optical

response in the dispersion stage. Fig. 10 displays their UV–VIS optical absorption spectra resulting after the correction for the baseline absorbance of the solvent (i.e. ethanol).

From the point of view of the general optical properties of MgB_2 in its normal state, anisotropic plasma edge frequencies $\omega_{p,a}$ and $\omega_{p,c}$ have been reported in the in-plane and out-of-plane crystallographic directions, respectively, along with the presence of a feature related to the $\sigma \rightarrow \pi$ interband transition [45–49]. However, their details strongly depend on sample characteristics, like doping and crystal quality [50,51]. In this respect, we consider that the LPE method used for our sample preparation, even if already starting from high-purity MgB_2 raw materials [37], should have further enriched the purity of the individual MgB_2 nanoparticles because a much smaller exfoliation rate is expected for typical impurities like MgO, whose ionic bonds make it isotropic. For this reason, we prefer to compare our optical results with the ones obtained for high-quality epitaxial MgB_2 films.

Fig. 10 shows that all of the three suspensions share the presence of the same feature located at about 489 nm, which is fixed at $\omega_{p,a} = 20449$ cm^{-1} and represents a small "shoulder" (hence the label "s" in Fig. 10) of another broader peak, which has been labelled as "P". In terms of energy, the "shoulder" corresponds to $E = 2.54$ eV and has been associated to the plasma frequency of the quasi-2D in-plane σ-bands within the framework of a simple Drude model for the optical conductivity [52]. Apparently, this plasma edge undergoes no shift as a function of the sonication duration, which means on the one hand that the relevant parameters of the charge carriers (like their density) are unaffected, and on the other hand that the average size of the MgB_2 nanoparticles in all of the samples is too large to observe quantum size effects [53,54].

Concerning the broad peak "P", its centre is positioned at about 22925 cm^{-1}, corresponding to about $E = 2.84$ eV. In high-quality epitaxial films, the region in the range 2.55–2.90 eV has been associated with the ab-plane $\sigma \rightarrow \pi$ interband transition, with a centre at approximately 2.78 eV [49,55]. This fact induces the origin of peak "P" to be ascribed to the $\sigma \rightarrow \pi$ transition. It is also interesting that the position of this peak seems to be insensitive to the duration of the sonication process, whereas its height increases on increasing the sonication time and finally it becomes dominant with respect to the shoulder "s". Since the presence of quantum size effects has already been excluded, a reasonable interpretation could be represented by the hypothesis that the accumulation of defects in the MgB_2 nanosheets on increasing the sonication time also increases the interband scattering rate, inducing an increase of the optical absorbance. Therefore, these optical data, on the whole, confirm that the MgB_2 nanoparticles obtained via LPE preserve a *metallic* (albeit defective) nature with a predominant 2D character corresponding to the ab-plane,
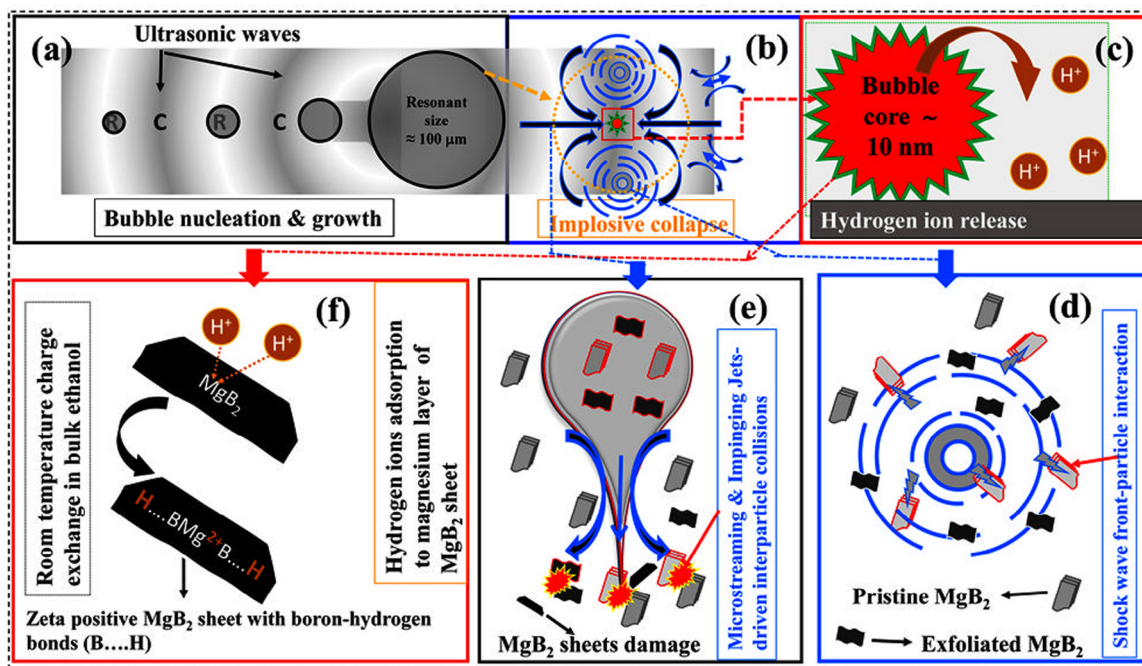
Fig. 9. Schematic overview of the exfoliation physicochemical process taking place in our experiments. (a) Micro-bubble nucleation and growth in the rarefied regions of the liquid; (b) implosive bubble collapse into a nanometric core after reaching the resonant size of 150-200 μm; (c) high-energy-density conditions achieved in the collapsed core (equivalent to $T \approx 5000$ K) produce solvent radical species, the most abundant being H$^+$; (d) shockwave fronts generated by the collapsed core interact with the particles nearby, resulting in exfoliation or fragmentation (depending on reciprocal orientation); (e) particle–particle collisions induced by microstreams and microjets originating from the bubble implosion: particles are transported and accelerated by the microjets and collide with other stationary particles in the bulk solvent; (f) diffusion of H$^+$ ions out of the collapsed core and subsequent adsorption on the surface of exfoliated sheets.
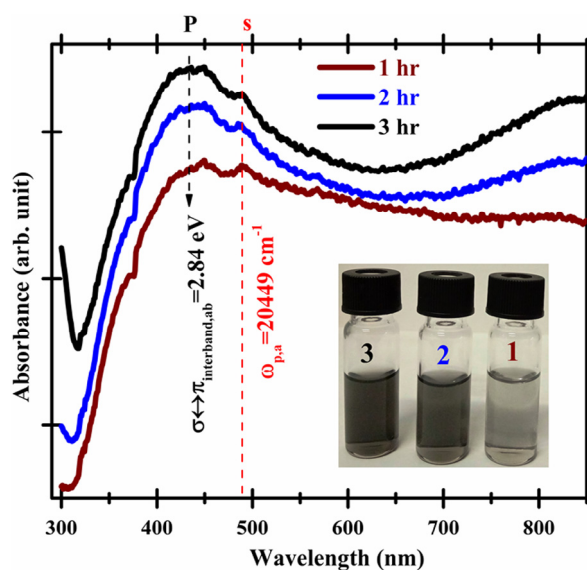

Fig. 10. UV–Visible optical absorption spectra of the supernatant liquids obtained after 1 h (wine curve), 2 h (blue curve) and 3 h (black curve) of MgB$_2$ sonication processes. The inset shows the glass vials containing the nano-MgB$_2$ supernatant liquids collected for these measurements. Vertical dashed lines represent a guide to the eye to highlight important physical features. (For interpretation of the references to colour in this figure legend, the reader is referred to the web version of this article.)

Fig. 11. Raman spectra of the 3 h sonicated MgB$_2$ dispersion in ethanol (wine curve) and of the corresponding precursor bulk-MgB$_2$ powder (red curve). Spectral features important for lattice vibrations and surface coordination are numbered from 1 to 6. The blue curve represents the spectral data collected for pure ethanol. (For interpretation of the references to colour in this figure legend, the reader is referred to the web version of this article.)

but without reaching a size range where quantum confinement effects become detectable.

Fig. 11 reports the Raman spectroscopy data measured for the precursor MgB$_2$ powder and for the 3 h sonicated MgB$_2$ dispersion in ethanol, in order to elucidate some physicochemical features of the MgB$_2$ nanoparticles revealed by their low-energy lattice excitations.

For MgB$_2$ bulk samples (space group I6/mmm), the factor-group analysis predicts four modes at the Γ point: B_{1g}, E_{2g}, A_{2u} and E_{2u}, of which only E_{2g} is Raman active. This mode is generally observed as a broad asymmetric peak around 605 cm^{-1} (75 meV) [56–58], but in the case of our measurements (red curve) it cannot be clearly distinguished from the background. Instead, the spectrum of the bulk MgB$_2$ shows an intense fluorescence signal at high wavenumbers (from about 2000 to 3500 cm^{-1}), which makes it difficult to recognize other signals.
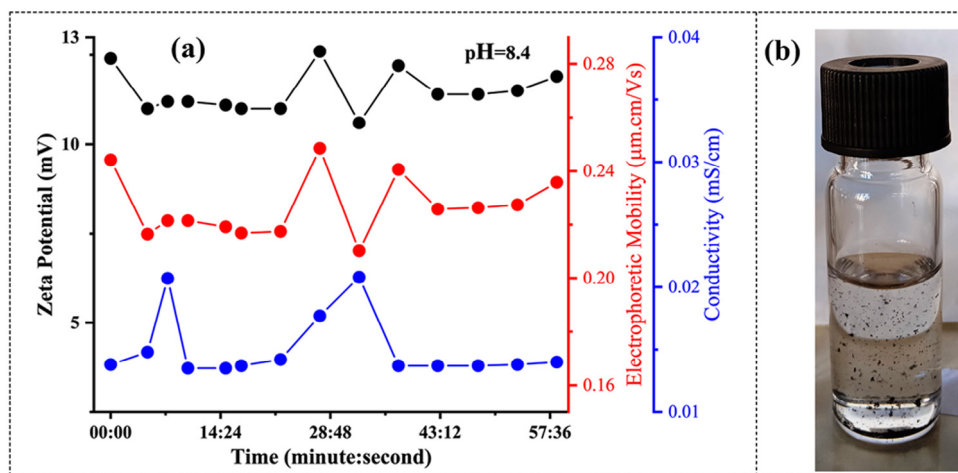
Fig. 12. (a) Physicochemical measurements of 1 h sonicated MgB$_2$ nanoparticles in ethanol as a function of time: zeta potential (black solid circles), electrophoretic mobility (red solid circles) and electrical conductivity (blue solid circles); (b) photographic snapshot of 1 h sonicated MgB$_2$ nanoparticle aggregates observed in the laboratory environment after 48 h of storage (photograph taken just after few seconds of manual shaking). (For interpretation of the references to colour in this figure legend, the reader is referred to the web version of this article.)

This problem could be related to the small size of the hexagonal-like platelets of this bulk sample. Indeed, it has been reported that Raman spectra of bulk MgB$_2$ can be very sensitive to acquisition and sample conditions, and that larger grain sizes typically enhance the observation of well-defined Raman peaks [56,58].

On the other hand, in the spectrum of the 3 h sonicated MgB$_2$ dispersion (wine curve), more signals are observed. Apart from the peaks corresponding to ethanol, the most important contributions to the spectrum are observed at 300, 500, 610, 730 and 800 cm^{-1} (labelled as peaks n.1, n.2, n.3, n.4 and n.5, respectively). On the basis of the literature, the feature at 610 cm^{-1} can be identified with the well-known E_{2g} stretching mode involving the in-plane displacement of B atoms, which is strongly coupled with the σ electronic band [56–58]. Concerning the other peaks, it is important to mention that, on the basis of experimental IR and Raman data, and also DFT calculations, it has been proposed that a reduced symmetry in the lattice can induce the presence of extra peaks [56]. Actually, the measured positions of the extra peaks correspond approximately to the ones reported for the PDOS calculated in MgB$_2$ super-lattices with reduced symmetry and so they can be correlated with the presence of few-layer sheets with a distorted lattice, as also testified by the TEM and STM analyses.

It is also worth noting that this spectrum shows fluorescence, albeit different from that of the bulk sample. In this case the position of the maximum of fluorescence emission (around 2436 cm^{-1}, i.e. peak n.6) corresponds to the range of intense B-H stretching modes [59,60]. Therefore, this is an indication that a surface hydrogenation process could take place during sonication, as expected from the H$^+$ production and adsorption mechanisms shown in Fig. 9(c) and (f). To confirm this hypothesis, we performed a measurement of the zeta potential over a timeframe of 1 h for the 1 h sonicated supernatant solution. The corresponding results are reported in Fig. 12.

It is possible to notice that no time dependence can be observed for the measured quantities over the selected timescale, implying that all of the data are statistically homogeneous and provide the average values of 11.4 ± 0.6 mV, 0.23 ±0.01 μm cm/Vs and 15 ± 2 μS/cm for the zeta potential, the electrophoretic mobility and the electrical conductivity, respectively. Concerning the zeta potential, it should be noticed that its positive sign confirms the Raman indications about the presence of adsorbed H$^+$ ions on the surface of the nanoparticles, different from what is typically observed in exfoliation experiments in water, where the

zeta potential is negative [21]. On the contrary, our experimental situation seems to be more similar to the one of nanodiamonds, where the presence of graphite-like planes with sp^2 bonds at their surfaces promotes nanoparticle hydrogenation [61]. However, the relatively small average value of the zeta potential of our colloidal dispersions corresponds to an incipient instability. Indeed, Fig. 12(b) clearly shows how flocculation starts within 48 h from sonication.

4. Conclusions

We have successfully demonstrated a sonication process to induce exfoliation of high-purity MgB$_2$ powders into nanoparticles. The evolution of the products from few-layer MgB$_2$ nanosheets to 3D agglomerates of nanograins with increasing the sonication time has been monitored, with indications that particle-shockwave and particle–particle interactions represent the dominant mechanisms during the exfoliation and aggregation stages, respectively. TEM, STM and spectroscopic investigations have revealed that the obtained MgB$_2$ nanoparticles preserve their crystal structure and their metallic nature with an enhancement of their 2D features, most likely induced by their few-layer thickness. No chemical alteration has been detected in MgB$_2$ because of the low-frequency sonication process, apart from hydrogen-termination of the nanoparticle surfaces. The corresponding colloidal dispersions show incipient instability and start flocculating within 48 h.

This study provides important preliminary information useful to implement the LPE process in different applications of MgB$_2$, like basic superconductivity studies, antibacterial coating or nano-drug preparation.

CRediT authorship contribution statement

Santanu Kumar Padhi: Conceptualization, Methodology, Investigation, Formal analysis, Visualization, Writing – original draft. **Xiaolin Liu:** Validation, Resources. **Maria Carmen Valsania:** Investigation, Formal analysis. **Luca Andreo:** Investigation, Formal analysis. **Angelo Agostino:** Validation, Resources. **Andrea Alessio:** Investigation, Software. **Linda Pastero:** Investigation, Formal analysis. **Alessia Giordana:** Investigation, Formal analysis. **Zhilin Wu:** Investigation, Formal analysis. **Giancarlo Cravotto:** Resources, Supervision. **Marco Truccato:** Resources, Writing – review & editing, Supervision, Project administration, Funding acquisition.

Declaration of competing interest

The authors declare that they have no known competing financial interests or personal relationships that could have appeared to influence the work reported in this paper.

Data availability

Data will be made available on request.

Acknowledgements

S.K.P., A. Agostino, A. Alessio and M.T. acknowledge the Italian Ministry of Education, University and Research (MIUR) and the EU for financial support, project ERA.NET II−BIOMB. S.K.P., A. Alessio and M.T. also acknowledge partial support from the "Departments of Excellence" (L. 232/2016) grant, funded by MIUR, Italy. S.K.P. is also thankful to Prof. Roberto Rabezzana for help in the observation of Tyndall scattering. Prof. Francesco Turci is also duly acknowledged for instrument training and for the Z-potential measurement obtained with the equipment acquired by the Interdepartmental Center "G. Scansetti" for Studies on Asbestos and Other Toxic Particulates with a grant from Compagnia di San Paolo, Torino, Italy.

Appendix A. Supplementary data

Supplementary material related to this article can be found online at https://doi.org/10.1016/j.nanoso.2023.101016.

References

[1] J.N. Coleman, M. Lotya, A. O'Neill, S.D. Bergin, P.J. King, U. Khan, K. Young, A. Gaucher, S. De, R.J. Smith, I.V. Shvets, S.K. Arora, G. Stanton, H.-Y. Kim, K. Lee, G.T. Kim, G.S. Duesberg, T. Hallam, J.J. Boland, J.J. Wang, J.F. Donegan, J.C. Grunlan, G. Moriarty, A. Shmeliov, R.J. Nicholls, J.M. Perkins, E.M. Grieveson, K. Theuwissen, D.W. McComb, P.D. Nellist, V. Nicolosi, Two-dimensional nanosheets produced by liquid exfoliation of layered materials, Science 331 (2011) 568–571, http://dx.doi.org/10.1126/science.1194975.

[2] V. Nicolosi, M. Chhowalla, M.G. Kanatzidis, M.S. Strano, J.N. Coleman, Liquid exfoliation of layered materials, Science 340 (2013) 1226419, http://dx.doi.org/10.1126/science.1226419.

[3] L. Niu, J.N. Coleman, H. Zhang, H. Shin, M. Chhowalla, Z. Zheng, Production of two-dimensional nanomaterials via liquid-based direct exfoliation, Small 12 (2016) 272–293, http://dx.doi.org/10.1002/smll.201502207.

[4] F.I. Alzakia, S.C. Tan, Liquid-exfoliated 2D materials for optoelectronic applications, Adv. Sci. 8 (2021) 2003864, http://dx.doi.org/10.1002/advs.202003864.

[5] V. Paolucci, G. D'Olimpio, L. Lozzi, A.M. Mio, L. Ottaviano, M. Nardone, G. Nicotra, P. Le-Cornec, C. Cantalini, A. Politano, Sustainable liquid-phase exfoliation of layered materials with nontoxic polarclean solvent, ACS Sustain. Chem. Eng. 8 (2020) 18830–18840, http://dx.doi.org/10.1021/acssuschemeng.0c04191.

[6] H. Chacham, J.C.C. Santos, F.G. Pacheco, D.L. Silva, R.M. Martins, J.P. Del'Boccio, E.M. Soares, R. Altoé, C.A. Furtado, F. Plentz, B.R.A. Neves, L.G. Cançado, Controlling the morphology of nanoflakes obtained by liquid-phase exfoliation: Implications for the mass production of 2D materials, ACS Appl. Nano Mater. 3 (2020) 12095–12105, http://dx.doi.org/10.1021/acsanm.0c02598.

[7] C.A. Howard, Exfoliating large monolayers in liquids, Nature Mater. 20 (2021) 130–131, http://dx.doi.org/10.1038/s41563-020-00907-y.

[8] M. Dular, T. Požar, J. Zevnik, R. Petkovšek, High speed observation of damage created by a collapse of a single cavitation bubble, Wear. 418–419 (2019) 13–23, http://dx.doi.org/10.1016/j.wear.2018.11.004.

[9] S. Barcikowski, A. Plech, K.S. Suslick, A. Vogel, Materials synthesis in a bubble, MRS Bull. 44 (2019) 382–391, http://dx.doi.org/10.1557/mrs.2019.107.

[10] T. Prozorov, R. Prozorov, K.S. Suslick, High velocity interparticle collisions driven by ultrasound, J. Am. Chem. Soc. 126 (2004) 13890–13891, http://dx.doi.org/10.1021/ja049493o.

[11] S.J. Doktycz, K.S. Suslick, Interparticle collisions driven by ultrasound, Science 247 (1990) 1067–1069, http://dx.doi.org/10.1126/science.2309118.

[12] R. Pecha, B. Gompf, Microimplosions: Cavitation collapse and shock wave emission on a nanosecond time scale, Phys. Rev. Lett. 84 (2000) 1328–1330, http://dx.doi.org/10.1103/PhysRevLett.84.1328.

[13] M. Dular, B. Stoffel, B. Širok, Development of a cavitation erosion model, Wear 261 (2006) 642–655, http://dx.doi.org/10.1016/j.wear.2006.01.020.

[14] D. Sahoo, B. Kumar, J. Sinha, S. Ghosh, S.S. Roy, B. Kaviraj, Cost effective liquid phase exfoliation of MoS_2 nanosheets and photocatalytic activity for wastewater treatment enforced by visible light, Sci. Rep. 10 (2020) 10759, http://dx.doi.org/10.1038/s41598-020-67683-2.

[15] M.S. Gilliam, A. Yousaf, Y. Guo, D.O. Li, A. Momenah, Q.H. Wang, A.A. Green, Evaluating the exfoliation efficiency of quasi-2D metal diboride nanosheets using hansen solubility parameters, Langmuir 37 (2021) 1194–1205, http://dx.doi.org/10.1021/acs.langmuir.0c03138.

[16] H. Kaur, R. Tian, A. Roy, M. McCrystall, D.V. Horvath, G. Lozano Onrubia, R. Smith, M. Ruether, A. Griffin, C. Backes, V. Nicolosi, J.N. Coleman, Production of quasi-2D platelets of nonlayered iron pyrite (FeS_2) by liquid-phase exfoliation for high performance battery electrodes, ACS Nano. 14 (2020) 13418–13432, http://dx.doi.org/10.1021/acsnano.0c05292.

[17] H. Gunda, L.E. Klebanoff, P.A. Sharma, A.K. Varma, V. Dolia, K. Jasuja, V. Stavila, Progress, challenges, and opportunities in the synthesis, characterization, and application of metal-boride-derived two-dimensional nanostructures, ACS Mater. Lett. 3 (2021) 535–556, http://dx.doi.org/10.1021/acsmaterialslett.1c00086.

[18] M.E. Jones, R.E. Marsh, The preparation and structure of magnesium boride, MgB_2, J. Am. Chem. Soc. 76 (1954) 1434–1436, http://dx.doi.org/10.1021/ja01634a089.

[19] E. Nishibori, M. Takata, M. Sakata, H. Tanaka, T. Muranaka, J. Akimitsu, Bonding nature in MgB_2, J. Phys. Soc. Japan 70 (2001) 2252–2254, http://dx.doi.org/10.1143/JPSJ.70.2252.

[20] M.R. Koblischka, S. Roth, A. Koblischka-Veneva, T. Karwoth, A. Wiederhold, X.L. Zeng, S. Fasoulas, M. Murakami, Relation between crystal structure and transition temperature of superconducting metals and alloys, Metals 10 (2020) 158, http://dx.doi.org/10.3390/met10020158.

[21] S.K. Das, A. Bedar, A. Kannan, K. Jasuja, Aqueous dispersions of few-layer-thick chemically modified magnesium diboride nanosheets by ultrasonication assisted exfoliation, Sci. Rep. 5 (2015) 10522, http://dx.doi.org/10.1038/srep10522.

[22] R. Saraswat, A.L. James, K. Jasuja, High yield synthesis of boron-based nanosheets, Adv. Appl. Ceram. 118 (2019) 209–216, http://dx.doi.org/10.1080/17436753.2019.1584481.

[23] A.L. James, K. Jasuja, Chelation assisted exfoliation of layered borides towards synthesizing boron based nanosheets, RSC Adv. 7 (2017) 1905–1914, http://dx.doi.org/10.1039/C6RA26658D.

[24] S. Li, H. Gunda, K.G. Ray, C.-S. Wong, P. Xiao, R.W. Friddle, Y.-S. Liu, S. Kang, C. Dun, J.D. Sugar, R.D. Kolasinski, L.F. Wan, A.A. Baker, J.R. Lee, J.J. Urban, K. Jasuja, M.D. Allendorf, V. Stavila, B.C. Wood, Spontaneous dynamical disordering of borophenes in MgB_2 and related metal borides, Nat. Commun. 12 (2021) 6268, http://dx.doi.org/10.1038/s41467-021-26512-4.

[25] B.Z. Xu, S.P. Beckman, Quantum confinement induced band gaps in MgB_2 nanosheets, 2D Mater. 3 (2016) 031003, http://dx.doi.org/10.1088/2053-1583/3/3/031003.

[26] B. Ao, Z. Zhang, T. Tang, Y. Zhao, Potential enhancement of superconductivity in MgB_2 nanosheets: First-principles calculations, Chem. Phys. Lett. 591 (2014) 185–188, http://dx.doi.org/10.1016/j.cplett.2013.11.045.

[27] J. Bekaert, A. Aperis, B. Partoens, P.M. Oppeneer, M.V. Milošević, Evolution of multigap superconductivity in the atomically thin limit: Strain-enhanced three-gap superconductivity in monolayer MgB_2, Phys. Rev. B 96 (2017) 094510, http://dx.doi.org/10.1103/PhysRevB.96.094510.

[28] J. Bekaert, L. Bignardi, A. Aperis, P. van Abswoude, C. Mattevi, S. Gorovikov, L. Petaccia, A. Goldoni, B. Partoens, P.M. Oppeneer, F.M. Peeters, M.V. Milošević, P. Rudolf, C. Cepek, Free surfaces recast superconductivity in few-monolayer MgB_2: Combined first-principles and ARPES demonstration, Sci. Rep. 7 (2017) 14458, http://dx.doi.org/10.1038/s41598-017-13913-z.

[29] Z. Liu, B. Wang, Biaxial strain engineering on the superconducting properties of MgB_2 monolayer, Mater. Chem. Phys. 290 (2022) 126637, http://dx.doi.org/10.1016/j.matchemphys.2022.126637.

[30] J. Shen, Y. He, J. Wu, C. Gao, K. Keyshar, X. Zhang, Y. Yang, M. Ye, R. Vajtai, J. Lou, P.M. Ajayan, Liquid phase exfoliation of two-dimensional materials by directly probing and matching surface tension components, Nano Lett. 15 (2015) 5449–5454, http://dx.doi.org/10.1021/acs.nanolett.5b01842.

[31] J. Shen, J. Wu, M. Wang, P. Dong, J. Xu, X. Li, X. Zhang, J. Yuan, X. Wang, M. Ye, R. Vajtai, J. Lou, P.M. Ajayan, Surface tension components based selection of cosolvents for efficient liquid phase exfoliation of 2D materials, Small 12 (2016) 2741–2749, http://dx.doi.org/10.1002/smll.201503834.

[32] R. Abhinandan, S. Pranav Adithya, D. Saleth Sidharthan, K. Balagangadharan, N. Selvamurugan, Synthesis and characterization of magnesium diboride nanosheets in alginate/polyvinyl alcohol Scaffolds for bone tissue

engineering, Colloids Surf. B Biointerfaces 203 (2021) 111771, http://dx.doi.org/10.1016/j.colsurfb.2021.111771.

[33] M. Fan, Y. Wen, D. Ye, Z. Jin, P. Zhao, D. Chen, X. Lu, Q. He, Acid-responsive H_2-releasing 2D MgB$_2$ nanosheet for therapeutic synergy and side effect attenuation of gastric cancer chemotherapy, Adv. Healthc. Mater. (2019) http://dx.doi.org/10.1002/adhm.201900157.

[34] Z. Jin, D. Chen, P. Zhao, Y. Wen, M. Fan, G. Zhou, Y. Wang, Q. He, Coordination-induced exfoliation to monolayer bi-anchored MnB2 nanosheets for multimodal imaging-guided photothermal therapy of cancer, Theranostics 10 (2020) 12.

[35] T.A. Ranathunge, D.G.G.P. Karunaratne, R.M.G. Rajapakse, D.L. Watkins, Doxorubicin loaded magnesium oxide nanoflakes as pH dependent carriers for simultaneous treatment of cancer and hypomagnesemia, Nanomaterials 9 (2019) 208, http://dx.doi.org/10.3390/nano9020208.

[36] Y. Meng, L. Chen, Y. Chen, J. Shi, Z. Zhang, Y. Wang, F. Wu, X. Jiang, W. Yang, L. Zhang, C. Wang, X. Meng, Y. Wu, W. Bu, Reactive metal boride nanoparticles trap lipopolysaccharide and peptidoglycan for bacteria-infected wound healing, Nature Commun. 13 (2022) 7353, http://dx.doi.org/10.1038/s41467-022-35050-6.

[37] S.K. Padhi, N. Baglieri, V. Bonino, A. Agostino, L. Operti, N.D. Batalu, M.C. Chifiriuc, M. Popa, M. Burdusel, M.A. Grigoroscuta, G.V. Aldica, D. Radu, P. Badica, M. Truccato, Antimicrobial activity of MgB$_2$ powders produced via reactive liquid infiltration method, Molecules 26 (2021) 4966, http://dx.doi.org/10.3390/molecules26164966.

[38] P. Badica, N.D. Batalu, M.C. Chifiriuc, M. Burdusel, M.A. Grigoroscuta, G. Aldica, I. Pasuk, A. Kuncser, M. Enculescu, M. Popa, L.G. Marutescu, I. Gheorghe, O. Thamer, C. Bleotu, G. Gradisteanu Pircalabioru, L. Operti, V. Bonino, A. Agostino, M. Truccato, MgB$_2$ powders and bioevaluation of their interaction with planktonic microbes, Biofilms, and Tumor Cells, J. Mater. Res. Technol. 12 (2021) 2168–2184, http://dx.doi.org/10.1016/j.jmrt.2021.04.003.

[39] P. Badica, N.D. Batalu, M. Burdusel, M.A. Grigoroscuta, G. Aldica, M. Enculescu, G. Gradisteanu Pircalabioru, M. Popa, L.G. Marutescu, B.G. Dumitriu, L. Olariu, A. Bicu, B. Purcareanu, L. Operti, V. Bonino, A. Agostino, M. Truccato, M.C. Chifiriuc, Antibacterial composite coatings of MgB$_2$ powders embedded in PVP matrix, Sci. Rep. 11 (2021) 9591, http://dx.doi.org/10.1038/s41598-021-88885-2.

[40] P. Badica, N.D. Batalu, M.C. Chifiriuc, M. Burdusel, M.A. Grigoroscuta, G.V. Aldica, I. Pasuk, A. Kuncser, M. Popa, A. Agostino, L. Operti, S.K. Padhi, V. Bonino, M. Truccato, Sintered and 3D-printed bulks of MgB$_2$-based materials with antimicrobial properties, Molecules 26 (2021) 6045, http://dx.doi.org/10.3390/molecules26196045.

[41] S.K. Das, K. Jasuja, Chemical exfoliation of layered magnesium diboride to yield functionalized nanosheets and nanoaccordions for potential flame retardant applications, ACS Appl. Nano Mater. 1 (2018) 1612–1622, http://dx.doi.org/10.1021/acsanm.8b00101.

[42] T. Prozorov, R. Prozorov, A. Snezhko, K.S. Suslick, Sonochemical modification of the superconducting properties of MgB$_2$, Appl. Phys. Lett. 83 (2003) 2019–2021, http://dx.doi.org/10.1063/1.1609248.

[43] A. Yousaf, M.S. Gilliam, S.L.Y. Chang, M. Augustin, Y. Guo, F. Tahir, M. Wang, A. Schwindt, X.S. Chu, D.O. Li, S. Kale, A. Debnath, Y. Liu, M.D. Green, E.J.G. Santos, A.A. Green, Q.H. Wang, Exfoliation of quasi-two-dimensional nanosheets of metal diborides, J. Phys. Chem. C 125 (2021) 6787–6799, http://dx.doi.org/10.1021/acs.jpcc.1c00394.

[44] S. Das, P. Sharma, Wavelength dependent photoionisation of ethanol clusters: Generation of hydrogen like C^{5+} ions at terawatt laser intensity, Phys. Chem. Chem. Phys. 24 (2022) 11979–11985, http://dx.doi.org/10.1039/D2CP00742H.

[45] M.-O. Mun, Y.J. Kim, Y. Park, J.H. Kim, S.H. Moon, H.N. Lee, H.G. Kim, B. Oh, Normal-state optical response functions of MgB2 superconductor, J. Supercond. 15 (2002) 475–477.

[46] Y. Fudamoto, S. Lee, Anisotropic electrodynamics of MgB$_2$ detected by optical reflectance, Phys. Rev. B. 68 (2003) 184514, http://dx.doi.org/10.1103/PhysRevB.68.184514.

[47] A.-G. Kussow, A. Akyurtlu, A. Semichaevsky, N. Angkawisittpan, MgB$_2$-based negative refraction index metamaterial at visible frequencies: Theoretical analysis, Phys. Rev. B. 76 (2007) 195123, http://dx.doi.org/10.1103/PhysRevB.76.195123.

[48] A. Balassis, E.V. Chulkov, P.M. Echenique, V.M. Silkin, First-principles calculations of dielectric and optical properties of MgB$_2$, Phys. Rev. B. 78 (2008) 224502, http://dx.doi.org/10.1103/PhysRevB.78.224502.

[49] A.B. Kuzmenko, Multiband and impurity effects in infrared and optical spectra of MgB$_2$, Phys. C Supercond. 456 (2007) 63–74, http://dx.doi.org/10.1016/j.physc.2007.02.008.

[50] D. Di Castro, M. Ortolani, E. Cappelluti, U. Schade, N.D. Zhigadlo, J. Karpinski, Infrared properties of Mg$_{1-x}$Al$_x$($B_{1-y}C_y$)$_2$ single crystals in the normal and superconducting state, Phys. Rev. B. 73 (2006) 174509, http://dx.doi.org/10.1103/PhysRevB.73.174509.

[51] T. Kakeshita, S. Lee, S. Tajima, Anisotropic drude response and the effect of anisotropic C substitution in Mg($B_{1-x}c_x$)$_2$, Phys. Rev. Lett. 97 (2006) 037002, http://dx.doi.org/10.1103/PhysRevLett.97.037002.

[52] Y.-S. Seo, J.H. Lee, W.N. Kang, J. Hwang, Revisiting optical properties of MgB$_2$ with a high-quality sample prepared by a HPCVD method, Sci. Rep. 7 (2017) 8977, http://dx.doi.org/10.1038/s41598-017-09248-4.

[53] B. Balasubramanian, T. Maruyama, Evidence of an enhanced interband absorption in Au nanoparticles: Size-dependent electronic structure and optical properties, Appl. Phys. Lett. 87 (2005) http://dx.doi.org/10.1063/1.2077834.

[54] H.S. Zhou, I. Honma, H. Komiyama, J.W. Haus, Controlled synthesis and quantum-size effect in gold-coated nanoparticles, Phys. Rev. B. 50 (1994) 12052–12056, http://dx.doi.org/10.1103/PhysRevB.50.12052.

[55] E. Baldini, A. Mann, L. Benfatto, E. Cappelluti, A. Acocella, V.M. Silkin, S.V. Eremeev, A.B. Kuzmenko, S. Borroni, T. Tan, X.X. Xi, F. Zerbetto, R. Merlin, F. Carbone, Real-time observation of phonon-mediated $\sigma - \pi$ interband scattering in MgB$_2$, Phys. Rev. Lett. 119 (2017) 097002, http://dx.doi.org/10.1103/PhysRevLett.119.097002.

[56] J.A. Alarco, A. Chou, P.C. Talbot, I.D.R. Mackinnon, Phonon modes of MgB$_2$: Super-lattice structures and spectral response, Phys. Chem. Chem. Phys. 16 (2014) 24443–24456, http://dx.doi.org/10.1039/C4CP03449J.

[57] K.-P. Bohnen, R. Heid, B. Renker, Phonon dispersion and electron-phonon coupling in MgB$_2$ and AlB$_2$, Phys. Rev. Lett. 86 (2001) 5771–5774, http://dx.doi.org/10.1103/PhysRevLett.86.5771.

[58] A. Bateni, E. Erdem, W. Häßler, M. Somer, High-quality MgB$_2$ nanocrystals synthesized by using modified amorphous nano-boron powders: Study of defect structures and superconductivity properties, AIP Adv. 9 (2019) 045018, http://dx.doi.org/10.1063/1.5089488.

[59] L. Hai-Wen, K. Kikuchi, T. Sato, Y. Nakamori, N. Ohba, M. Aoki, K. Miwa, S. Towata, O. Shin-ichi, Synthesis and hydrogen storage properties of a single-phase magnesium borohydride Mg(BH$_4$)$_2$, Mater. Trans. 49 (2008) 2224–2228, http://dx.doi.org/10.2320/matertrans.MA200807.

[60] A. Bateni, Novel approach for synthesis of magnesium borohydride, Mg(BH$_4$)$_2$, Energy Procedia 29 (2012) 26–33, http://dx.doi.org/10.1016/j.egypro.2012.09.005.

[61] L. Ginés, S. Mandal, Ashek-I-Ahmed, C.-L. Cheng, M. Sow, O.A. Williams, Positive zeta potential of nanodiamonds, Nanoscale 9 (2017) 12549–12555, http://dx.doi.org/10.1039/C7NR03200E.

Article

Limitations of Bulk Diamond Sensors for Single-Cell Thermometry

Andrea Alessio [1] , Ettore Bernardi [2,*] , Ekaterina Moreva [2] , Ivo Pietro Degiovanni [2] , Marco Genovese [2] and Marco Truccato [1]

1. Physics Department, University of Turin, Via P. Giuria 1, 10125 Turin, Italy
2. Istituto Nazionale di Ricerca Metrologica, Strada delle Cacce 91, 10135 Turin, Italy
*   Correspondence: e.bernardi@inrim.it

Abstract: The present paper reports on a Finite Element Method (FEM) analysis of the experimental situation corresponding to the measurement of the temperature variation in a single cell plated on bulk diamond by means of optical techniques. Starting from previous experimental results, we have determined—in a uniform power density approximation and under steady-state conditions—the total heat power that has to be dissipated by a single cell plated on a glassy substrate in order to induce the typical maximum temperature increase $\Delta T_{glass} = 1$ K. While keeping all of the other parameters constant, the glassy substrate has been replaced by a diamond plate. The FEM analysis shows that, in this case, the maximum temperature increase is expected at the diamond/cell interface and is as small as $\Delta T_{diam} = 4.6 \times 10^{-4}$ K. We have also calculated the typical decay time in the transient scenario, which resulted in $\tau \approx 250$ μs. By comparing these results with the state-of-the-art sensitivity values, we prove that the potential advantages of a longer coherence time, better spectral properties, and the use of special field alignments do not justify the use of diamond substrates in their bulk form.

Keywords: bio-sensing; diamond temperature sensors; finite element analysis

1. Introduction

Temperature plays a central role in cell metabolism. Temperature acts as a parameter, e.g., regulating the speed of ion channel opening [1], but, in turn, it is also affected by cell activity, e.g., mitochondrial activity induces intracellular temperature variations [2]. Furthermore, an increase in temperature is related to pathological conditions, such as cancerous cells [3], Parkinson's disease, and Alzheimer's diseases [4]. Considering this central role, temperature measurement at the intracellular scale gives an essential insight into understanding the cell's behavior both in normal and pathological conditions, with the perspective of improving the medical treatment of diseases.

From a theoretical point of view, there is still some debate about the presence of a general thermodynamical principle governing biological processes. In particular, the minimum entropy production principle is valid only in the linear response regime [5]. A recent idea, named dissipation-driven adaptation [6], has been proposed that considers far-from-equilibrium conditions, even if some criticisms have already been raised [7]. Measuring the temperature near the cellular organelles can shed light on this topic, giving information about the dissipation rate of specific metabolic processes.

In recent years, an increase in local temperature of up to a few Celsius degrees has been detected as a consequence of calcium stress [8] or of the use of drugs that increase the heat produced during cellular respiration [9–11]. The power needed to justify this temperature increase has been calculated to exceed by a few orders of magnitude what is expected from thermodynamic considerations [12–15]. A way to tackle this problem can be based on the simultaneous measurements of temperature at the intracellular level by using different methods to check for consistency of the different measurement results.

Several intracellular thermometry solutions are reported in the literature, ranging from fluorescent molecular thermometers [16] to quantum dots [17] to rare earth nanoparticles [18].

In particular, color centers in nanodiamonds have been widely used in the past few years for intracellular temperature measurements due to their significant advantages [19,20]. Nitrogen-Vacancy (NV) centers have been used in combination with Optically Detected Magnetic Resonance (ODMR); see [21,22] and the references therein. ODMR consists of the measurement, by optical means, of the resonance frequency of the electronic ground state of the NV centers [23]. Group IV defects in diamond [24], such as Silicon-Vacancy (SiV) [25,26], Germanium-Vacancy (GeV) [27], and Tin-Vacancy (SnV) [28], have been used [29] as thermometers, taking advantage of the temperature-dependent shift in their photoluminescence spectra. In the future, they might be used for intracellular measurement.

In general, nanodiamonds achieve nanometric resolution, are biocompatible [30,31], and can be functionalized [32]. A recent work [33] has experimentally proved, using SiV centers, that a nanoscale heat source leads to a significant temperature gradient at the submicrometric scale in an aqueous solution, whereas another very significant contribution has demonstrated the first measurement of temperature effects related to the synaptic activity at the intracellular level, using NV centers [34]. On the other hand, nanodiamonds present a short coherence time [35,36], considering ODMR measurements, and a degree of imperfection that limits spectral properties [37], which is detrimental for any measurement involving photoluminescence spectra. Concerning this last point, the use of diamond crystallites of micrometer size and with a high aspect ratio, called diamond microneedles, is interesting. Indeed, microneedles are enriched with color centers at the synthesis stage, leading to better structural and optical properties compared to nanodiamonds [38].

From the point of view of thermal measurements, both a nanodiamond and a diamond microneedle are much smaller than a cell. So, the temperature of the nanodiamond, or of the diamond microneedle, equilibrates to that of the cell, as demonstrated by Finite Element Analysis (see Supplementary Materials in Ref. [38]), leading to the possibility of sensing the temperature at the nanometric scale.

The possibility of using bulk diamonds instead of nanodiamonds would be interesting. Considering ODMR measurements on NV ensembles, nanodiamonds present a lower sensitivity compared to bulk diamonds, because of their shorter coherence time (as already mentioned), the lower density of their color centers, and the difficulty in taking advantage of the field alignment [39] and laser polarization [40]. On the contrary, a bulk diamond allows ODMR measurements with micrometric spatial resolution on the x-y plane using a focused laser beam and nanometric resolution along the z-direction using a diamond with a thin layer of NV centers [41]. Furthermore, a bulk diamond can be nanostructured to form an array of diamond nanopillars, leading to the possibility of guiding the growth of the cell network [42] and to further improvements in sensitivity due to the pillars acting as optical waveguides [43].

The main problems with measuring intracellular temperature using a bulk diamond are represented by its large mass compared to that of the cell and by its high thermal conductivity. As a result, the cell temperature equilibrates quickly on a short temporal and spatial scale to the bulk temperature, which acts similarly to a thermal bath. This implies, in general, a short acquisition time and a short distance from the cell in order to be able to measure a temperature signal inside the cell.

The aim of this paper is to model and quantify, by means of Finite Element Analysis, the temporal and spatial scale of a thermal signal produced by cellular processes for a cell adhered to a bulk diamond. We consider both the transient and stationary cases, discussing whether it is possible to measure a cellular temperature given the relevant spatio–temporal scale and the state-of-the-art sensitivities of diamond-based probes.

The paper is organized as follows: In the **Materials and Methods** section, the model used for Finite Element Analysis is described, and the thermal parameters for the different components of the model are presented. In the **Results** section, first, in a steady-state scenario, we estimate the total heat power dissipated P_{diss} by a cell adhered to a glass substrate, considering a temperature increase of $\Delta T_{glass} = 1$ K, which is typical of recent experiments [9,34]. Then, we calculate the temperature profiles induced by the same power

P_{diss} but for a cell adhered to a bulk diamond substrate. We calculate also the typical decay time in the transient scenario. In the **Discussion** section, we examine the possibility of measuring the calculated temperature profiles, considering the state-of-the-art experimental sensitivities. In the **Conclusions** section, we comment on the limitations of the proposed model, and we propose future works.

2. Materials and Methods

Finite Element Analysis

Finite Element Analysis is performed by means of the COMSOL Multiphysics software package, v 5.5 (COMSOL AB: Stockholm, Sweden). A 3D model with cylindrical symmetry is used (see Figures 1a and 2a) and is filled with a mesh of up to 274,525 triangular elements, with a minimum element size of 5 nm. A mesh sensitivity analysis has been carried out and reported in Figure S1 in Supplementary Material. Numerical simulations were carried out on a computer with 88 GB of RAM and two processors with a clock of 2.4 GHz, and the computation times did not exceed 5 min.
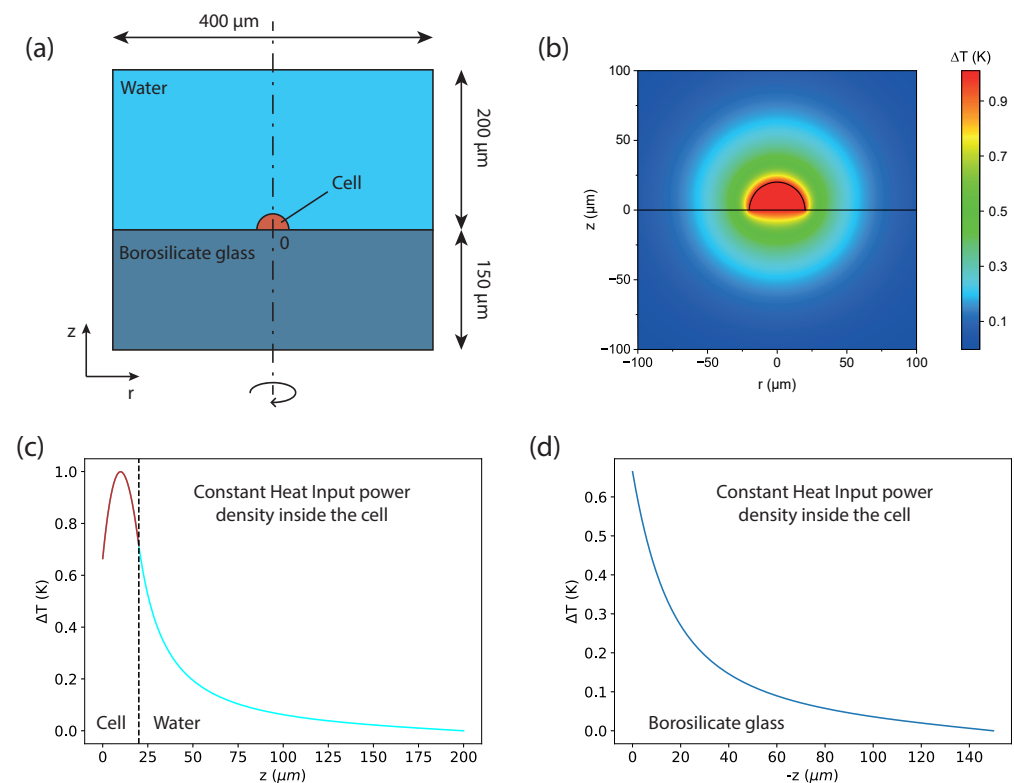

Figure 1. (**a**) Sketch of the model used for the cell–water–borosilicate experimental setup: (i) the cell, colored in orange, modeled as a hemisphere of 40 μm of diameter; (ii) the water environment, colored in blue, above the cell, modeled as a cylinder with a base of 400 μm and a height of 200 μm; and (iii) the borosilicate sample, colored in dark blue below the cell, modeled as a cylinder with a base of 400 μm and a height of 150 μm. The total dissipated heat power integrated over the whole cell is fixed at $P_{diss} = 1.04 \times 10^{-4}$ *W* and corresponds to a heat power density Q that is constant throughout the cell. The temperature of the boundaries is fixed at 310.15 K (37.00 °C). (**b**) Map of the temperature increase in the z-r plane. (**c**) Temperature increase profile along the positive z-axis, i.e., inside the cell and then in the water, and along negative z (**d**). In (**c**,**d**), the radial position is always $r = 0$ μm. All of the temperatures are represented in terms of their increase ΔT with respect to the temperature of the boundaries (37.00 °C).
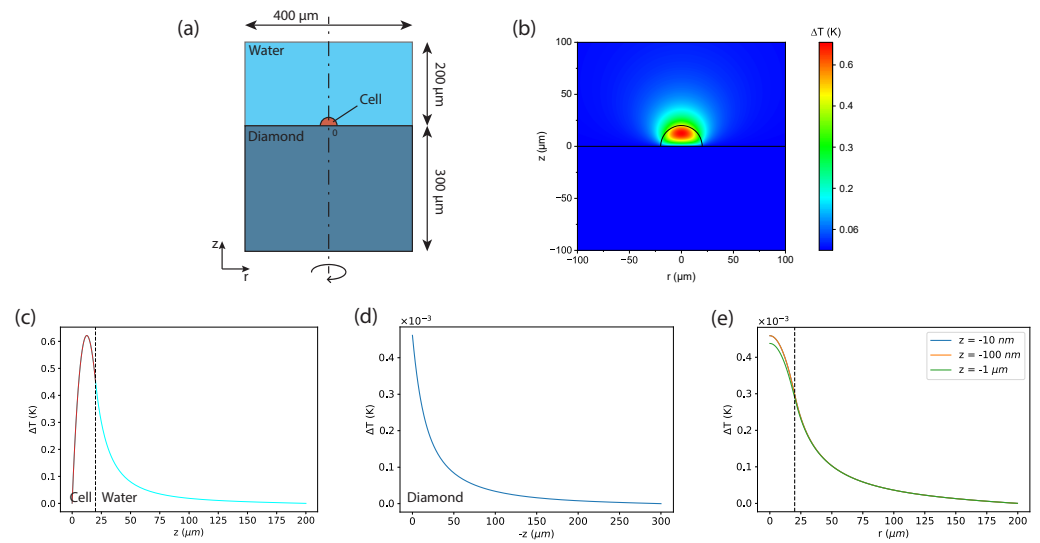
Figure 2. Results of the stationary scenario. (**a**) Sketch of the model using cell–water–diamond: (i) the cell, colored in orange, modeled as a hemisphere of 40 μm of diameter; (ii) the water environment, colored in blue, above the cell, modeled as a cylinder of a base of 400 μm and a height of 200 μm; and (iii) the bulk diamond sample, colored in light blue below the cell, modeled as a cylinder with a base of 400 μm and a height of 300 μm. The origin of the frame of reference is located at the center of the cell hemisphere. The total dissipated heat power integrated over the whole cell is fixed at $P_{diss} = 1.04 \times 10^{-4}$ W and corresponds to a heat power density Q that is constant throughout the cell. The temperature of the boundaries is fixed at 310.15 K (37.00 °C). (**b**) Map of the temperature increase in the z-r plane. (**c**) Temperature increase profile along the positive z-axis, i.e., inside the cell and then in the water, and along negative z (**d**), i.e., inside the diamond. (**c**,**d**) have different scales. In (**c**,**d**), the radial position is always $r = 0$ μm. (**e**) Spatial decay along r of the temperature increase for z = −0.01 μm, z = −0.1 μm, and z = −1 μm, i.e., at 3 different depths inside diamond. All of the panels show the temperature increase with respect that of the boundaries (37.00 °C).

For the stationary scenario, the classical time-independent heat equation is implemented [44]:

$$\nabla \cdot (-k \nabla T) = Q \tag{1}$$

Dirichlet boundary conditions are imposed by setting the temperature of the external surfaces of the model at the fixed value $T_{boundary} = 310.15$ K, i.e., 37.00 °C. The heat source Q is defined as a uniform power density generated by the cell. This power density is fine-tuned in order to have a maximum temperature inside the cell of 311.15 K, i.e., a maximum temperature difference of 1 K, when the cell is in contact with a borosilicate glass substrate, as it was experimentally observed in [34] (see Figure 1). A precision of 10^{-5} K is necessary for the specification of the boundary conditions due to the minimal temperature differences resulting from the simulations.

The very same power density is then inserted in the stationary simulation with a diamond substrate; see Figure 2.

For the time-dependent case (see Figure 3), the equation considered is [44]:

$$\rho c_p \frac{\partial T}{\partial t} + \nabla \cdot (-k \nabla T) = 0, \tag{2}$$

where the same boundary conditions have been imposed as for the stationary scenario, and the initial state at $t = 0$ has been set as the solution obtained from the stationary simulation.
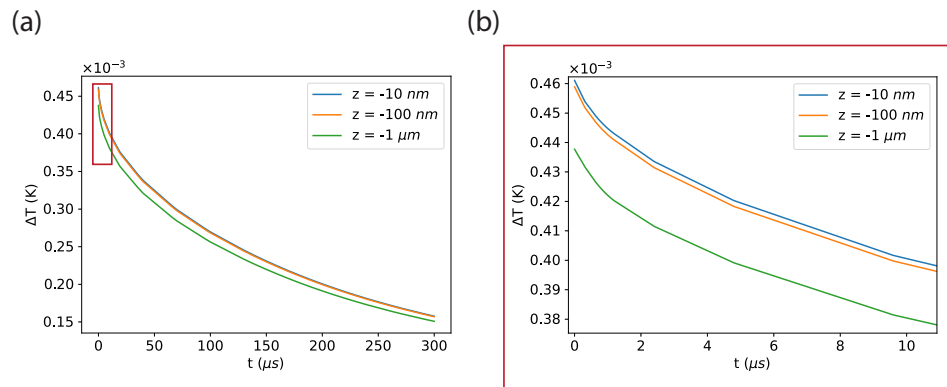
(a)

(b)

Figure 3. Results of the transient scenario for cell–water–diamond. This scenario starts, at $t = 0$, with the temperature increase calculated in the previous stationary scenario. The temperature increases inside the diamond are plotted as a function of time for the points (r = 0 μm, z = −0.01 μm), (r = 0 μm, z = −0.1 μm), and (r = 0 μm, z = −1 μm) for the first 300 μs (**a**) and for the first 10 μs (**b**).

The thermal parameters used for the different materials are reported in Table 1; we use the parameters reported in [45] for the cell and the ones present in the COMSOL [46] database for the other materials.

Table 1. Parameters used for the different materials in the model.

	k [W/(m·K)]	ρ [kg/m^3]	c_p[J/(kg·K)]
Diamond	2500	3515	516
Borosilicate glass	1.13	2230	754
Cell [45]	0.565	1050	3682
Water	0.62	994	4177

This time-dependent model has already been experimentally validated in previous studies [47], where the propagation of the heat deposited by a synchrotron X-ray nanobeam was investigated as a function of time, with a minimum time resolution of the order of one ps.

3. Results

As mentioned before, for glassy substrates the typical temperature difference ΔT_{glass}, measured inside cells, ranges in the order of magnitude of a few Kelvins, as reported for different phenomena ranging from thermogenesis due to a mitochondrial uncoupler [9] to temperature variations related to an increase in synaptic activity [34]. Indeed, it is important to underline that, in Ref. [34], the cell adhered to a Petri dish, whereas, in our model, we consider the cell to be adhered to a bulk diamond, which has a much higher heat conductivity with respect to the Petri dishes; therefore, a much smaller temperature difference ΔT_{diam} is expected in this case.

In order to estimate ΔT_{diam}, we first consider a cell adhered to a glass substrate surrounded by water (Figure 1a), and we calculate the dissipated heat power P_{diss} that causes a temperature difference $\Delta T_{glass} = 1$ K between the center of the cell and the boundaries of the glass substrate. Then, we consider a cell adhered to a bulk diamond surrounded by water (Figure 2a) in two different scenarios:

- The Stationary Scenario. In this scenario, the total heat power dissipated in the interior of the cell is the same value P_{diss} as for the glassy substrate. In this case, we study the stationary temperature distribution both along the radial direction and in the vertical direction z inside the diamond. In particular, we calculate the temperature difference ΔT_{diam} between the center of the cell and the diamond substrate. This study gives us

information about how close to the cell the sensor should be placed to measure the signal coming from a stationary phenomenon. Considering our recent results [34], we assume that the temporal duration of the phenomenon is 60 s.

- The Transient Scenario. In this scenario, at $t = 0$, we impose the same spatial distribution of the temperature difference as the one calculated in the stationary scenario, and keep the same boundary conditions at 310.15 K as well. In this case, it is essential to determine the behavior of the temperature as a function of time at a certain depth z in the bulk diamond. This study provides information on how fast and how close to the cell the measurement should be carried out to resolve a very fast change in the cell temperature.

We considered a 300 μm thick diamond; this value is typical of commercial diamond substrates, and it corresponds to the thickness of a substrate that we used in a previous experiment [39]. Regarding the shape and size of the cell, it must be considered that both vary according to the cell's function. The cell considered here has a hemispherical shape and is 40 μm in diameter because the eukaryotic cell size varies from 1 to 100 μm [48].

3.1. Estimation of the Total Dissipated Heat Power

The results regarding the estimation of the total dissipated heat power are represented in Figure 1. First, we considered the model in Figure 1a with the temperature of the glass and water fixed at 310.15 K (37.00 °C) and with a fixed dissipated heat power density Q inside the cell. We then varied Q until we obtained a maximum stationary temperature difference of $\Delta T_{glass} = 1$ K at the center of the cell. By using this procedure, we found a value of $P_{diss} = 1.04 \times 10^{-4}$ W after integration over the whole cell volume.

In all plots, we show the temperature increase with respect to the temperature of the boundaries. The temperature increase map is represented in Figure 1b, whereas the temperature increase profiles along the z-direction inside the cell/water and in the glass are represented in Figure 1c,d, respectively. The origin of the frame of reference is located at the center of the cell hemisphere. It can be noted that along the z-axis the temperature increase reaches a maximum at approximately 10 microns above the center of the cell and then decays on a spatial scale of a few tens of microns. Furthermore, the temperature increase at the cell–glass interface has already reduced by more than 0.3 K with respect to the value of its maximum (Figure 1c). The value of P_{diss} found with this procedure is much greater than the value of 10^{-8} W attributed to the power consumption of the cell [49]. This is in accord with what was discussed in [12,13] and has already been mentioned in the Introduction of this paper.

3.2. Stationary Scenario for Diamond

Figure 2 presents the results regarding the stationary scenario. Additionally, in these plots, we consider the temperature increase with respect to the temperature of the boundaries. We calculate the temperature maps (Figure 2b) and the corresponding profiles along the vertical z-direction inside the cell, in the water (Figure 2c), and in the diamond (Figure 2d). We also calculate the temperature increase profile along the radial direction r at different depth values, z, inside the diamond (Figure 2e). The origin of the frame of reference is located at the center of the cell hemisphere. The most interesting outcomes are the following:

- The maximum temperature increase between the center of the cell and the bulk diamond $\Delta T_{diam} = 0.63$ K is not so small compared to the one with the borosilicate $\Delta T_{glass} = 1$ K.
- The temperature difference steeply decreases from its maximum towards the interface with the diamond, passing from ΔT ($z = 20\,\mu m$) $= 0.6$ K to ΔT ($z = 0\,\mu m$) $= 4.6 \times 10^{-4}$ K. This means that more than 99.9% of the temperature increase ΔT_{diam} takes place inside the cell, which is out of the sensing region for sensors relying on bulk diamonds.

- The temperature difference between the cell/diamond interface and the boundaries is extremely small, about 4.6×10^{-4} K at most.

Further information can be gained by looking at the temperature profiles along the radial direction r. The temperature increase below the center of the cell and the boundaries is similar for the different depths, but, in all cases, it is extremely small, around 4.6×10^{-4} K. Moving away from the center of the cell, the temperature increase is reduced by a factor of two $r = 30\,\mu\text{m}$ and and by one order of magnitude at $r = 100\,\mu\text{m}$.

3.3. Transient Scenario

The results regarding the transient scenario are presented in Figure 3. This scenario starts at $t = 0$ with the spatial distribution of the temperature increase corresponding to the solution obtained from the stationary simulation. We calculate the temporal behavior of the temperature increases below the center of the cell for three depths: 0.01 μm, 0.1 μm, and 1 μm, for the first 300 μs (see Figure 3a). A zoom-in on the results corresponding to the first 10 microseconds is shown in Figure 3b. It can be noted that the temperature equilibrates to $\Delta T_{diam} = 0$ on a time scale of hundreds of μs for each depth.

However, for the shallowest points, this process starts from a slightly higher temperature, corresponding to $\Delta T_{diam} = 4.6 \times 10^{-4}$ K for z = −0.01 μm and z = −0.1 μm, whereas $\Delta T_{diam} = 4.4 \times 10^{-4}$ K for z = −1 μm.

4. Discussion

Let us now discuss the feasibility of a temperature measurement for the two scenarios presented in the Results section. The discussion will be divided into the following steps:

- Description of the experimental procedure.
- Estimation of the sensitivity.
- Comparison of the estimated sensitivity with state-of-the-art sensitivities.

For the **stationary scenario**, the experimental procedure requires measurement of the temperature difference between two points: the one just below the center of the cell and the other outside the cell. This measurement could be carried out by using a gradiometric setup, e.g., a gradiometer exploiting Optically Detected Magnetic Resonance that employs two laser excitation beams focused on the two selected points.

The fluorescence emerging from the two positions should be collected simultaneously. Then, the temperature difference between the two spots can be calculated from the difference between the two fluorescence signals. The sensitivity η, in general, can be expressed as $\eta = \sigma\sqrt{\tau}$ where σ is the minimum detectable signal and τ is the temporal width chosen for the measurement. In order to be able to measure a signal of the mean value $\hat{s}$, it is necessary that $\hat{s}$ is greater than σ, so the minimal required sensitivity is $\eta_{req} = \hat{s}\sqrt{\tau}$. Obviously, a smaller value for the sensitivity is preferable. Let us consider Figure 2e: We measure at one point below the center of the cell and simultaneously at a distance $r = 60\,\mu\text{m}$ from the center of the cell, choosing as a reference $z = -1\,\mu\text{m}$. This leads to a signal $\hat{s} = 3.6 \times 10^{-4}$ K. Then, we set $\tau = 60$ s, in agreement with Ref. [34], where an increase in the temperature of 1 K is detected after the stimulation of the cell with a drug increasing the synaptic activity. Hence, we need a sensitivity of $\eta_{req}(-1\,\mu\text{m}) = 2.8 \times 10^{-3} \frac{\text{K}}{\sqrt{\text{Hz}}}$. This value is two orders of magnitude smaller than the best sensitivity achieved in Petrini et al. (2020) [21], i.e., $\eta_{bio} = 0.35 \frac{\text{K}}{\sqrt{\text{Hz}}}$ for intracellular temperature measurement with a biocompatible optical power of 1 mW.

For the **transient scenario**, the procedure would consist first of the measurement of the temperature just below the center of the cell in the absence of the transient phenomenon, i.e., 310.15 K, and then of the measurement of the temperature at the same point in the presence of the transient phenomenon. The last step of the procedure would be the evaluation of the difference between the temperatures in the two previous cases. For the shallowest points at z = −0.01 μm and z = −0.1 μm, we can estimate $\hat{s} = 2.5 \times 10^{-4}$ K, considering the arithmetic mean of the temperature difference profiles in Figure 3 and $\tau = 300$ μs. This

corresponds to the required sensitivity of $\eta_{req}(-0.01\ \mu m) = 4.3 \times 10^{-6} \frac{K}{\sqrt{Hz}}$. For z = −1 μm, we can estimate $\hat{s} = 2.4 \times 10^{-4}$ K and $\tau = 300$ μs, corresponding to a required sensitivity of $\eta_{req}(-1\ \mu m) = 4.2 \times 10^{-6} \frac{K}{\sqrt{Hz}}$. These two values of sensitivity are very similar but, in this case as well, very far from the best sensitivity achieved in Ref. [21].

5. Conclusions

In summary, we have calculated the total dissipated heat power that creates a stationary increase of 1 K between the internal part of a cell and the surroundings, according to what was reported in a previous experiment, i.e., glass below the cell and water above. We then moved to another hypothetical environment composed of a diamond below the cell and water above. We used the calculated dissipated heat power to demonstrate that it is challenging to resolve both the transient phenomenon of a fast-changing temperature and the one where the temperature difference between the cell and the diamond is considered stationary.

It is worth mentioning that a related experimental study has been presented by Tanos et al. (2020) [50], where the focus was on the possibility of realizing wide-field thermal imaging with a bulk diamond, considering a two-dimensional heater that generates a fixed power. In their paper, the authors confirm, in the specific condition of their experiment, the general finding of our paper, i.e., that bulk diamonds cannot be exploited for sensing a local temperature increase because of their efficient thermalization properties. Specifically, we have focused our study on the relevant case of intracellular temperature measurements, whose expected experimental conditions are well known given our experimental results [34].

In our model, we have considered uniform heating inside the cell, but, from a biological point of view, it is more correct to consider a localized source of power dissipated in the correspondence of each mitochondrion, the organelle that generates most of the chemical energy needed by the cell. From this point of view, it would be interesting to extend the analysis conducted in the present paper by considering several sources of power dissipated in the interior of the cell, studying also the appearance of gradients inside the cell. Furthermore, in our model we consider a non-structured bulk diamond with a size of hundreds of micrometers, but nanostructured diamonds would probably perform better as temperature sensors. It is possible to fabricate single crystal diamond membranes with thickness values around 100 nanometers [51]: in this case, the smaller mass of the membrane and the reduced diamond cross-section area that are available for heat transfer out of the cell region should lead to a greater temperature difference between membrane regions beneath the cell and far away from it, even for the dissipated heat power treated in this paper. The arrays of diamond nanopillars should also show similar advantages compared to those of bulk diamonds: the reduced cross-section area of the pillars should limit the heat flux across the pillar bases towards the bulk diamond, leading to a smaller temperature difference between the cell and the location of the NV centers.

Author Contributions: Conceptualization, E.B., M.T., E.M., I.P.D., and M.G. (leading the quantum optics group); simulations, A.A. and M.T.; formal analysis, E.B., A.A., and M.T.; writing—original draft preparation, E.B., M.T., E.M., I.P.D., M.G., and A.A.; writing—review and editing, E.B., M.T., E.M., I.P.D., M.G., and A.A.; visualization, A.A.; supervision, M.T. and M.G. All authors have read and agreed to the published version of the manuscript.

References

1. Hille, B. Ionic channels in excitable membranes. Current problems and biophysical approaches. *Biophys. J.* **1978**, *22*, 283–294. [CrossRef] [PubMed]
2. De Meis, L.; Ketzer, L.A.; Da Costa, R.M.; De Andrade, I.R.; Benchimol, M. Fusion of the endoplasmic reticulum and mitochondrial outer membrane in rats brown adipose tissue: Activation of thermogenesis by Ca^{2+}. *PLoS ONE* **2010**, *5*, e9439. [CrossRef] [PubMed]
3. Monti, M.; Brandt, L.; Ikomi-Kumm, J.; Olsson, H. Microcalorimetric investigation of cell metabolism in tumour cells from patients with non-Hodgkin lymphoma (NHL). *Scand. J. Haematol.* **1986**, *36*, 353–357. [CrossRef] [PubMed]
4. Ghavami, M.; Rezaei, M.; Ejtehadi, R.; Lotfi, M.; Shokrgozar, M.A.; Abd Emamy, B.; Raush, J.; Mahmoudi, M. Physiological temperature has a crucial role in amyloid beta in the absence and presence of hydrophobic and hydrophilic nanoparticles. *ACS Chem. Neurosci.* **2013**, *4*, 375–378. [CrossRef] [PubMed]
5. Prigogine, I.; Nicolis, G. Biological order, structure and instabilities1. *Q. Rev. Biophys.* **1971**, *4*, 107–148. [CrossRef] [PubMed]
6. England, J.L. Statistical physics of self-replication. *J. Chem. Phys.* **2013**, *139*, 09B623. [CrossRef] [PubMed]
7. Baiesi, M.; Maes, C. Life efficiency does not always increase with the dissipation rate. *J. Phys. Commun.* **2018**, *2*, 045017. [CrossRef]
8. Yang, J.M.; Yang, H.; Lin, L. Quantum dot nano thermometers reveal heterogeneous local thermogenesis in living cells. *ACS Nano* **2011**, *5*, 5067–5071. [CrossRef]
9. Fujiwara, M.; Sun, S.; Dohms, A.; Nishimura, Y.; Suto, K.; Takezawa, Y.; Oshimi, K.; Zhao, L.; Sadzak, N.; Umehara, Y.; et al. Real-time nanodiamond thermometry probing in vivo thermogenic responses. *Sci. Adv.* **2020**, *6*, eaba9636. [CrossRef]
10. Kiyonaka, S.; Kajimoto, T.; Sakaguchi, R.; Shinmi, D.; Omatsu-Kanbe, M.; Matsuura, H.; Imamura, H.; Yoshizaki, T.; Hamachi, I.; Morii, T.; et al. Genetically encoded fluorescent thermosensors visualize subcellular thermoregulation in living cells. *Nat. Methods* **2013**, *10*, 1232–1238. [CrossRef]
11. Chrétien, D.; Bénit, P.; Ha, H.H.; Keipert, S.; El-Khoury, R.; Chang, Y.T.; Jastroch, M.; Jacobs, H.T.; Rustin, P.; Rak, M. Mitochondria are physiologically maintained at close to 50 C. *PLoS Biol.* **2018**, *16*, e2003992. [CrossRef] [PubMed]
12. Baffou, G.; Rigneault, H.; Marguet, D.; Jullien, L. A critique of methods for temperature imaging in single cells. *Nat. Methods* **2014**, *11*, 899–901. [CrossRef] [PubMed]
13. Macherel, D.; Haraux, F.; Guillou, H.; Bourgeois, O. The conundrum of hot mitochondria. *Biochim. Biophys. Acta (BBA)-Bioenerg.* **2021**, *1862*, 148348. [CrossRef] [PubMed]
14. Suzuki, M.; Plakhotnik, T. The challenge of intracellular temperature. *Biophys. Rev.* **2020**, *12*, 593–600. [CrossRef] [PubMed]
15. Sotoma, S.; Zhong, C.; Kah, J.C.Y.; Yamashita, H.; Plakhotnik, T.; Harada, Y.; Suzuki, M. In situ measurements of intracellular thermal conductivity using heater-thermometer hybrid diamond nanosensors. *Sci. Adv.* **2021**, *7*, eabd7888. [CrossRef] [PubMed]
16. Okabe, K.; Sakaguchi, R.; Shi, B.; Kiyonaka, S. Intracellular thermometry with fluorescent sensors for thermal biology. *Pflügers Arch.-Eur. J. Physiol.* **2018**, *470*, 717–731. [CrossRef] [PubMed]
17. Li, M.; Chen, T.; Gooding, J.J.; Liu, J. Review of carbon and graphene quantum dots for sensing. *ACS Sens.* **2019**, *4*, 1732–1748. [CrossRef] [PubMed]
18. Vetrone, F.; Naccache, R.; Zamarrón, A.; Juarranz de la Fuente, A.; Sanz-Rodríguez, F.; Martinez Maestro, L.; Martin Rodriguez, E.; Jaque, D.; Garcia Sole, J.; Capobianco, J.A. Temperature sensing using fluorescent nanothermometers. *ACS Nano* **2010**, *4*, 3254–3258. [CrossRef]
19. Kucsko, G.; Maurer, P.C.; Yao, N.Y.; Kubo, M.; Noh, H.J.; Lo, P.K.; Park, H.; Lukin, M.D. Nanometre-scale thermometry in a living cell. *Nature* **2013**, *500*, 54–58. [CrossRef]
20. Fujiwara, M.; Shikano, Y. Diamond quantum thermometry: From foundations to applications. *Nanotechnology* **2021**, *32*, 482002. [CrossRef]
21. Petrini, G.; Moreva, E.; Bernardi, E.; Traina, P.; Tomagra, G.; Carabelli, V.; Degiovanni, I.P.; Genovese, M. Is a quantum biosensing revolution approaching? Perspectives in NV-assisted current and thermal biosensing in living cells. *Adv. Quantum Technol.* **2020**, *3*, 2000066. [CrossRef]
22. Wu, Y.; Weil, T. Recent developments of nanodiamond quantum sensors for biological applications. *Adv. Sci.* **2022**, *9*, e2200059. [CrossRef] [PubMed]

23. Gruber, A.; Drabenstedt, A.; Tietz, C.; Fleury, L.; Wrachtrup, J.; Borczyskowski, C.v. Scanning confocal optical microscopy and magnetic resonance on single defect centers. *Science* **1997**, *276*, 2012–2014. [CrossRef]

24. Bradac, C.; Gao, W.; Forneris, J.; Trusheim, M.E.; Aharonovich, I. Quantum nanophotonics with group IV defects in diamond. *Nat. Commun.* **2019**, *10*, 5625. [CrossRef] [PubMed]

25. Choi, S.; Agafonov, V.N.; Davydov, V.A.; Plakhotnik, T. Ultrasensitive all-optical thermometry using nanodiamonds with a high concentration of silicon-vacancy centers and multiparametric data analysis. *ACS Photonics* **2019**, *6*, 1387–1392. [CrossRef]

26. Nguyen, C.T.; Evans, R.E.; Sipahigil, A.; Bhaskar, M.K.; Sukachev, D.D.; Agafonov, V.N.; Davydov, V.A.; Kulikova, L.F.; Jelezko, F.; Lukin, M.D. All-optical nanoscale thermometry with silicon-vacancy centers in diamond. *Appl. Phys. Lett.* **2018**, *112*, 203102. [CrossRef]

27. Fan, J.W.; Cojocaru, I.; Becker, J.; Fedotov, I.V.; Alkahtani, M.H.A.; Alajlan, A.; Blakley, S.; Rezaee, M.; Lyamkina, A.; Palyanov, Y.N.; et al. Germanium-vacancy color center in diamond as a temperature sensor. *ACS Photonics* **2018**, *5*, 765–770. [CrossRef]

28. Alkahtani, M.; Cojocaru, I.; Liu, X.; Herzig, T.; Meijer, J.; Küpper, J.; Lühmann, T.; Akimov, A.V.; Hemmer, P.R. Tin-vacancy in diamonds for luminescent thermometry. *Appl. Phys. Lett.* **2018**, *112*, 241902. [CrossRef]

29. Bradac, C.; Lim, S.F.; Chang, H.C.; Aharonovich, I. Optical nanoscale thermometry: From fundamental mechanisms to emerging practical applications. *Adv. Opt. Mater.* **2020**, *8*, 2000183. [CrossRef]

30. Guarina, L.; Calorio, C.; Gavello, D.; Moreva, E.; Traina, P.; Battiato, A.; Ditalia Tchernij, S.; Forneris, J.; Gai, M.; Picollo, F.; et al. Nanodiamonds-induced effects on neuronal firing of mouse hippocampal microcircuits. *Sci. Rep.* **2018**, *8*, 2221. [CrossRef]

31. Troise, L.; Hansen, N.W.; Olsson, C.; Webb, J.L.; Tomasevic, L.; Achard, J.; Brinza, O.; Staacke, R.; Kieschnick, M.; Meijer, J.; et al. In vitro recording of muscle activity induced by high intensity laser optogenetic stimulation using a diamond quantum biosensor. *AVS Quantum Sci.* **2022**, *4*, 044402. [CrossRef]

32. Jariwala, D.H.; Patel, D.; Wairkar, S. Surface functionalization of nanodiamonds for biomedical applications. *Mater. Sci. Eng. C* **2020**, *113*, 110996. [CrossRef] [PubMed]

33. Romshin, A.M.; Zeeb, V.; Martyanov, A.K.; Kudryavtsev, O.S.; Pasternak, D.G.; Sedov, V.S.; Ralchenko, V.G.; Sinogeykin, A.G.; Vlasov, I.I. A new approach to precise mapping of local temperature fields in submicrometer aqueous volumes. *Sci. Rep.* **2021**, *11*, 14228. [CrossRef]

34. Petrini, G.; Tomagra, G.; Bernardi, E.; Moreva, E.; Traina, P.; Marcantoni, A.; Picollo, F.; Kvaková, K.; Cígler, P.; Degiovanni, I.P.; et al. Nanodiamond–Quantum Sensors Reveal Temperature Variation Associated to Hippocampal Neurons Firing. *Adv. Sci.* **2022**, *9*, 2202014. [CrossRef] [PubMed]

35. Tisler, J.; Balasubramanian, G.; Naydenov, B.; Kolesov, R.; Grotz, B.; Reuter, R.; Boudou, J.P.; Curmi, P.A.; Sennour, M.; Thorel, A.; et al. Fluorescence and spin properties of defects in single digit nanodiamonds. *ACS Nano* **2009**, *3*, 1959–1965. [CrossRef] [PubMed]

36. Naydenov, B.; Dolde, F.; Hall, L.T.; Shin, C.; Fedder, H.; Hollenberg, L.C.; Jelezko, F.; Wrachtrup, J. Dynamical decoupling of a single-electron spin at room temperature. *Phys. Rev. B* **2011**, *83*, 081201. [CrossRef]

37. Lindner, S.; Bommer, A.; Muzha, A.; Krueger, A.; Gines, L.; Mandal, S.; Williams, O.; Londero, E.; Gali, A.; Becher, C. Strongly inhomogeneous distribution of spectral properties of silicon-vacancy color centers in nanodiamonds. *New J. Phys.* **2018**, *20*, 115002. [CrossRef]

38. Golubewa, L.; Padrez, Y.; Malykhin, S.; Kulahava, T.; Shamova, E.; Timoshchenko, I.; Franckevicius, M.; Selskis, A.; Karpicz, R.; Obraztsov, A.; et al. All-Optical Thermometry with NV and SiV Color Centers in Biocompatible Diamond Microneedles. *Adv. Opt. Mater.* **2022**, *10*, 2200631. [CrossRef]

39. Moreva, E.; Bernardi, E.; Traina, P.; Sosso, A.; Tchernij, S.D.; Forneris, J.; Picollo, F.; Brida, G.; Pastuović, Ž.; Degiovanni, I.; et al. Practical applications of quantum sensing: A simple method to enhance the sensitivity of nitrogen-vacancy-based temperature sensors. *Phys. Rev. Appl.* **2020**, *13*, 054057. [CrossRef]

40. Magaletti, S.; Mayer, L.; Le, X.P.; Debuisschert, T. Magnetic sensitivity enhancement via polarimetric excitation and detection of an ensemble of NV centers. *arXiv* **2023**, arXiv:2301.12758.

41. Bernardi, E.; Moreva, E.; Traina, P.; Petrini, G.; Tchernij, S.D.; Forneris, J.; Pastuović, Ž.; Degiovanni, I.P.; Olivero, P.; Genovese, M. A biocompatible technique for magnetic field sensing at (sub) cellular scale using Nitrogen-Vacancy centers. *EPJ Quantum Technol.* **2020**, *7*, 13. [CrossRef]

42. Losero, E.; Jagannath, S.; Pezzoli, M.; Goblot, V.; Babashah, H.; Lashuel, H.A.; Galland, C.; Quack, N. Neuronal growth on high-aspect-ratio diamond nanopillar arrays for biosensing applications. *Sci. Rep.* **2023**, *13*, 5909. [CrossRef] [PubMed]

43. McCloskey, D.J.; Dontschuk, N.; Broadway, D.A.; Nadarajah, A.; Stacey, A.; Tetienne, J.P.; Hollenberg, L.C.; Prawer, S.; Simpson, D.A. Enhanced widefield quantum sensing with nitrogen-vacancy ensembles using diamond nanopillar arrays. *ACS Appl. Mater. Interfaces* **2020**, *12*, 13421–13427. [CrossRef] [PubMed]

44. Incropera, F.P.; DeWitt, D.P.; Bergman, T.L.; Lavine, A.S. *Fundamentals of Heat and Mass Transfer*; Wiley: New York, NY, USA, 1996; Volume 6.

45. Mcintosh, R.L.; Anderson, V. A comprehensive tissue properties database provided for the thermal assessment of a human at rest. *Biophys. Rev. Lett.* **2010**, *5*, 129–151. [CrossRef]

46. *COMSOL Multiphysics* ®, version 5.5; COMSOL AB: Stockholm, Sweden, 2019. Available online: www.comsol.com (accessed on 1 September 2023).

47. Bonino, V.; Torsello, D.; Prestipino, C.; Mino, L.; Truccato, M. Time and space resolved modelling of the heating induced by synchrotron X-ray nanobeams. *J. Synchrotron Radiat.* **2020**, *27*, 1662–1673. [CrossRef] [PubMed]
48. Mason, K.A.; Losos, J.B.; Singer, S.R.; Raven, P.H.; Johnson, G.B. *Biology*; McGraw-Hill Education: New York, NY, USA, 2017.
49. Loesberg, C.; van Miltenburg, J.; van Wuk, R. Heat production of mammalian cells at different cell-cycle phases. *J. Therm. Biol.* **1982**, *7*, 209–213. [CrossRef]
50. Tanos, R.; Akhtar, W.; Monneret, S.; Favaro de Oliveira, F.; Seniutinas, G.; Munsch, M.; Maletinsky, P.; Le Gratiet, L.; Sagnes, I.; Dréau, A.; et al. Optimal architecture for diamond-based wide-field thermal imaging. *AIP Adv.* **2020**, *10*, 025027. [CrossRef]
51. Fairchild, B.A.; Olivero, P.; Rubanov, S.; Greentree, A.D.; Waldermann, F.; Taylor, R.A.; Walmsley, I.; Smith, J.M.; Huntington, S.; Gibson, B.C.; et al. Fabrication of ultrathin single-crystal diamond membranes. *Adv. Mater.* **2008**, *20*, 4793–4798. [CrossRef]
52. Fraczek, E.; Savitski, V.G.; Dale, M.; Breeze, B.G.; Diggle, P.; Markham, M.; Bennett, A.; Dhillon, H.; Newton, M.E.; Kemp, A.J. Laser spectroscopy of NV-and NV0 colour centres in synthetic diamond. *Opt. Mater. Express* **2017**, *7*, 2571–2585. [CrossRef]

Check for updates

Improving the control of the electroforming process in oxide-based memristive devices by X-ray nanopatterning†

Lorenzo Mino, [iD] *[a] Valentina Bonino, [iD] [b] Andrea Alessio,[c] Federico Picollo, [iD] [c] Andrei Kuncser,[d] Ionel Mercioniu,[d] Aurel-Mihai Vlaicu,[d] Petre Badica,[d] Rosaria Brescia, [iD] [e] Matteo Fretto,[f] Kalle Goss, [iD] [g] Regina Dittmann [iD] [g] and Marco Truccato [iD] [c]

We explored the possibility to guide the forming process in a Ta/TiO$_2$/Pt memristive device using an X-ray nanopatterning procedure, which enables the manipulation of the oxygen content at the nanoscale. The irradiation of selected areas of the sample by a 65×58 nm^2 synchrotron X-ray nanobeam locally generated oxygen vacancies which resulted in the formation of a conductive filament in the desired position in the material. The subsequent application of an electric field between the electrodes was exploited to achieve reversible bipolar resistive switching. A multitechnique characterization was then performed, highlighting a local increase in the height of the crystal and the formation of a dislocation network, associated with the presence of Wadsley defects. Our results show that X-ray nanopatterning could open new avenues for a more deterministic implementation of electroforming in oxide-based memristive devices.

^{a} Department of Chemistry, Interdepartmental Centre NIS, University of Torino, via P. Giuria 7, Torino, Italy, 10125, Italy. E-mail: lorenzo.mino@unito.it

^{b} European Synchrotron Radiation Facility (ESRF), 71 Avenue des Martyrs, BP 220, 38043 Grenoble Cedex 9, France

^{c} Department of Physics, University of Torino, Interdepartmental Centre NIS, via P. Giuria 1, Torino, Italy, 10125, Italy

^{d} National Institute of Materials Physics, Street Atomistilor 405A, Magurele, Ilfov, 077125, Romania

^{e} Electron Microscopy Facility, Italian Institute of Technology (IIT), Via Morego 30, Genova, 16163, Italy

^{f} Istituto Nazionale di Ricerca Metrologica (INRiM), Strada delle Cacce 91, 10135, Torino, Italy

^{g} Peter Gruenberg Institute – Electronic Materials (PGI-7), Forschungszentrum Juelich GmbH and JARA-FIT, 52425 Juelich, Germany

† Electronic supplementary information (ESI) available. See DOI: https://doi.org/10.1039/d4tc01815j

1. Introduction

Over the last five decades, the race for chip miniaturization has led to faster, smaller and cheaper electronics, as predicted by Moore's law. The scaling down of integrated circuits was possible, thanks to the progress in lithographic techniques.[1,2] In conventional processes, the desired pattern should be defined on a photoresist, which is irradiated, using a suitable mask, to induce some difference in the chemical resistance to the developing solution. Then, the pattern defined in the organic material must be transferred to the underlying electronically active material by the etching process.[1] The ability to project a clear image of a small feature onto the target material is limited by the wavelength of the light that is used, according to Rayleigh's criterion, requiring a progressive increase of the photon energy to improve the resolution.[2] To push these limits, also the use of X-ray lithography has been explored; however, problems in the fabrication of suitable masks, in mask-wafer positioning, and related to diffraction effects have hindered its development.[3–5] In this context, our group has developed an alternative approach, namely X-ray nanopatterning (XNP),[6] which is a maskless process employing high brilliance synchrotron X-ray nanobeams to directly modify the properties, inducing the formation of crystal defects, in selected areas of the material. The XNP method has been initially applied to induce oxygen vacancies (V$_O$) in superconducting oxides with loosely bound oxygen atoms and further to fabricate Josephson devices without etching the material.[6–8] Then, the process was extended to oxides with tightly bound oxygen atoms, like TiO$_2$, where the creation of X-ray-induced V$_O$ led to a local increase of the material electrical conductivity.[9,10]

The possibility to manipulate the oxygen content at the nanoscale by XNP could be extremely interesting for the fabrication of oxide-based electronic devices, such as memristors. Memristive devices, which can retain a state of internal resistance based on the history of applied voltage and current, are attracting increasing interest for several applications ranging from non-volatile memories to neuromorphic computing.[11–15] Memristors

are typically fabricated by inserting a metal oxide (*e.g.* TiO_2, $SrTiO_3$, HfO_2) between two metal electrodes and then inducing a reversible change of its electrical properties.[16] The switch between a high resistance state (HRS) and a low resistance state (LRS) is usually achieved by applying proper voltage pulses to induce the migration of V_O, thus promoting the formation or rupture of conductive filaments between the two metal electrodes.[17,18] One of the main issues hindering the large-scale applications of these devices is the initial electroforming step to create the V_O filament in the metal oxide, which has a stochastic nature, resulting in significant device-to-device variations.[19] The microscopic reason for this behaviour has been ascribed to the nonregular shape of the filaments and the variable concentration of V_O associated to the competitive growth of multiple prefilaments during the forming process.[20,21] Our idea is to exploit the ability of XNP to locally generate V_O to guide the initial electroforming step, "drawing" conductive filaments in precise positions of the samples, and then apply suitable voltage pulses to achieve reversible switching from a HRS to a LRS.

2. Materials and methods

2.1. TiO_2 annealing and patterning

$TiO_2(110)$ rutile single crystals ($10 \times 10 \times 0.5$ mm^3), one side polished, were purchased from CRYSTAL GmbH. The devices were fabricated by depositing two metal electrodes on the (110) single crystal surface previously annealed at 300 °C in a H_2/Ar (4%) atmosphere for 2 hours. This annealing step is performed to increase the concentration of oxygen vacancies in TiO_2 and, therefore, to increase the sample conductivity. The contact geometry is shown in Fig. 1A. One electrode is made of Ta (60 nm in thickness), while the other one is made by depositing 110 nm of Au on top of 10 nm of Pt. This configuration provides the asymmetry generally needed to observe bipolar resistive switching.

2.2. Electrical measurements

For online monitoring, the samples were mounted onto a sample holder compatible with the nanobeam experimental setup and connected with a two-terminal configuration to its

Fig. 1 (A) Schematic layout of the metal contacts deposited on the TiO_2 rutile single crystal to perform electrical characterizations. The dotted red line highlights the part of the sample that has been irradiated using the X-ray nanobeam. (B) Photograph of the experimental setup employed at the ESRF ID16B beamline showing the alignment optical microscope, the XRF detector and the sample mounted on the sample holder used for online electrical characterization.

contact pads by means of Ag wires 50 μm in diameter. The sample holder was interfaced through coaxial cables to a Keithley 6487 picoammeter/voltage source with high input impedance (10^{11} Ω) and good current resolution (10 fA) with high accuracy (0.3%). The acquisition was controlled by a computer *via* a GPIB employing a software program developed with LabVIEW. To acquire cyclic current–voltage characteristics, the sampling rate was set to 250 ms.

2.3. X-ray nanobeam irradiation

X-ray irradiation was performed at the long-canted beamline ID16B-NA of the European Synchrotron Radiation Facility (ESRF) in Grenoble, France. The primary beamline optics are located next to the in-vacuum undulator source to preserve the coherence of the beam, while the Kirkpatrick–Baez mirrors, which act as focusing optics, are placed very close to the sample position (165 m far from the undulator source) to obtain a higher degree of demagnification. The experimental setup (Fig. 1B) includes an optical microscope to visualize the region of interest in the sample, a piezo positioning stage to raster-scan it under the X-ray nanoprobe and an energy dispersive Si drift detector to acquire the XRF signals.

We operated in the pink beam mode without a double crystal monochromator ($\Delta E/E \approx 10^{-2}$) to obtain a higher photon flux at the sample position. The X-ray nanopatterning procedure was performed at 17.5 keV with beam sizes at the focal plane of 65×58 nm^2 (vertical × horizontal), as evaluated by the knife-edge scan method. The photon flux on the sample was 1.7×10^{11} ph s^{-1}. The XRF maps were collected with a counting time of 0.1 s per point using a 2 mm Si filter to avoid sample modifications.

2.4. Conductive atomic force microscopy

AFM and C-AFM maps were obtained using a Cypher S AFM from Asylum Research (Oxford Instruments Group) equipped with a dual gain ORCA cantilever holder. The two gains of the current amplifier of the cantilever holder were, respectively, 1 nA V^{-1} and 1 μA V^{-1}. For conductive AFM measurements, an HQ:CSC17/AL-BS tip (n-type silicon) from μMasch was employed. During the acquisition of the C-AFM maps, the tip was grounded through the current amplifier and the sample was biased at 6 V through a 50 μm Ag wire connected to the Au electrode.

2.5. Scanning electron microscopy

SEM images were acquired using an Inspect F^{TM} electron microscope with a field emission gun (FEG) from FEI Company. Accelerating voltages from 5 to 30 kV were used.

2.6. Transmission electron microscopy

TEM investigations were performed using a Tecnai F20 (Thermo Fisher Scientific Inc.), operated at 200 kV, with a TWIN objective lens (for the pristine sample) and a JEOL 2100 (JEOL, Ltd) instrument, operated at 200 kV, equipped with a high-resolution polepiece (for the irradiated sample). The TEM lamellas were extracted by the SEM-FIB technique using a TESCAN model LYRA 3 XMU instrument after coating the samples with a Pt conductive layer.
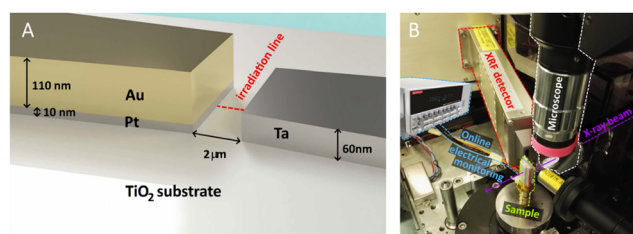
3. Results and discussion

The devices under investigation were based on annealed TiO_2 rutile single crystals with two series of electrical contacts (see Fig. 1A and the Experimental section): the first electrode, based on Ta, is expected to form an ohmic contact, while the second electrode, realized with Pt covered by Au, should give rise to a Schottky barrier. The gap between each couple of electrodes was 2 μm: this region was modified using the X-ray nanobeam to achieve the device resistive switching. The Ta/TiO$_2$/Pt devices were mounted on a customized sample holder to perform *in situ* two-probe electrical measurement in the ESRF ID16B-NA nanobeam setup (Fig. 1B) to study the variations in the electrical conductivity of the sample after X-ray irradiation. After a preliminary alignment using an optical microscope (Fig. 1B), the region of interest in the sample was precisely located by X-ray fluorescence (XRF) maps.

In the first step of our experiment, we ''wrote'' a single irradiation line connecting the Ta and Pt electrodes using the X-ray nanobeam with a step of 200 nm and an irradiation time of 25 s per point, resulting in a fluence of 9.9×10^{11} J m^{-2}. Then, we investigated the effect of the X-ray exposure by using atomic force microscopy (AFM) without performing any preliminary electrical characterization (*i.e.* no electrical bias has been applied to the device before the AFM measurements). The topographic map (Fig. 2A) shows a minimal local variation (<2 nm) in the height of the crystal induced by the exposure to the synchrotron nanobeam. On the other hand, the conductive atomic force microscopy (C-AFM) map (Fig. 2B) highlights the presence of a superficial conductive channel in the irradiated region. This behavior can be ascribed to the formation of oxygen vacancies in the TiO_2 lattice, induced by the X-ray nanobeam. Indeed, the absorption of hard X-ray photons triggers the generation of photoelectrons, followed by de-excitation processes in the fs timescale which give rise to the production of fluorescence radiation and Auger electrons.[22,23] The secondary and Auger electrons, while travelling in the oxide, produce electron–hole couples that can be responsible for knock-on and bond breaking processes.[24–26] These phenomena have been previously studied by Monte Carlo simulations for superconducting oxides,[26] showing that the secondary electrons can modify the sample properties for hundreds of nanometers around the X-ray nanobeam impact point, thus influencing the best spatial resolution that can be achieved in the X-ray nanopatterning process. Finally, at

very high photon fluxes, as in our experiment, the scarcity of conduction electrons in insulating samples can slow down the restoration of the local electrical neutrality, inducing Coulomb repulsion between positive charges and subsequent ion ejection.[24,27,28] All these phenomena can induce bond breaking, favouring the generation of point defects, essentially V$_O$, which behave as n-dopants enhancing the local TiO_2 conductivity.[29,30] Conversely, local heating effects by the X-ray nanobeam, which were proven to be potentially relevant in modifying the oxygen content in superconducting oxides,[8,31,32] are expected to be negligible for the TiO_2 crystal.

We moved then to investigate the effect of applying a voltage after realizing the irradiation line connecting the Ta and Pt metal contacts. Fig. 3A shows that, in a pristine sample, applying a voltage in the −30 V to 30 V range does not induce significant changes in the electrical properties (curve 1). Conversely, after X-ray nanobeam exposure, we observe a forming process (curve 2) which brings the sample to a LRS and then back to a HRS in the negative voltage range. Fig. 3B and C show the SET and RESET processes, typical of bipolar resistive switching.[33] More *I–V* curves after multiple ON–OFF cycles, which show the reproducibility of the HRS and of LRS, are presented in Fig. S1 (ESI†). At a readout voltage of +1 V, the LRS resistance ranges between 6 and 7 kΩ, while the HRS varies between 14 and 17 kΩ. During the *I–V*
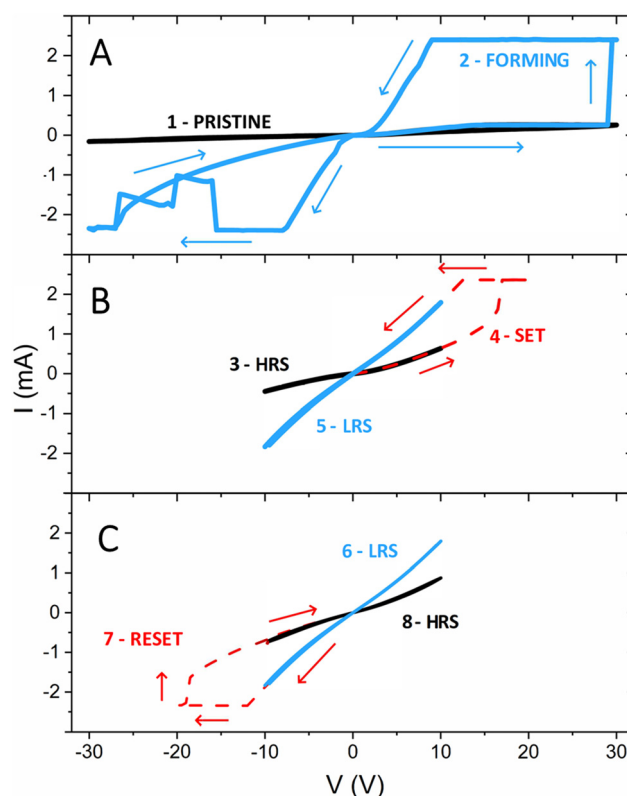

Fig. 3 *I–V* curves of the Ta/TiO$_2$/Pt device: (A) acquired before (curve 1) and after (curve 2) an X-ray irradiation line between two metal electrodes at maximum X-ray photon flux, inducing resistive switching; (B) readout of the high resistance state (HRS, curve 3), set process (curve 4) and readout of the low resistance state (LRS, curve 5); (C) readout of the LRS (curve 6), reset process (curve 7) and readout of the HRS (curve 8).
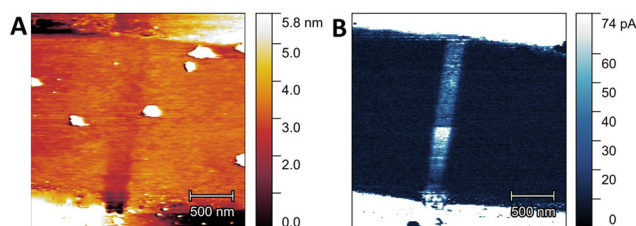

Fig. 2 Topographic AFM (A) and current C-AFM (B) maps of the Ta/TiO$_2$/Pt device after X-ray nanobeam irradiation without previously applying any bias.

measurements, the written states were stable over the observed time frame of a few minutes, demonstrating sufficient retention for this proof-of-principle experiment.

The observed behaviour is significantly different with respect to previous experiments performed on Au/TiO$_2$/Au samples where an increase of the material conductivity upon X-ray exposure was achieved, but no surface conductivity and reversible resistive switching were observed.[9] This observation can be explained by the absence of ohmic contacts leading to lower initial V$_O$ concentration in the material and to lower currents flowing between the two Au electrodes with more limited migration of the V$_O$ created by the X-ray nanobeam and less intense Joule heating. It is also important to note that for photon fluxes $<10^{10}$ ph s^{-1} (corresponding to an irradiance of $ca.$ 8×10^9 W m^{-2}) we observe only a volatile resistance decrease due to the presence of photogenerated electrons, which is proportional to the photon flux and is completely reversible upon stopping the irradiation, as discussed in detail in our previous publication.[9]

Fig. 4 shows the SEM images of the Ta/TiO$_2$/Pt device after the forming process. We can see an evident surface roughening in the tip of the Ta electrode, likely due to an oxidation process triggered by the high current flowing during the forming process. Moreover, we can note the presence of a bump between the electrodes in the region irradiated by the X-ray nanobeam.

A more detailed investigation was then performed using atomic force microscopy (Fig. 5). Topographic maps (Fig. 5A) highlight a local increase in the height of the crystal of about 100 nm, centered on the irradiated line. The bump has a conical shape, already observed in previous TEM studies of conductive filaments generated by electroforming in Pt/TiO$_2$/Pt stacks.[34] Considering that the Ta contact was grounded, while
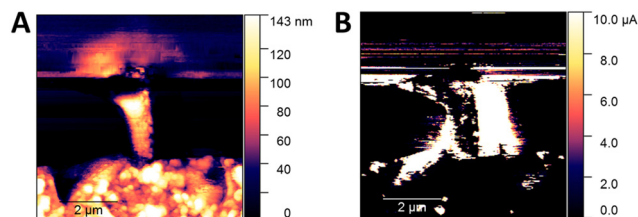

Fig. 5 Topographic AFM (A) and current C-AFM (B) maps of the Ta/TiO$_2$/Pt device after X-ray guided forming and electrical characterization (as shown in Fig. 3).

the Pt one was positively biased during the forming process, we can infer that the voltage applied promoted a reorganization of the oxygen vacancies generated by the X-ray nanobeam with a significant local increase of the current density. The consequent temperature rise due to Joule heating favors the diffusion and generation of V$_O$, which result in the growth of a conductive filament from the cathode toward the anode.[35]

Parallel C-AFM maps show (Fig. 5B) an increase in the surface conductivity of the TiO$_2$ crystal, which is more evident in the borders of the bump. A previous study[10] using space-resolved X-ray excited optical luminescence (XEOL) showed that these higher conductivity regions are associated with a lower intensity of a XEOL signal centered at 830 nm, which is attributed to the radiative recombination of electrons trapped in intra-band gap states with free holes in the valence band.[36] These states have been ascribed to the presence of lattice defects like V$_O$ or Ti interstitials.[37] Interestingly, it has been reported that an increasing concentration of V$_O$ is correlated to a decrease of this NIR photoluminescence emission[36] since these defects provide a non-radiative recombination path to photoexcited electrons. Thus, we could infer that, following X-ray guided forming, a higher concentration of V$_O$ is induced in our device in the regions around the bump. This hypothesis would also explain the increase in the electrical conductivity observed in our samples, since a higher concentration of V$_O$ at the Pt/TiO$_2$ interface lowers
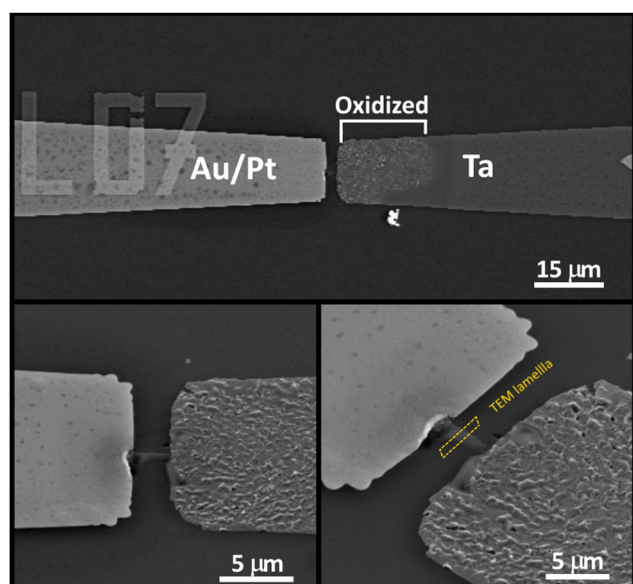

Fig. 4 SEM images of the Ta/TiO$_2$/Pt device after X-ray guided forming and electrical characterization (as shown in Fig. 3). The dotted yellow box highlights the part of the sample where the lamella for TEM analyses (see Fig. 6) has been cut.
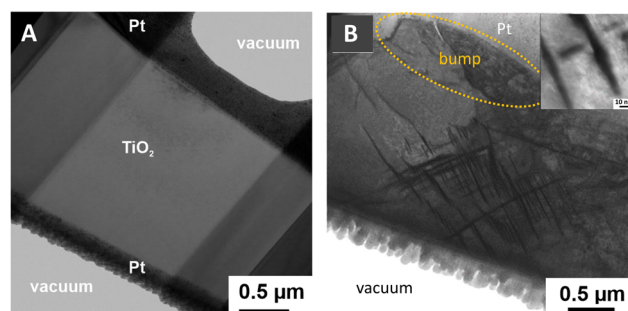

Fig. 6 BF-TEM images of lamellas obtained by FIB milling from (A) a pristine TiO$_2$ crystal and (B) the Ta/TiO$_2$/Pt device after X-ray guided forming and electrical characterization (as shown in Fig. 3). The part of the sample where the lamella has been cut is shown in Fig. 4. In (B), the protective platinum layer deposited during the FIB milling process is brighter than the TiO$_2$ crystal due to diffraction contrast. The bump region is highlighted by a dotted yellow ellipse. The inset shows a magnification of the dislocation region.

the Schottky barrier height, improving the injection of the charge carriers.[38,39]

Structural modifications occurring in the sample due to X-ray irradiation were investigated by BF-TEM analysis on a lamella cut by FIB milling (see the Experimental section) in the irradiated region, in the position shown in Fig. 4, to be compared with a similar lamella cut from a pristine TiO_2 sample. From Fig. 6A, we can see that, as expected, the pristine crystal does not show any evidence of structural defects. Conversely, in the top part of Fig. 6B, the bump region can be identified (marked by a dotted white ellipse), as already highlighted by SEM and AFM. Moreover, in the subsurface region close to the bump, we can note the presence of a dislocation network, better visible in the inset of Fig. 6B. These structures can be compatible with the presence of Wadsley defects, which are shear faults induced by an increased concentration of V_O, already observed in previous *in situ* TEM studies of rutile TiO_2 resistive switching under electrical bias.[40] This kind of defect has been reported to play an important role in the reduction process of TiO_2, which can lead to the formation of a variety of Magneli phases with the general stoichiometry Ti_nO_{2n-1}.[41,42] Indeed, according to the literature the process starts with the formation of some V_O, which can be hosted in a limited amount into the rutile lattice, then the V_O point defects start to aggregate along preferential crystallographic directions forming extended defects, which subsequently can possibly lead to a mixture of Ti_nO_{2n-1} compounds with different n.[43,44] Both experimental results and DFT calculations showed that ordered extended line defects, as the ones observed in Fig. 6B, allow electron conduction mediated by occupied defect states of Ti 3d character,[45,46] in agreement with the results obtained by C-AFM.

4. Conclusions

By exploiting the ability of intense synchrotron radiation X-ray nanobeams to locally generate oxygen vacancies (V_O) in oxides, we were able to realize conductive filaments in desired positions of our TiO_2 crystals between the Pt and Ta metal contacts. The successive application of suitable voltage pulses allowed us to order the X-ray induced V_O, achieving a significant local increase of the current density with associated Joule heating. This process favors the diffusion and generation of V_O, which leads to the growth of a conductive filament from the cathode toward the anode suitable for the device fabrication (for a complete scheme of the different steps of the X-ray nanopatterning process, see Fig. S2 in the ESI†). The I–V curves recorded after this electroforming procedure showed bipolar resistive switching. Moreover, (C-)AFM maps acquired on the final Ta/TiO_2/Pt device highlighted a local increase in the height of the crystal in the irradiated region, associated with a decrease of the surface electrical resistivity. BF-TEM analysis in the filament region confirms the formation of a dislocation network, ascribed to the aggregation of V_O point defects along preferential crystallographic directions to form extended line defects, which are involved in the increased electrical conduction. These

structures are compatible with the presence of Wadsley defects, which can possibly lead to the formation of Magneli phases.

The X-ray guided forming protocol discussed in this paper, although it was limited to a proof of concept and was not employed for the fabrication of a specific electronic device, can create new opportunities for fabricating oxide-based memristive devices. Specifically, this method could be utilized in future systematic studies to enhance process control and reduce the device-to-device variability possibly arising from conventional electroforming. Moreover, this study further confirms that the X-ray nanopatterning technique can be an effective tool for the nanofabrication of oxides, able to locally increase or decrease the material conductivity.

Author contributions

Lorenzo Mino: conceptualization, investigation, visualization, writing – original draft; Valentina Bonino: investigation, writing – review & editing, visualization; Andrea Alessio: investigation; Federico Picollo: investigation, visualization; Andrei Kuncser: investigation; Ionel Mercioniu: investigation; Aurel-Mihai Vlaicu: investigation; Petre Badica: investigation, writing – review & editing; Rosaria Brescia: investigation, visualization; Matteo Fretto: investigation; Kalle Goss: investigation; Regina Dittmann: conceptualization, supervision; Marco Truccato: investigation, conceptualization, supervision.

Data availability

The data are available from the corresponding author upon reasonable request.

Conflicts of interest

There are no conflicts to declare.

Acknowledgements

References

1 S. Okazaki, *Microelectron. Eng.*, 2015, **133**, 23–35.
2 E. Sharma, R. Rathi, J. Misharwal, B. Sinhmar, S. Kumari, J. Dalal and A. Kumar, *Nanomaterials*, 2022, **12**, 2754.

3 J. R. Maldonado and M. Peckerar, *Microelectron. Eng.*, 2016, **161**, 87–93.

4 F. Romanato, L. Businaro, L. Vaccari, S. Cabrini, P. Candeloro, M. De Vittorio, A. Passaseo, M. T. Todaro, R. Cingolani, E. Cattaruzza, M. Galli, C. Andreani and E. Di Fabrizio, *Microelectron. Eng.*, 2003, **67–8**, 479–486.

5 F. Cerrina, *J. Phys. D: Appl. Phys.*, 2000, **33**, R103–R116.

6 M. Truccato, A. Agostino, E. Borfecchia, L. Mino, E. Carat, A. Pagliero, N. Adhlakha, L. Pascale, L. Operti, E. Enrico, N. De Leo, M. Fretto, G. Martinez-Criado and C. Lamberti, *Nano Lett.*, 2016, **16**, 1669–1674.

7 A. Pagliero, L. Mino, E. Borfecchia, M. Truccato, A. Agostino, L. Pascale, E. Enrico, N. De Leo, C. Lamberti and G. Martinez-Criado, *Nano Lett.*, 2014, **14**, 1583–1589.

8 L. Mino, V. Bonino, A. Agostino, C. Prestipino, E. Borfecchia, C. Lamberti, L. Operti, M. Fretto, N. De Leo and M. Truccato, *Sci. Rep.*, 2017, **7**, 9066.

9 L. Mino, V. Bonino, F. Picollo, M. Fretto, A. Agostino and M. Truccato, *Adv. Electron. Mater.*, 2019, **5**, 1900129.

10 A. Alessio, V. Bonino, T. Heisig, F. Picollo, D. Torsello, L. Mino, G. Martinez-Criado, R. Dittmann and M. Truccato, *Phys. Status Solidi RRL*, 2021, **15**, 2100409.

11 J. J. S. Yang, D. B. Strukov and D. R. Stewart, *Nat. Nano-technol.*, 2013, **8**, 13–24.

12 M. A. Zidan, J. P. Strachan and W. D. Lu, *Nat. Electron.*, 2018, **1**, 22–29.

13 R. Dittmann and J. P. Strachan, *APL Mater.*, 2019, **7**, 110903.

14 X. Duan, Z. Cao, K. Gao, W. Yan, S. Sun, G. Zhou, Z. Wu, F. Ren and B. Sun, *Adv. Mater.*, 2024, **36**, 2310704.

15 B. Sun, Y. Chen, G. Zhou, Z. Cao, C. Yang, J. Du, X. Chen and J. Shao, *ACS Nano*, 2024, **18**, 14–27.

16 K. X. Sun, J. S. Chen and X. B. Yan, *Adv. Funct. Mater.*, 2021, **31**, 2006773.

17 S. Kim, S. Choi and W. Lu, *ACS Nano*, 2014, **8**, 2369–2376.

18 S. Menzel, U. Bottger, M. Wimmer and M. Salinga, *Adv. Funct. Mater.*, 2015, **25**, 6306–6325.

19 J. H. Yoon, J. M. Zhang, X. C. Ren, Z. R. Wang, H. Q. Wu, Z. Y. Li, M. Barnell, Q. Wu, L. J. Lauhon, Q. F. Xia and J. J. Yang, *Adv. Funct. Mater.*, 2017, **27**, 9.

20 C. Baeumer, R. Valenta, C. Schmitz, A. Locatelli, T. O. Mentes, S. P. Rogers, A. Sala, N. Raab, S. Nemsak, M. Shim, C. M. Schneider, S. Menzel, R. Waser and R. Dittmann, *ACS Nano*, 2017, **11**, 6921–6929.

21 M. Rao, H. Tang, J. Wu, W. Song, M. Zhang, W. Yin, Y. Zhuo, F. Kiani, B. Chen, X. Jiang, H. Liu, H. Y. Chen, R. Midya, F. Ye, H. Jiang, Z. Wang, M. Wu, M. Hu, H. Wang, Q. Xia, N. Ge, J. Li and J. J. Yang, *Nature*, 2023, **615**, 823–829.

22 L. Mino, G. Agostini, E. Borfecchia, D. Gianolio, A. Piovano, E. Gallo and C. Lamberti, *J. Phys. D: Appl. Phys.*, 2013, **46**, 423001.

23 L. Mino, E. Borfecchia, J. Segura-Ruiz, C. Giannini, G. Martinez-Criado and C. Lamberti, *Rev. Mod. Phys.*, 2018, **90**, 025007.

24 J. Cazaux, *J. Microsc.*, 1997, **188**, 106–124.

25 S. P. Hau-Riege, *High-Intensity X-Rays Interaction with Matter*, Wiley-VCH, Weinheim, 2011.

26 D. Torsello, L. Mino, V. Bonino, A. Agostino, L. Operti, E. Borfecchia, E. Vittone, C. Lamberti and M. Truccato, *Phys. Rev. Mater.*, 2018, **2**, 014801.

27 M. L. Knotek and P. J. Feibelman, *Surf. Sci.*, 1979, **90**, 78–90.

28 S. Tanaka, K. Mase and S. Nagaoka, *Surf. Sci.*, 2004, **572**, 43–58.

29 P. Knauth and H. L. Tuller, *J. Appl. Phys.*, 1999, **85**, 897–902.

30 M. K. Nowotny, T. Bak and J. Nowotny, *J. Phys. Chem. B*, 2006, **110**, 16270–16282.

31 L. Mino, E. Borfecchia, A. Agostino, C. Lamberti and M. Truccato, *J. Electron Spectrosc. Relat. Phenom.*, 2017, **220**, 69–75.

32 V. Bonino, D. Torsello, C. Prestipino, L. Mino and M. Truccato, *J. Synchrot. Radiat.*, 2020, **27**, 1662–1673.

33 D. S. Jeong, H. Schroeder and R. Waser, *Electrochem. Solid-State Lett.*, 2007, **10**, G51–G53.

34 D. H. Kwon, K. M. Kim, J. H. Jang, J. M. Jeon, M. H. Lee, G. H. Kim, X. S. Li, G. S. Park, B. Lee, S. Han, M. Kim and C. S. Hwang, *Nat. Nanotechnol.*, 2010, **5**, 148–153.

35 K. C. Tang, A. C. Meng, F. Hui, Y. Shi, T. Petach, C. Hitzman, A. L. Koh, D. Goldhaber-Gordon, M. Lanza and P. C. McIntyre, *Nano Lett.*, 2017, **17**, 4390–4399.

36 D. K. Pallotti, L. Passoni, P. Maddalena, F. Di Fonzo and S. Lettieri, *J. Phys. Chem. C*, 2017, **121**, 9011–9021.

37 S. Wendt, P. T. Sprunger, E. Lira, G. K. H. Madsen, Z. S. Li, J. O. Hansen, J. Matthiesen, A. Blekinge-Rasmussen, E. Laegsgaard, B. Hammer and F. Besenbacher, *Science*, 2008, **320**, 1755–1759.

38 Y. G. Zhou, Z. Z. Zhang, Z. W. Fang, M. Qiu, L. Ling, J. L. Long, L. Chen, Y. C. Tong, W. Y. Su, Y. F. Zhang, J. C. S. Wu, J. M. Basset, X. X. Wang and G. H. Yu, *Proc. Natl. Acad. Sci. U. S. A.*, 2019, **116**, 10232–10237.

39 T. Tamura, S. Ishibashi, K. Terakura and H. M. Weng, *Phys. Rev. B: Condens. Matter Mater. Phys.*, 2009, **80**, 195302.

40 R. J. Kamaladasa, A. A. Sharma, Y. T. Lai, W. Chen, P. A. Salvador, J. A. Bain, M. Skowronski and Y. N. Picard, *Microsc. Microanal.*, 2015, **21**, 140–153.

41 K. Szot, C. Rodenbücher, G. Bihlmayer, W. Speier, R. Ishikawa, N. Shibata and Y. Ikuhara, *Crystals*, 2018, **8**, 241.

42 Y. Liu, J. Yang, Y. Liu, J. Zheng, W. Lee, J. Shi, J. Horlyck, J. Xie, Y. Y. Tay, T. T. Tan, D. Yu, R. Mole, G. McIntyre, C. Zhang, C. Y. Toe, T. D. Waite, J. Scott, Y. Wang, T. Wu, S. Han and S. Li, *Energy Environ. Sci.*, 2020, **13**, 5080–5096.

43 K. Szot, M. Rogala, W. Speier, Z. Klusek, A. Besmehn and R. Waser, *Nanotechnology*, 2011, **22**, 254001.

44 X. Wu, N. Yang, Y. Ji, X. He, Q. Li, R. Jiang, Z. Lei, Z. Liu and J. Sun, *CrystEngComm*, 2023, **25**, 1146–1158.

45 S. G. Park, B. Magyari-Kope and Y. Nishi, *IEEE Electron Device Lett.*, 2011, **32**, 197–199.

46 M. Rogala, G. Bihlmayer, W. Speier, Z. Klusek, C. Rodenbücher and K. Szot, *Adv. Funct. Mater.*, 2015, **25**, 6382–6389.